UNIVERSITÉ D'ORLÉANS

ÉCOLE DOCTORALE SCIENCES ET TECHNOLOGIES

Institut des Sciences de la Terre d'Orléans

THÈSE présentée par :

Anne POMMIER

soutenue le : **23 novembre 2009**

pour obtenir le grade de : **Docteur de l'université d'Orléans**

Discipline : Sciences de la Terre et de l'Univers

Propriétés électriques des magmas

THÈSE dirigée par :
Michel PICHAVANT Directeur de recherche, ISTO, Orléans

RAPPORTEURS :
Roberto SCANDONE Professeur, Università di Roma 3, Italie
Benoît VILLEMANT Professeur, IPG, Paris, France

JURY:

Pascal TARITS	Professeur, IUEM, Brest, Président du jury
Roberto SCANDONE	Professeur, Università di Roma 3, Italie, Rapporteur
Benoît VILLEMANT	Professeur, IPG, Paris, Rapporteur
Reid F. COOPER	Professeur, Brown University, USA, Examinateur
Mohammed MALKI	Professeur, Université d'Orléans, Examinateur
Mathieu ROSKOSZ	Maître de conférences, Université de Lille 1, Examinateur
Michel PICHAVANT	Directeur de recherche, ISTO, Orléans, Directeur de thèse
Fabrice GAILLARD	Chargé de recherche, ISTO, Orléans, Co-encadrant

ἕν οἶδα ὅτι οὐδὲν οἶδα.

A Alphonsine Mossand,
Charlotte Pommier
et Marie-Jean Mossand

REMERCIEMENTS

Ma première pensée est pour Michel. Merci de m'avoir tendu la main il y a six ans, lorsque je suis venue frapper à votre porte avec la volonté quelque peu tenace d'étudier la volcanologie… Je vous remercie de votre confiance, d'avoir cru en moi, de votre patience aussi (!) et de votre bienveillance. Merci pour le soutien sans faille que vous m'avez accordé et pour avoir été là dans les moments difficiles, de manière à la fois discrète, délicate et prévenante. Un grand merci à mon co-encadrant, Fabrice, pour sa confiance, son dynamisme, sa bonne humeur (et sa patience aussi…), pour ses idées et conseils géniaux. J'ai bénéficié d'un encadrement de thèse extraordinaire grâce à ces deux personnes et je suis la première à en mesurer la chance. Me permettre d'être autonome et de m'épanouir dans mon travail, être toujours disponible pour discuter, me donner l'opportunité de présenter nos résultats dans les congrès… la liste est longue. Je tiens à leur témoigner ma profonde reconnaissance et mon infini respect. Je remercie tous les autres membres du jury pour m'avoir fait l'honneur de considérer mon travail et d'avoir participé à ma soutenance.

Merci à Pascal Tarits et Sophie Hautot pour cette très belle collaboration géophysique. J'ai adoré travailler avec vous deux à l'IUEM dans une atmosphère non seulement très productive mais aussi très amicale et je vous remercie d'avoir pris le temps de me faire découvrir la MT (ce qui était un challenge !)… Je remercie également Mohammed Malki pour m'avoir permis de réaliser des expériences au CEMHTI et pour sa gentillesse. Ringrazio un altro collaboratore ed amico, Luca Carrichi. E stato un piacere andare all'AGU, discovere « la Paterson » e parlare della cucina della pasta con te ! Tante grazie. Merci à Bruno Scaillet pour son style direct et les discussions fructueuses, en particulier en ce qui concerne le Vésuve. Je suis reconnaissante à l'université de Bari et à l'INGV-Napoli pour m'avoir accueillie pendant quelques semaines.

Le travail que j'ai effectué pendant ma thèse n'aurait été possible sans les compétences de nombreuses personnes de l'ISTO. En particulier, je remercie Rémi Champallier, Philippe Teulat, Jean-Michel Bény, Olivier Rouer, Nathalie Pothier, Didier Bellenoue et Laurent Peilleron. Merci aux autres membres de l'ISTO à qui j'ai eu à faire pendant ces années. J'adresse un immense merci à ma courageuse collègue de bureau, Mouna ElMekki, pour son soutien dans les moments durs et son amitié précieuse. Je remercie aussi chaleureusement Jon Castro, Mattia Pistone et Mickaël Laumonier. Merci à mes étudiants de Polytech', qui ont pris part à mon expérience de l'enseignement, m'ont donné confiance en moi et m'ont évité de mettre des œillères en me focalisant sur ma thèse, ainsi qu'à mes collègues moniteurs pour leur sympathie, en particulier Mourad Essalhi.

J'adresse ma profonde reconnaissance à celui qui est un ami très cher plus qu'un collègue, Alain Burgisser (compatriote de Jean-Jacques, qui plus est...!). Merci pour ton soutien, ton écoute, tes conseils toujours avisés et surtout pour ces discussions qui m'ont si souvent soustraite au quotidien. Merci à toi et Tina pour tous ces bons moments partagés que je ne suis pas prête à oublier. Qu'Alexandre Dumas, Ayn Rand, Michel Butor (!) et les autres viennent peupler nos discussions pendant encore longtemps…

Je remercie mes Parents, ma sœur Sophie, Nicolas et leur petit rayon de soleil Alexandre (ma petite Luciole) pour leur affection. Un grand merci également aux familles Mossand et Polyak pour leur adorable soutien depuis huit ans. Je remercie infiniment « mon grand frère » Seb (Lami), Fred et David, dont l'amitié me donne tant d'énergie depuis des années. Merci à vous d'être toujours là… et de rêver avec moi sous les étoiles. J'adresse ma profonde reconnaissance à Jacques-Marie, la seconde main tendue à Orléans, sans laquelle il m'aurait été difficile de tracer ma route. Merci de m'avoir entendue, et pas seulement écoutée… Merci enfin à toutes ces autres personnes qui comptent, en particulier Guillaume, et aussi Emilie, Alexandre et François.

Table des matières *Table of contents*

Chapitre 1 : Introduction générale *General introduction* 11

Summary 17
Approches et objectifs (*Approaches and objectives*) 18

Chapitre 2 : Techniques expérimentales et analytiques *Experimental and analytical techniques* 27

Objectifs de ce chapitre 29
2.1. Matériaux de départ 31
2.2. Synthèse des verres et préparation des échantillons 31
2.2.1. Obtention d'un verre 31
2.2.2. Hydratation en autoclave à chauffage interne 32
2.2.3. Préparation de l'échantillon pour la cellule de mesure électrique 35
2.3. Appareillage expérimental et analytique 35
2.4. Analyses au microscope, MEB et microsonde électronique 36
2.5. Détermination de la teneur en eau 37
2.6 Analyse du FeII/FeIII 38
2.7. Mesure des propriétés électriques 40
2.7.1. Mesure de la conductivité électrique des verres et liquides silicatés par spectroscopie d'impédance : concepts de base 40
2.7.2. Acquisition des données 41
2.8. Re-évaluation de la conductivité électrique des melts silicatés 46
Références 47

Re-evaluation of the electrical conductivity of silicate melts (article) 49
Abstract 49
1. Introduction 49
2. Experiments 51
2.1. Starting products 51
2.2. Basic concepts of complex impedance measurements 51
2.3. Experimental setups 52
2.4. Reduction of the data and calibration 55
2.5. Chemical characterization of the samples 56
3. Results 56
4. Discussion 59
5. Conclusion 65
Acknowledgements 65
References 65

Chapitre 3 : Propriétés électriques des magmas hydratés et anhydres sous pression *Electrical properties of hydrous and dry magmas under pressure* 69

Objectifs de ce chapitre 71

Laboratory measurements of electrical conductivity of hydrous and dry Mt. Vesuvius melts under pressure (article) 73
Abstract 73
1. Introduction 74
2. Basic concepts of electrical conductivity and previous works 75
3. Experiments 77
3.1. Starting products 77
3.2. Experimental equipment and procedures 79
3.3. Analytical techniques 80
3.4. Conductivity measurements 80
3.4.1. Conductivity cell and electrical measurements 80
3.4.2. Data reduction 85
4. Results 87
4.1. Interaction processes between conductivity cell and sample 87
4.2. Effect of temperature and melt composition 88
4.3. Effect of pressure 90
4.4. Effect of water 92
5. Discussion 93
5.1. Transport mechanisms 93
5.2. Calculation of electrical conductivity of natural melts 97
5.3.Volcanological implications for Mt. Vesuvius 99
6. Conclusions 100
Acknowledgments 101
References 102

Appendices (Appendixes) 108
Appendice 1 : Effet des cristaux et des bulles sur la conductivité électrique 108
A.1.1. Intégration de l'effet des cristaux par des formalismes mathématiques 108
A.1.2. Importance de l'effet des bulles sur la conductivité électrique 111
Appendice 2 : Temps de relaxation électrique 114
A.2.1. Définition et calcul du temps de relaxation électrique 114
A.2.2. Effet des différents paramètres sur le temps de relaxation électrique 115
A.2.3. Comparaison avec le temps de relaxation obtenu par des mesures de viscosité 118
Références 120

Chapitre 4 : Modèle direct de la conductivité électrique du Vésuve *Forward modelling of the electrical conductivity of Mount Vesuvius* 123

Objectifs de ce chapitre 125

A new petrological and geophysical investigation of the present-day plumbing system of Mount Vesuvius (article) 127
Abstract 127
1. Introduction 128
2. Volcanological background and petrological constraints 129
3. Laboratory and field electrical studies applied to Mount Vesuvius 132
4. Petro-physical resistivity model 135
5. Results 140
5.1. Effect of a superficial conductor on the electrical response 140
5.2. Effect of a deep conductive body 142
5.3. Joint effect of shallow and deep conductive bodies 142
6. Discussion 148

6.1. Brine storage conditions 148
6.2. Conditions on the presence of magma at a shallow depth (depth <3-4km) 149
6.2.1. Hypothesis of a shallow magma chamber 149
6.2.2. Cooling intrusion from the 1631-1944 period 150
6.3. Possible deep magma chamber beneath Mount Vesuvius (depth >3-4km) 150
6.4. Comparison with seismic wave velocities 153
7. Conclusions 154
Acknowledgements 154
References 155

Chapitre 5 : Etude cinétique de l'état redox des liquides basaltiques par la lorgnette de la conductivité électrique *Study of the kinetics of the redox state of basaltic liquids using the electrical conductivity* 163

Objectifs de ce chapitre 165

Study of the kinetics of the redox state of basaltic liquids using the electrical conductivity (article) 167
Abstract 167
1. Introduction 167
2. Previous works 168
3. Experiments 170
3.1. Starting products 170
3.2. Experimental setup 171
3.3. Experimental strategy 172
3.4. Acquisition and reduction of the electrical data 176
3.5. Analytical techniques 177
4. Results 178
4.1. Melt-conductivity cell interactions 178
4.2. Effect of oxygen fugacity and temperature on the electrical conductivity 179
4.3. Time-dependent changes in electrical conductivity during redox reaction 182
4.4. Variations in major element chemical concentrations 184
4.5. FeO concentrations and evolution of glass Fe^{2+}/Fe^{3+} 186
5. Discussion 186
5.1. Ferrous / ferric ratio and electrical conductivity 186
5.1.1. Why does the ferrous/ferric ratio change the electrical conductivity ? 186
5.1.2. Time evolution of the electrical conductivity and ferrous/ferric ratio 188
5.2. Determination of a bulk diffusion coefficient and transport properties 189
5.3. Redox dynamics 192
6. Conclusion and redox exchanges in Nature 198
Acknowledgements 199
References 199
Appendix1: On the difference between oxygen self-diffusion and chemical diffusion coefficients 204
Appendix2: Estimation of a normalized driving force 205
Appendix3: Relation of the mobile species fluxes to the evolution of the inner redox front 206

Chapitre 6 : Bilan et conclusions *Summary and conclusions* 209

Suggestions pour de prochaines études (*Suggestions for future research*) 214

Chapitre 1

Introduction générale

(General introduction)

Par définition, un magma (du grec τὸ μαγμα : pâte pétrie) est une suspension de liquide (couramment appelé *melt*[1] dans la suite du manuscrit), de cristaux et de bulles. Les propriétés physiques et chimiques des melts silicatés reflètent leur structure, gouvernée par diverses interactions à l'échelle atomique (Navrotsky, 1995). La connaissance des propriétés physico-chimiques des magmas permet de localiser, de caractériser et de suivre l'évolution des magmas dans la croûte et le manteau terrestres. Des études spectroscopiques (par ex. Allwardt et al., 2004) ont montré que les études in-situ sont nécessaires pour étudier la structure des silicates. Par ailleurs, certaines propriétés fondamentales étant communes aux magmas, verres et céramiques, l'étude des magmas ne s'attache pas seulement à interpréter des problèmes géologiques, mais trouve également une application au monde industriel (biens manufacturés, stockage des déchets).

Les mesures électriques sur des électrolytes solides en laboratoire ont été considérablement développées par la communauté des sciences des matériaux, à partir de la seconde moitié du XXème siècle. En effet, l'électrochimie des solides à haute température a des applications industrielles fondamentales liées aux techniques de stockage et aux procédés de conversion d'énergie. La théorie des propriétés électriques des électrolytes solides s'est inspirée de celle développée antérieurement pour les électrolytes liquides, en particulier les solutions aqueuses (Noyes et al., 1907 ; Fogo et al., 1954 ; Franck, 1956 ; Quist and Marshall, 1968).

Un défi majeur pour les mesures électriques a été de s'affranchir des phénomènes de polarisation au sein des matériaux, qui peuvent se définir comme la séparation des charges électriques positives et négatives sous l'influence d'un champ électrique. Une solution pour réduire ce problème est de faire circuler dans la cellule de mesure un courant faible, ce qui permet d'éviter des effets de chauffage, de changements irréversibles au niveau des électrodes et donc d'éliminer certains problèmes de polarisation. Par ailleurs, la réponse électrique d'un semi-conducteur (conductivité et constante diélectrique) montrant une dispersion en fonction de la fréquence (Koops, 1951), les études se sont orientées vers des mesures de la réponse

[1] Le terme de melt fait référence à un passage de l'état solide (vitreux) à l'état liquide. Une traduction de « silicate melt » par « liquide silicaté » ne serait ni complète, ni totalement correcte (par ex., Kress et al., 1989). « Liquide surfondu » est une traduction possible. Cependant, le terme « melt » étant couramment utilisé, cet anglicisme sera utilisé dans la suite du manuscrit.

électrique de la cellule en faisant varier la fréquence et en faisant circuler un faible courant. Reste à discriminer, lors de l'analyse de cette réponse électrique, les autres phénomènes de polarisation persistants créés dans la cellule de mesure. Différentes méthodes de visualisation des données ont alors été développées. Elles sont basées sur des représentations graphiques complexes (partie réelle vs partie imaginaire) de différentes grandeurs : l'impédance complexe Z* (Armstrong et al., 1975), l'admittance complexe Y*=1/Z* (Bauerle, 1969), la permittivité complexe ε* (McCrum et al., 1967) et le module complexe M*=1/ε* (Grant et al., 1977). Ces études portent le plus souvent sur des solides polycristallins (par exemple, la β-alumine (Hodge et al., 1976 ; Grant et al., 1977)). Les deux grandeurs les plus couramment utilisées, à savoir l'impédance et le module complexes, sont complémentaires, l'impédance permettant de distinguer les effets inter-cristallins (électrodes, joints de grains) et le module les effets intra-cristallins (grains) (Grant et al., 1977).

Les études présentées dans le présent manuscrit concernent les mesures d'impédance complexe. Par définition, l'impédance électrique, qui est un nombre complexe, mesure l'opposition totale au flux de courant en réponse à un signal AC (Roberts and Tyburczy, 1999). (Notons que le courant électrique utilisé pour les études électriques est le plus souvent alternatif (AC), car, contrairement à un courant continu (DC), il limite le phénomène de polarisation à l'interface avec les électrodes). La technique adoptée est la spectroscopie d'impédance, appliquée pour la première fois aux électrolytes solides par Bauerle (1969). Cette technique est efficace pour étudier les processus de conduction à haute température dans les solides, car elle permet de discriminer les différents effets de polarisation observés lors d'un scan en fréquence (Bruin and Franklin, 1981 ; Déportes et al., 1994). Des techniques de mesure électrique autres que la spectroscopie d'impédance ont été utilisées antérieurement à Bauerle (1969) pour mesurer la réponse électrique de matériaux, comme celles de Bockris et al. (Bockris et al., 1952 ; Bockris and Mellors, 1956) ou celles de Volarovich, pionnières en ce qui concerne l'application des mesures électriques acquises à différentes pressions et températures aux matériaux géologiques (Volarovich and Tolstoi, 1936 ; Volarovich and Bondarenko, 1960 ; Volarovich et al., 1962). Les mesures d'impédance électrique des matériaux géologiques se concrétisent dans la seconde moitié du XXème siècle. Les études concernent aussi bien les minéraux, les roches que les verres et liquides silicatés (synthétiques et naturels) (Tyburczy et Fisler, 1995). L'interprétation des spectres d'impédance des matériaux géologiques a été étudiée en détail (Roberts et Tyburczy, 1994 ; Huebner et Dillenburg, 1995, Roling, 1999). Contrairement à la communauté de science des matériaux qui effectue principalement des mesures à quatre électrodes (e.g. Malki and Echegut, 2003), la

communauté géologique effectue des mesures à deux électrodes, incluant la contribution des électrodes à la conductivité mesurée. Une étude méthodologique approfondie a été établie dans cette thèse pour qualifier et quantifier l'importance de l'effet des électrodes (Pommier et al., 2009, AmMin, sous presse).

Une application fondamentale des mesures électriques sur des matériaux géologiques concerne l'évaluation des risques volcaniques, via la caractérisation des réservoirs magmatiques présents sous les volcans actifs, et aussi des réservoirs de magma stockés à plus grande profondeur (asthénosphère). En effet, l'étude des propriétés électriques des roches, melts silicatés et minéraux en laboratoire permet de mieux comprendre la réponse électrique du terrain et notamment d'interpréter les anomalies détectées par les sondages électromagnétiques.

De nombreuses études concernent le principal minéral présent dans le manteau, à savoir l'olivine et ont caractérisé la dépendance de la réponse électrique de ce minéral à la température (T), la pression (P), la fugacité en oxygène (fO_2) et l'orientation cristallographique des grains (par ex. Duba, 1972 ; Sato, 1986 ; Wanamaker, 1994 ; Schock et al., 1989 ; Wanamaker and Duba, 1993a,b ; Constable and Duba, 1990, 2002 ; Constable and Roberts, 1997 ; ten Grotenhuis et al., 2004; Du Frane et al., 2005). Les propriétés électriques des roches partiellement fondues ont été étudiées dans des conditions de pression et température pertinentes pour le manteau (Shankland and Waff, 1977 ; Roberts and Tyburczy, 1994, 1999 ; Partzsch et al., 2000 ; Yoshino et al., 2004 ; Maumus et al., 2005). Des modèles ont été proposés à partir de ces mesures en laboratoire pour reproduire les différentes conductivités du manteau terrestre (Wannamaker, 1986 ; Xu et al., 2000 ; Park and Ducea, 2003 ; Toffelmier and Tyburczy, 2007). Les mesures électriques en laboratoire sont un outil nécessaire aux magnétotelluriciens avec, par exemple, l'identification de zones de stockage de magma détectées dans l'asthénosphère (par ex., Yoshino et al., 2006).

Les études des propriétés des magmas à des conditions crustales sont un peu moins répandues. Si quelques études se sont intéressées aux magmas peu riches en alcalins (basaltes à dacite) (Waff and Weill, 1975 ; Rai and Manghnani, 1977 ; Tyburczy and Waff, 1983, 1985 ; Scarlato et al., 2005), ce n'est que récemment que des études approfondies sur d'autres types de magmas ont été réalisées (Gaillard, 2004 concernant une rhyolite, Pommier et al. 2008 concernant les compositions tephritiques à phonolitiques, Poe et al., 2008, concernant une tephriphinolite). L'effet des volatils (en particulier celui de l'eau) sur la conductivité électrique des liquides silicatés à ces conditions crustales a été peu étudié (Lebedev and

Khitarov, 1964 ; Satherley and Smedley, 1985 ; Gaillard, 2004 ; Pommier et al., 2008-Chapitre 3) et seuls les travaux de Gaillard et Pommier et al. ont bénéficié des progrès relatifs à la précision de la mesure de la conductivité électrique (spectroscopie d'impédance). Le lien entre mesures électriques en laboratoire et sur le terrain (magnétotellurique) est abordé dans cette thèse d'une manière tout à fait nouvelle qui consiste à utiliser les données en laboratoire et les observations du terrain pour établir un modèle direct de la conductivité d'un édifice volcanique. Cette étude a été appliquée au Vésuve, dont l'intérêt réside dans la dangerosité de ce volcan situé dans une zone très densément peuplée.

Le présent manuscrit s'est focalisé sur les mesures électriques en les reliant aux propriétés physico-chimiques des melts silicatés. Un autre objectif fondamental des mesures électriques en laboratoire est d'explorer les propriétés de transport dans les verres et liquides silicatés, de manière à comprendre les modalités des processus de diffusion au sein des matériaux, à l'échelle microscopique (atomique). La transition vitreuse (Tg) peut être clairement identifiée au moyen des mesures électriques (Bagdassarov et al., 2004 ; Pommier et al., 2008). Ainsi, l'étude des mécanismes de transport a concerné à la fois le domaine vitreux (T<Tg) et le domaine liquide (T>Tg). La connaissance issue des études en science des matériaux, avec notamment la détermination de l'énergie d'activation et aussi du temps de relaxation (Moynihan, 1998), peut s'appliquer aux matériaux géologiques. Elle identifie un transport « activé » dans le domaine vitreux et un transport « assisté (et activé) » dans le domaine liquide, les deux mécanismes reposant sur la formation de défauts responsables du transport et la migration dans le verre des porteurs de charge correspondants (Déportes et al., 1994). Les études dans le domaine vitreux ont montré que les conductivités électronique et ionique contribuent à la conductivité globale (Cooper et al., 1996), la conductivité électronique étant particulièrement importante dans les verres riches en fer (Barczynski and Murawski, 2002). Le domaine liquide est caractérisé par une conductivité d'origine ionique (cationique) et les alcalins ont été identifiés comme étant les principaux porteurs de charge dans les melts silicatés (Heinemann and Frischat, 1992 ; Kanehisa, 1992 ; Gaillard, 2004 ; Pommier et al., 2008), car étant les espèces les plus mobiles (Jambon and Carron, 1976 ; Jambon, 1982 ; Henderson et al., 1985 ; Dunn and Ratliffe, 1990 ; Roselieb and Jambon, 1997). La conduction des protons et leur spéciation dans les melts silicatés hydratés soulève le problème de leur contribution dans la conductivité mesurée : si l'eau est sous forme d'espèce chargée (H^+, H_3O^+), elle est porteuse de charge alors que s'il s'agit d'une espèce neutre (H_2, OH, H_2O), son rôle consistera à faciliter la mobilité des alcalins à l'intérieur de la structure

(*silica framework*) et son effet sur la conductivité sera indirect. La seconde hypothèse semble être privilégiée (Zhang and Stolper, 1991 ; Behrens et al., 2002 ; Gaillard et al., 2003).

Si des études ont tenté de relier conductivité électrique et viscosité (par ex. Pfeiffer, 1998), une correspondance directe est difficile à établir entre les deux grandeurs physiques, la viscosité s'attachant essentiellement à la structure du melt, dominée par l'assemblage de tétraèdres de silice, alors que la conductivité traduit la mobilité des porteurs de charge. Le lien entre diffusion du porteur de charge (auto-diffusion) et conductivité est beaucoup plus évident, permettant d'identifier les contributions individuelles des espèces mobiles (utilisation de la formule de Nernst-Einstein (cf Chapitres 3 et 5). Cette thèse a montré qu'il est aussi possible de relier diffusion chimique et conductivité électrique, en utilisant la réponse électrique d'un liquide silicaté pour suivre la cinétique de réactions chimiques, notamment des réactions redox (Pommier et al., 2009, en révision).

Summary

In situ measurements are requested to understand the physical and chemical properties of magmas. Electrical measurements have been developed by the material science community and have been then applied to geological materials. With the intention of minimizing polarization phenomena, improvements of electrical measurements considered scans in frequency with a low current. Different methods exist, the most common consisting in the measurement of the complex impedance. This method is the one used in this manuscript. Impedance spectroscopy measures the total opposition to current flow in response to an AC signal. Two main techniques are used, based on two- and four-electrode measurements. We conducted a methodological study that allowed to qualify and to quantify for both setups the importance of the electrode effect on the measured conductivity.

A fundamental application of electrical measurements performed on geological materials consists in the interpretation of electrical anomalies in the Earth's crust and mantle. If numerous studies have investigated the electrical properties of mantle rocks and minerals, few are dedicated to the electrical response of magmas at conditions relevant to study the Earth crust. We investigated the electrical properties of Mount Vesuvius magmas and linked laboratory and field measurements through the elaboration of a forward model of the electrical conductivity of the volcanic edifice.

The electrical measurements performed in this manuscript have been related to the transport properties of the investigated silicate melts and glasses with, in particular, the identification of the glass transition and the determination of activation energies. The

correlation between self-diffusivities of mobile species and conductivity allowed the identification of the main charge carriers in the investigated samples (using the Nernst-Einstein equation). We also showed that it is possible to use the electrical response of a sample to monitor in real time the kinetics and diffusion mechanisms of a chemical reaction.

Approches et objectifs *(Approaches and objectives)*

Le présent manuscrit est organisé en chapitres individuels, chacun comportant un article publié, accepté, en révision ou prochainement soumis. Par conséquent, chaque chapitre possédant sa propre introduction, il ne sera présenté ici qu'une simple vue d'ensemble.

Les objectifs de cette thèse sont triples : 1) Acquérir des données expérimentales sur les variations du comportement électrique des liquides et verres silicatés en fonction de leur composition, teneur en eau, température, pression et fugacité en oxygène et les interpréter en termes de propriétés de transport. 2) Joindre à ces données expérimentales des contraintes pétrologiques et des données géophysiques pour établir un modèle direct de la conductivité électrique d'un édifice volcanique (en l'occurrence, le Vésuve). 3) Utiliser l'outil conductivité électrique comme sonde pour étudier l'évolution d'une réaction chimique (oxydoréduction), à l'échelle atomique, au sein d'un magma.

Le chapitre 2 fournit une description détaillée des techniques expérimentales et analytiques utilisées, en particulier en ce qui concerne l'acquisition des données électriques en fonction des différents paramètres mentionnés ci-dessus. La stratégie expérimentale ainsi que les problèmes rencontrés sont discutés. L'investigation méthodologique de la technique de spectroscopie d'impédance est illustrée par l'article intitulé "Re-evaluation of the electrical conductivity of silicate melts" (*American Mineralogist*, sous presse), qui est une étude réalisée en collaboration avec M. Malki (CEMHTI, Orléans).

Le chapitre 3 présente les résultats des mesures électriques effectuées sur différents produits éruptifs du Vésuve, sur une large gamme de température (domaines vitreux et liquide), de pression, de composition et de teneur en eau. Un modèle de la conductivité électrique des magmas du Vésuve est proposé et une première comparaison avec les données du terrain est ébauchée. Cette étude est intitulée "Laboratory measurements of hydrous and dry Mt. Vesuvius melts", publiée au *Journal of Geophysical Reasearch*, 2008. Le passage de la conductivité électrique d'un verre ou d'un melt à celle d'un magma est abordé via la discussion de modèles mathématiques intégrant l'effet des cristaux. Une expérience de

décompression réalisée sur une obsidienne hydratée a également permis d'aborder l'effet des bulles sur la conductivité. Une dernière section est dédiée au temps de relaxation électrique.

Le chapitre 4 est dédié à la concrétisation du lien entre mesures expérimentales en laboratoire et mesures sur le terrain (magnétotelluriques). Il s'agit de la construction d'un modèle direct de la conductivité électrique au Vésuve, à partir des mesures électriques présentées dans le Chapitre 3, de profils magnétotelluriques, de contraintes pétrologiques et de données géochimiques de la littérature. L'initiation à la technique de mesure électrique sur le terrain (mesures magnétotelluriques) s'est effectuée avec A. Siniscalchi (Università di Bari) et Z. Petrillo (INGV, Napoli). L'élaboration du modèle direct est le fruit d'une collaboration avec P. Tarits et S. Hautot (IUEM, Brest). Cette étude est présentée sous la forme d'un article prochainement soumis à G-cubed (*Geochemistry Geophysics Geosystems*), intitulé "Forward modelling of the electrical conductivity of Mount Vesuvius".

Le chapitre 5 est consacré à l'étude des cinétiques et des mécanismes redox dans les melts basaltiques. Les mesures électriques sont utilisées ici comme sonde pour étudier les changements de la réponse électrique de l'échantillon en fonction du temps, au cours d'une réaction redox (réductions et oxydations). Ces variations sont interprétées en termes de diffusion des espèces mobiles au sein du melt. Un modèle reposant sur les flux conjoints de cations et de trous d'électrons, opposés au flux d'oxygène en transit dans l'échantillon a été établi. Cette étude est acceptée au journal *Geochimica et Cosmochimica Acta* sous le titre "Time-dependent changes of the electrical conductivity of basaltic melts with redox state".

The present thesis has been organized in individual chapters, each of them having an article either published, or accepted or in revision or in preparation. As a consequence, each chapter has its own introduction and, therefore, only a brief overview will be provided here.

The objectives of this thesis are three-fold: 1) To acquire experimental data regarding variations of the electrical behaviour of silicate glasses and liquids in function of their composition, water content, pressure and oxygen fugacity and to interpret these data in terms of transport properties. 2) To relate these experimental data to petrological constraints and geophysical data in order to elaborate a forward model of the electrical conductivity of a volcanic edifice (in this case, Mount Vesuvius). 3) To use the electrical conductivity tool as a probe to investigate the evolution of a chemical reaction (redox reaction) at an atomic scale within a magma.

Chapter 2 provides a detailed description of the experimental and analytical techniques used in this thesis, and deals in particular with the acquisition of electrical data in function of the different parameters mentioned above. The experimental strategy as well as the problems encountered is discussed. The methodological investigation of the impedance spectroscopy technique is illustrated by an article entitled "Re-evaluation of the electrical conductivity of silicate melts" (American Mineralogist, in press), and is a collaboration with M. Malki (CEMHTI, Orléans).

Chapter 3 presents the results of electrical measurements performed on Mount Vesuvius eruptive products on wide ranges of temperature (glassy and liquid domains), pressure, composition and water content. A model of the electrical conductivity of Mount Vesuvius magmas is proposed and a first comparison with field data is drafted. This study is entitled "Laboratory measurements of hydrous and dry Mt. Vesuvius melts", Journal of Geophysical Research, 2008. The transition from the electrical conductivity of a glass or a melt to the one of a magma is considered via the discussion of mathematical models integrating the effect of crystals. A decompression experiment conducted on a hydrous obsidian also allowed to deal with the effect of bubbles on the conductivity. A last section is dedicated to the electrical relaxation time.

Chapter 4 is dedicated to the link between experimental measurements in laboratory and in the field (magnetotelluric). This project regards the elaboration of a forward model of the electrical conductivity of Mount Vesuvius, based on the electrical measurements presented in Chapter 3, magnetotelluric profiles, petrological constraints and geochemical data from the literature. The introduction to the technique of electrical measurements in the field has been performed with A. Siniscalchi (Università di Bari) and Z. Petrillo (INGV, Napoli). The elaboration of a forward model results from a collaboration with P. Tarits et S. Hautot (IUEM, Brest). This study is presented as an article in preparation for G-cubed (Geochemistry Geophysics Geosystems), and entitled "Forward modelling of the electrical conductivity of Mount Vesuvius".

Chapter 5 is dedicated to the study of redox kinetics and mechanisms in basaltic melts. Electrical measurements are used here as a probe to investigate the changes in the electrical response of the sample with time, during a redox reaction (reductions and oxidations). These variations are interpreted in terms of diffusion of mobile species within the melt. A model based on cooperative fluxes of cation and electron holes, in opposition to oxygen fluxes in transit in the sample has been established. This study is accepted in Geochimica et

Cosmochimica Acta and is entitled "Time-dependent changes of the electrical conductivity of basaltic melts with redox state".

Références

Allwardt, J.R., B.C. Schmidt, and J.F. Stebbins, 2004. Structural mechanisms of compression and decompression in high-pressure $K_2Si_4O_9$ glasses: an investigation utilizing Raman and NMR spectroscopy of glasses and crystalline materials. *Chemical Geology*, 213, 137-151.

Armstrong, R.D., and K. Taylor, 1975. Impedance of solid electrolyte cells over frequency range 10^{-3} to 108Hz. *Journal of Electroanalytical Chemistry*, 63(1), 9-17.

Bagdassarov, N. S., J. Maumus, B. Poe, A. B. Slutskiy, and V. K. Bulatov, 2004. Pressure dependence of Tg in silicate glasses from electrical impedance measurements. *Physics and Chemistry of Glasses, 45*(3), 197-214.

Barczynski, R. J., and L. Murawski, 2002. Mixed electronic-ionic conductivity in transition metal oxide glasses containing alkaline ions. *Journal of Non-Crystalline Solids, 307*, 1055-1059.

Bauerle, J.E., 1969. Study of solid electrolyte polarization by a complex admittance method. *Journal of Physics and Chemistry of Solids*, 30: 2657-2670.

Behrens, H., R. Kappes, and P. Heitjans, 2002. Proton conduction in glass - an impedance and infrared spectroscopic study on hydrous BaSi2O5 glass. *Journal of Non-Crystalline Solids*, 306(3), 271-281.

Bockris, J. O'M., J.A. Kitchener, S. Ignatowicz, and J.W. Tomlinson, 1952. Electric conductance in liquid silicates. *Transactions of the Faraday Society*, 48, 75-91.

Bockris, J. O'M., and G.W. Mellors, 1956. Electric conductance in liquid lead silicates and borates. *Journal of Physics and Chemistry*, 60, 1321-1328.

Bruin, H.J., and A.D. Franklin, 1981. An impedance spectroscopy model for electron transfer reactions at an electrode/solid electrolyte interface. *Journal of Electroanalytical Chemistry*, 118, 405-418.

Constable, S. and A. Duba, 1990. Electrical conductivity of olivine, a dunite and the mantle. *Journal of Geophysical Research*, 95(B5), 6967-6978.

Constable, S. and A. Duba, 2002. Diffusion and mobility of electrically conducting defects in olivine. *Physics and Chemistry of Minerals*, 29(7), 446-454.

Constable, S., and J.J. Roberts, 1997. Simultaneous modelling of thermopower and electrical conduction in olivine. *Physics and Chemistry of Glasses*, 24, 319-325.

Cooper, R. F., J. B. Fanselow, and D. B. Poker, 1996. The mechanism of oxidation of a basaltic glass: Chemical diffusion of network-modifying cations. *Geochimica et Cosmochimica Acta*, 60(17), 3253– 3265, doi:10.1016/0016-7037(96)00160-3.

Déportes, C., M. Duclot, P. Fabry, J. Fouletier, A. Hammou, M. Kleitz, E. Siebert et J.L. Souquet, 1994. Electrochimie des solides, Collection Grenoble Sciences, ISBN 2-86883-447-7, 440pp.

Duba, A., 1972. Electrical conductivity of olivine. *Journal of Geophysical Research*, 77(14), 2483-2495.

Du Frane, W.L., J.J. Roberts, D.A. Toffelmier, and J.A. Tyburczy, 2005. Anisotropy of electrical conductivity in dry olivine. *Geophysical Research Letters*, 32(24), doi: 10.1029/2005GL023879.

Dunn, T. and W.A. Ratliffe, 1990. Chemical diffusion of ferrous iron in a peraluminous sodium aluminosilicate melt-0.1MPa to 2.0GPa. *Journal of Geophysical Research-Solid Earth*, *95*(B10), 15665-15673.

Fogo, J.K., S.W. Benson, and C.S. Copeland, 1954. The electrical conductivity of supercritical solutions of sodium chloride and water. *Journal of Chemical Physics*, 22(2), 212-216.

Franck, E.U., 1956. Hochverdichteter Wasserdampf I. Elektrolytische Leitfähigkeit in KCl-H_2O-Lösungen bis 750°C. *Z. Phys. Chem.* 8 1/2, p. 92 Neue Folge

Gaillard, F., B. Schmidt, S. Mackwell, and C. McCammon, 2003. Rate of hydrogen-iron redox exchange in silicate melts and glasses. *Geochimica et Cosmochimica Acta*, 67(13), 2427 – 2441, doi:10.1016/S0016-7037(02)01407-2.

Gaillard, F., 2004. Laboratory measurements of electrical conductivity of hydrous and dry silicic melts under pressure. *Earth and Planetary Science Letters*, 218(1–2), 215–228, doi:10.1016/S0012-821X(03)00639-3.

Grant, R.J., M.D. Ingram, and A.R. West, 1977. An investigation of B-alumina electrolytes by electric modulus spectroscopy. *Electrochimica Acta*, 22, 729-734.

Heinemann, I., and G.H. Frischat, 1992. The sodium transport mechanism in Na2O.2SiO2 glass determined by the Chemla experiments. *Physics and Chemistry of Glasses*, 34, 255-260.

Henderson, P., J. Nolan, G. C. Cunningham, and R. K. Lowry, 1985. Structural control and mechanisms of diffusion in natural silicate melts. *Contributions to Mineralogy and Petrology*, *89*(2-3), 263-272.

Hodge, I. M., Ingram, M. D., and West, A. R., 1976. Impedance and modulus spectroscopy of polycrystalline solid electrolytes. *Journal of Electroanalytical Chemistry*, 74: 125-143.

Huebner, J. S., and R. G. Dillenburg, 1995. Impedance spectra of hot, dry silicate minerals and rock: qualitative interpretation of spectra. *American Mineralogist*, *80*(1-2), 46-64.

Jambon, A., 1982. Tracer diffusion in granitic melts: experimental results for Na, K, Rb, Cs, Ca, Sr, Ba, Ce, Eu, to 1300°C and a model of calculation. *Journal of Geophysical Research-Solid Earth*, *87*(B13), 10797-10810.

Jambon, A., and J.P. Carron, 1976. Diffusion of Na, K, Rb and Cs in glasses of albite and orthoclase composition. *Geochimica et Cosmochimica Acta*, 40(8), 897-903.

Kanehisa, M.A., 1992. Alkali content dependence of the ionic conductivity of oxide glasses. *Journal of Non-Crystalline Solids*, 151(1-2),155-159.

Koops, C.G., 1951. On the dispersion of resistivity and dielectric constant of some semiconductors at audiofrequencies. *Physical Review*, 83(1), 121-124.

Kress, V.C., D. Williams, and I.S.E. Carmichael, 1989. When is a silicate melt not a liquid. *Geochimica et Cosmochimica Acta*, 57(3), 1687-1692.

Lebedev, E.B., and N.I. Khiratov, 1964. Dependence of the beginning of melting of granite and the electrical conductivity of its melt on high vapour pressure. *Geochemistry International*, 1, 193-197.

Malki, M., and P. Echegut, 2003. Electrical conductivity of the $CaO\text{-}SiO_2$ system in the solid and the molten states. J. Non-Cryst. Solids, 323: 131-136.

Maumus, J., N. Bagdassarov, and H. Schmeling, 2005. Electrical conductivity and partial melting of mafic rocks under pressure. *Geochimica et Cosmochimica Acta*, *69*(19), 4703-4718.

McCrum, N.G., B.E. Read, and G. Williams, 1967. Anelastic and dielectric effects in polymeric solids, Wiley, London, p.111.

Moynihan, C.T., 1998. Description and analysis of electrical relaxation data for ionically conducting glasses and melts. *Solid State Ionics*, 105 (1998) 175^183.

Navrotsky, A., 1995. Energetics of silicate melts, in *Reviews in Mineralogy, Structure, dynamics and properties of silicate melts*, Vol. 32, pp 121-143.

Noyes et al., 1907. The electrical conductivity of aqueous solutions. Publication No63, Carnegie Institution of Washington, Washington, D.C.

Park, S. K., and M. N. Ducea, 2003. Can in situ measurements of mantle electrical conductivity be used to infer properties of partial melts? *Journal of Geophysical Research-Solid Earth*, *108*(B5), 2270.

Partzsch, G. M., F. R. Schilling, and J. Arndt, 2000. The influence of partial melting on the electrical behavior of crustal rocks: laboratory examinations, model calculations and geological interpretations. *Tectonophysics*, *317*(3-4), 189-203.

Pfeiffer, T., 1998. Viscosities and electrical conductivities of oxidic glass-forming melts. *Solid State Ionics, 105*, 277-287.

Poe, B.T., Romano, C., Varchi, V., Misiti, V., and Scarlato, P., 2008**.** Electrical conductivity of a phonotephrite from Mt. Vesuvius: The importance of chemical composition on the electrical conductivity of silicate melts. *Chemical Geology*, 256 (3-4): 193-202.

Pommier, A., Gaillard, F., Pichavant, M., Scaillet, B., 2008. Laboratory measurements of electrical conductivities of hydrous and dry Mount Vesuvius melts under pressure. *Journal of Geophysical Research*, 113, B05205, doi:10.1029/2007JB005269.

Pommier, A., M. Malki, F. Gaillard, and M. Pichavant, 2009. Methodological re-evaluation of the electrical conductivity of silicate melts, *Am. Mineralogist*, accepted.

Pommier, A., Gaillard, F., Pichavant, M., 2009. Modeling the time-dependent changes in electrical conductivity of basaltic melts with redox state, *Geochimica et Cosmichimica Acta*, in revision.

Quist, A.V., and W.L. Marshall, 1968. Electrical conductances of aqueous sodium chloride solutions from 0 to 800°C and at pressures to 4000 bar. *Journal of Physics and Chemistry*, 72 2, p. 684.

Rai, C.S., and Manghnani, M.H., 1977. Electrical conductivity of basalts to 1550°C. In *Magma genesis: Bulletin 96*, Oregon Department of Geology and Mineral Industries, edited by H.J.B. Dick, pp 219-232, Portland, OR.

Roberts, J. J., and J. A. Tyburczy, 1994. Frequency dependent electrical properties of minerals and partial-melts. *Surveys in Geophysics*, *15*(2), 239-262.

Roberts, J. J., and J. A. Tyburczy, 1999. Partial-melt electrical conductivity: Influence of melt composition. *Journal of Geophysical Research-Solid Earth*, *104*(B4), 7055-7065.

Roling, B., 1999. What do electrical conductivity and electrical modulus spectra tell us about the mechanisms of ion transport processes in melts, glasses, and crystals? *Journal of Non-Crystalline Solids*, *244*(1), 34-43.

Roselieb, K. and A. Jambon, 1997. Tracer diffusion of potassium, rubidium, and cesium in a supercooled jadeite melt. *Geochimica et Cosmochimica Acta*, 61(15), 3101-3110.

Satherley, J., and S. I. Smedley, 1985. The electrical conductivity of some hydrous and anhydrous molten silicates as a function of temperature and pressure. *Geochimica Et Cosmochimica Acta*, *49*, 769-777.

Sato, H., 1986. High-temperature AC electrical properties of olivine single crystal with varying oxygen partial pressure – Implications for the point defect chemistry. *Physics of the Earth and Planetary Interiors*, 41(4), 269-282.

Scarlato, P., et al. (2004), High-pressure/high-temperature measurements of electrical conductivity in basaltic rocks from Mount Etna, Sicily, Italy. *Journal of Geophysical Research*, 109(B4), doi: doi:10.1029/2003JB002666.

Shankland, T.J. and H.S. Waff, 1977. Partial melting and electrical conductivity anomalies in upper mantle. *Journal of Geophysical Research*, 82(33), 5409-5417.

Schock R.N., A.G. Duba and T.J. Shankland, 1989. Electrical conduction in olivine. *Journal of Geophysical Research*, 94(B5), 5829-5839.

ten Grotenhuis S.M., M.R. Drury, C.J. Peach, and C.J. Spiers, 2004. Electrical properties of fine-grained olivine: evidence for grain boundary transport. *Journal of Geophysical Research*, 109(B6), doi: 10.1029/2003JB002799.

Toffelmier, D.A. and J.A. Tyburczy, 2007. Electromagnetic detection of a 410-km-deep melt layer in the southwestern United States. *Nature*, 447(7147), 991-994.

Tyburczy, J. A., and D. K. Fisler, 1995. Electrical properties of minerals and melts, *Mineral Physics and Crystallography, A Handbook of Physical Constants*, pp.185-208, AGU, Whashington, D.C.

Tyburczy, J. A., Waff, H. S., 1983. Electrical conductivity of molten basalt and andesite to 25 kilobars pressure: Geophysical significance and implications for charge transport and melt structure. *Journal of Geophysical Research*, 88(B3), 2413–2430, doi:10.1029/JB088iB03p02413.

Tyburczy, J. A., Waff, H. S., 1985. High pressure electrical conductivity in naturally occurring silicate liquids, in Point Defects in Minerals, *Geophysical Monograph Series*, vol. 31, edited by R. N. Shock, pp. 78– 87, AGU, Washington, D.C.

Volarovich, M.P. and A.T. Bondarenko, 1960. Study of frequency dependence of electrical properties of igneous rocks of the Kol'skli Peninsula.

Volarovich, M.P. and D.M. Tolstoi, 1936. The simultaneous measurement of viscosity and electrical conductivity of some fused silicates at temperatures up to 1400°C. *Journal of the Society of Glass Technology*, 20, 54-60.

Volarovich M.P., A.T. Bondarenko, and Parkhomenko, 1962. The influence of pressure on the elec-trical properties of rocks. Proceedings of the Institute of Physics of Earth, Moscow, 23, 80-90.

Waff, H. S., and Weill, D. F., 1975. Electrical conductivity of magmatic liquids: effects of temperature, oxygen fugacity and composition. *Earth and Planetary Science Letters*, 28: 254–260.

Wanamaker, B.J., 1994. Point defect diffusivities in San Carlos olivine derived from reequilibration of electrical conductivity following changes in oxygen fugacity. *Geophysical Research Letters*, 21(1), 21-24.

Wanamaker B.J., and A. Duba, 1993a. Electrical conductivity of San Carlos olivine along [100] under oxygen buffered and pyroxene buffered conditions and implications for defect equilibria. *Journal of Geophysical Research*, 98(B1), 489-500.

Wanamaker B.J., and A. Duba, 1993b. Electrical conductivity of polycrystalline olivine containing a silicate glass. *Geophysical Research Letters*, 20(19), 2107-2110.

Wannamaker, P.E., 1986. Electrical conductivity of water-undersaturated crustal melting. *Journal of Geophysical Research*, 91(B6), 6321-6327.

Xu, Y., Shankland, T.J., Duba, A.G., and Poe, B.T., 2000. Laboratory-based electrical conductivity in the Earth's mantle. *Journal of Geophysical Research*, 105: 27865-27872.

Yoshino, T., M.J. Walter, and T. Katsura, 2004. Connectivity of molten Fe alloy in peridotite based on in situ electrical conductivity measurements: implications for core formation in terrestrial planets. *Earth and Planetary Science Letters*, 222, 625-643.

Yoshino, T., Matsuzaki, T., Yamashita, S., and Katsura, T., 2006. Hydrous olivine unable to account for conductivity anomaly at the top of the astenosphere. *Nature*, 443: 973-976.

Zhang, Y., E. M. Stolper, 1991. Water diffusion in a basaltic melt, *Nature, 351*, 306-309.

Chapitre 2

Techniques expérimentales et analytiques

(*Experimental and analytical techniques*)

Objectifs du chapitre

Ce chapitre présente de façon détaillée les procédures expérimentales et les techniques analytiques. La synthèse des verres de départ secs et hydratés est expliquée, incluant les étapes de l'hydratation d'un échantillon en autoclave. La stratégie adoptée pour les mesures à différentes pressions et températures est également considérée. Les détails concernant les techniques analytiques utilisées dans le présent manuscrit sont présentés. Les échantillons ont été caractérisés par microscopie optique, microscopie électronique à balayage (MEB) et microsonde. En ce qui concerne les échantillons hydratés, la teneur en eau a été analysée avant et après l'expérience en effectuant des analyses par spectroscopie infrarouge (FTIR) et le titrage Karl Fisher (KFT). Concernant l'étude redox, le ratio fer ferrique/fer ferreux a été déterminé par dosage colorimétrique. Une grande partie de ce chapitre est dédiée aux mesures de conductivité électrique utilisant la technique de spectroscopie d'impédance. Cette technique permet de réaliser des mesures *in situ* et en temps réel avec une grande précision. L'impédance complexe de l'échantillon est mesurée en effectuant un scan en fréquence de 10^6 à <1Hz. Une étude méthodologique (Pommier et al., 2009, American Mineralogist, sous presse) confronte les mesures à deux et quatre électrodes. La contribution des électrodes, dans l'appareillage à deux électrodes, à la conductivité électrique mesurée a été qualifiée et quantifiée en effectuant notamment une expérience en court-circuit. L'effet des électrodes est non négligeable pour les melts peu résistifs et à haute température. Une comparaison avec des études antérieures a permis de corriger la base de données de la conductivité des melts naturels.

This chapter presents a detailed view of the experimental procedures and analytical techniques. The synthesis of the starting dry and hydrous glasses is explained, including the steps of the sample hydration in internally heated pressure vessel. The strategy adopted for measurements at different pressures and temperatures is also considered. Details regarding the analytical techniques used in this manuscript are presented. The samples were characterized using optical microscope, SEM and electron microprobe. As regards hydrous samples, the water content was analysed before and after the experiment using infra-red spectroscopy (FTIR) and Karl Fisher Titration (KFT). As regards the redox study, the

ferric/ferrous ratio was determined by wet chemistry analyses. A large part of this chapter is dedicated to the electrical measurements using impedance spectroscopy. This technique allows to perform in situ and real-time measurements with accuracy. The complex impedance of the sample is measured by performing a scan in frequency, from 10^6 to <1Hz. A methodological study (Pommier et al., 2009, American Mineralogist, accepted) confronted two-electrode vs four-electrode measurements. The contribution of the electrodes of the two-electrode setup to the measured electrical conductivity has been qualified and quantified, by performing, in particular, a short-circuit experiment. The electrode effects were found to be non-negligible for low-resistive melts and at high temperature. A comparison with previous studies allowed to correct the database of the conductivity of natural melts.

2.1. Matériaux de départ

Les matériaux de départ sont des échantillons naturels du Vésuve (Italie), du Kilauea (USA) ainsi qu'une obsidienne (sud de l'Islande). Un échantillon synthétique (borosilicate provenant du CEMHTI) a été également utilisé dans l'étude présentée à la fin de ce chapitre.

Les échantillons du Vésuve consistent en une tephrite issue d'une éruption strombolienne de la période médiévale (7-8ème siècle), une tephriphonolite provenant de l'éruption subplinienne Pollena (472 ap. JC) et une phonolite de l'éruption plinienne Pompéi (79 ap. JC). Ils ont été choisis de manière à être représentatifs des produits éruptifs émis par le volcan, soulignant à la fois la diversité de composition chimique et la diversité de styles éruptifs. Par ailleurs, l'étude des propriétés électriques de ces laves particulières (très potassiques) revêt un caractère novateur. L'échantillon du Kilauea est un basalte issu d'un conduit actif du volcan Pu'u' 'O'o collecté en 2007 (T. Orr, USGS). Il a été utilisé pour l'étude des phénomènes redox (Chapitre 5). Sa composition est proche de celle des MORB (Mid-Ocean Ridge Basalt), qui sont les magmas les plus répandus à la surface du globe. L'état redox des basaltes reflétant l'état d'oxydation des régions sources, ils ont des implications importantes en ce qui concerne l'évolution du manteau terrestre (Christie et al., 1986). Les basaltes sont en fait considérés comme étant de bons candidats pour étudier l'évolution et la différenciation de la planète Terre, une évolution grandement dépendante de celle des conditions redox (par ex., Frost and McCammon, 2005). Une obsidienne naturelle (Gaillard, 2004) a été hydratée et utilisée pour quantifier l'importance des bulles dans les mesures électriques (Chapitre 3). L'échantillon synthétique, un borosilicate, a été choisi en raison de sa très forte teneur en sodium et de son très fort degré de polymérisation, dont l'intérêt direct concernant les mesures électriques sera abordé par la suite.

2.2. Synthèse des verres et préparation des échantillons

2.2.1. Obtention d'un verre

Tous ces matériaux de départ ont été réduits en poudre dans un mortier en agate puis portés en température de manière à obtenir un verre de départ chimiquement homogène. La composition de ces verres est donnée aux Chapitres 2 et 5 (échantillons du Kilauea et borosilicate) et au Chapitre 3 (échantillons du Vésuve et obsidienne).

La fusion de poudre de roche est réalisée à pression atmosphérique, à 1400-1500°C, dans un four de type *Piezoceram* (Figure 2.1). La poudre est placée dans un creuset de platine ou, en ce qui concerne les expériences avec mesures électriques à 4 électrodes (cf fin de ce

chapitre), dans un creuset en alumine. Des fusions d'une heure chacune ont été réalisées, avec ajout de poudre de roche avant chaque nouvelle fusion, et ce jusqu'à l'obtention d'un volume de verre suffisant (i.e. hauteur de verre dans le creuset > 1cm). Une fois sorti du four, le verre refroidit dans le creuset à l'air ambiant, sans trempe rapide, pour éviter l'apparition de craquelures qui le fragiliseraient. Le verre obtenu est dépourvu de bulles (à échelle micrométrique). Des cylindres de verres sont ensuite forés directement dans le creuset. En ce qui concerne les matériaux les plus dépolymérisés (tephrite, basalte), très peu de cylindres se sont cassés lors du forage, alors que les autres cylindres de verre (tephriphonolite, phonolite) ont été plus difficiles à extraire (rendement variant de ½ à ⅔).

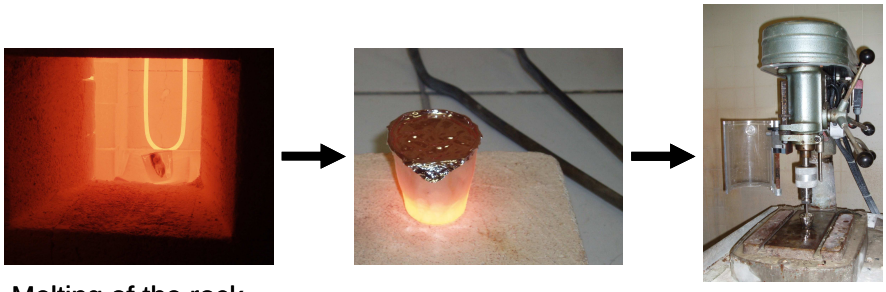


Figure 2.1 : Steps of the glass synthesis and glass cylinders drilling.

2.2.2. Hydratation en autoclave à chauffage interne

Différentes méthodes ont été testées pour préparer une capsule hydratée (cf Pommier, 2006, rapport de stage ingénieur et de Master de Recherche), la méthode la plus efficace étant exposée ci-dessous. Pour procéder à l'hydratation d'un échantillon, comme indiqué Figure 2.2, le cylindre de verre est d'abord placé dans une capsule de métal noble (Pt ou Au), un capuchon de même métal soudé à l'arc à une extrémité du tube (soudure de type « boîte de conserve »). Une quantité connue d'eau déminéralisée, correspondant au %m d'eau que l'on souhaite injecter dans l'échantillon, est ensuite ajoutée à l'aide d'une micropipette. La capsule est entourée d'un papier absorbant régulièrement humidifié et plongé dans de l'azote liquide, de manière à maintenir la quantité d'eau introduite gelée dans la capsule. Ainsi, lors de la soudure d'un second capuchon pour fermer totalement la capsule, l'eau introduite ne se volatilise pas. La capsule est régulièrement pesée de manière à quantifier précisément le volume d'eau introduit et aussi pour détecter les éventuelles pertes en eau au cours de la soudure. Cette soudure est alors testée de deux manières : 1) le bain d'huile : la capsule fermée est immergée dans un bécher rempli d'huile chaude et les éventuelles fuites sont

immédiatement indiquées par l'échappement de bulles d'eau de la capsule. L'avantage de ce test est de permettre la localisation de la partie mal soudée et donc de rectifier la soudure. 2) L'étuve : la capsule fermée est placée dans une étuve (~150°C) pendant 1h environ puis pesée à sa sortie de manière à voir si la capsule a gardé l'eau introduite ou si des fuites ont permis à l'eau de s'échapper. L'inconvénient de cette méthode est de ne pas permettre de ressouder la capsule avant que toute l'eau ne soit partie. Les deux tests ont été faits pour chaque hydratation, le bain d'huile puis l'étuve. La capsule est ensuite placée dans un autoclave à chauffage interne *(Internally Heated Pressure Vessel,* Figure 2.3*)*, aux conditions (P,T) dictées par la teneur en eau à introduire dans le verre (Burnham, 1975). La durée de l'hydratation dépend du coefficient de diffusion de l'eau dans le type de matériau de départ (Watson, 1994 ; Zhang and Stolper, 1991), des dimensions et de la géométrie de l'échantillon. En l'occurrence, pour une géométrie cylindrique, le phénomène de diffusion de l'eau obéit à l'équation suivante :

$$\frac{\partial C}{\partial t} = \frac{1}{r}\frac{\partial}{\partial r}\left(rD\frac{\partial C}{\partial r}\right) \qquad (1)$$

Avec C (%m) la concentration en eau, t le temps (s), r le rayon du cylindre (m), D le coefficient de l'eau dans le matériau (m²/s). La solution correspondant à cette équation est donnée par le formalisme suivant (Crank, 1975):

$$\frac{C - C_0}{C_1 - C_0} = 1 - \frac{2}{a}\sum_{n=1}^{\infty}\frac{\exp(-D\alpha_n^2 t).J_0(r\alpha_n)}{\alpha_n.J_1(a\alpha_n)} \qquad (2)$$

Avec C (%m) la concentration en eau au temps t, C_0 (%m) sa concentration initiale, C_1 (%m) sa concentration finale, a le rayon maximal du cylindre (m), J_i (x) la fonction de Bessel à l'ordre i et α_n les racines de l'équation $J_0(a\alpha_n)=0$. Par mesure de sécurité, la durée de l'hydratation obtenue par l'équation de diffusion a été interprétée comme étant une valeur minimale et a toujours été largement dépassée dans la pratique. Par exemple, l'hydratation de la tephriphonolite du Vésuve (VS88-65B) à 1.9%m s'est effectuée à 100MPa et 1200°C, pendant ~60h, l'équation de diffusion préconisant une durée d'au moins 20h (en considérant D_{H2O}~1.10^{-10}m²/s, Watson, 1994). A la fin de l'hydratation, la capsule est trempée rapidement, afin d'éviter la cristallisation de l'échantillon. Une fois sortie de l'autoclave, la capsule est pesée.

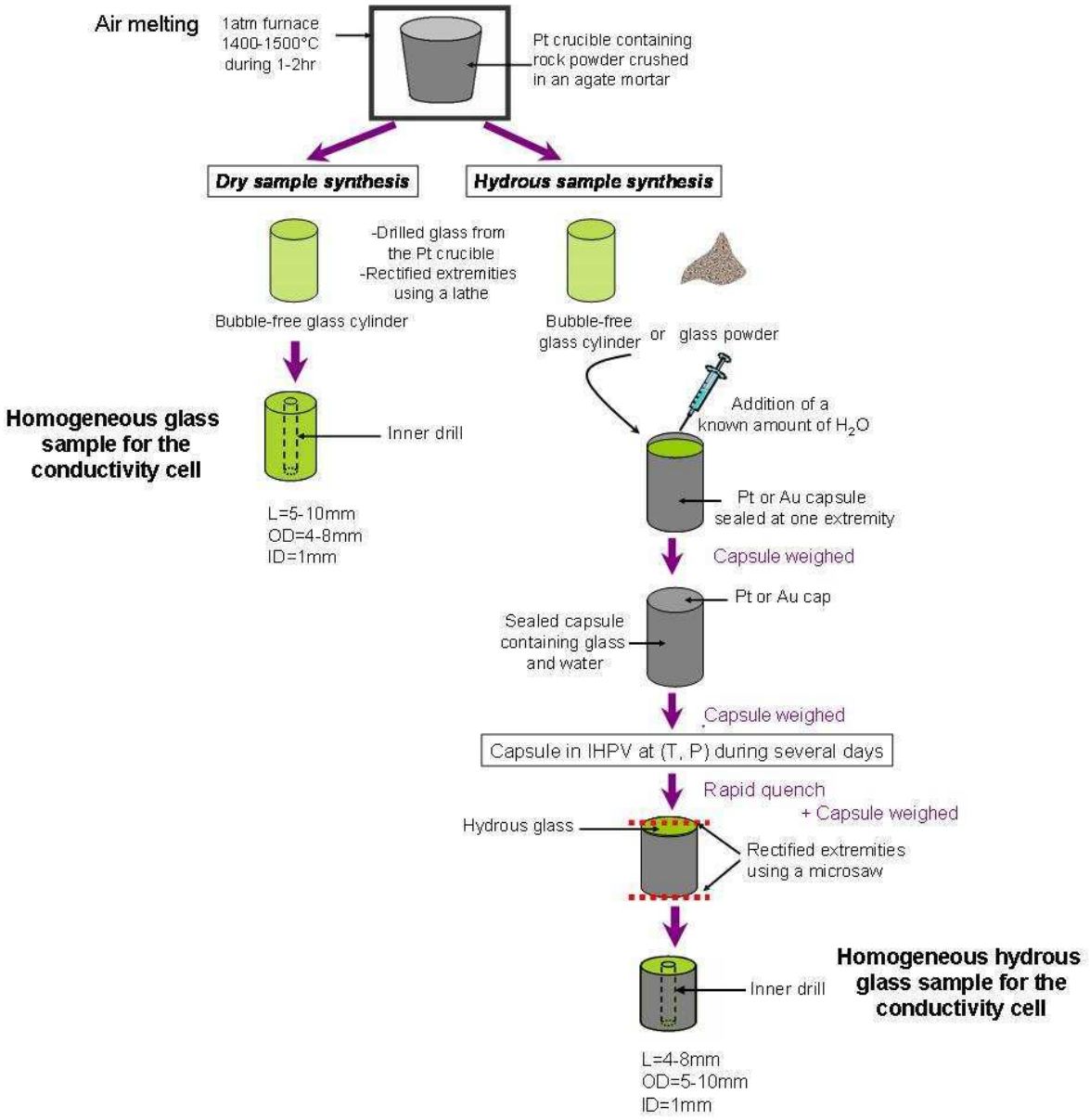
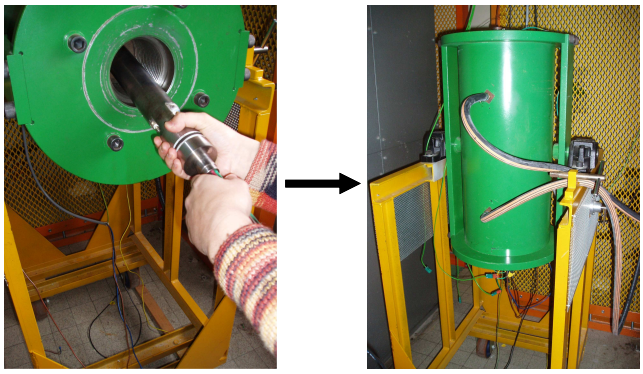


Figure 2.2 : Sketch of the sample synthesis. The preparation of a dry sample is shown on the left part, while the steps regarding the hydration process for hydrous sample synthesis are presented on the right part. See text for details.



Introduction of the Mo furnace containing the capsule in the IHPV

Synthesis of the hydrous glass under defined (T,P) conditions

Figure 2.3 : Pictures presenting the synthesis of hydrous starting glass using an Internally Heated Pressure Vessel. Gas medium is Ar. Duration of the experiment is determined using diffusion formalism (see text).

2.2.3. Préparation de l'échantillon pour la cellule de mesure électrique

Que l'échantillon vitreux cylindrique soit sec ou hydraté, ses deux faces sont rectifiées au tour ou à la microscie, de manière à ce qu'elles soient parallèles. Les mesures électriques nécessitant de bien contraindre la géométrie de l'échantillon, le cylindre doit être le plus parfait possible. L'échantillon est ensuite fixé à sa base à l'aide d'une résine (*Crystalbond*, Aremco) sur une plaque de verre et foré en son centre (diamètre du foret : 1mm, Figure 2.2). La maîtrise de cet aspect technique de la préparation de l'échantillon a été acquise progressivement, essentiellement dû au fait de la précision et de l'argutie requises.

2.3. Appareillage expérimental et stratégie

Les mesures électriques ont été effectuées à pression atmosphérique dans des fours à 1bar à atmosphère contrôlée et sous pression en utilisant un autoclave à chauffage interne (IHPV, ISTO), le gaz sous pression étant l'argon. Les détails concernant l'équipement expérimental sont mentionnés aux Chapitres 3 et 5.

Quelle que soit la pression de l'expérience (entre 0.1 et 400 MPa), les mesures électriques ont été effectuées dans le verre ou dans le liquide, i.e. en dehors de l'intervalle de cristallisation (cf 2.7.). Le choix de ne pas faire de mesures électriques en présence de cristaux est expliqué au paragraphe 2.7. Pour les expériences en autoclave, des mesures étant effectuées dans les domaines vitreux et liquide à différentes pression, il est inévitable de traverser l'intervalle de cristallisation. Les stratégies expérimentales adoptées ont permis de ne traverser qu'une seule fois l'intervalle de cristallisation et donc de minimiser le développement des cristaux dans l'échantillon (Figure 2.4).

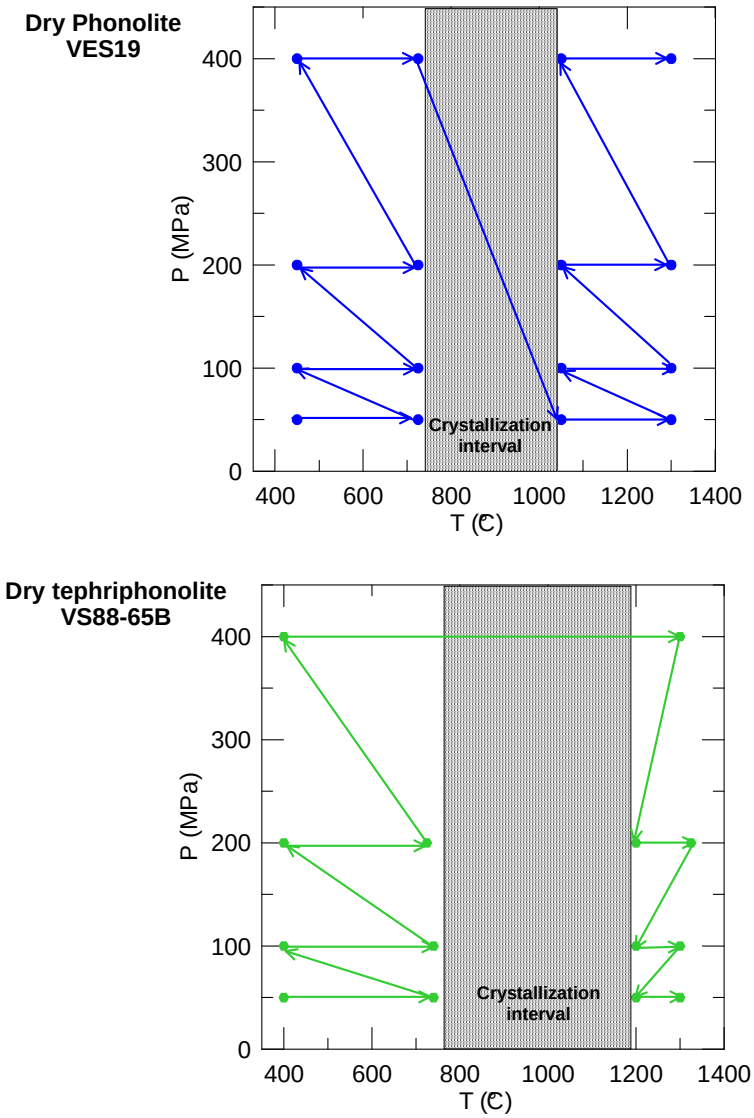


Figure 2.4 : Experimental strategy for electrical measurements under pressure. The P-T paths for the experiments on the dry phonolite and the dry tephriphonolite were adopted because they allow to cross only once the interval of crystallization, preventing from the growth of crystals at the electrode/melt interface.

2.4. Analyses au microscope, MEB et microsonde électronique

Tous les échantillons ont été observés au microscope optique de type Leica à l'ISTO, avant et après les expériences. Les échantillons du Chapitre 3 ont été systématiquement analysés au microscope électronique à balayage (MEB) à Orléans (*JEOL* Winset JSM 6400, Polytech'Orléans-ISTO), dans le double objectif de caractériser les interfaces échantillon-composants de la cellule de conductivité et de détecter la présence de cristaux dans les expériences auxiliaires ayant permis la détermination de l'intervalle de cristallisation.

La composition chimique de chaque échantillon a été déterminée par microsonde électronique à Orléans (*Camebax SX-50*, BRGM-CNRS-Université d'Orléans). Les conditions d'analyse sont 15 kV, 6 nA, 10s sur le pic et 5 s sur le fond. Pour l'analyse des verres, un faisceau défocalisé a été utilisé (8-10 µm) alors que l'analyse des cristaux s'est effectuée au moyen d'un faisceau focalisé (1-2 µm). Les standards utilisés pour la calibration

de la microsonde sont les suivants : une albite naturelle, pour le sodium et le silicium; une orthose naturelle, pour le potassium; un corindon synthétique, pour l'aluminium; une pyrophanite synthétique, pour le manganèse et le titane; une hématite naturelle, pour le fer; une olivine naturelle proche du pôle forstérite, pour le magnésium; un grenat ferro-calcique naturel (andradite), pour le calcium; une chromite synthétique, pour le chrome.

En plus d'être utilisée pour effectuer des analyses ponctuelles, la microsonde électronique a également été employée pour réaliser des profils de concentration dans certains échantillons, dans le but d'observer d'éventuelles interactions à l'interface échantillon-électrodes, échantillon-céramique et aussi de suivre les variations de composition chimique d'un échantillon soumis à un changement des conditions redox (Chapitre 5).

2.5. Détermination de la teneur en eau

La teneur en eau des échantillons hydratés (Chapitres 3) a été déterminée par deux techniques différentes : l'analyse infra-rouge (FTIR) et la Titration Karl Fisher (KFT).

L'objectif de l'analyse infra-rouge (spectromètre *Nicolet Magna 760* relié à un microscope Nic-Plan, ISTO, Orléans) a été de vérifier l'homogénéité de la teneur en eau dans les échantillons de départ. Une source de type Si-C (Globar) ou de type lumière blanche, un détecteur MTC/A et une séparatrice CaF_2 ont été utilisés. Ces conditions optimisent l'analyse dans le domaine spectral de l'eau (pic à 4500 cm^{-1} pour OH et 5200 cm^{-1} pour l'eau moléculaire). Les spectres ont été collectés sur un intervalle de longueur d'onde s'étendant de 2000 à 7400cm^{-1} (résolution de 4 ou 8cm^{-1}), accumulés pendant 128 scans sur des échantillons préalablement polis sur deux faces parallèles. Pour chaque spectre obtenu en un point de l'échantillon, la mesure de la hauteur des deux pics (OH et H_2O moléculaire), correspondant à l'absorbance, a permis d'obtenir la teneur en eau, calculée avec la loi de Beer-Lambert (par ex. Hanna, 1972):

$$[H_2O]=[OH]+[H_2Omol]=(A_{4500}/(\varepsilon_{4500}.e))+(A_{5200}/(\varepsilon_{5200}.e)) \quad (3)$$

$[H_2O]$ étant la teneur en eau dans l'échantillon (%m), A_i l'absorbance à une longueur d'onde i (cm^{-1}), ε_i l'absorptivité (ou coefficient d'extinction) molaire à une longueur d'onde i ($L.mol^{-1}.cm^{-1}$) et e l'épaisseur de l'échantillon (cm). Les valeurs de ε proviennent de la littérature (Newman et al., 1986). Les analyses infrarouges effectuées en différents points d'un même échantillon ont permis, dans le cas d'inhomogénéité de répartition de l'eau, de quantifier les variations de $[H_2O]$ et, dans le cas d'homogénéité de répartition, d'obtenir une valeur moyenne de la teneur en eau de l'échantillon. Un exemple de spectres est présenté Figure 2.5.

Les analyses ont été effectuées sur une tephriphonolite hydratée (VS88-65B) et la détermination de la hauteur des pics ont permis de déterminer une teneur en eau pour chaque point, situé à divers endroits de la capsule, la moyenne de ces teneurs conduisant à une teneur en eau globale (ici, 1.9%m).

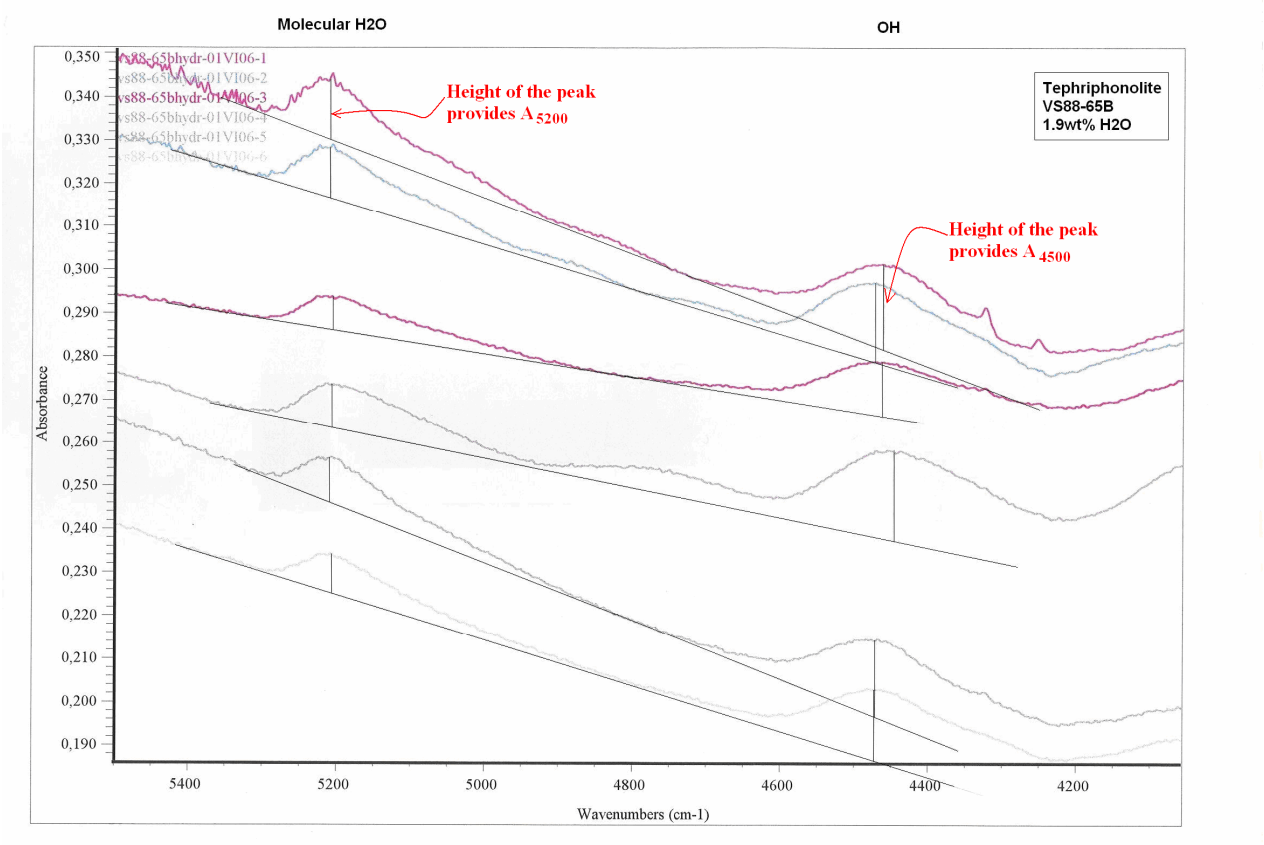


Figure 2.5: Infrared absorption spectra for the hydrous tephriphonolitic glass (VS88-65B) synthesized at 1200°C, 100MPa. Analyses were performed at different positions in the capsule. The height of the two peaks (molecular water and OH) was determined graphically (black lines) and corresponding water content was calculated knowing the thickness of the glass sample (determined for each spectrum) and using the Beer-Lambert's law (Eq. 3).

Dans le cas où une mesure globale (*bulk*) de la teneur en eau dans l'échantillon était suffisante (Chapitre 3), un dosage par la méthode KFT a également été effectué (Pommier et al., 2008). La méthode utilisée correspond à celle décrite dans les études de Westrich (1987), Behrens et al. (1996).

2.6 Analyse du Fe^{II}/Fe^{III}

Des dosages colorimétriques ont été effectués pour analyser la concentration en fer ferreux (FeO), dans le cadre des expériences redox (Chapitre 5). Les étapes du dosage sont

présentées Figure 2.6. Le dosage redox par colorimétrie est une méthode d'analyse couramment utilisée pour déterminer de manière globale (*bulk*) la concentration en FeO dans les melts silicatés (e.g. Magnien et al., 2008 ; Gaillard et al., 2003 ; Wilson, 1960). Avec cette méthode, l'échantillon, réduit en poudre, est d'abord dissout par une solution HF+H_2SO_4, à une température de 275°C. Les proportions sont les suivantes : au moins 25mg de verre broyé, 7mL H_2SO_4 (dilué à 50%) et 0.3mL HF). En pratique, la solution contenant le verre dissout est mélangée à 7mL d'H_2SO_4, 5mL d'H_3PO_4 et une cuiller d'acide borique. De l'eau distillée est ajoutée jusqu'à obtenir 100mL de cette solution à doser.

La solution titrante (dichromate de potassium) permet d'oxyder le fer ferreux en fer ferrique selon la réaction suivante (une mole de solution titrante permet d'oxyder 6 moles de fer ferreux en fer ferrique) :

$$Cr_2O_7^{2-} + 14H^+ + 6Fe^{2+} \leftrightarrow 2Cr^{3+} + 7H_2O + 6Fe^{3+} \qquad (4)$$

L'utilisation de diphénylamine sulfonate de baryum comme un indicateur coloré permet d'indiquer l'équivalence par un changement de couleur du mélange qui se teinte en violet. La teneur en FeO est déduite par la formule suivante :

$$FeO(\%m) = \frac{6.C_{K2Cr2O7}.Veq.M_{FeO}}{M_{K2Cr2O7}.m_{sample}}.100 \qquad (5)$$

avec FeO la concentration en fer ferreux de l'échantillon (%m), C la concentration en $K_2Cr_2O_7$ (0.3514g/L), Veq le volume équivalent (L), M_x la masse molaire de x (g/mol), m_{sample} la masse de l'échantillon (g).

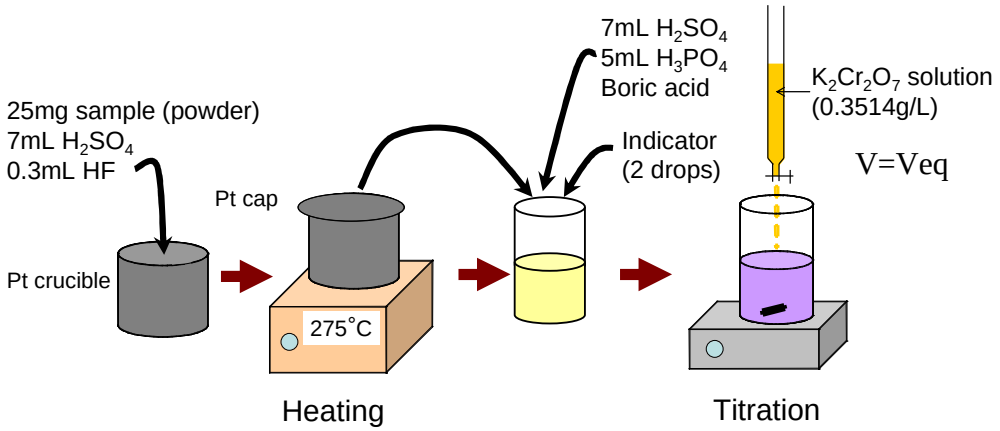


Figure 2.6 : Sketch of the steps for colorimetric titration. The first steps show the sample preparation prior to the titration. The titration is completed once the colour of solution containing the sample turns violet-purple. The volume of reagent added from the burette allows to determine the content of ferrous iron in the sample powder and, thus, to deduce the content of ferric iron.

2.7. Mesure des propriétés électriques

2.7.1. Mesure de la conductivité électrique des verres et liquides silicatés par spectroscopie d'impédance : concepts de base

La conductivité électrique (ou son inverse, la résistivité électrique) représente l'aptitude d'un porteur de charge à diffuser (en l'occurrence, dans un verre ou liquide silicaté) suite à l'application d'un potentiel électrique. La dépendance de la conductivité à la température et à la pression est représentée au travers de la loi d'Arrhénius (Arrhénius, 1889) :

$$\sigma = \frac{1}{\rho} = \sigma_0 . \exp\left(\frac{-Ea - P.\Delta V}{\Re . T} \right) \qquad (6)$$

avec σ la conductivité électrique (ohm^{-1}.m^{-1}), ρ la résistivité électrique (ohm.m), σ_0 le facteur pré-exponentiel (ohm^{-1}.m^{-1}), Ea l'énergie d'activation (J/mol), P la pression (MPa), ΔV le volume d'activation (cm^3/mol), T la température (K) et $\Re$ la constante des gaz parfaits. Le facteur pré-exponentiel est influencé par la température (valeurs plus élevées pour T>Tg, Pommier, 2006) et exprime l'agencement à l'échelle atomique (Déportes et al., 1994 ; Caillot et al. 1994) :

$$\sigma_0 = \frac{F^2 . l^2}{6\Re . T} . \nu^0 . C \qquad (7)$$

Avec F la constante de Faraday (C/mol), l la distance moyenne de saut d'un porteur de charge (m), nu0 la fréquence de vibration des cations en position interstitielle (Hz), C la concentration du porteur de charge (mol/cm^3).

Dans les melts silicatés, la conductivité électrique est essentiellement contrôlée par les ions, la conductivité globale (*bulk*) mesurée représentant la somme des contributions individuelles (Gaillard, 2004). Chaque contribution peut être quantifiée en utilisant la loi de Nernst-Einstein (par ex., Gaillard, 2004):

$$\sigma_i = \frac{D_i . q_i^2 . N_i}{k_B . T . Hr} \qquad (8)$$

où D_i est le coefficient de diffusion d'un ion i (m²/s), q_i sa charge (C), N_i la concentration de i (m^{-3}), k_B la constante de Boltzmann, T la température absolue (K) et Hr le rapport de Haven. Hr sert à exprimer les mécanismes de migration des porteurs de charge dans le melt (Chakraborty, 1995).

2.7.2. Acquisition des données

La conductivité électrique est obtenue à partir de la mesure de l'impédance complexe. L'appareil utilisé est un spectromètre d'impédance (Solartron, Schlumberger) acquis par l'ISTO en 2006. Selon le manuel d'utilisation, la précision sur la mesure d'impédance liée à l'impédance-mètre varie de 0.1 à 0.2%. Les mesures sont effectuées à l'aide de deux électrodes, quelques mesures à quatre électrodes ont été réalisées au CEMHTI (collaboration avec M. Malki), en utilisant le même appareil de mesure. Les mesures 4 électrodes sont couramment utilisées en science des matériaux alors que les mesures 2 électrodes sont largement majoritaires en géologie. Les deux techniques sont comparées dans l'article Pommier et al. 2009, accepté, présenté à la fin de ce chapitre. Les cellules de mesures utilisées (configuration 2 électrodes à 1bar, sous pression et configuration 4 électrodes) sont présentées Figure 1 dans l'article ci-après et au Chapitre 3.

L'impédance complexe, Z* (ou Z) est composée d'une partie réelle (Z') et d'une partie imaginaire (Z'') :

$$Z^* = Z' - jZ'' \quad (\text{avec } j^2=-1) \quad (8)$$

La partie réelle Z' correspond sans ambiguïté à la résistance électrique de l'échantillon, R (ohm). Cela signifie que. Z* = Z' = R quand Z''= 0, comme illustré Figure 2.7. Z'' traduit les phénomènes capacitifs (Z''<0) et inductifs (Z''>0). Z est mesurée en effectuant un scan en fréquence (de 10^6 à <1Hz). Pour visualiser la réponse électrique, la représentation dans le plan de Nyquist (représentant Z' en fonction de Z'') est préférée à la représentation exponentielle de Z (représentant le module et la phase en fonction de la fréquence), le premier type de représentation permettant d'extraire facilement la partie purement résistive de l'impédance du verre ou liquide silicaté. La réponse électrique du matériau correspond à un assemblage de résistance et condensateur, comme montré Figure 2.7B.

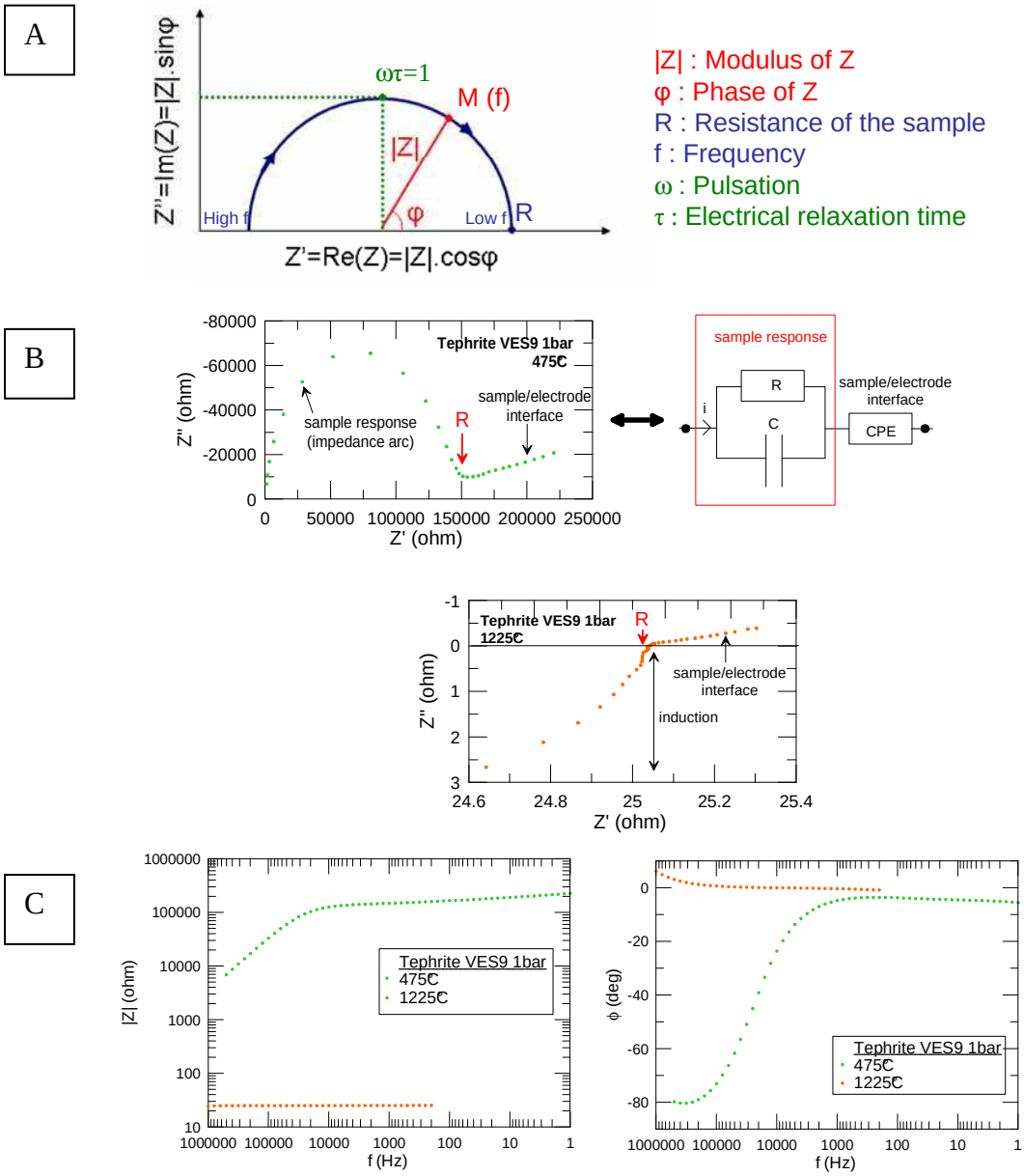


Figure 2.7: A) Sketch of the typical electrical response of a glass to a scan in frequency, in the Nyquist plan (real vs imaginary part), after Déportes et al. (1994). The electrical resistance R of the sample corresponds graphically to the intersection between the impedance spectra and the real axis. B) Example of the electrical response of the tephritic sample VES9 at 1bar, 475°C and 1225°C, in the Nyquist plan and electrical analog circuit (after Huebner and Dillenburg, 1995). A fit circle (Zview software) provides R = R_{sample} = $1.47.10^{5}$ohm, and C=$4.7.10^{-11}$F. The electrical response of the electrolyte corresponds to the association of a resistance, a capacitor and a Constant Phase Element (CPE) (in series or in parallel). C) Exponential representation of the complex impedance in B), consisting in presenting both the modulus and the phase as a function of the frequency.

Si les spectres obtenus dans le domaine vitreux sont des arcs d'impédance, ceux obtenus dans le domaine liquide présentent des perturbations dues à l'inductance des électrodes (Simonnet, 2003). Il est toutefois possible de corriger le signal dans le domaine liquide, en soustrayant à l'impédance Z mesurée la mesure de l'impédance parasite (Figure 2.8). Cette dernière a été obtenue avec une expérience de mesure en court-circuit (Pommier et al., 2009, accepté, cf fin de ce chapitre). Cependant, la valeur Z corrigée obtenue présente un demi-cercle de polarisation qui ne représente pas exactement Z liquide, du fait de la persistance de certains phénomènes de polarisation des électrodes (Simonnet, 2003). Cet arc d'impédance ne permet pas d'avoir accès au temps de relaxation. Notons que dans le domaine vitreux, l'impédance de l'échantillon est tellement grande comparée à celle des électrodes que la correction de Z mesurée est inutile.

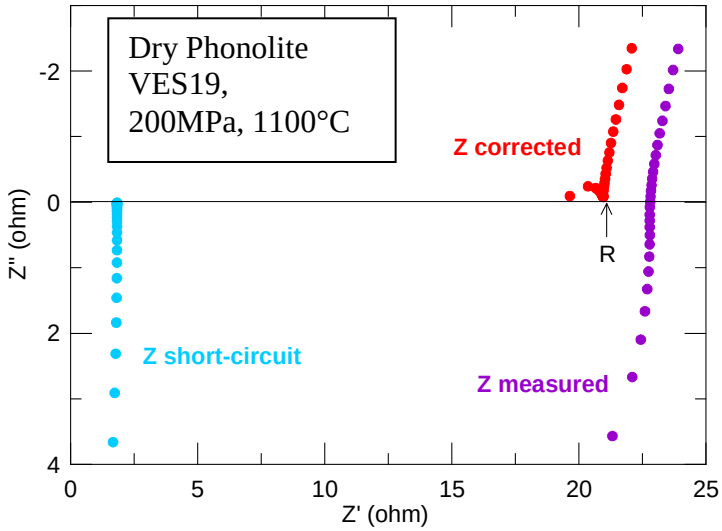


Figure 2.8: Measured and corrected impedances for the dry phonolite at 1100°C, 200MPa using 2-electrode measurements. Correction was done by performing a short-circuit experiment. The real part of Z short-circuit, representing the contribution of the electrodes, is about 2ohms. The value of the corrected electrical conductivity is obtained using the resistance value R and Eq. 8.

Une fois la valeur de résistance R (ohm) obtenue, la conductivité correspondante σ $(ohm.m)^{-1}$ est obtenue à l'aide du facteur géométrique G (m) :

$$\sigma = 1/(RG) \qquad (9)$$

Pour les mesures à 2 électrodes, l'échantillon a une géométrie cylindrique, inspirée de l'étude de Gaillard (2004). Ce type de cellule de mesure assure une bonne cohésion de l'assemblage ainsi qu'une géométrie de l'échantillon constante au cours de l'expérience. De plus, avec cette géométrie, l'échantillon se fixe facilement après les cannes de l'obturateur de l'autoclave

(mesures sous pression) et après le porte-échantillon du four à 1atm. Le détail des connexions pour lier de manière optimale le spectromètre d'impédance à la cellule de conductivité placée dans le four 1atm ou l'autoclave a été étudié dans Pommier (2006), rapport de stage ingénieur et de Master de Recherche. Les autres configurations de la cellule de mesure présentées dans la littérature sont comparées dans l'article Pommier et al., 2009, accepté.

Pour chaque mesure à (P, T) fixées, les mesures sont réitérées jusqu'à l'obtention d'une valeur de résistance stable. Dans la plupart des cas, cette stabilité est immédiate. Mais il arrive que le temps d'atteinte d'une valeur stable soit beaucoup plus long, comme illustré Figure 2.9. Ces changements au cours du temps sont liés à des changements chimiques. Dans le cas de la Figure 2.9, ils sont attribués à la dissolution des cristaux de leucite, la mesure étant effectuée à la frontière du liquidus. En assimilant les cristaux de leucite à des sphères, l'utilisation d'un formalisme de diffusion (Crank, 1975, cf Chapitre 3, Eq. 14) a permis de déterminer le coefficient de diffusion lié à la dissolution des cristaux. En considérant un rayon moyen de sphère de 300microns, d'après des observations au microscope, une valeur de $1.2.10^{-14}m^2/s$ est obtenue. Dans le Chapitre 5, la sensibilité de la conductivité électrique aux changements chimiques a été utilisée pour suivre l'évolution des réactions redox au cours du temps dans l'échantillon.

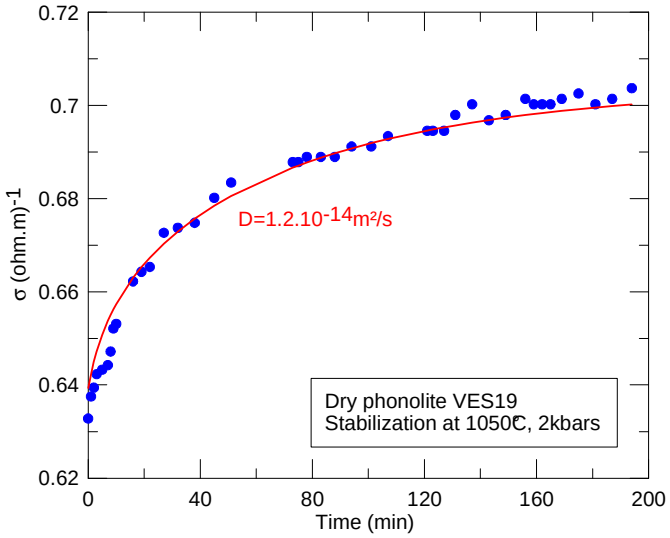


Figure 2.9: Time-dependence of the electrical response of the dry phonolitic melt at 1050°C, 200MPa. The long time span (~180min) requested to reach a stable value is attributed to the dissolution of crystals (leucite) formed while crossing the interval of crystallization (during the heating cycle), since this temperature is close to the liquidus temperature. The fit corresponds to the formalism of diffusion in a crystal –assimilated to a sphere (Crank, 1975) and provides a diffusivity value of $1.2.10^{-14}m^2/s$, considering an average radius for the crystals of leucite of 300microns.

Les mesures ont été effectuées dans des verres et des liquides silicatés, i.e. en dehors de l'intervalle de cristallisation. En effet, les premières expériences réalisées pendant le stage ingénieur/M2R (Pommier, 2006) ont montré que les cristaux se développent préférentiellement à l'interface avec les électrodes et sont donc une source de pollution de la réponse électrique mesurée (Figure 2.10).

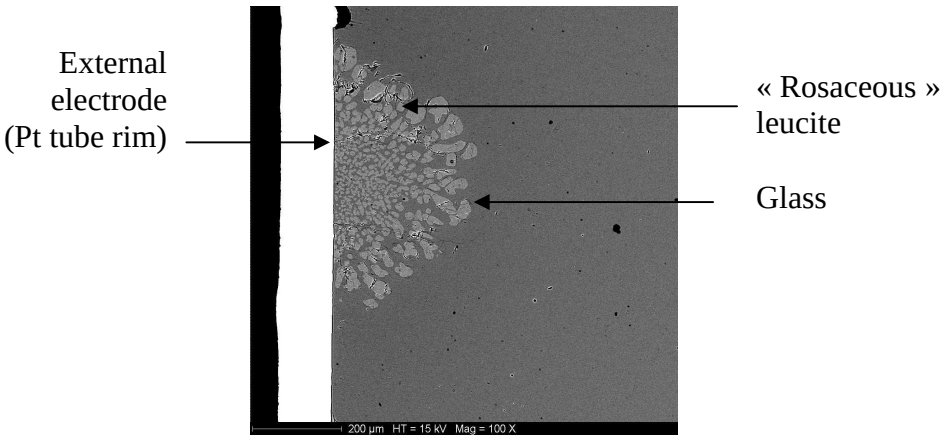


Figure 2.10: SEM photomicrograph of the dry phonolite sample at 1bar. The preferential growth of leucite on the Pt electrode wall (rosaceous shape) is clearly visible.

Par ailleurs, la mesure électrique étant globale (bulk), la contribution du liquide et des cristaux est mesurée sans connaître leurs proportions respectives. Par conséquent, il n'est pas possible de contrôler précisément ce qui est mesuré. L'effet des cristaux, ainsi que celui des bulles, sera discuté au Chapitre 3, en considérant notamment les différents modèles mathématiques permettant d'obtenir la conductivité électrique d'un magma, σ_{magma}, à partir de $\sigma_{liquide,}$ $\sigma_{cristaux}$ et σ_{bulles}. Les domaines vitreux et liquides ont été identifiés en réalisant des trempes (*wire loop technique*) d'échantillon à différentes températures à 1bar (Figure 2.11).

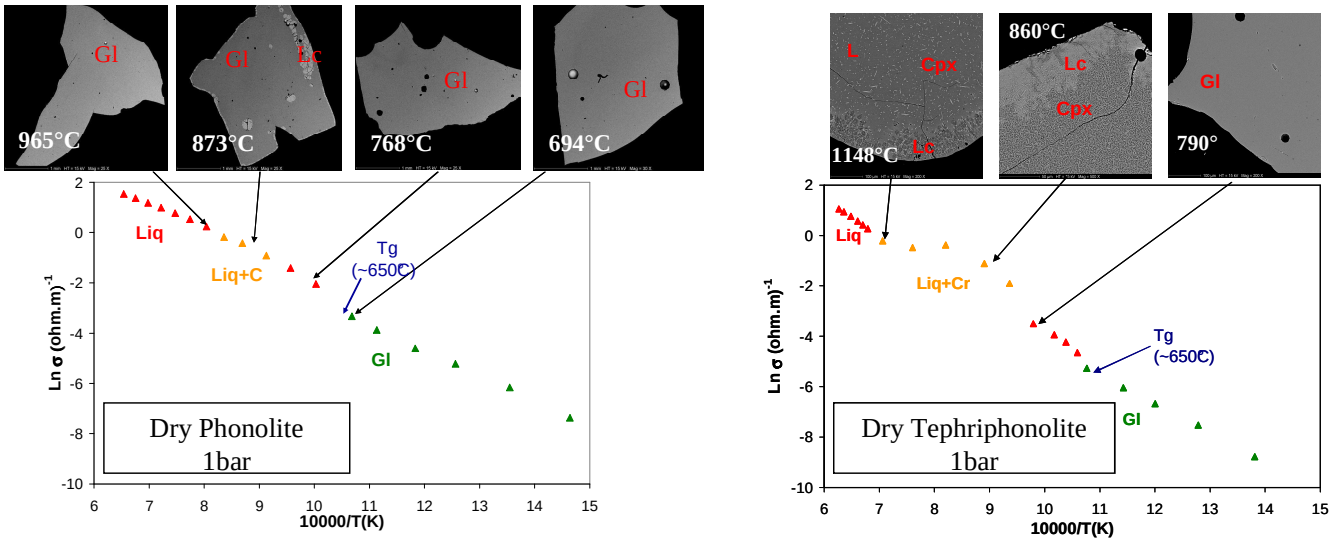


Figure 2.11: Conductivity as a function of temperature for the dry phonolite and the dry tephriphonolite from Mt. Vesuvius, at 1bar. Measurements in both the glass and liquid regions. The glass transition is identified as a kink in slope. The effect of crystals is not visible in the phonolite sample. This can be explained by the small time span spent to cross the intervall of crystallization that probably prevents the crystals from growing in the conductivity cell. SEM photographs correspond to pieces of samples placed close to the conductivity cell and quenched at different temperatures (wire loop technique).

2.8. Re-évaluation de la conductivité électrique des melts silicatés

Les mesures électriques en laboratoire sur des melts silicatés sont utilisées pour interpréter les anomalies géophysiques (en l'occurrence, magnétotelluriques). Sur la base de mesures à 2 et 4 électrodes, nous avons montré, dans l'article qui suit, que l'influence de la cellule électrique du système à 2 électrodes sur la conductivité mesurée (ou son inverse, la résistivité) peut avoir une importance significative pour les melts peu résistifs et augmente avec la température. A 1400°C, la résitivité des melts très conducteurs mesurée avec 2 électrodes peut atteindre six fois la valeur de résistivité mesurée avec 4 électrodes. Une expérience en court-circuit est nécessaire pour corriger les données à 2 électrodes. La contribution des électrodes a été aussi estimée pour des échantillons d'études antérieures, pour lesquelles la résistance de la cellule électrique peut être aussi élevée que la résistance de l'échantillon. Une correction des données de résistivité de la littérature est proposée et les valeurs des paramètres énergétiques correspondants (activation d'énergie et facteur pré-exponentiel) sont recommandées.

Références

Arrhenius, S. (1889) On the reaction velocity of the inversion of cane sugar by acids, translated and published in M.H. Back and K.J. Laidler, eds., Selected readings in Chemical Kinetics, Oxford, Pergamon, 1967.

Behrens, H., C. Romano, M. Nowak, F. Holtz, and D. B. Dingwell (1996) Near-infrared spectroscopic determination of water species in glasses of system $MAlSi_3O_8$ (M=Li, Na, K): An interlaboratory study, Chemical Geology, *128*(1-4), 41-63.

Burnham, C.W. (1975) Water and magmas: a mixing model. Geochimica et Cosmochimica Acta, 39, 1077-1084.

Caillot, E., Duclot, M. J., Souquet, J.L., and Levy, M. (1994) A unified model for ionic transport in alkali disilicates below and above the glass transition. Physics and Chemistry of Glasses, 35(1), 22-27.

Chakraborty, S. (1995) Diffusion in silicate melts. In Structure, Dynamics and Properties of silicate melts, Reviews in mineralogy, 32, 411-503.

Christie, D.M., Carmichael, I.S.E., and Langmuir, C.H. (1986) Oxidation states of mid-ocean ridge basalt glasses. Earth and Planetary Science Letters 79 (3-4), 397-411.

Crank, J. (1975) The Mathematics of Diffusion. 2nd ed., 440 pp., Claredon, Oxford, U.K.

Déportes, C., M. Duclot, P. Fabry, J. Fouletier, A. Hammou, M. Kleitz, E. Siebert, and J.L. Souquet (1994) Electrochimie des solides, Collection Grenoble Sciences, Pug, Grenoble, 437p.

Frost, D. J., and C. A. McCammon (2008) The redox state of the Earth's mantle, *Annual Rev. Earth and Planet. Sciences*, 36, 389-420.

Gaillard, F., Pichavant M., and Scaillet B. (2003) Experimental determination of activities of FeO and Fe2O3 components in hydrous silicic melts under oxidizing conditions. Geochim. Cosmochim. Acta, 67 (22), 4389-4409.

Gaillard, F. (2004) Laboratory measurements of electrical conductivity of hydrous and dry silicic melts under pressure. Earth and Planetary Science Letters, 218 (1–2): 215–228, doi:10.1016/S0012-821X(03)00639-3.

Hanna, M.W. (1972) Introduction à la mécanique quantique. Ediscience, Paris, pp234.

Huebner, J. S., and R. G. Dillenburg (1995) Impedance spectra of hot, dry silicate minerals and rock: qualitative interpretation of spectra, American Mineralogist, 80(1-2), 46-64.

Magnien, V., Neuville D. R., Cormier L., Roux J., Hazemann J.-L., de Ligny D., Pascarelli S., Vickridge I., Pinet O., and Richet P. (2008) Kinetics and mechanisms of iron redox reactions in silicate melts: the effects of temperature and alkali cations. Geochimica et Cosmochimica Acta, 72(8), 2157-2168 .

Newman, S., Stolper, E.M., and Epstein, S. (1986) Measurement of water in rhyolitic glasses-calibration of an infrared spectroscopic technique. American Mineralogist, 71(11-12), 1527-1541.

Pommier (2006) Etude des propriétés électriques des magmas hydratés sous pression-application au Vésuve. Rapport de stage ingénieur de recherche, Master Sciences et Technologies, Polytech'Orléans, Université d'Orléans, 40pp.

Pommier, A., Gaillard, F., Pichavant, M., and Scaillet, B. (2008) Laboratory measurements of electrical conductivities of hydrous and dry Mount Vesuvius melts under pressure. Journal of Geophysical Research, 113, B05205, doi:10.1029/2007JB005269.

Pommier, A., Gaillard, F., Malki, M., and Pichavant, M. (2009) Re-evaluation of the electrical conductivity of silicate melts, American Mineralogist, accepted.

Simonnet, C., Phalippou, J., Malki, M., and Grandjean, A. (2003) Electrical conductivity measurements of oxides from molten state to glassy state. Reviews of Scientific Instruments, 74 (5): 2805-2810.

Watson, E. B. (1994) Diffusion in volatile-bearing magmas. In *Volatiles in Magmas*, edited, pp. 371-411, Mineralogical Soc America, Washington.

Westrich, H. R. (1987) Determination of water in volcanic glasses by Karl-Fischer titration, Chemical Geology, *63*(3-4), 335-340.

Wilson, A. D. (1960) The micro-determination of ferrous iron in silicate minerals by a volumetric and colorimetric method. Analyst, 85, 823– 827.

Zhang, Y.X., and Stolper, E.M. (1991) Water diffusion in a basaltic melt, Nature, 351, 306-309.

Re-evaluation of the electrical conductivity of silicate melts

Article accepté le 29 septembre 2009 au journal American Mineralogist

A. Pommier[1], F. Gaillard[1], M. Malki[2] and M. Pichavant[1]

[1]*CNRS/INSU, Université d'Orléans, Université François Rabelais-Tours, Institut des Sciences de la Terre d'Orléans (ISTO), UMR 6113, Campus Géosciences, 1A rue de la Férollerie, 45071 Orléans cedex 2, France*

[2]*CNRS, Conditions Extrêmes et Matériaux : Haute Température et Irradiation (CEMHTI), UPR 3079, 1D avenue de la Recherche Scientifique, 45071 Orléans cedex 2, France*

Abstract

Electrical impedance measurements in laboratory on silicate melts are used to interpret magnetotelluric anomalies. On the basis of two- and four-electrode measurements, we show that the influence of the electrodes of the 2-electrode system on the measured resistivity can be of significant importance for low-resistivity melts and increases with temperature. At 1400°C, the resistivity of very conductive melts measured with two electrodes can reach six times the resistivity value measured with four electrodes. A short-circuit experiment is needed to correct the 2-electrode data. Electrodes contribution is also estimated for samples from other studies, for which the resistance of the electrical cell can be as high as the resistance of the sample. A correction of the resistivity data from the literature is proposed and values of the corresponding Arrhenian parameters are recommended.

Keywords: impedance measurements, resistivity, melts.

1. INTRODUCTION

The knowledge of the electrical properties of melts is needed for the interpretation of magnetotelluric profiles (Wannamaker et al. 2008; Yoshino et al. 2006; Tarits et al. 2004; Müller and Haak 2004; Roberts and Tyburczy 1999). For example, both magnetotelluric data and electrical measurements in laboratory allowed the identification of partial melt in the asthenosphere below the East Pacific Rise (Yoshino et al. 2006). The information provided by electrical measurements in laboratory is of significant interest to the interpretation of geophysical anomalies, in terms of quantitative constraints placed on potential conductive magma reservoirs (Pommier et al. 2008; Gaillard et al. 2008) and for the elaboration of

conductivity models (Xu et al. 2000). Since electrical conductivity (or resistivity) is extremely sensitive to small chemical and physical changes, it represents a subtle probe for studying silicate melts properties under controlled and variable conditions (T, P, composition and fO_2) (Pommier et al. 2008; Gaillard and Iacono Marziano 2005; Gaillard 2004; Tyburczy and Waff 1985, 1983). Several studies have contributed to improve the technique of electrical impedance measurements over the past decades (e.g. Lupotto et al. 1987; Hodge et al. 1976; Bauerle 1969).

Experimental difficulties raised by electrical measurements include the maintenance of a well-constrained electrical cell geometry and the necessity to limit the interactions between the sample and the components of the electrical cell. In addition, the problem of the contribution of the electrical response of the electrodes to the measured resistance can be of non negligible importance (Tyburczy and Waff 1983) and needs to be quantified. Most electrical measurements of natural silicate melts are 2-electrode based, whereas the 4-electrode system is mostly used by the material science community. The resistance of the electrodes ($R_{electrodes}$) is included in the impedance measured by the 2-electrode system, which can affect the electrical response of the sample (effective resistance), particularly for low resistivity melts. It is therefore important to evaluate the contribution of the electrodes in the experimental conductivity database for silicate melts. Because this problem concern most of the current database of electrical resistivities of natural melts, it also raises a direct implication in the interpretation of magnetotelluric profiles in molten or partially molten regions of the Earth's crust and mantle.

The main goal of this study is to address the influence of the electrode configuration on the measurement of the resistivity of melts in laboratory. We measured the electrical response of three silicate melts (a basalt, a phonolite and a borosilicate) using two different techniques, based on 2- and 4-electrode measurements. Experiments were conducted at 1 bar and in the T range [800-1430°C]. The influence of the electrical response of the electrodes on the 2-electrode data was identified, demonstrating the need for a significant correction of the impedance measurements. Errors on resistivity values of silicate melts due to electrodes contribution were estimated for the investigated samples as well as for samples from other studies. We recommend values of corrected Arrhenian parameters for the calculation of electrical resistivity of natural silicate melts.

2. EXPERIMENTS

2.1. Starting products

The three starting materials were a borosilicate synthetized at the CEMHTI (CNRS-Orléans, France), a phonolite from Mt. Vesuvius (Pommier et al., 2008), and an alkali basalt from the Pu'u' 'O'o volcano (Kilauea). The composition of the Kilauea basalt is close to the typical composition of MORB-type basalts. The samples were chosen for their differences in chemical composition and their geological interest. The starting materials were finely crushed, melted in air at 1400°C during ~1h and quenched into a glass. The composition of the starting glasses is presented in Table 1. For the 2-electrode measurements, the starting materials were melted in air in a Pt crucible and the resulting bubble-free glass was drilled to cylinders (Pommier et al. 2008). For the 4-electrode measurements, the starting materials were melted in an alumina crucible which was directly used in the electrical conductivity measurements (Simonnet et al.2003).

2.2. Basic concepts of complex impedance measurements

Complex impedance measurements allow to study conduction processes by discriminating most of polarization effects observed during a scan in frequency (Bruin and Franklin, 1981). While the electrical resistance of geologic materials has been measured for almost one century (e.g. Volarovich and Tolstoi, 1936), impedance measurements applied to solid electrolytes are more recent (Bauerle, 1969; Tyburczy et Fisler, 1995 and references therein). The interpretation of impedance spectra in terms of transport mechanisms has been widely investigated (Roberts et Tyburczy, 1994; Huebner et Dillenburg, 1995; Roling, 1999).

Impedance spectroscopy consists in recording the electrical impedance of a material at variable frequency. An ac current is delivered between two "current electrodes" and an induced ac voltage drop is measured between two "voltage electrodes". The complex impedance Z* is deduced, $Z^*=U^*/I^*$, U* being the voltage drop vector and I* being the current vector (Simonnet et al. 2003). In the 2-electrode system, current and voltage electrodes are conveyed through only two electrodes.

The complex impedance Z* is the sum of a real and an imaginary parts: $Z^*=R+jX$, R being the electrical resistance and X the reactance. Thus, the determination of the electrical resistance of a material consists in extracting the real part of the complex impedance $Z^*_{material}$ (Bagdassarov et al. 2004; Gaillard 2004; Pommier et al. 2008). The electrical resistivity ρ (ohm.m) is deduced from the value of R (ohm) by using the following relation:

$$\rho = G.R \qquad (1)$$

where G is the geometric factor (m) and depends on the dimensions of the material studied and on the distance between electrodes.

Table 1: Composition of the starting glasses.

Sample	Borosilicate	Phonolite	Kilauea basalt
SiO_2	50	55.73	49.96
TiO_2	0	0.16	2.41
Al_2O_3	8	21.94	13.24
FeOt	2	1.95	10.88
MnO	0	-	0.13
MgO	0	0.19	7.50
CaO	0	2.87	10.58
Na_2O	22	6.11	2.29
K_2O	0	10.14	0.38
B_2O_3	18	-	-
Total	100	99.09	97.89

2.3. Experimental setups

The two experimental setups are presented in Figure 1a. 2-electrode experiments were performed at the ISTO and 4-electrode experiments at the CEMHTI (Orléans, France). All experiments were conducted in air. In both cases, the glass sample was placed in the hot spot of the furnace. Temperature, monitored with a Eurotherm controller, was measured by a type S thermocouple, placed adjacent to the conductivity cell, and is known to within ±2°C. Impedance was measured in response to an AC signal in the 1Hz-1MHz frequency range using an impedance gain/phase analyzer (Solartron 1260, Schlumberger Co.), the voltage amplitude being 0.1 to 0.5V.

In the 2-electrode configuration, the two groups of welded electrodes are connected to a Pt tube (external electrode) and a Pt wire (internal electrode), respectively. The cylindrical geometry of the sample (L from 3.5 to 9mm; OD from 4.5 to 7.5mm and ID=1mm) implies the electrical resistivity to be coaxially measured. An alumina plug prevents the two electrodes from being in contact with each other (Pommier et al. 2008). In the 4-electrode configuration, two Pt sheets serve as current electrodes and two Pt wires measure the voltage drop. The four electrodes are connected separately to the impedance spectrometer and the resistivity is measured between the wires. These Pt foils are totally immersed in the liquid sample contained in the alumina crucible (L>10mm; OD=30mm). As shown in Figure 2,

measurements performed at different immersion depths of the electrodes underline that the wetting effect on the measured electrical resistance is negligible for an immersion >5mm (similarly to Gaillard et al. 2008 for very conductive carbonate liquids with high wetting properties). All 4-electrode measurements were performed at an immersion depth of ~8mm. The precision of the immersion depth of the electrodes in the melt is controlled by a mechanical displacement system allowing the depth to be determined with a good precision (0.02mm, Malki and Echegut 2003).

Equivalent electrical circuits are presented in Figure 1b for both configurations. The different components of the electrodes (conductivity cell parts + connecting metallic wires) are associated in series with the effective complex impedance of the sample (Z^*_{sample}). Contrary to the 2-electrode system, the current in the 4-electrode setup is not delivered in the loop of measurement of the potential. As a result, the electrical impedance of the cell is not involved in the measured impedance ($Z^*_{measured}$) and:

$$Z^*_{measured} = Z^*_{sample} + Z''_{induct} \qquad (2)$$

where Z''_{induct} (the imaginary part X of $Z^*_{electrodes}$) represents the inductive effects of the electrodes and was found to be negligible for frequencies <0.1MHz (Simonnet 2004). According to Figure 1b, the impedance measured using a 2-electrode system can be written:

$$Z^*_{measured} = Z^*_{sample} + Z^*_{electrodes} = [R+jX]_{sample} + [R_{Pt\ parts} + Z''_{induct} + (R_{pol} // C_{pol})]_{electrodes} \qquad (3)$$

where $R_{Pt\ parts}$ is the resistance of the Pt tube and Pt wires (Figure 1a) and the association R_{pol} // C_{pol} represents the polarization effects (ionic double-layer). The best method for estimating the electrode contributions is to conduct a short-circuit experiment. Because Pt resistivity is temperature-dependent, short-circuit measurements must be done at temperature. This experiment consists in connecting the two electrodes with a small Pt wire (Figure 1a). Electrical measurements are performed on an empty cell (i.e. without sample) and $Z^*_{short\text{-}circuit} = Z^*_{electrode}$.

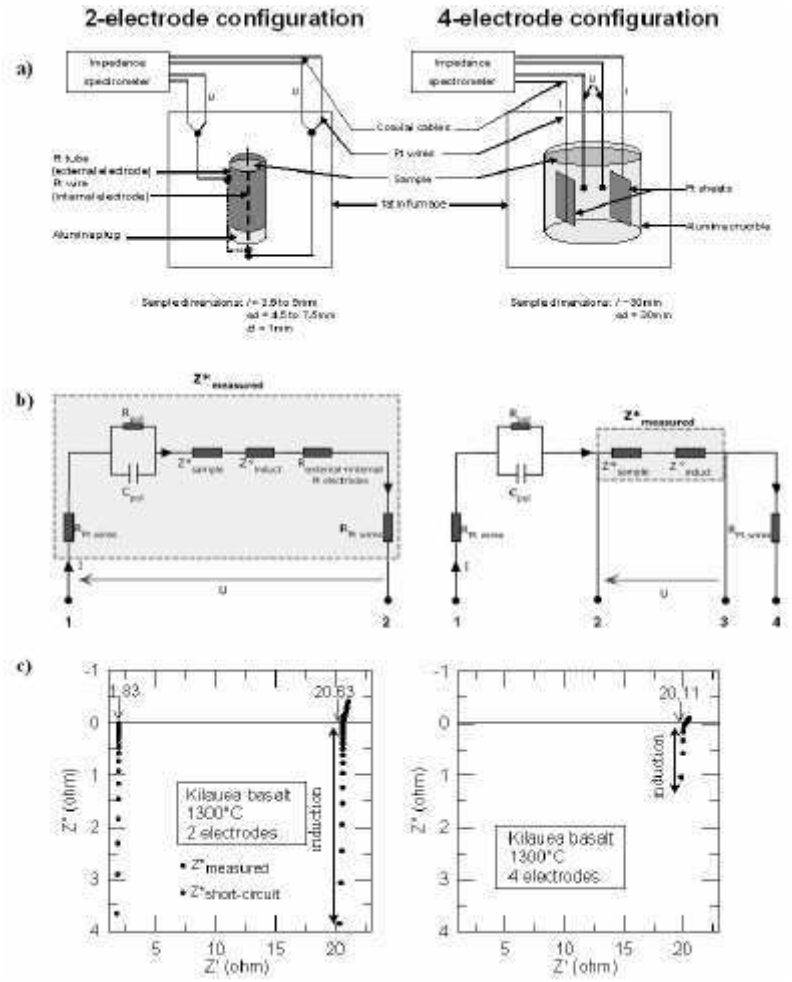


Figure 1: 2-electrodes and 4-electrode configurations. a) Drawing of the electrical cells connected to the impedance spectrometer. U and I represent the "voltage" and "current electrodes", respectively. The connection of the 2 electrodes for the short-circuit experiment is represented by the dashed line. Note that the short-circuit experiment is performed on a free-sample cell. b) Equivalent circuit of both cells. With the 2-electrode setup, the resistance of the electrodes is counted in the measured impedance (Z*measured). See text for details. c) Electrical responses observed in the Nyquist plan (Z', Z") for the Kilauea basalt at 1300°C. The resistance of the sample R(ohm) is obtained for Z" = 0 and represents the real part of the complex impedance (Z'). The higher value of R in the 2-electrode system is attributed to the contribution of the resistance of the two electrodes. The short-circuit measurements underline the contribution of the cell in the 2-electrode configuration.

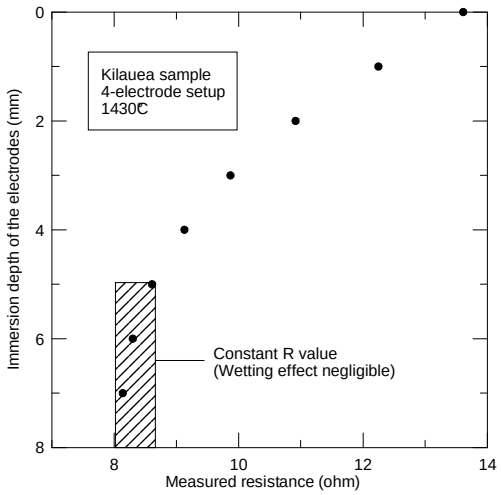


Figure 2: Changes in electrical resistance as a function of the immersion depth of the 4-electrode system.

2.4. Data reduction and calibration

An example of the electrical response of the sample to a scan in frequency is presented in the complex plane (Z', Z") Figure 1c. Graphically, the value of the electrical resistance R corresponds to the intersection of the electrical response with the real axis (i.e. Z"=0). The first part of the response (Z'<R and Z">0) represents the induction effects whereas the second part (Z>R and Z"<0) is attributed to the impedance of the interface between the sample and the electrode (Huebner and Dillenburg 1995).

The determination of the resistivity value ρ requires the determination of the geometric factor G (Eq. 1). For the 4-electrode configuration, G was determined through the calibration of the cell. Calibration was performed using three aqueous KCl solution (0.01, 0.1 and 1M) of known resistivity at room temperature. Standard liquids are generally used for this calibration (Wu and Koch, 1991). The geometric factor of the 4-electrode cell is calculated by measuring the resistance R of the KCl solution and using Eq. 1. Similar values of G were obtained using the different KCl solutions and the geometric factor was found to be 0.039m. For the 2-electrode configuration, the diffusion formalism in a cylinder in which diffusion is coaxial (Crank 1975) showed that G can be written as follows:

$$G = \frac{2\pi L}{\ln(d_{ext}/d_{\text{int}})} \qquad (4)$$

where L is the length of the cylindrical glass sample, d_{ext} is the outer diameter and d_{int} the internal diameter. A constant value of the geometric factor during the experiment is assumed. The uncertainty on ρ due to error propagation of typical uncertainties on R, L, d_{ext} and d_{int} is in the range of 7-12.5% for all melts. Eq. 4 yielded values of G ranging from 0.015 to 0.019m.

These values were confirmed by the calibration of the 2-electrode setup cell using KCl solution (1M).

2.5. Chemical characterization of the samples

Most glass samples were analyzed after the experiment with a Camebax SX-50 electron microprobe in order to check for interactions between the sample and the cell parts (Pt and alumina). Analyses were conducted at 15 kV, 6 nA, 10 s on peak and 5 s on background. No significant variations in oxides contents were measured in the samples after 2-electrode experiments, in agreement with the observations of other studies using similar electrical cells (Pommier et al. 2008; Gaillard 2004). Iron was found to be present at very low concentrations (<0.5wt%) in the Pt electrodes from the 2-electrode setup. Iron depletion was thus too small to change significantly the FeO content of the melt. Therefore, we considered that iron loss was of minor importance in this study. Electron microprobe traverses were performed in one sample from the 4-electrode experiments in order to estimate the contamination of the melt by the alumina crucible. Al_2O_3 enrichment was found to affect the melt on a distance <1mm from the Al_2O_3 crucible/melt interface. The melt volume occupied by the immersed electrodes (see Figure 1a) is not spatially concerned by the contaminated melt. A contamination of the whole volume of melt due to convection can be excluded, due to the small value of the Rayleigh number (<200, Jaupart and Tait 1995).

3. RESULTS

The electrical resistivities of the three investigated melts measured using the 2 and 4 electrode configurations are presented Figure 3. For both configurations, measurements during heating and cooling cycles yielded similar resistivity values, which demonstrates reproducibility (in agreement with Pommier et al. 2008 and Malki and Echegut 2003). The short-circuit experiment was performed with the 2-electrode system, from 800 to 1400°C. A resistance from 1.5 to 2ohm was measured in this T-range, corresponding to the contributions of the electrodes. The configuration adopted for the short-circuit experiment (Figure 1a) does not take into account the resistance of the conductivity cell (Pt tube and inner Pt wire). The resistance of these two Pt parts was calculated on the investigated T range using the known resistivity of Pt and Eq. 1. At 1200°C, the resistance of the Pt tube and inner wire (external and internal electrodes, respectively) represent less than 1% of the resistance of the conductivity cell, the 99% corresponding to the Pt wires (cf Figure 1a). This result underlines

the very low contribution of the Pt tube and inner wire to the whole electrode resistance and validates the configuration used for the short-circuit experiment. For all 2-electrode experiments, the resistance of the electrodes was deduced from the measured resistance at each T:

$$R_{sample} = R_{measured} - R_{electrodes} \quad (5)$$

and

$$\rho_{sample} = \rho_{corrected} = G.R_{sample} \quad (6)$$

These corrected resistivity values correspond to the "2-electrode corrected" data in Figure 3. The good agreement between 2-electrodes corrected data and 4-electrode data is clearly shown.

The principal result shown in Figure 3 is that the 2-electrode setup used in this study implies a low correction on the measured resistivity values of low-conductive melts (phonolite and basalt), while electrical measurements of high-conductive melts (borosilicate) require either to perform a short-circuit experiment in order to quantify the electrodes contributions or the use of a 4-electrode setup. The correction on 2-electrode data of resistivity values of the basaltic liquid only represents between 2 and 10% of the 4-electrode value and is thus negligible for our coaxial experimental setup. The correction of the 2-electrode data was found to increase with temperature. This can be easily understood since the electrical resistivity of silicate melts decreases with increasing T whereas the resistivity of Pt wires has the opposite behaviour. As shown in Figure 3, the influence of the electrodes affects dramatically the resistivity of the less resistive melt (borosilicate). Indeed, at 1400°C, the resistivity measured with the 2-electrode system (0.05ohm.m) is six times higher than the resistivity value given by the 4-electrode system (0.008ohm.m). A slight but noticeable difference was observed for the data of the phonolitic melt at the highest temperatures: at 1260°C, the resistivity value from the 2-electrode experiment is 0.1ohm.m greater than the value measured in the 4-electrode experiment, corresponding to an error on the 4-electrode value of 37% ($=100.((\rho_{2\text{-electrode}}-\rho_{4\text{-electrode}})/\rho_{4\text{-electrode}})= 100.(0.1/0.27)$).

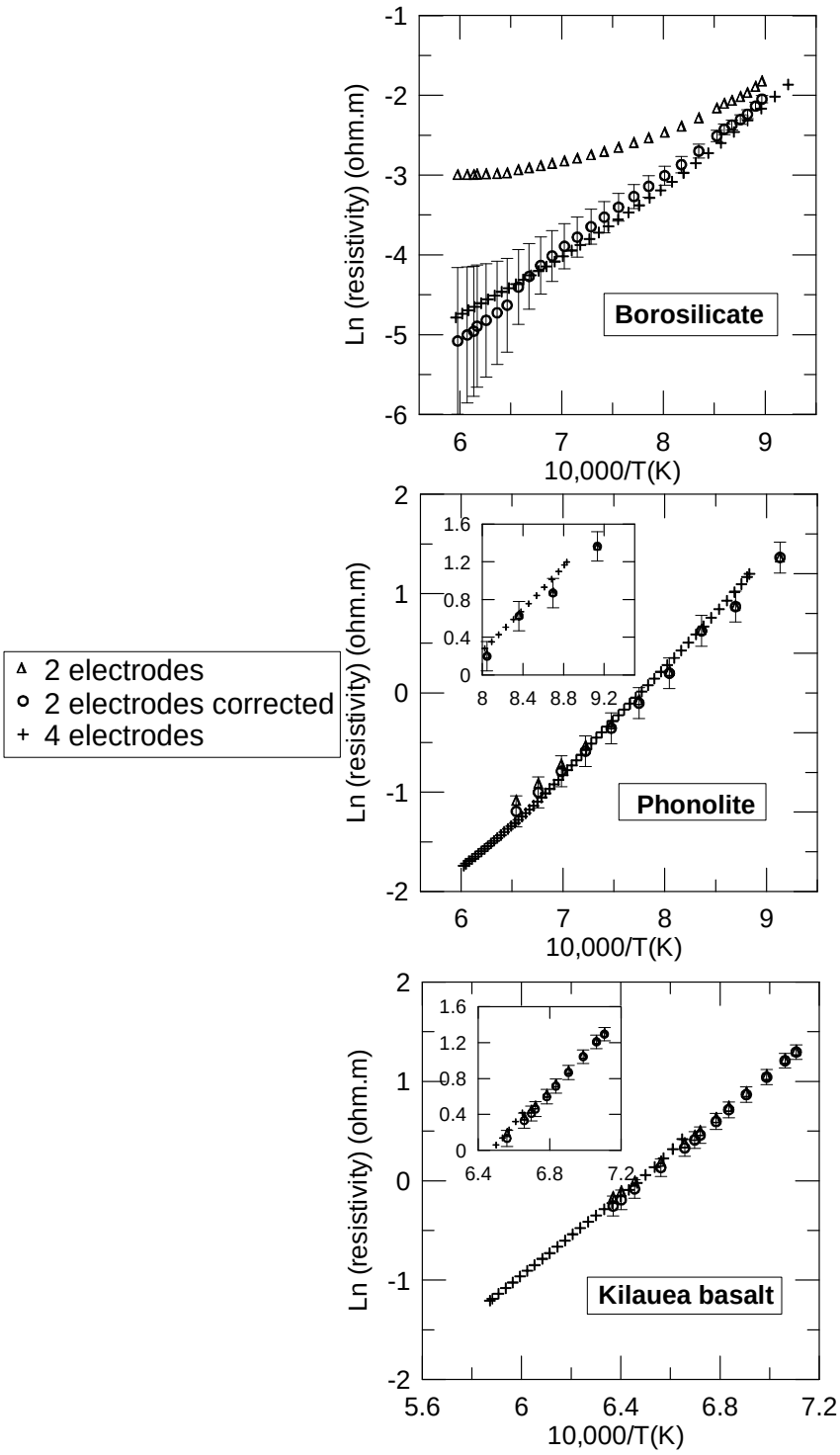


Figure 3: Dependence of the electrical resistivity with temperature for the three investigated melts using 2-electrode (triangles) and 4-electrodes (asterisks) configurations. Circles correspond to the 2-electrode data without the contribution of the resistivity of the electrodes ("2-electrode corrected"). See text for details. Inset graphs focus on the high temperatures data. Error bars shown for the 2-electrode corrected data.

Measurements were performed at high temperatures on a large interval. The temperature dependence of the electrical response of the investigated samples is shown in Figure 3. All the data can be fitted by an Arrhenian formalism:

$$\sigma = \frac{1}{\rho} = \sigma_0 . \exp\left[\frac{-Ea}{R.T}\right] \qquad (7)$$

with σ the electrical conductivity $(ohm.m)^{-1}$, ρ the electrical resistivity (ohm.m), σ_0 the pre-exponential factor $(ohm.m)^{-1}$, Ea the activation energy (J/mol), R the universal gas constant $(J.mol^{-1}.K^{-1})$ and T the temperature (K). Values of the Arrhenian parameters calculated from 4-electrode measurements are similar to those from 2-electrode corrected measurements and are presented in Table 2.

Table 2: Values of the energetic parameters.

Sample	Corrected* $Ln\sigma_0$ $(ohm.m)^{-1}$	Uncorrected° $Ln\sigma_0$ $(ohm.m)^{-1}$	Corrected* Ea (kJ/mol)	Uncorrected° Ea (kJ/mol)
Borosilicate	10 *(1.5; 0.1)*	5 *(0.5; 0.1)*	73 *(14; 1)*	31 *(5.5; 2)*
Phonolite	8 *(0.6; 0.1)*	7 *(0.5; 0.2)*	83 *(7; 2)*	79 *(5; 2)*
Kilauea basalt	14 *(1.5; 0)*	13 *(1.5; 0.1)*	177 *(22; 1)*	167 *(17; 2)*

* Corresponds to results from 2-electrode measurements corrected. Similar results with the 4-electrode measurements. See text for details.
° Corresponds to results from 2-electrode measurements.
Relative errors and standard deviations in terms of least unit cited on Ea and $Ln\sigma_0$ values are shown in parentheses *(error; standard deviation).*
Error propagation has been estimated using the error on Lnσ and Eq. 7.

$$\Delta Ln\sigma = (1/\sigma).\Delta\sigma = \left|\frac{-1}{2\pi R^2 l}.Ln\frac{de}{di}\right|\Delta R + \left|\frac{-1}{2\pi R l^2}.Ln\frac{de}{di}\right|\Delta l + \left|\frac{1}{2\pi R l}.\frac{1}{de}\right|\Delta de + \left|\frac{-1}{2\pi R l}.\frac{1}{di}\right|\Delta di$$

with ΔX the error on X, ΔR=0.5ohm, and Δde=Δdi=Δl=0.1mm.

4. DISCUSSION

Experiments performed with our 2-electrode setup have underlined the importance of the contributions of the electrodes to the measured resistivities of very low resistivity materials. Comparison was made with other 2-electrode setups from other studies. Setups characteristics are listed in Table 3 and results are presented in Figure 4. The 2-electrode setup used in this study is similar to the setup used in Pommier et al. (2008) (experiments on dry and hydrous tephritic to phonolitic samples), Gaillard and Iacono Marziano (2005)

(basalt) and Gaillard (2004) (dry and hydrous rhyolite). Only the sample dimensions slightly changed, modifying the value of G (Eq. 4). The results of the short-circuit experiment performed in this study can be applied to correct the results from the studies mentioned above. Our setup was compared with the techniques presented in Rai and Manghnani (1977) (basalts), Waff and Weill (1975) (trachyte and andesite) and Presnall et al. (1972) (synthetic basalt). The electrical response of the electrodes was estimated using indications given in the different studies. For studies using the loop technique (Rai and Manghnani 1977; Waff and Weill 1975), the resistance of the electrodes corresponds to the sum of the resistances of two metallic wires, calculated as follows:

$$R_{wire} = \rho_{wire} \cdot \frac{l}{S} \qquad (8)$$

with ρ_{wire} the resistivity of the metal (ohm.m) (given in the literature), l the length of the wire (m) and S the cross-section area of the wire (m^2). Regarding the study from Presnall et al. (1972), the resistance of the Pt wires was estimated using Eq. 8 and the resistance of the conductivity cell was calculated using Eq. 1 for the adopted cell geometry (consisting in two Pt crucibles fitted into each other). The sum of both resistances (wires and conductivity cell) corresponds to the resistance of the electrodes. An error of ~20% is assumed on calculations of R_{cell}, due to the lack of information regarding the length of metallic wires or the geometry cell.

The contributions of the electrodes to the measured resistance were estimated using the $R_{measured}/R_{electrodes}$ ratio for this and previous 2-electrode studies, and are presented in Figure 4. The coaxial setup used in our laboratory is efficient for measuring the electrical properties of dry natural silicate melts ($R_{measured}/R_{electrodes}$ >5) and the correction of the electrodes contributions will not significantly modify the measured resistance. In Gaillard (2004) and Pommier et al. (2008), the lowest values of the $R_{measured}/R_{electrodes}$ ratio were obtained for the hydrous rhyolite and hydrous phonolite, respectively, i.e. the most conductive investigated samples. For these samples, $R_{electrodes}$ represents 10 to 40% of R_{sample}, the contribution of the electrodes to the measured resistance increasing with increasing T. The low values of the ratio for the borosilicate from this study and carbonatites from Gaillard et al. (2008) underline the need in conducting short-circuit experiments prior to 2-electrode measurements on very conductive melts. In Gaillard et al. (2008), who performed 4-electrode measurements, a comparison between 4-electrode and 2-electrode data on $(Na,K,Ca_{0.25})_2(CO_3)_2$ at 740°C has shown that electrodes are less conductive than the carbonatite melt. Using a 2-electrode setup similar to the one of the present study implies that

the correction of the resistance of the electrodes is not needed for low conductivity values, while it can be critical for high electrical conductivity values.

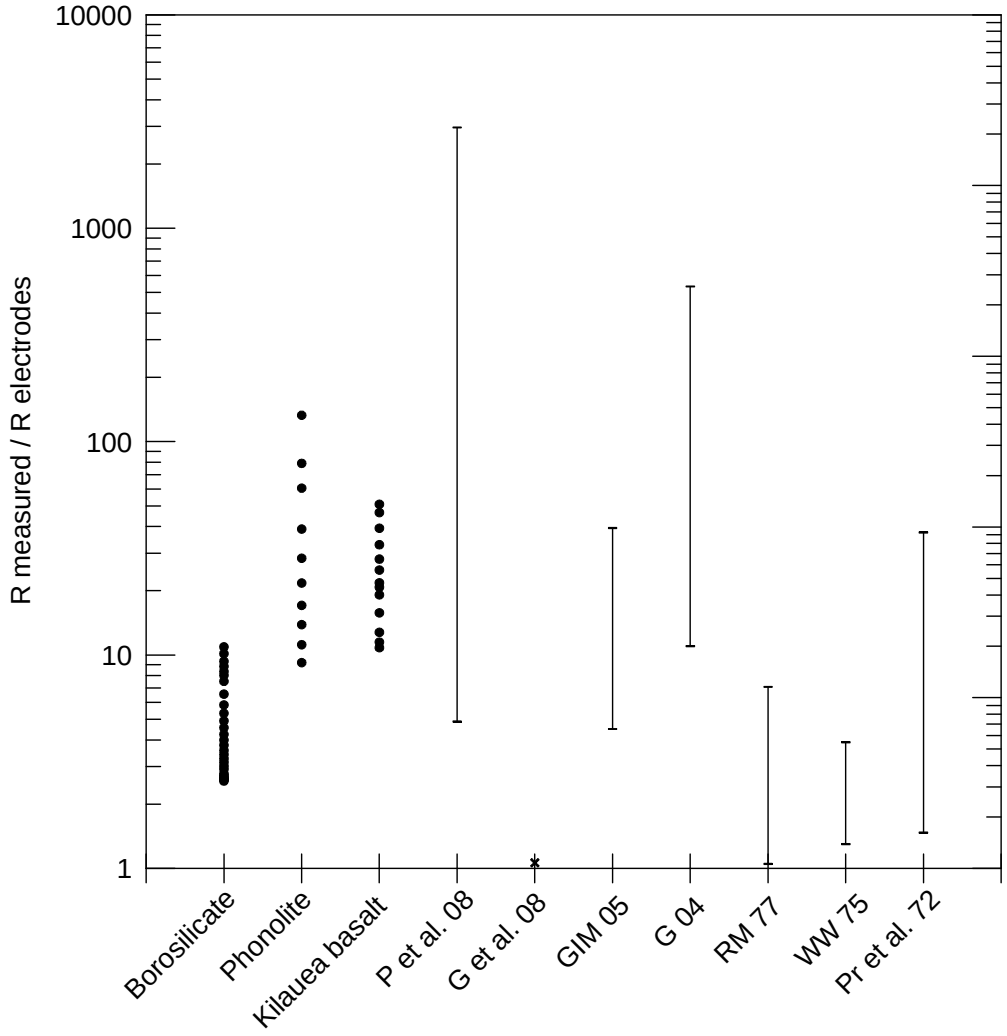


Figure 4: Ratio of the measured resistance and the resistance of the electrodes for this study and other studies of the electrical conductivity of silicate melts using 2-electrode measurements. P et al. 08: Pommier et al. (2008), G et al. 08 : Gaillard et al. (2008), GIM 05 : Gaillard and Iacono Marziano (2005), G 04 : Gaillard (2004), RM 77 : Rai and Manghnani (1977), WW 75 : Waff and Weill (1975), Pr et al. 72 : Presnall et al. (1972). The lower the ratio, the higher the contribution of the electrical cell to the measured resistance.

Table 3: Characteristics of the 2-electrode setups used in previous studies.

Source [1]	Technique	External electrode		Internal electrode		Geometric factor of the sample (m)
		Material	Dimensions (mm)	Material	Dimensions (mm)	
P et al.08	Cylindrical cell	Pt tube	L : 5-10, D : 5 Thickness : 0.2	Pt wire	L:10-15, D:1	1.4-1.8.10^{-2}
G04	Cylindrical cell	Pt tube	L : 30, D : 6 Thickness : 0.2	Pt wire	L:30, D:1	1.4.10^{-2}
RM77	Loop technique	80%Pt-20%Rh wire	L: 7, D: 0.64	80%Pt-20%Rh wire	L: ~7, D: 0.241	3.6.10^{-2}
WW75 (W76)	Loop technique	80%Pt-20%Rh wire	L: 7, D: 0.64	90%Pt-10%Rh wire	L: ~7, D: 0.241	3.6.10^{-2}
Pr et al.72	Hemispherical cell	Pt hemispherical crucible	L:~20, D:20	Pt hemispherical crucible	L~10: D: 5	~7.10^{-2}

[1] P et al.08 : Pommier et al. (2008), G04 : Gaillard (2004), RM77: Rai and Manghnani (1977), WW75 : Waff and Weill (1975), W76: Waff (1976), Pr et al.72 : Presnall et al. (1972).

The critical parameter controlling the electrodes contribution is the dimensions of the metallic wires. According to Eq. 8, the smaller the diameter and the longer the length of a metallic wire, the higher the resistance of the wire and, thus, of the electrodes. This is particularly critical for measurements using the loop technique, since the cell components are two long metallic wires of small diameter (~0.2 to 0.6mm) (Rai and Manghnani 1977; Waff and Weill 1975). The calculation of the sample geometric factor as well as technical considerations regarding these two previous studies is detailed in Waff (1976). The adopted configuration leads to an important contribution of the electrodes to the measured resistance: $R_{electrodes}$ ~5ohm at 1500°C for both studies, while $R_{measured}$ is about 6 to 10ohm at the same temperature. An important effect of the electrodes on the electrical measurements was also calculated for the setup used in Presnall et al. (1972): at 1500°C, the contribution of the electrodes to the measured resistivity represents 30%.

Whatever the 2-electrode setup used, the electrodes contribution decreases with temperature. As a consequence, the correction of 2-electrode measurements is negligible for low conductivity values, such as the conductivity of silicate glasses and solids (e.g. Wanamaker and Duba, 1993; Behrens et al. 2002; Poe et al. 2008; Pommier et al. 2008).

Errors on resistivity values determined using a 2-electrode system can be importance in the interpretation of magnetotelluric anomalies. Laboratory data are needed to interpret high conductive zones detected in the Earth's interior and, particularly, to put constraints on the composition and storage conditions of the melt. Depending on the cell configuration and the length of the connecting metallic wires, measured resistance can be twice as great as the effective resistance of the melt, because of electrodes contributions (Figure 4). A similar change in the electrical response of a silicate melt is observed when increasing the temperature of several hundreds of °C or adding a few wt% of water (Pommier et al. 2008; Gaillard 2004; Tyburczy and Waff 1983, 1985). The identification of the electrodes contributions (Figure 4) in the electrical measurements from other studies allowed the correction of resistivity values. Based on these corrected resistivities, we have determined Arrhenian laws for each melt. The corresponding Arrhenian parameters, $Ln\sigma_0$ and Ea, are presented in Table 4 and compared to the original published values. These corrected values allow the determination of the electrical resistivity of natural melts on a wide range of chemical composition. The improvement of the interpretation of anomalies detected by geophysical methods is also a matter of electrical measurements in laboratory, including the technical concern of the contributions of the electrodes.

Table 4: Recommended values of the Arrhenian parameters of silicate melts after the correction of 2-electrode measurements.

Rock type[1]	Source [2]	Original $Ln\sigma_0$ $(ohm.m)^{-1}$	Corrected $Ln\sigma_0$ $(ohm.m)^{-1}$	Original Ea (kJ/mol)	Corrected Ea (kJ/mol)	Correction on ρ at 1300°C (%)[3]
Tephrite[4]	P et al.08	12	13 (2.5)	142	160 (30)	9
Phonotephrite[4]	P et al.08	10	11.5 (0.5)	117	140 (7)	10.5
Hydrous phonotephrite (3.5)	P et al.08	10	10 (0.4)	105	109 (4)	17◆
Phonolite[4]	P et al.08	9.1	10 (0.5)	94	105 (5)	20
Hydrous phonolite (1.1)	P et al.08	7.1	7.8 (1.5)	66	77 (18)	18◆
Hydrous phonolite (5.6)	P et al.08	7.3	7.8 (1.3)	61	72 (17)	20*
Rhyolite[4]	G04	6.7	7.5 (0.5)	70.5	93 (5)	6
Hydrous rhyolite (3)	G04	6.5	6 (0.5)	61	69 (6)	8
Tholeiite	RM77/WW75	12/12	19 (1.5)/22 (2)	135/141	220 (15)/250 (27)	27/40
Alkali olivine basalt	RM77, WW75	6/9.3	16 (2.5)/17 (1.5)	115/104	176 (30)/200 (20)	34/25
Mugearite	RM77	8.3	13 (1.5)	88	148 (18)	27
Trachyte	RM77	5.8	8.8 (0.6)	50	80 (6)	41
Latite	WW75	6.4	10 (1.2)	64	106 (15)	27
Andesite	WW75	6.1	10 (5)	62	116 (7)	23
Synthetic basalt	Pr et al.72	13	18.2 (4.5)	141	213 (55)	5.5

[1] For hydrous melts, the numbers in parentheses correspond to the water content (wt%).
[2] P et al.08 : Pommier et al. (2008), G04 : Gaillard (2004), RM77: Rai and Manghnani (1977), WW75 : Waff and Weill (1975), Pr et al.72 : Presnall et al. (1972).
[3] Corresponds to $100.(1-(\rho_{sample}/\rho_{measured}))$.
[4] Experiments under pressure (0.1-400MPa).
◆ Values at T_{max}=1275°C. * Value at T_{max}=1250°C.

Relative errors on corrected Ea and $Ln\sigma_0$ values are shown in parentheses and have been estimated using the errors on $Ln\sigma$ and the Arrhenian equation (Eq. 7). See Table 2 for the equation used for error propagation on cylindrical cells (P et al.08, G04). For the wire loop technique and the technique used in Pr et al., 72, the equation used is:

$$\Delta Ln\sigma = \left(\left| \frac{Rcell}{G^2} \right| .\Delta G + \left| \frac{-1}{G} \right| .\Delta Rcell \right) .\sigma \text{ , with } \Delta X \text{ the error on X, } \Delta G=10\%G \text{ (geometric factor), } \Delta Rcell=20\%Rcell \text{ (cell electrical resistance).}$$

5. CONCLUSION

Electrical impedance measurements using 2-electrode and 4-electrode systems have been used to discriminate the electrodes contributions of the 2-electrode setup to the measured resistance. The electrodes contributions are dominated by the electrical response of the connecting metallic wires and are successfully eliminated by performing a short-circuit experiment. A correction of the electrodes contribution is possible only if the dimensions (in particular, the length of the metallic wires) are well constrained. The 2-electrode setup used in this study is particularly efficient for measuring the electrical resistivity of low-conductive melts (like most natural silicate melts), whereas the electrode contribution can be important for very conductive melts (like carbonatites). Significant electrode effects, particularly for low-resistive melts and at HT were observed for other 2-electrode setups from previous studies. Errors on the corresponding resistivity values of the melts can be non-negligible in the interpretation of magnetotelluric anomalies. A correction of the database of the resistivity of natural melts was performed and recommended values of Arrhenian parameters were proposed.

Acknowledgements

This paper is part of the Ph.D. of A. Pommier. The authors are grateful to T. Orr for providing the Kilauea sample. The authors are grateful to G. Henderson for the editing work work and two anonymous reviewers for thorough comments. This study has been supported by the French national agency for research, ANR JC05-42707 (Electrovolc) attributed to F. Gaillard.

References

Bagdassarov, N.S., Maumus, J., and Poe, B.T. (2004) Pressure dependence of Tg in silicate glasses from electrical impedance measurements. Physics and Chemistry of Glasses, 45 (3): 197-214.

Bauerle, J.E. (1969) Study of solid electrolyte polarization by a complex admittance method. Journal of Physics and Chemistry of Solids, 30: 2657-2670.

Behrens, H., Kappes, R., and Heitjans, P. (2002) Proton conduction in glass – an impedance and infrared spectroscopic study on hydrous BaSi2O5 glass. Journal of Non-Crystalline Solids, 306 (3): 271-281.

Bruin, H.J., and Franklin, A.D. (1981) An impedance spectroscopy model for electron transfer reactions at an electrode/solid electrolyte interface. *Journal of Electroanalytical Chemistry*, 118, 405-418.

Crank, J. (1975) The Mathematics of Diffusion. 2nd ed., 440 pp., Claredon, Oxford, U.K.

Gaillard, F. (2004) Laboratory measurements of electrical conductivity of hydrous and dry silicic melts under pressure. Earth and Planetary Science Letters, 218 (1–2): 215–228, doi:10.1016/S0012-821X(03)00639-3.

Gaillard, F., and Iacono-Marziano, G. (2005) Electrical conductivity of magma in the course of crystallization controlled by their residual liquid composition. Journal of Geophysical Research, 110, B06204, doi:10.1029/ 2004JB003282.

Gaillard, F., Malki, M., Iacono-Marziano, G., Pichavant, M., and Scaillet, B. (2008) Carbonatite melts and electrical conductivity in the astenosphere. Science, 322: 1363-1365.

Hodge, I. M., Ingram, M. D., and West, A. R. (1976) Impedance and modulus spectroscopy of polycrystalline solid electrolytes. Journal of Electroanalytical Chemistry, 74: 125-143.

Huebner, J. S., and Dillenburg R. G. (1995) Impedance spectra of hot, dry silicate minerals and rock: Qualitative interpretation of spectra. American Mineralogist, 80 (1– 2): 46–64.

Jaupart, C., and Tait, S. (1995) Dynamics of differentiation in magma reservoirs. J Journal of Geophysical Research, 100, B9: 17615-17656.

Lupotto, P., Villa, M., and Ciodelli, G. (1987) Simple methods to improve the performances of network analysers in electrochemical analyses. Journal of Physics E-Scientific Instruments, 20: 634-636.

Malki, M., and Echegut, P. (2003) Electrical conductivity of the CaO-SiO_2 system in the solid and the molten states. Journal of Non-Crystalline Solids, 323: 131-136.

Müller, A., and Haak, V. (2004) 3-D modelling of the deep electrical conductivity of Merapi volcano (Central Java): integrating magnetotellurics, induction vectors and the effects of steep topography. Journal of Volcanological and Geothermal Research, 138: 205-222.

Poe, B.T., Romano, C., Varchi, V., Misiti, V., and Scarlato, P. (2008) Electrical conductivity of a phonotephrite from Mt. Vesuvius: The importance of chemical composition on the electrical conductivity of silicate melts. Chemical Geology, 256 (3-4): 193-202.

Pommier, A., Gaillard, F., Pichavant, M., and Scaillet, B. (2008) Laboratory measurements of electrical conductivities of hydrous and dry Mount Vesuvius melts under pressure. Journal of Geophysical Research, 113, B05205, doi:10.1029/2007JB005269.

Presnall, D.C., Simmons, C.L., and Porath, H. (1972) Changes in electrical conductivity of a synthetic basalt during melting. Journal of Geophysical Research, 77 (29): 5665-5672.

Rai, C.S., and Manghnani, M.H. (1977) Electrical conductivity of basalts to 1550°C. In Magma genesis: Bulletin 96, Oregon Department of Geology and Mineral Industries, edited by H.J.B. Dick, pp 219-232, Portland, OR.

Roberts, J. J., and Tyburczy, J. A. (1994) Frequency dependent electrical properties of minerals and partial-melts. *Surveys in Geophysics*, *15*(2), 239-262.

Roberts, J. J., and Tyburczy, J. A. (1999) Partial-melt electrical conductivity: Influence of melt composition. Journal of Geophysical Research, 104(B4), 7055–7065, doi:10.1029/1998JB900111.

Roling, B. (1999) What do electrical conductivity and electrical modulus spectra tell us about the mechanisms of ion transport processes in melts, glasses, and crystals? *Journal of Non-Crystalline Solids*, *244*(1): 34-43.

Simonnet, C., Phalippou, J., Malki, M., and Grandjean, A. (2003) Electrical conductivity measurements of oxides from molten state to glassy state. Reviews of Scientific Instruments, 74 (5): 2805-2810.

Simonnet, C. (2004) Conductivité électrique des verres et fonts d'oxydes. Effet de l'incorporation de particules RuO2. Thèse du CEA-Valrho, site de Marcoule, pp 176.

Tarits, P., Hautot, S., and Perrier, F. (2004) Water in the mantle : results from electrical conductivity beneath the French Alps. Geophysical Research Letters, 31: L06612, doi:10.1029/2003GL019277.

Tyburczy, J. A., and Fisler, D. K. (1995) Electrical properties of minerals and melts, *Mineral Physics and Crystallography, A Handbook of Physical Constants*, pp.185-208, AGU, Whashington, D.C.

Tyburczy, J. A., and Waff, H. S. (1983) Electrical conductivity of molten basalt and andesite to 25 kilobars pressure: Geophysical significance and implications for charge transport and melt structure. Journal of Geophysical Research, 88(B3): 2413–2430, doi:10.1029/JB088iB03p02413.

Tyburczy, J. A., and Waff, H. S. (1985) High pressure electrical conductivity in naturally occurring silicate liquids. In Point Defects in Minerals, Geophys. Monogr. Ser., vol. 31, edited by R. N. Shock, pp. 78– 87, AGU, Washington, D.C.

Volarovich, M.P. and Tolstoi, D.M. (1936) The simultaneous measurement of viscosity and electrical conductivity of some fused silicates at temperatures up to 1400°C. *Journal of the Society of Glass Technology*, 20: 54-60.

Waff, H. S., and Weill, D. F. (1975) Electrical conductivity of magmatic liquids: effects of temperature, oxygen fugacity and composition. Earth and Planetary Science Letters., 28: 254–260.

Wanamaker, B.J., and Duba A. (1993) Electrical conductivity of polycrystalline olivine containing a silicate glass. Geophysical Research Letters, 20(19): 2107-2110.

Wannamaker, P.E., Hasterok, D.P., Johnston, J.M., Stodt, J.A., Hall, D.B., Sodergren, T.L., Pellerin, L., Maris, V., Doerner, W.M., Groenewold, K.A., and Unsworth, M.J. (2008) Lithospheric dismemberment and magmatic processes of the Great Basin-Colorado Plateau transition, Utah, implied from magnetotellurics. G cubed, 9 (5), doi:10.1029/2007GC001886.

Wu, Y.C., and Koch, W.F. (1991) Absolute determination of electrolytic conductivity for primary standard KCl solutions from 0°C to 50°C. Journal of Solution Chemistry, 20: 391-401.

Xu, Y., Shankland, T.J., Duba, A.G., and Poe, B.T. (2000) Laboratory-based electrical conductivity in the Earth's mantle. Journal of Geophysical Research, 105: 27865-27872.

Yoshino, T., Matsuzaki, T., Yamashita, S., and Katsura, T. (2006) Hydrous olivine unable to account for conductivity anomaly at the top of the astenosphere. Nature, 443: 973-976.

Chapitre 3

Propriétés électriques des magmas hydratés et anhydres sous pression

(*Electrical properties of hydrous and dry magmas under pressure*)

Objectifs de ce chapitre

L'interprétation quantitative des anomalies magnétotelluriques (MT) en contexte volcanique nécessite la réalisation de mesures de conductivité électrique en laboratoire sur des compositions magmatiques naturelles. Les conductivités électriques de trois laves du Vésuve (Italie) ont été mesurées à l'aide d'un spectromètre d'impédance. Les expériences ont été conduites sur des verres et des liquides entre 400 et 1300°C, à pression atmosphérique et à plus hautes pressions (jusqu'à 400MPa). Des échantillons à la fois secs et hydratés ont été étudiés, la teneur en eau allant jusqu'à 5.6%m H_2O. Un changement dans le mécanisme de conduction correspondant à la transition vitreuse (Tg) a été systématiquement observé. Les données de conductivité ont été reproduites pour chaque échantillon par des lois d'Arrhénius, de part et d'autre de Tg. La conductivité électrique augmente avec la température et augmente dans l'ordre tephrite, phonotephrite à phonolite. Pour les trois compositions étudiées, augmenter la pression diminue la conductivité, bien que l'effet de la pression soit relativement faible. Des volumes d'activation similaires ont été obtenus pour les trois compositions (ΔV=16–24$cm^3.mol^{-1}$). Augmenter la teneur en eau du liquide accroît la conductivité. La comparaison des énergies d'activation (Ea) issues de la conductivité et de l'auto-diffusion du sodium, ainsi que l'utilisation de la loi de Nernst-Einstein ont permis d'identifier le sodium comme porteur de charges principal dans nos liquides et probablement dans les verres correspondants. Nos données et celles d'études antérieures mettent en évidence une corrélation entre les paramètres arrhéniens Ea and σ_0. Une méthode semi-empirique permettant la détermination de la conductivité électrique des liquides magmatiques naturels est proposée, dans laquelle Ea est calculée sur la base du modèle d'Anderson-Stuart, σ_0 est obtenu à partir de la loi de compensation et ΔV est déterminé à partir de nos données expérimentales. Le modèle permet de calculer la conductivité électrique pour l'ensemble des compositions des liquides du Vésuve et prédit également de manière satisfaisante la réponse électrique d'autres compositions de melts. Les données de conductivité électrique pour les melts et les magmas du Vésuve sont légèrement inférieures à l'anomalie électrique révélée par les études magnétotelluriques.

Un magma étant une suspension à trois phases (liquide, solide, gaz), l'intégration de l'effet des cristaux et des bulles sur la conductivité électrique des magmas est considérée plus en

détail à la fin de ce chapitre (Appendice 1), de même que la notion de temps de relaxation des échantillons étudiés (Appendice 2).

Laboratory measurements of electrical conductivity of hydrous and dry Mt. Vesuvius melts under pressure

Article publié dans le Journal of Geophysical Research, VOL. 113, B05205, doi:10.1029/2007JB005269, 2008.

Pommier A.[1,2], Gaillard F. [1,2], Pichavant M. [1,2], Scaillet B. [1,2]

[1]*Université d'Orléans, Institut des Sciences de la Terre d'Orléans, UMR 6113, 45067, Orléans, France*

[2]*CNRS/INSU, Institut des Sciences de la Terre d'Orléans, UMR 6113, 45071 Orléans, France*

Abstract

Quantitative interpretation of MT anomalies in volcanic regions requires laboratory measurements of electrical conductivities of natural magma compositions. The electrical conductivities of three lava compositions from Mt. Vesuvius (Italy) have been measured using an impedance spectrometer. Experiments were conducted on both glasses and melts between 400 and 1300°C, and both at ambient pressure in air and at high pressures (up to 400MPa). Both dry and hydrous (up to 5.6 wt% H_2O) melt compositions were investigated. A change of the conduction mechanism corresponding to the glass transition was systematically observed. The conductivity data were fitted by sample-specific Arrhenius laws on either side of Tg. The electrical conductivity increases with temperature and is higher in the order tephrite, phonotephrite to phonolite. For the three compositions investigated, increasing pressure decreases the conductivity, although the effect of pressure is relatively small. The three compositions investigated have similar activation volumes (ΔV=16-24 cm^3/mol). Increasing the water content of the melt increases the conductivity. Comparison of activation energies (Ea) from conductivity and sodium diffusion, and use of the Nernst-Einstein relation allow sodium to be identified as the main charge carrier in our melts and presumably also in the corresponding glasses. Our data and those of previous studies highlight the correlation between the Arrhenius parameters Ea and σ_0. A semi-empirical method allowing the determination of the electrical conductivity of natural magmatic liquids is proposed, in which the activation energy is modelled on the basis of the Anderson-Stuart model, σ_0 being obtained from the compensation law and ΔV fitted from our experimental data. The model enables the electrical conductivity to be calculated for the entire

range of melt compositions at Mt. Vesuvius and also predicts satisfactorily the electrical response of other melt compositions. Electrical conductivity data for Mt. Vesuvius melts and magmas are slightly lower than the electrical anomaly revealed by MT studies.

1. Introduction

Electrical conductivity anomalies are revealed by magnetotelluric surveys in volcanic regions [Jones, 1999; Partzsch et al., 2000; Hoffmann-Rothe et al., 2001; Brasse et al., 2002; Scarlato et al., 2004]. Their interpretation requires experimental data and models of electrical conductivity for natural magmas. Electrical conductivity reveals the mobility of charge carriers in the presence of a gradient in electrical potential. Therefore, this property is extremely sensitive to chemical composition, as well as to phase assemblages and texture [Roberts and Tyburczy, 1999]. As a first step, models of electrical conductivity of silicate melts as a function of composition are needed. Gaillard [2004] presented electrical conductivity data for a silicic melt composition at different temperatures and pressures up to 400 MPa. An increase in conductivity associated with the addition of water was observed. Gaillard and Iacono-Marziano [2005] demonstrated changes in electrical conductivity during crystallization of an intermediate composition magma and attributed the modifications observed to variations in the composition of the residual melt. Here, we use these approaches to provide the first measurements of electrical conductivity for the potassic series of Mount Vesuvius (Italy). The electrical conductivity is essentially rate controlled by the mobility of charge carriers, the information sampled by impedance spectra attracts attention because it can be used to express processes of mass transfer within a silicate melt.

Eruptive products coming from the high-risk volcanic complex Mount Vesuvius were considered in this study. Several geophysical measurements [Zollo et al., 1996, 1998; Di Maio et al., 1998; Auger et al., 2001; Manzella et al., 2004; Nunziata et al., 2006] detected anomalies under Mount Vesuvius at a depth ranging approximately from 6 to >20 km above sea level. In particular, the magnetotelluric (MT) data show evidence for a low-resistivity zone at a depth of approximately 6–8 km. Seismic studies [Zollo et al., 1996, 1998; Auger et al., 2001; Nunziata et al., 2006] have identified a low-velocity layer at comparable depths and characterize this zone as being less resistive than its local environment. Such an anomalous layer, imaged both by the electromagnetic and the seismic data, may be interpreted as a molten magma chamber (see

references above). To test this hypothesis, data on the electrical conductivity of Mount Vesuvius magmas are required. This study aims at proposing such data. A comparison between laboratory and field measurements of electrical conductivity is an essential tool for improving the interpretation of geophysical data and for better defining geostructural features [Roberts and Tyburczy, 1999]. Previously, Scarlato et al. [2004] have used electrical conductivity measurements to assist the geophysical interpretations on the internal structure of Mount Etna. The use of laboratory measurements to interpret field data presents an innovative aspect for any region of Italy [Scarlato et al., 2004] and the interest in studying Mount Vesuvius particularly stands in its important and dangerous potential activity.

In this study, electrical conductivity measurements are presented for thephrite to phonolite melt compositions. Because of the extremely wide range of compositions of Earth magmas, the current database on electrical conductivity of silicate melts does not cover the whole spectrum of composition [Gaillard and Iacono-Marziano, 2005]. By providing data on the electrical response of tephritic to phonolitic magmas (low SiO2 and alkali-rich melts), this study will also contribute to enlarge the data set of the conductivity of terrestrial magmas. The main experimental parameters include temperature, pressure and the water content of the melt, the conductivity measurements being obtained both for dry and hydrous melts. A model fitting the electrical conductivity data has been established and is valid for the entire range of compositions considered in this paper. We compare our laboratory data with field measurements at Mount Vesuvius and then discuss the likelihood of a magma storage zone.

2. Basic concepts of electrical conductivity and previous works

As with diffusivity and viscosity, the electrical conductivity of a material expresses the aptitude of charge carriers to diffuse in this material when an electrical potential is applied. It is function of several parameters such as T, P and composition [Tyburczy and Waff, 1983, 1985; Roberts and Tyburczy, 1999]. The pressure and temperature dependency of the electrical conductivity is described by an Arrhenius law:

$$\sigma = \sigma_0 . \exp\left(\frac{- Ea - P.\Delta V}{\Re . T} \right) \qquad (1),$$

where σ is the conductivity ($Ohm^{-1}.m^{-1}$), σ_0 the pre-exponential factor ($Ohm^{-1}.m^{-1}$), Ea the activation energy (J), P the pressure (MPa), ΔV the activation volume (cm^3/mol), T the temperature (K) and $\Re$ the universal gas constant.

For silicate glasses and melts, two different electrical conductivity regimes can be distinguished, respectively below and above Tg (the glass transition temperature, *Dingwell*, 1995; *Angell*, 2001; *Bagdassarov et al.*, 2001). The Arrhenius law applies to silicate glasses (e.g. *Caillot et al.*, 1994). In contrast, above Tg, a non Arrhenian behavior is sometimes observed, which can be accounted for by various formalisms, as the empirical VTF [e.g. *Hess and Dingwell*, 1996; *Pfeiffer*, 1998]:

$$\sigma = A_{VTF}.\exp\left(\frac{B_{VTF}}{T - T_0}\right) \qquad (2)$$

(where A, B and T_0 are adjustable parameters) or the Caillot [*Caillot et al.*, 1994] laws. In this study, an Arrhenian formalism was successfully applied above Tg for the three compositions investigated.

The electrical conductivity in amorphous silicates (glasses and melts) is essentially controlled by ionic mobility, electronic mobility being significant for specific conditions (low T) and compositions (iron-rich glasses, *Barczynski and Murawski* [2002]). The conductivity measured in amorphous silicates reflects the mobility of several charge carrier ions, the total conductivity being the sum of the individual conductivities [*Gaillard*, 2004]. In most cases, the conductivity is dominated by only one or two ionic species. Ionic conductivity is related to diffusive transport of charge carriers within the melt, as expressed by the Nernst-Einstein equation:

$$\sigma_i = \frac{D_i.q_i^2.N_i}{k_B.T.Hr} \qquad (3),$$

where D_i is the coefficient of diffusion of a ion i (m^2/s), q_i its charge (C), N_i the concentration of i (m^{-3}), k_B the Boltzmann constant ($1.38.10^{-23}$ J/K), T the absolute temperature (K) and Hr the Haven ratio. Hr expresses the mechanisms of migration of charge carriers within the melt. It generally ranges between 0.2 and 1 for amorphous silicates [*Heinemann and Frischat*, 1993] and is usually taken equal to 1 for rhyolitic melts [*Gaillard*, 2004 and references therein].

The electrical conductivity of silicate melts has been demonstrated to be pressure dependent [*Tyburczy and Waff*, 1983, 1985; *Bagdassarov et al.*, 2004*; Gaillard*, 2004], although in some studies performed on multiphase assemblages and at high pressure (>1 GPa) no influence of pressure was detected [*Scarlato et al.*, 2004; *Maumus et al.*, 2005]. Regarding the influence of water, *Gaillard* [2004] observed an increase in conductivity and a decrease of the activation

energy with increasing water content, consistent with sodium mobility under dry and hydrous conditions. The strong decrease in the conductivity of hydrous phonolitic melts found by *Satherley and Smedley* [1985] is probably the consequence of a H_2O loss, especially at high temperatures. *Gaillard and Iacono Marziano* [2005] performed experiments on multiphase (crystals+liquid) assemblages and showed the importance of residual melt composition on conductivity measurements. This point stresses the need for systematic investigations of the effect of melt composition on electrical conductivity.

3. Experiments

3.1. Starting products

The starting materials were three natural samples from the Mt. Vesuvius eruptive activity: a phonolite (VES19) from the AD 79 (Pompei) eruption [*Cioni et al.,* 1995], a phonotephrite (VS88-65B) from the AD 472 (Pollena) eruption [*Rosi and Santacroce,* 1983] and a tephrite (VES9) from a 8th century eruption [*Cioni*, unpublished data] (Figure 1).

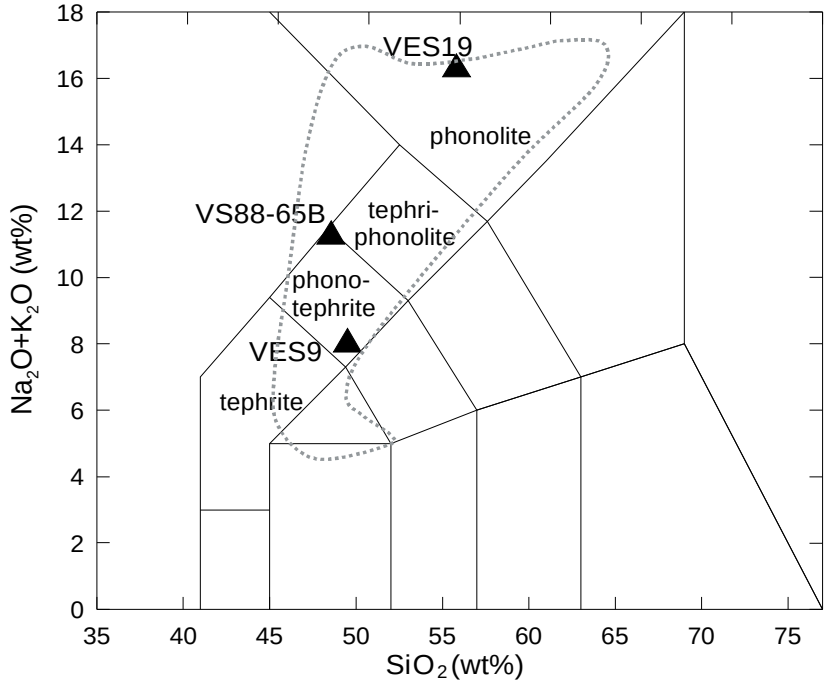


Figure 1 : Total alkali vs silica (TAS plot) showing the composition of the starting rock samples : tephrite (VES9), phonotephrite (VS88-65B) and phonolite (VES19). See text for provenance of the samples and eruptions. The area delimited by the dashed line is the range of products erupted by Mt. Vesuvius since 10 kyrs [Ayuso et al., 1998].

Both dry and hydrous glass samples prepared from the natural rocks were used for the electrical conductivity measurements. Each rock was finely crushed in an agate mortar. The powder was dried and then melted in air at 1500°C during ~1h. Quenching was performed in air and the resulting bubble-free glass was drilled to cylinders (either 5 or 8 mm OD, length between 4 and 8 mm). These dry glass cylinders were directly used in the electrical conductivity measurements. The composition of the dry glasses is given in Table 1 and shown in Figure 1. They cover the entire spectrum of differentiation observed at Mt.Vesuvius over the last 10 kyr [*Ayuso et al.*, 1998]. With progressive differentiation, i.e. from tephrite to phonolite, SiO_2, Al_2O_3, Na_2O and K_2O increase while FeOt, MgO and CaO decrease. The dry glasses have NBO/T ratios (number of non-bridging oxygens divided by number of tetrahedral cations), calculated considering all Fe as FeO and neglecting the presence of Ti [*Mysen and Richet*, 2005], decreasing from 0.73 (tephrite), 0.46 (phonotephrite) to 0.11 (phonolite), i.e. become more polymerised with progressive differentiation. Because of the presence of appreciable halogen concentrations in the phonolite (Table 3.1), the calculated NBO/T value should be considered as a minimum.

Table 1 : Compositions of starting glasses.

Sample	VES9	VS88-65B	VES19
Eruption	VII-VIII century	Pollena (472AD)	Pompei (79AD)
Rock type	Tephrite	Phonotephrite	Phonolite
SiO2	49.24	48.54	55.73
FeO_{total}	7.20	5.79	1.95
Na2O	1.97	3.54	6.11
K2O	5.98	7.70	10.14
Al2O3	15.14	17.95	21.94
MgO	6.26	3.26	0.19
CaO	11.46	9.09	2.87
P2O5	0.94	0.46	0.07
F	0.14	-	0.37
TiO2	0.96	0.69	0.16
Cl	0.12	-	0.30
SO3	0.05	-	0.02
Total	99.48	97.27	99.85
NBO/T	0.73	0.46	0.11

The hydrous glasses were synthesised by hydrating cylinders (either 5 or 10 mm OD) of dry glasses at high pressure. The glass cylinders were loaded into either Pt or Au capsules together with a known amount of water. The capsules were sealed by arc-welding. The hydration experiments were performed at 1250°C and 200MPa (VES19+~1 wt%H_2O; VS88-65B+~3.5 wt%H_2O) and at 1050°C and 300MPa (VES19+~6 wt%H_2O). For each concentration of water, the duration of the hydration experiment was determined from the diffusivity of water [*Watson,* 1994], and lasted from 3h to more than 20h, depending on the water content and the geometry of our glass cylinders [*Crank,* 1975]. The hydration experiments yielded hydrous glass samples with 1.1 wt%H_2O (VES19), 3.5 wt%H_2O (VS88-65B) and 5.6 wt%H_2O (VES19), as determined by Karl Fischer Titration. No hydrous glass sample is available for the tephrite (VES9). The hydrous glass samples, which are all bubble-free at a micrometer scale, were drilled to cylinders (5 mm OD, length between 4 and 8 mm), which were then loaded into the conductivity cell.

3.2. Experimental equipment and procedures

Conductivity measurements at ambient pressure were conducted in a vertical furnace. All experiments were performed in air. Temperature, monitored with a *Eurotherm* controller, was measured by a type-S thermocouple, placed adjacent to the conductivity cell, and is known to within +/- 2°C. Both the conductivity cell and the thermocouple were located in the 3 cm hot spot of the furnace.

Experiments at high pressures (both hydration and conductivity experiments) were performed in an internally heated pressure vessel (IHPV), working vertically with argon as the pressure medium [*Di Carlo et al.,* 2006]. Total pressure was measured by a transducer and is known to within +/- 2 MPa. A double winding Mo furnace was used. Temperature was monitored with a *Eurotherm* controller and recorded by two thermocouples adjacent to the sample (thermal gradient <5°C). Although the fO_2 in the IHPV experiments is not precisely known, the use of pure argon (i.e. H-free atmosphere) as pressure medium maintained relatively oxidizing redox conditions [*Gaillard,* 2004*; Di Carlo et al.,* 2006], even if less oxidizing than in the ambient pressure experiments performed in air.

3.3. Analytical techniques

A SEM (JEOL WINSET JSM 6400, Polytech'Orléans-ISTO) was systematically used in back-scattered mode (1) to investigate processes at the interfaces between the sample and the conductivity cell and (2) to detect the presence of crystals in auxiliary experiments performed to define the crystallisation interval of the three samples at 1 bar.

A Camebax SX-50 electron microprobe (BRGM-CNRS-Université d'Orléans, Orléans) was used to analyse (1) the starting glasses, (2) the experimental products (glasses and crystals) after the conductivity measurements and (3) the components of the conductivity cell (electrodes and alumina ceramic parts, Figure 3) after the conductivity measurements. Analyses were conducted at 15 kV, 6 nA, 10 s on peak and 5 s on background. A defocused beam (8-10 μm) was used to analyse glasses whereas a focused (1-2 μm) beam was used to analyse crystals.

The water content of hydrous samples was measured by Karl Fischer Titration (KFT) at ISTO, Orléans [*Westrich,* 1987*; Behrens et al.,* 1996]. Glass samples of at least 10mg were analysed to ensure reproducibility and accuracy. Duplicate analyses were performed and the results averaged (Table 2). To check the homogeneity of water, the starting glasses were analysed by FTIR using a Nicolet Magna 760 instrument attached to a Nic-Plan microscope [*Gaillard et al.,* 2001]. A Globar SiC source, a MTC/A detector and a CaF_2 beamsplitter were used. Spectra were collected over the 2000-7400 cm^{-1} range with a 4 or 8 cm^{-1} resolution and accumulated during 128 scans on double polished samples prepared from each glass. Water concentrations calculated from various analytical spots were identical, showing that water is distributed homogeneously.

3.4. Conductivity measurements

3.4.1. Conductivity cell and electrical measurements

For all experiments, we adopted a two-electrode configuration [e.g. *Bagdassarov et al.,* 2001], with the electrical impedance being radially measured. The inner electrode (a 1 mm Pt wire) was inserted in the centre of previously drilled glass cylinders. A Pt tube surrounding the sample (OD: 5 mm, thickness: 0.2 mm) served as the external electrode. Two distinct configurations were retained for the conductivity cell. The 0.1 MPa measurements used an open cell with the inner electrode inserted from the top (Figure 3.2a) and the high pressure a closed cell with the inner electrode inserted from the bottom (Figure 2b). For the 0.1 MPa experiments,

the conductivity cell is terminated at its bottom by a drilled alumina plug, while the top is in direct contact with air (Figure 2a). For the high pressure experiments, the Pt tube is circle-welded at its basis on a Pt cap and separated from the glass sample by an alumina disk. The other extremity of the conductivity cell consists of a drilled alumina plug (Figure 2b). For both configurations, the alumina plug is glued onto the Pt tube by using a low thermal expansion inorganic cement (Ceramabond). The stability of the cell geometry is essentially ensured by the Pt tube and the alumina plug. Examination of the cell after the experiments confirmed that the initial geometry was conserved. Some melt migration along the walls of the Pt tube was observed in the 0.1 MPa experiments but its influence on geometry is negligible [*Gaillard*, 2004]. Sometimes the low-viscosity tephritic melt flowed through the drilled alumina plug, in which case results were discarded and the experiment repeated. The experiment was also repeated when a gas bubble grew in the glass cylinder, as observed from inspection of the conductivity cell. Note that with the cell geometries described in Figure 3, alumina and the inorganic cement may potentially contribute to the measured conductivity, in addition to the silicate sample. However, 0.1 MPa measurements of the conductivity of the inorganic cement showed that its influence is negligible, and *Gaillard* [2004] and *Gaillard and Iacono Marziano* [2005] have shown that the influence of alumina can also be neglected. Therefore, the silicate sample is the unique conductive path of the used cell assembly.

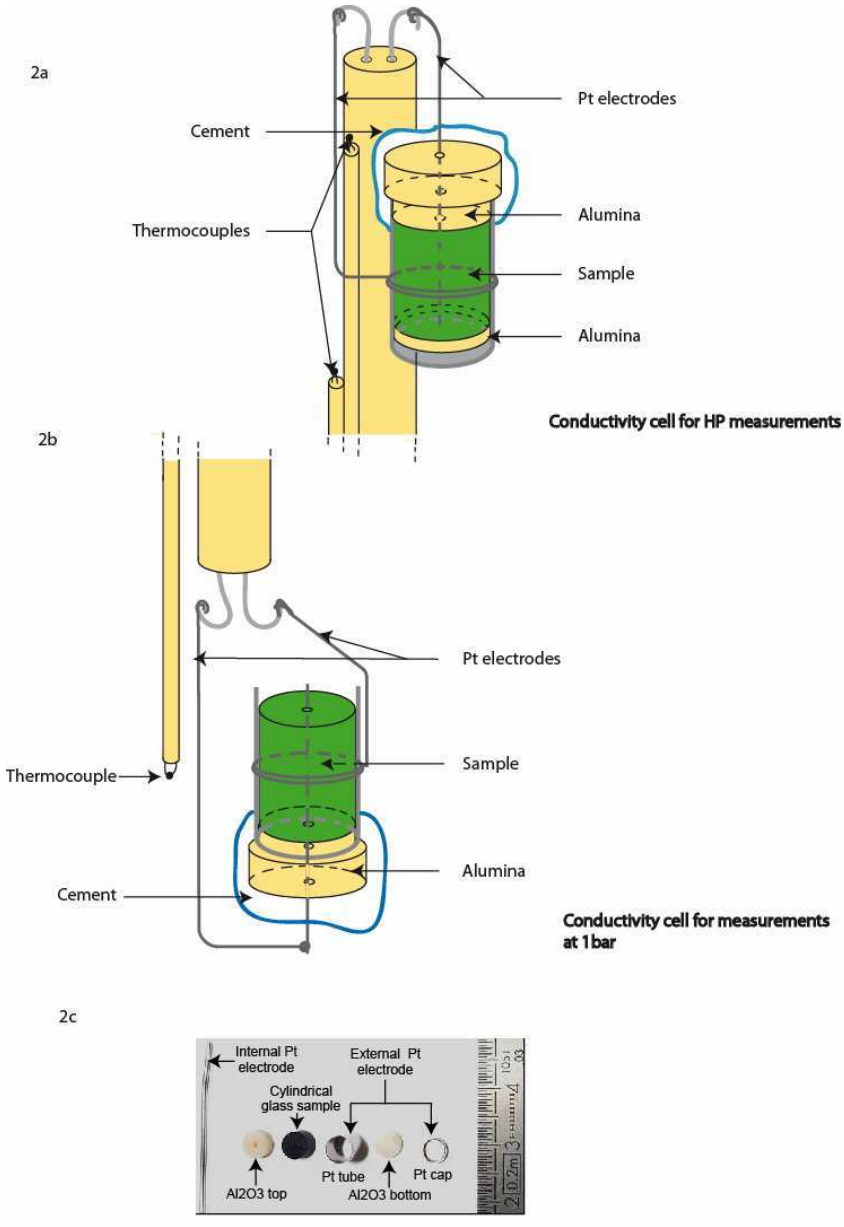


Figure 2 : Description of the conductivity cells : a) 1 atm cell ; b) high pressure cell ; c) Exploded view of the high pressure conductivity cell showing the glass sample, the Pt tube and cap serving as external electrode, the Pt wire serving as internal electrode and the alumina parts. See text for explanations.

In this study, electrical conductivities were derived from complex impedance spectroscopy [*Roberts and Tyburczy,* 1994]. Electrical impedances of samples were determined at variable frequencies using a *Solartron 1260 Impedance Gain Phase Analyser, (Schlumberger*

Co.), equipped with *Zview* software package [*Huebner and Dillenburg,* 1995*; Gaillard,* 2004*; Maumus et al.,* 2005]. For each measurement, frequencies were scanned from 1 Hz to 10^6 Hz. Perturbations on electric signals were reduced by minimizing the length of coaxial cables between the impedance spectrometer and the sample. At 0.1 MPa, electrical measurements were performed along heating cycles from ~400°C to ~1300°C, i.e. the electrical conductivities of glass and liquid were measured sequentially. At high pressures, electrical conductivities of glass were measured first by keeping temperatures below Tg, while pressure was varied. Then, temperature was increased so as to reach the stable liquid region and electrical conductivities were recorded at different pressures. In order to demonstrate reproducibility, electrical results obtained along heating cycles were checked against measurements at selected temperatures along cooling cycles. We also checked our experimental setup by comparing the electrical conductivity of a borosilicate with data obtained using the procedure of *Malki and Echegut* [2003] (Malki, personal communication, 2007), which uses geometries different from this study. No noticeable differences in electrical conductivity values were noticed for this composition between 300 and 900°C, which lends confidence to the validity of our method, particularly for the calculation of the geometric factor.

Although this paper is aimed at the presentation of electrical conductivity data for glasses and liquids, partial crystallisation of the samples was occasionally observed. Additional quenching experiments were performed on each sample to delineate the crystallisation intervals at 0.1 MPa, identified in the T range [≥800°C-liquidus (depending on the composition, see Table 2)]; the crystallisation is heterogeneous, mainly occurring on the walls of the Pt electrodes and is essentially out of equilibrium. This process was heavily marked for the tephritic and phonotephritic samples, whereas the phonolite VES19 weakly crystallised. The interpretation of the conductivity values in terms of liquid and crystals contributions was not possible since the amount of crystals in the conductivity cell could not be characterised. Therefore, electrical conductivity data acquired in the crystallisation range are neither presented (except for VES19 at 0.1 MPa, see 4.2.) nor considered in the interpretations below.

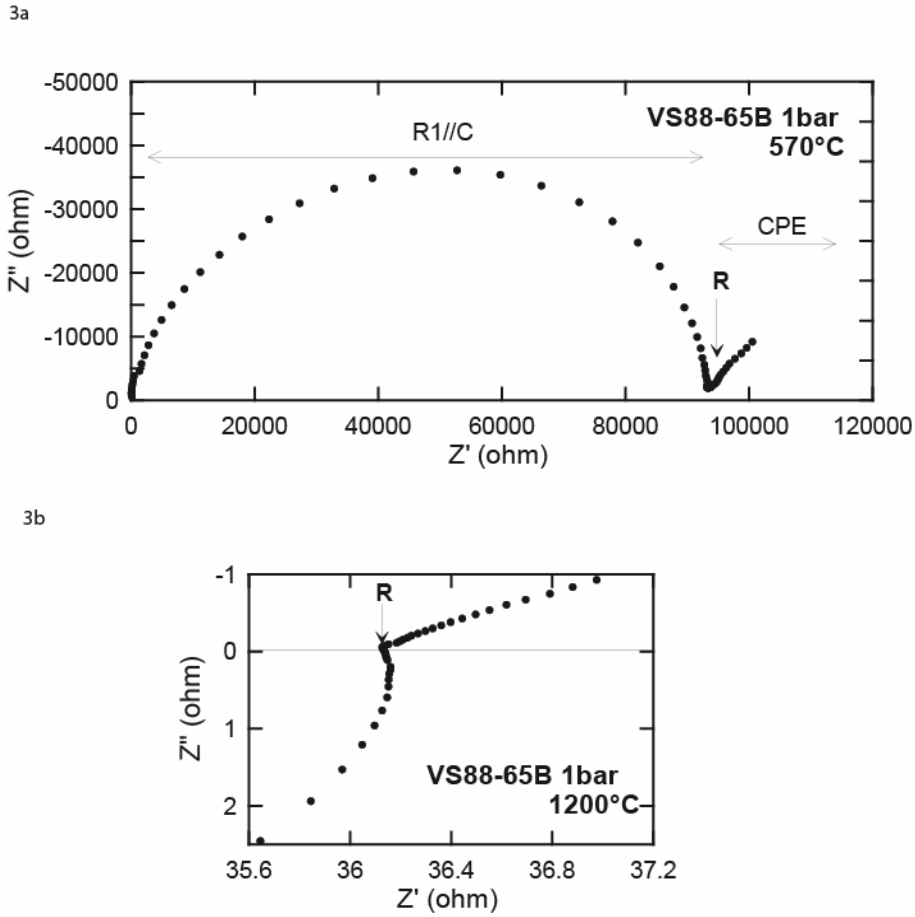


Figure 3 : Electrical responses observed in the Nyquist plan (Z', Z") for the dry phonotephrite sample (VS88-65B) at 1 atm, 570°C (a) and 1 atm, 1200°C (b). The first part of the response (semi-circle, for Z'<R) represents the electrical response of the sample while the second part, (mostly linear, for Z'>R), represents the effect of the interface between the sample and the electrode. Impedance arcs were observed only at low temperatures (below ~750°C, a). At higher temperatures, no impedance arcs were observed (b). R (resistance of the sample (ohm)) is obtained for Z"=0 and represents the real part of the complex impedance (Z', see text). The electrical response of the sample corresponds to the association of a resistor connected in parallel to a capacitor (R1//C) and a Constant Phase Element with another resistor (R2+CPE) [Huebner and Dillenburg, 1995].

Table 2: Description of experiments.

Sample	Apparatus	H_2O (wt%) before exp.	H_2O (wt%) after exp.	P (MPa)	T range (°C)[c]	Duration (h)
VES19	1 atm furnace	0	0	0.1	407-1256	7
VES19[a]	IHPV	0	0	50	450-1301	4
VES19[a]	IHPV	0	0	100	450-1300	4.5
VES19[a]	IHPV	0	0	200	450-1301	4.25
VES19[a]	IHPV	0	0	400	449-1306	3.5
VES19	IHPV	1.1[b]	0.9[b]	200	352-1276	7
VES19	IHPV	5.6[b]	3.1[b]	300	450-1250	7.5
VS88-65B	1 atm furnace	0	0	0.1	451-1323	28
VS88-65B[a]	IHPV	0	0	200	399-1325	6
VS88-65B[a]	IHPV	0	0	400	402-1300	9
VS88-65B	IHPV	3.5[b]	2.0[b]	200	408-1275	6.5
VES9	1 atm furnace	0	0	0.1	460-717	8.5
VES9	1 atm furnace	0	0	0.1	1205-1302	1
VES9[a]	IHPV	0	0	50	448-1300	17.5
VES9[a]	IHPV	0	0	200	448-1300	3.25
VES9[a]	IHPV	0	0	400	446-1299	3.25

[a] Same sample.
[b] Water contents determined by Karl Fischer Titration.
[c] Includes the interval of crystallization : ~[800; 930°C] for VES19, ~[850; 1200°C] for VS88-65B, ~[870; 1200°C] for VES9. Values within these intervals are not considered.

3.4.2. Data reduction

The electrical response of the sample to a scan in frequency is directly observed in the Nyquist plan (Z', Z"), since the complex impedance can be written as the sum of a real and an imaginary parts, Z'+jZ", with $j^2=-1$ (Figure 3). As previously underlined, [e.g. *Huebner and Dillenburg*, 1995], the first part of the response (semi-circle, for Z'<R, where R is the electrical resistance of the sample) represents the electrical response of the sample, whereas the second part, (mostly linear, for Z'>R), represents the effect of the interface between the sample and the

electrode. The whole measured response can be modelled by a RC-CPE circuit [*Huebner and Dillenburg*, 1995] (Figure 3).

The shape of impedance spectra changed with temperature: at low temperatures (below ~750°C) an impedance arc was observed in the high frequency part; at higher temperatures, no impedance was recorded. However, the quasi-linear portion in the low frequency range was observed in both temperature domains and its intersection with the real axis yielded the value of the resistance of the sample (Figure 3).

For given T and P conditions, electrical measurements were repeated until a stable value of R was reached (generally rapidly within a few minutes, Figure 4a). In the case of experiments that partially crystallised during the heating cycle, attainment of the stable liquid region required dissolution of all pre-existing crystals. Crystal dissolution is marked by a progressive increase in electrical conductivity and, to be completed, needed durations of the order of a few hours (Figure 4b).

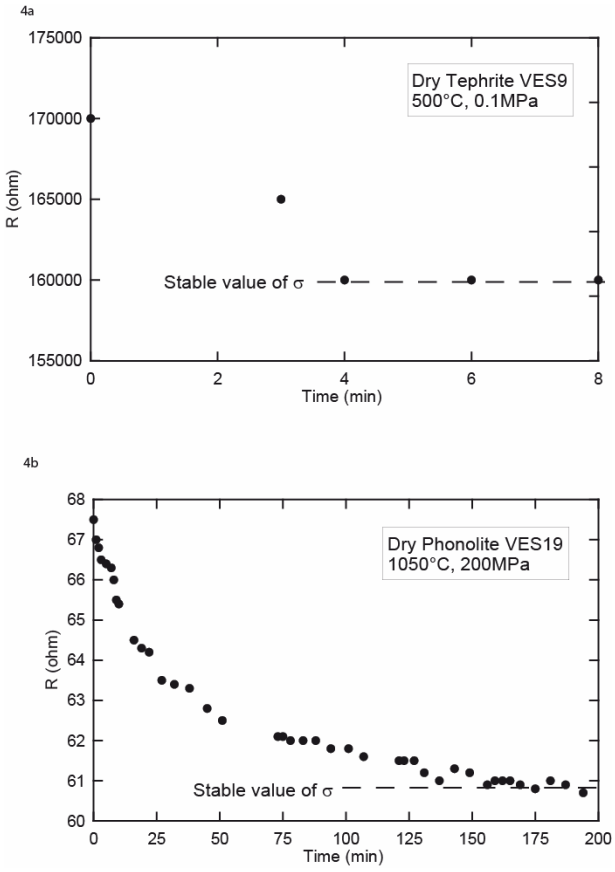


Figure 4 : Types of evolution of the electrical resistance with time illustrated by the tephrite sample VES9 and the phonolite sample VES19. (a) corresponds to the normal case where a stable value of electrical conductivity is reached in a few minutes. In contrast, in (b), the attainment of a stable conductivity value requires several hours. This behavior is interpreted as reflecting the slow dissolution of pre-existing crystals (in that particular case, most probably leucite) formed during heating up.

The electrical conductivity σ is obtained from the electrical resistance R of the sample by using the relation [e.g. *Gaillard*, 2004]:

$$\sigma = \frac{1}{G.R} \qquad (4)$$

$$\text{where } G = \frac{2\pi L}{\ln\left[\frac{d_{ext}}{d_{\text{int}}}\right]} \qquad (5)$$

G is the geometric factor (from ~1.4 to $1.8.10^{-2}$ m), L the length of the sample (m), and d_{ext} and d_{int} are respectively the external and internal diameters of the glass cylinder (m). In this study, L, d_{ext} and d_{int} are assumed to be constant, since the geometry of the conductivity cell is essentially conserved during the experiments. Error propagation of typical uncertainties on L, d_{ext}, d_{int} and R (at low temperatures, R is known to +/- 5 Ohm and, at high temperatures, to +/- 0.5 Ohm) shows that the uncertainty on σ is in the range 3.6-8%, except for VES19 at high temperatures (1200-1300°C): 8-10.3%.

4. Results

4.1. Interaction processes between conductivity cell and sample

In order to characterize chemical interaction processes between components of the conductivity cell and sample that could affect the measurements, the interfaces between glass and Pt electrodes and glass and alumina have been carefully investigated after most electrical conductivity experiments.

Electron microprobe traverses performed across the Pt electrode – glass interfaces showed no significant variations in oxide concentrations, except for FeO. Interface FeO concentrations were depleted by ~10% in the high-pressure experiment performed on VES9, but showed significant change neither in the case of the 1 atm experiment on VES9 nor of the high-pressure experiment on VS88-65B (Table 2). Iron was found to be present at very low concentrations (<0.5%) in Pt electrodes from the 0.1 MPa experiments. However, in the high-pressure experiments, iron concentrations at the wt% level were sometimes detected in the outer rims of the Pt electrodes, consistent with more reducing conditions than at 0.1 MPa. Therefore, we conclude that iron loss to the electrodes was of minor importance in this study. Electron microprobe traverses across the Al_2O_3 plug – glass interface revealed the presence near the

alumina plug of an Al-, K-, Na-enriched and Si-, Fe-, Mg-depleted glass zone. However, these chemically anomalous zones are about 200-300 µm thick, represent only ~3% of the total height of the sample, and their presence was neglected in the interpretation of the results.

At the interface between the glass sample and alumina, a nearly continuous 10-25 µm thick layer of Al-Mg-Fe-spinel was observed for the phonotephritic and tephritic compositions. For the phonolitic composition, no spinel was observed and the interface is crystal-free. Because the electrical conductivity of Fe-Al-Mg spinel is known [*Nell et al.,* 1989], the contribution of the spinel and melt to the measured conductivity can be evaluated. Since the spinel and liquid arrangement corresponds to a parallel model, the measured electrical resistance (effective resistance) of the circuit can be written as follow [after *Glover et al.,* 2000]:

$$\frac{1}{R_{eff}} = \frac{\chi_{sp}}{R_{sp}} + \frac{(1-\chi_{sp})}{R_{liq}} \qquad (6)$$

where R_{eff} is the effective resistance (Ohm), χ_{sp} the volume fraction of spinel, R_{sp} the resistance of the spinel (Ohm) and R_{liq} the resistance of the studied sample (Ohm). The calculations show that, in the case of the phonotephritic melt, the measured conductivity corresponds to at least 99.998% of the conductivity of the melt and, in the case of the tephritic melt, to at least 99.500%. Thus, because the volume of spinel is much lower than the volume of the melt, the melt is the dominant electrical contributor.

4.2. Effect of temperature and melt composition

For the three samples investigated, electrical conductivity data are available in two distinct temperature domains, separated by an interval where crystallisation was observed. In both domains, increasing T increases the electrical conductivity (Figure 5). Good agreement is observed between data obtained along heating cycles and the few data points obtained along cooling cycles, which demonstrates reproducibility. The non-linearity between log σ and 10^4/T over the whole interval of temperature indicates a change of the conduction mechanism. Such a change in behavior, graphically represented by a kink in the conductivity data versus T plot (Figure 5), is classically interpreted as corresponding to the glass transition temperature (Tg) [*Dingwell,* 1995*; Angell,* 2001*; Bagdassarov et al.,* 2001]. It marks the transition between an activated (T<Tg) and an assisted (T>Tg) transport mechanism [*Déportes et al.,* 1994]. On Figure 3.5, Tg is located at ~670°C (+/-15°C) for the three compositions studied. For the three samples,

the increase in electrical conductivity between 450 and 1300°C is of about 4.5 log units for the tephrite and the phonotephrite, and 4 log units for the phonolite. At temperatures below Tg, the conductivity displays a linear increase with reciprocal temperature and the data can be fitted by sample-specific Arrhenius laws (Table 3). Above Tg, an empirical VTF formalism was first considered to fit the data. However, a low value of T_0 (the VTF temperature) was obtained, and the data in the liquid region were better fitted by sample-specific Arrhenius laws (Table 3). The use of σ_0/T instead of σ_0 in the Arrhenian formalism was also considered but did not improve the fit. In both glass and melt regions, $\sigma_{phonolite} > \sigma_{phonotephrite} > \sigma_{tephrite}$ so that the more polymerised the melt, the higher the conductivity. At 1200°C, the conductivity of the phonolite, the most polymerised sample, is 0.6 log unit higher than the conductivity of the tephrite, the less polymerised sample.

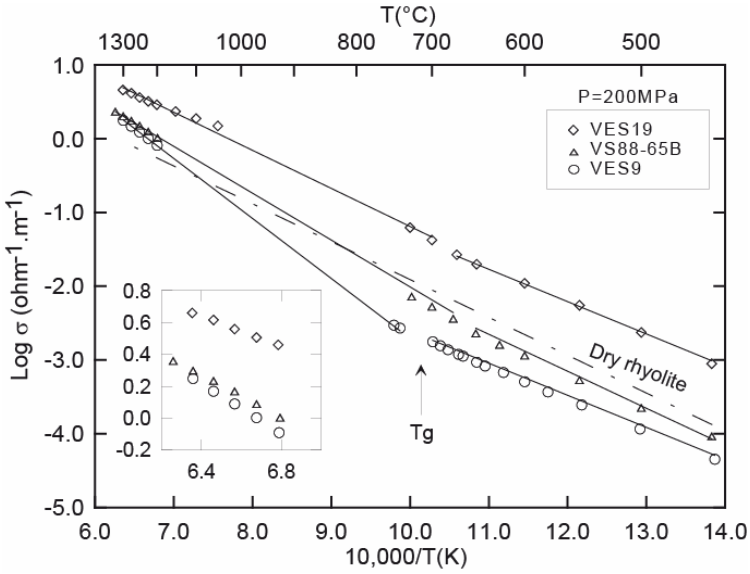


Figure 5 : Dependence of the electrical conductivity with temperature for the three samples studied. The electrical conductivity data are available in two distinct temperature domains, broadly corresponding to the glass and liquid regions. The inset graph focuses on the high temperature data. In the interval separating these two regions, no conductivity data for the liquid can be obtained because of partial crystallization. The kink in the electrical conductivity data is interpreted as the glass transition (Tg), located at ~670°C for the three samples. The straight lines are polybaric regressions calculated with the Arrhenius laws (Table 3). For comparison, the conductivity law for a dry obsidian is shown (dashed line, Gaillard, 2004).

Table 3 : Domains of validity and parameters of the Arrhenius laws[1].

Sample	H_2O (wt%)	P range (MPa)	T range (°C)	Ea (kJ/mol)	$Ln\sigma_0$ $(ohm.m)^{-1}$	ΔV (cm^3/mol)	Number of heating cycles
Below Tg							
VES19	0	0.1-400	450-671	81 (1)	7 (0)	18 (1)	5
VES19	1.1	200	352-500	86 (1)	7 (0)	18 (1) [2]	1
VES19	5.6	300	450-550	107 (6)	9 (1)	18 (1) [2]	1
VS88-65B	0	0.1-400	450-671	92 (4)	7 (1)	20 (2)	3
VS88-65B	3.5	200	455-630	129 (8)	13 (1)	20 (2) [2]	1
VES9	0	0.1-400	448-675	80 (3)	4 (0)	22 (2)	4
Above Tg							
VES19	0	0.1-400	700-1304	94 (1)	9 (0)	22 (2)	5
VES19	1.1	200	1050-1250	66 (1)	7 (0)	22 (2) [2]	1
VES19	5.6	300	1050-1250	61 (0)	7 (0)	22 (2) [2]	1
VS88-65B	0	0.1-400	675-1325	117 (2)	10 (0)	24 (3)	3
VS88-65B	3.5	200	1050-1275	105 (1)	10 (1)	24 (3) [2]	1
VES9	0	0.1-400	690-1301	142 (2)	12 (0)	16 (2)	4

[1] $Ln\sigma = Ln\ \sigma_0 - (Ea+P\Delta V)/ \Re T$.
[2] For hydrous samples, ΔV hydrous $= \Delta V$ dry.

4.3. Effect of pressure

As shown on Figure 6, increasing P decreases the conductivity. This effect was observed for the three compositions, both in the glass and liquid regions. The variation of electrical conductivity with pressure is between 0.5 and 0.25 log units in the glass and liquid regions, respectively, between 0.1 and 400 MPa. For example, at 1200°C, the electrical conductivity of the tephrite at 400 MPa decreases by ~50% relative to that at 0.1 MPa. These variations are in the same range than those observed by *Tyburczy and Waff* [1983] for tholeiitic-andesitic melts. Thus, our results confirm that the electrical conductivity is less dependent on pressure than on temperature [*Tyburczy and Waff*, 1983].

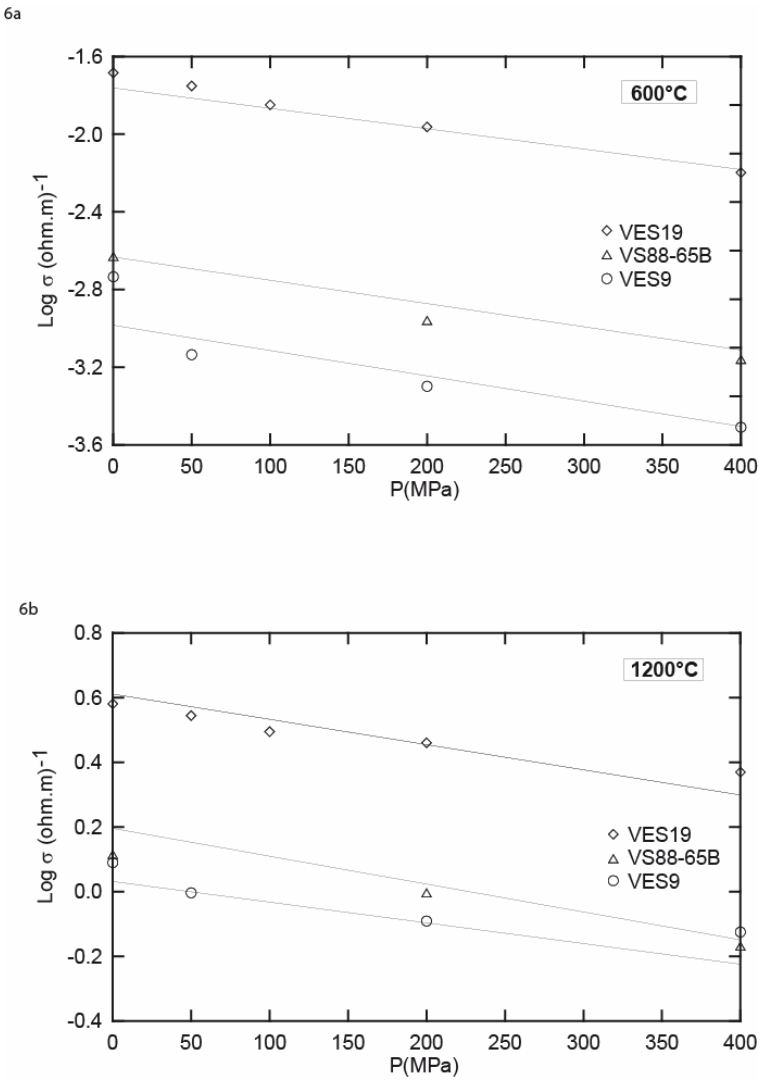


Figure 6 : Effect of pressure on the electrical conductivity in the glass (a) and the liquid (b) regions for the three samples. Only the data for the dry samples are shown. The straight lines are polybaric regressions calculated with the Arrhenius laws (Table 3). The effect of pressure is to decrease the electrical conductivity in both the glass and the liquid regions.

In detail, the decrease in conductivity with increasing pressure is more marked in the liquid than in the glass region and appears to vary with the nature of the starting sample (Fig 6b). The pressure effect is the smallest for the tephrite composition, whilst the phonotephrite and phonolite samples exhibit similar pressure dependences. This is consistent with the influence of pressure being related to the degree of melt polymerisation, the more polymerised the melt, the greater the pressure dependency of the electrical conductivity [*Tyburczy and Waff*, 1983].

Nevertheless, the compositional influence on the effect of pressure remains small, as illustrated by the similar ΔV values of the Arrhenius laws obtained for the three compositions (16-24 cm^3/mol, Table 3).

4.4. Effect of water

Conductivity data for hydrous phonotephrite and phonolite melts under pressure show that increasing the water content of the melt increases the conductivity (Figure 7). The influence of H_2O is more marked at low than at high temperature. In the Log σ vs 1/T plot, the slope of the Arrhenius equation flattens with increasing melt water concentration. This corresponds to a progressive decrease of Ea from 93 kJ/mol (dry), 68 kJ/mol (1.1 wt%H_2O) to 61 kJ/mol (5.6 wt%H_2O) for the phonolite sample (Table 3). This lowering of Ea due to water is consistent with the results of *Watson* [1994] for water diffusion and the results of *Gaillard* [2004] for electrical conductivity in more polymerised melts (rhyolite). At 1250°C, the increase in electrical conductivity per wt% of dissolved H_2O is about 0.1-0.2 log units with little difference between the two samples (Figure 7b).

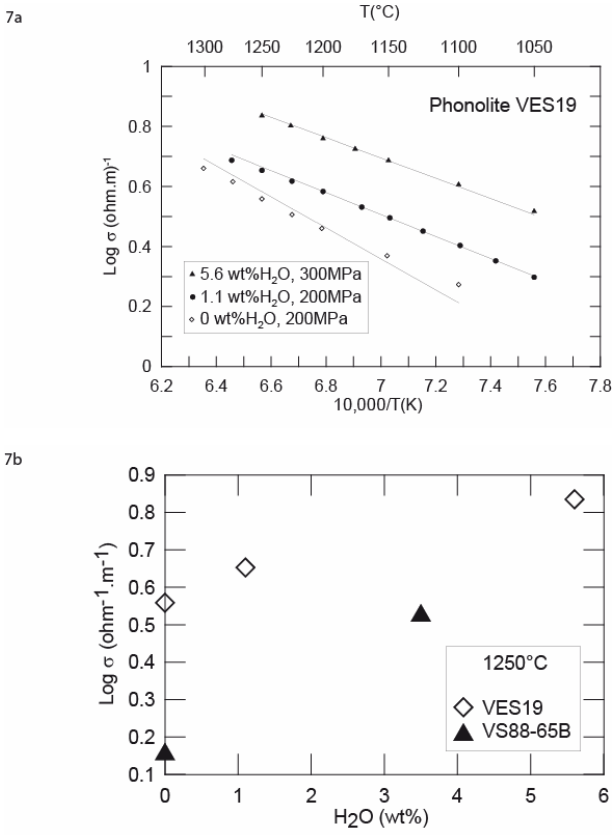


Figure 7 : Effect of water on the electrical conductivity. (a) Results for the phonolite composition sample from 1050 to 1300°C. (b) Variation of the electrical conductivity with the H_2O content of the liquid for the phonolite and the phonotephrite samples. The H_2O content corresponds to the initial H_2O concentration in the starting glass samples (Table 2). Data at 200 and 300 MPa.

Analysis of the glasses after the conductivity measurements shows that all hydrous samples are partially crystallised and have lost water to different extents (Table 2). Crystallisation in those samples is most probably related to the slow quenches that were applied after the completion of the electrical measurements. The loss of water probably occurs near the end of the experiment since (1) a regular and progressive increase of the electrical conductivity is observed with increasing melt water content and (2) the effect of water on conductivity is clearly marked on the whole T range. For the two heating cycles performed on hydrous phonolite liquids (Figure 7a), an influence of water is apparent until the highest temperatures investigated (1250 and 1276°C, Table 2), suggesting that the bulk of the water was still dissolved in the melts.

5. Discussion

5.1. Transport mechanisms

The evolution of the electrical conductivity with temperature demonstrates a dual behavior below and above the glass transition (Figure 5). For the three samples studied, two different Arrhenius laws (Table 3) are necessary to model the temperature and pressure dependence of the electrical conductivity, underlining the existence of two different transport mechanisms (conductivity regimes) within the studied samples (i.e. one in the glass region, the other in the liquid region) [*Dingwell,* 1995]. A similar value of Tg was observed for the three dry studied compositions (~670°C (+/-15°C), in agreement with the value obtained for a phonolite by *Giordano et al.* [2005]). Our conductivity measurements did not permit to determine a significant effect of pressure on Tg values. Previous work [*Bagdassarov et al.,* 2004] has shown only a small increase of Tg with pressure (a few °C/GPa).

Our determined values of activation volumes range between 16 and 24 cm^3/mol. These are comparable to those obtained by *Gaillard* [2004] on a rhyolite (20 cm^3/mol) and by *Tyburczy and Waff* [1985] on an andesite (17.9 cm^3/mol) at similar pressures (<1 GPa). However, at pressures >1 GPa, ΔV values are generally much lower (<6 cm^3/mol) than at lower pressures [*Tyburczy and Waff,* 1985]. This range of activation volumes is consistent with ΔV=5.4 cm^3/mol for an albite melt between 2.6 and 5.3 GPa [*Bagdassarov et al.,* 2004]. We conclude that our determined ΔV are similar to those derived from other studies at relatively low pressures.

Activation energies (Ea) from conductivity data [this study, *Presnall,* 1972; *Tyburczy and Waff,* 1983, 1985; *Park and Ducea,* 2003; *Scarlato et al.,* 2004; *Gaillard,* 2004; *Gaillard and Iacono Marziano,* 2005] can be compared with activation energies of diffusion data on sodium [*Henderson et al.,* 1985; *Jambon*, 1982] in Figure 8a. The sodium was indeed identified as the main charge carrier in silicic to basaltic melts [*Tyburczy and Waff,* 1983, 1985; *Gaillard,* 2004; *Gaillard and Iacono Marziano,* 2005]. Globally, Ea increases as NBO/T increases. Apart from the diffusion data for the Pitchstone rhyolite that shows an anomalously high Ea [*Henderson et al.,* 1985], there is good agreement between Ea derived from Na-diffusion and electrical conductivity. This allows us to interpret sodium as the dominant charge carrier in the liquid region of our studied samples.[1]

On Figure 8b, pre-exponential factors σ_0 are plotted versus activation energies Ea for both Na-diffusion and conductivity measured in compositions including basalt-andesite-phonolite-rhyolite. All data consistently plot on a single linear trend, which enlightens the influence of composition on Arrhenius parameters. The data of studies mentioned above, for conductivity measurements and for Na-diffusion measurements, are plotted. The data point of *Presnall et al.* [1972] suggests that the conductivity is also probably dominated by sodium in their synthetic basaltic melt. The dataset can be successfully fitted by a single trend, which is illustrated by the straight line on Figure 8b:

$$Ea = 12.5 Ln\sigma_0 - 9.9 \qquad (7)$$

where Ea is the electrical activation energy (kJ/mol) and σ_0 is the pre-exponential factor ($(Ohm.m)^{-1}$). Such a correlation between Arrhenius parameters is often mentioned in the literature as the compensation effect [*Wu and Zheng*, 2003]. Combination of Eq. 7 and Eq. 1 implies that all the conductivity data converge to a unique value at a given temperature, T_{char}, called the characteristic temperature, according to *Wu and Zheng* [2003]. We obtained a value of T_{char} of ~1290°C, corresponding to a conductivity of ~3.16 $(Ohm.m)^{-1}$. An increase of the value of Ea together with σ_0 is observed along with a decrease of the degree of polymerisation of the melt: the right part of the diagram (Ln σ_0>9) is characterised by high values of Ea and

[1] Note that the mixed-alkali effect was not investigated in this study. This effect is based on the fact that some physiscal properties of silicate melts (among them, the electrical conductivity) vary in a non-linear manner when an alkali oxide is gradually replaced by another. A rigourous investigation of the mixed-alkali effect would require to perform experiments on identical synthetic compositions, considering only the Na_2O/K_2O ratio as a parameter.

corresponds to tholeiitic, basaltic to tephritic melts, whereas in the left part (Ln σ_0<9) rhyolitic, andesitic to phonolitic melts present low values of Ea.

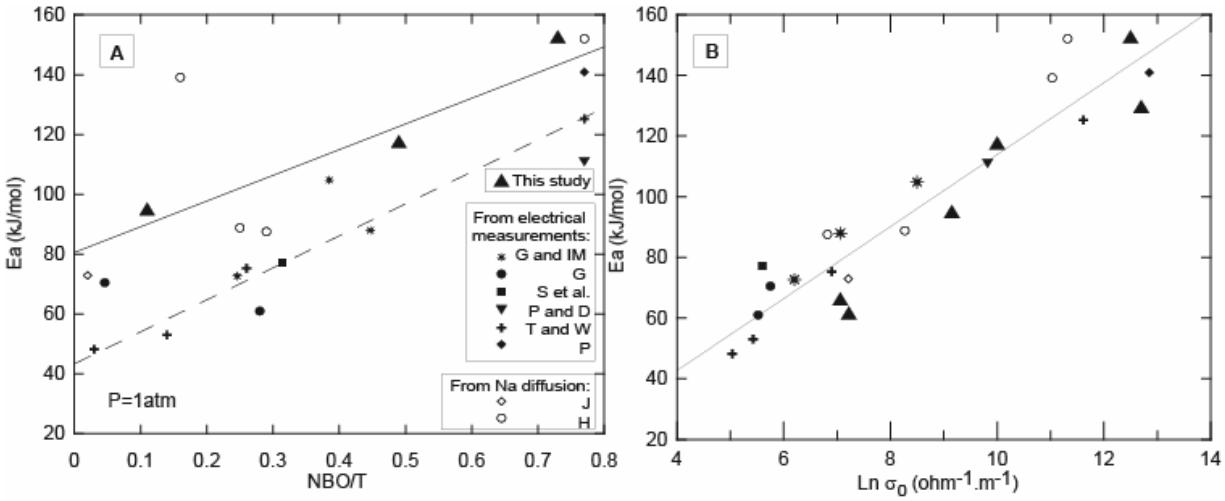


Figure 8 : (a) Comparison at 1 atm between activation energies (Ea) for ion mobility determined from electrical conductivity measurements (this study; Gaillard and Iacono Marziano, 2005; Scarlato et al., 2005 ; Gaillard, 2004; Park and Ducea, 2003 ; Tyburczy and Waff, 1983, 1985; Presnall, 1972) and Na diffusion experiments (Henderson, 1985; Jambon, 1982). Data for rhyolitic (NBO/T<0.1) to basaltic (0.7<NBO/T<0.8) anhydrous melts. The straight line is the fit corresponding to our data, the dashed line fits the data of Tyburczy and Waff. (b) Compensation plot for the conductivity of silicate melts. Data from this work, dry and hydrous products and the studies mentioned above. The straight line is the fit corresponding to the whole data (see text).

The nature of the main charge carriers in the liquid region, irrespective of the melt composition and the water content of the melt, is confirmed using the Nernst-Einstein equation (3), which shows that the alkali, particularly sodium, contribute to more than 80% of the total electrical conductivity. Calculation was performed at 1300°C with diffusivity data from *Alibert et al.,* 1980*; Henderson et al.,* 1985*; Wendlandt,* 1991*; Kress et al.,* 1993. The electrical conductivity contribution of each potential charge carrier (σ_i, i being the ion charge carrier : Na^+, K^+, Ca^{2+}, Mg^{2+}, Al^{3+}, Si^{4+} and also O^{2-}) was calculated. The Haven ratio Hr was taken equal to 1 [*Gaillard,* 2004], which is equivalent to assume that the charge carriers move independently through a direct interstitial mechanism [*Heinemann and Frischat,* 1993; *Roling,* 1999]. Attempts to calculate Hr directly from Eq.3 using measured electrical conductivities and diffusivities from

the literature yielded poorly constrained results because there are no Na diffusion data available for our studied compositions. Nevertheless, a value of Hr of 0.38 is obtained for our tephritic melt by using the diffusion coefficient for Na^+ in basaltic melt from Henderson et al. [1985]. We note that Gaillard and Iacono Marziano [2005] calculated a Haven ratio of 0.4 for their basaltic composition, which compares well with our estimation and suggests that depolymerised silicate melts tend to yield lower Hr values than polymerized ones.

For all compositions shown in Figure 8, at $T<T_{char}$, the more polymerised the melt, the greater the conductivity, i.e. charge carriers migrate faster in polymerised melts than in depolymerised melts. This is in agreement with the data of *Henderson et al.* [1985] and *Mungall* [2002] who stressed out that the diffusion of alkali in silicate melts increases with the degree of polymerisation. In the same way, the more polymerised the melt, the greater the viscosity. Thus, both the electrical conductivity and the viscosity react in the same direction to changes in the degree of polymerisation. Note that this is in apparent contradiction with Eyring's law, which specifies that the diffusion coefficient (or the electrical conductivity) would be inversely proportional to the viscosity [*Reid et al*., 2001]:

$$D = \frac{k_B T}{\eta \lambda} \qquad (8)$$

where D is the diffusion coefficient (m^2/s), k_B the Boltzmann constant, T the temperature (K), η the viscosity (Pa.s), and λ the translation distance of the diffusing ion (Å). This apparent contradiction can be explained since D in the Eyring's law refers to the mobility of the SiO_2 framework and not to the mobility of the alkali.

The positive effect of water on the electrical conductivity was clearly observed in this study. The magnitude of the effect of water is comparable to the one observed by *Gaillard* [2004] on rhyolitic melts. The conductivity enhancement was attributed to the effect of water incorporation in the rhyolitic melt on the mobility of Na. We can therefore anticipate that the increase in conductivity as water is incorporated in our melts reflects an enhancement of Na-mobility as well. Protons are not expected to contribute to the ionic conductivity in natural melts because hydrogen has been shown to move as neutral molecules (either H_2O or H_2) in alumino-silicate melts [*Zhang and Stolper,* 1991; *Gaillard et al.,* 2003; *Behrens et al.*, 2004]. *Behrens et al.* [2002] proposed that for hydrous $BaSi_2O_5$ glass, H^+ could significantly contribute to the measured conductivity, and attributed this finding to the strongly depolymerised character

(NBO/T=1.5) of the studied glass. However, the effectiveness of proton migration in silicate melts and its possible contribution to electrical charge transfer remain debated.

Because of the presence of iron in our samples, electronic conductivity can also occur, particularly in the glass region [*Cooper et al.*, 1996]. For instance, *Barczynski and Murawski* [2002] demonstrated that iron-rich glasses (from 20 to 32 wt% of FeO) are good electronic conductors at low T, and that small polaron hopping is a possible charge carrier transport process in such glasses. However, the Fe content of our three studied samples is much lower than in *Barczynski and Murawski* [2002]. In addition, the mean interatomic distance of iron in our studied materials is greater than 1nm (using chemical compositions from Table 1 and measured densities of anhydrous glasses). At such long distances, charge transfer between iron atoms are not anticipated (H. Behrens, personal communication).

5.2. Calculation of electrical conductivity of natural melts

Calculation of the electrical conductivity of natural melts requires three parameters to be specified: Ea, σ_0 and ΔV (Eq. 1). Below, we propose a semi-empirical method allowing the determination of these three parameters, both for the Vesuvius and other natural magmatic liquids.

As the activation energy Ea in our melts decreases with increasing sodium content and is probably function of the ionic characteristics of the charge carrier (ionic radius, valency, jump distance), we have used the Anderson-Stuart model to compute Ea values for natural melts [*Anderson and Stuart*, 1954; *Nascimento and Watanabe*, 2007 and references therein]. This model, initially based on ionic crystal and elasticity theories, predicts the activation energy of ionic conduction in silicate glasses. The activation energy, Ea, is expressed as the sum of two energies: the electrostatic binding energy, Eb, and the strain energy, Es, which are expressed as:

$$\begin{aligned} Ea &= Eb + Es, \\ Eb &= \frac{\beta . z_i . z_0 . e^2}{\gamma (r_i + r_O)} \\ Es &= 4\pi G \lambda (r_i - r_D)^2 \end{aligned} \qquad (9)$$

where β is the Madelung constant (taken equal to 0.23, *Nascimento and Watanabe* [2007]), z_i the valence of the mobile ion, and z that of the fixed counterion (O^{2-}), e the electronic charge (C), γ the covalency parameter (taken equivalent to the permittivity (F/m), *Anderson and Stuart* [1954]), r_i the ionic radius of i (m), r_O the ionic radius of the oxygen ion (m), G the shear

modulus (Pa), λ the jumping distance (m) and r_D the effective radius of the "doorway" through which the sodium passes (taken equal to $9.3.10^{-11}$ m, *Nascimento and Watanabe* [2007]). In our case, i corresponds to the sodium, the main charge carrier. *Nascimento and Watanabe* [2007] have proposed an empirical linear relation between γ, G and composition for binary SiO_2-K_2O glasses. We have assumed that, for our three studied compositions, γ and G vary linearly with the sodium content. Regressions of our data yield the following two empirical equations for γ and G:

$$\begin{cases} G = -2.107.10^{11}.wt\%Na_2O + 1.297.10^{12} \\ \gamma = 2.439.10^{-11}.wt\%Na_2O + 1.720.10^{-10} \end{cases} \qquad (10)$$

Since our data clearly show a decrease in Ea with increasing water content (Table 3), a water term has been added in the expression of Ea. The effect of the addition of water was considered to be essentially mechanical, inducing a local dilatation effect of the structure, allowing Na^+ ions to move more freely. Consequently, a modification of the Es term was introduced, since Es describes the mechanical forces applied on the charge carrier [*Nascimento and Watanabe*, 2007]. The strain energy Es of hydrous melts can be written as:

$$Es = 4\pi G\lambda(r_{Na} - r_D)^2 + 1000.(wt\%H_2O)^2 \qquad (11)$$

where $wt\%H_2O$ is the water content of the melt (wt%). Ea calculated from the Anderson-Stuart model (Eq. 9 to 11) are in good agreement with Ea determined for the three Vesuvius melt compositions (Table 3). Measured activation energies are reproduced with a correlation coefficient of 0.999 and an average error of 3% relative.

The pre-exponential term (σ_0) was calculated using the compensation law (Eq.7) applied to our compositions, with Ea calculated with Eq.9 to 11.

The Arrhenius laws obtained for the different experiments show grouped ΔV values (Table 3). Consequently, we have assumed that the ΔV term is independent of composition and water contents. ΔV was fitted from our experimental conductivity data with Ea being calculated from Eq. 9 to 11 and σ_0 from the compensation law. This yields an activation volume of 2.10^{-5} m^3/mol (i.e. 20 cm^3/mol), in the middle of the range of ΔV values of the Arrhenian equations (Table 3). The model (with Ea calculated using the Anderson-Stuart formalism, σ_0 from the compensation law and ΔV=20 cm^3/mol) reproduces measured conductivity values with a correlation coefficient of 0.985 and an average error of 11% relative. We have also tested the model against conductivity data from *Presnall* [1972], *Tyburczy and Waff* [1983, 1985],

Satherley and Smedley [1985, dry lava], *Park and Ducea* [2003], *Gaillard* [2004] and *Gaillard and Iacono Marziano* [2005]. We did not consider data from Na diffusion here. Indeed, the calculation of conductivities from Na diffusion using the Nernst-Einstein equation did not constrain sufficiently the value of σ, because of the lack of data about the value of the Haven ratio. The data of conductivity studies are reproduced with a difference less than 0.5 log-unit (except for the data about the tholeiite from Tyburczy and Waff and for the data of Gaillard and Giacono Marziano, which are reproduced with a difference between 0.5 and 0.7 log-unit). We conclude that the above model is able to calculate the electrical conductivity of common natural melts. Since Eq. 7 and 11 have been established for water contents ranging from 0 to 6 wt%, use of the model above 6 wt% is not recommended, since an increase of the water content of the melt can have a dilution effect on Na which, thus, may influence the conductivity [*Gaillard*, 2004]. In the same way, extrapolation of the model at pressures significantly above 400 MPa is not recommended, since experimental calibrating data are lacking above 400 MPa.

5.3. Volcanological implications for Mt. Vesuvius

As demonstrated by *Roberts and Tyburczy* [1999], the Archie's law conduction model may be used to estimate the electrical conductivity of magmatic suspensions. *Glover et al.* [2000] proposed the following equation to calculate the conductivity of a magma over the whole melt fraction range, knowing the individual conductivities of the crystals and the liquid:

$$\sigma_{magma} = \sigma_{cr}.(x_{cr})^{\left(\frac{\log(1-(x_{liq})^m)}{\log(1-x_{liq})}\right)} + \sigma_{liq}.(x_{liq})^m \quad (12),$$

where σ_{liq} is the conductivity of the liquid, σ_{cr} is the conductivity of crystals, σ_{magma} is the conductivity of the corresponding magma, x_{liq} and x_{cr} are the proportions (volume fraction) of the liquid and the crystals, respectively (x_{liq} =1- x_{cr}) and m the Archie cementation exponent. We used m=1.05 [*Gaillard and Iacono Marziano*, 2005]. For the case of Mt. Vesuvius magmas, crystals considered are mixtures of leucite and clinopyroxenes. *Tyburczy and Fisler* [1995] provide data on the electrical conductivity of these two mineral phases as a function of temperature. The electrical conductivity of the pure liquid phase is calculated by using an Arrhenian formalism, with Ea from Eq. 9-11 and σ_0 from the compensation law applied to our melts.

Using the modified Archie's law, the electrical conductivity of tephritic to phonolitic magmas can be estimated during crystallization. Typical phenocryst contents of Vesuvius eruptions ranges between 10 and 20% [*Rosi and Santacroce*, 1983; *Cioni et al.*, 1995]. Phenocryst modes of 50%Cpx and 50%Lc are assumed. For the phonolitic magma erupted during the Pompei eruption, the electrical conductivity calculations were carried out for a temperature of 815°C and a melt water concentration of 6 wt%H_2O [*Cioni et al.*, 1995; *Scaillet et al.*, 2008]. At a pressure of 200 MPa, conductivities calculated with the modified Archie's law range between 0.60 to 0.80 $(Ohm.m)^{-1}$. For the tephriphonolitic magma erupted during the Pollena eruption, a calculated conductivity range of 0.95-1.10 $(Ohm.m)^{-1}$ was obtained for a temperature of 1050°C, a pressure of 200 MPa and a melt water content of 3.5 wt% [*Scaillet et al.*, 2008]. For the tephritic magma, the calculated conductivity ranges between 0.40 and 0.60 $(Ohm.m)^{-1}$, for a temperature of 1100°C, a pressure of 200 MPa and a melt water content of 3 wt%. For comparison, the present models of electrical conductivity below Mt. Vesuvius yield a maximal value of ~1.30 $(Ohm.m)^{-1}$[*Di Maio*, 1998; *Petrillo*, unpublished data]. Therefore, there is no strict overlap between electrical conductivities measured below Mt. Vesuvius and values typical of magmas involved in the past activity of the volcano. However, this should not be taken to indicate the present-day absence of magma beneath Mt. Vesuvius. The typical spatial resolution of MT measurements does not rule out the possibility of the presence of a small magma reservoir. In addition, the magma-wall rock interface may be complex, with the presence of hydrothermal circulations and of a metasomatised thermal aureole [e.g. *Fulignati et al., 2004; 2005*], which would hamper the identification of magma from the inversion of the MT data. Yet, we note that the magmatic conductivity value the closest to the maximum measured from MT studies concerns the tephriphonolitic magma. Current models for Mt. Vesuvius favour a future eruption of tephriphonolite magma similar to the Pollena event [*Santacroce et al.*, 1987; 2005]. Increasing the crystal content of the magma above 20% or increasing the Lc/Cpx proportion above 1 would partially bridge the gap between magma and electrical conductivities measured by MT studies. The MT results could thus be compatible with a low-temperature crystal-rich magmatic system, consistent with the interpretations of seismic tomography data [*Zollo et al.*, 1998; *Auger et al.*, 2001].

6. Conclusions

Electrical impedance measurements have been used to discriminate the effects of temperature, pressure, and chemical composition, including water content, on the electrical response of three magmas from Mt. Vesuvius. Data were obtained in both the glass and melt regions. The conductivity increases with increasing temperature, melt water content and degree of polymerisation of the melt and decreases with pressure.

Electrical conductivity was identified to be essentially controlled by sodium migration in both the glass and melt regions. Data were fitted by Arrhenius laws, yielding activation energies (Ea) and activation volumes (ΔV) ranging from 61 to 142 kJ/mol and 16 to 24 cm^3/mol, respectively. Data from this and other studies were used to formulate a general compensation law, relating Ea and σ_0, valid over a wide compositional range.

A semi-empirical method allowing the determination of Ea, σ_0 and ΔV for natural magmatic liquids was constructed on the basis of our experimental data. The activation energy is modelled successfully on the basis of the Anderson-Stuart model, σ_0 is obtained from the compensation law and ΔV is fitted from our experimental conductivity data. The model enables the electrical conductivity to be calculated for the entire range of melt compositions at Mt. Vesuvius. It also predicts satisfactorily the electrical response of other melt compositions.

The laboratory-based electrical conductivity data for Mt. Vesuvius melts and magmas yield values slightly lower than the electrical anomaly revealed by MT studies performed at Mt. Vesuvius. Future modelling of the deep structure of Mt. Vesuvius on the basis of electrical measurements will have to integrate results from this study for the Vesuvius magmas.

Acknowledgments

This paper is part of the PhD of A. Pommier. The authors are grateful to P. Marianelli for providing the sample VS88-65B and R. Cioni for the sample VES9. We thank J-M Bény for his help in FTIR analyses. The authors are grateful to J. Tyburczy, J. Price and an anonymous reviewer for their careful and constructive reviews. We also thank R. Arculus for the editing work and A. Revil for his frank review and editing work. This study has been supported by the French national agency for research, ANR JC05-42707 (Electrovolc) attributed to F. Gaillard.

References

Alibert, C., and J. P. Carron (1980), Données expérimentales sur la diffusion des éléments majeurs entre verres ou liquides de compositions basaltique, rhyolitique et phonolitique, entre 900°C et 1300°C, à pression ordinaire, *Earth and Planetary Science Letters*, *47*(2), 294-306.

Anderson O.L., and D.A. Stuart (1954), Calculation of activation energy of ionic conductivity in silica glasses by classical methods, *Journal of American Society, 37* (12), 573-580.

Angell, C. A. (2001), Glass transition, in *Encyclopaedia of materials : science and technology*, eds. Buschow et al., Vol.4, pp. 3565-3575, Elsevier, Amsterdam.

Auger, E., P. Gasparini, J. Virieux, and A. Zollo (2001), Seismic evidence of an extended magmatic sill under Mt. Vesuvius, *Science*, *294*(5546), 1510-1512.

Ayuso, R. A., B. De Vivo, G. Rolandi, R.R. Seal, and A. Paone (1998), Geochemical and isotopic (Nd-Pb-Sr-O) variations bearing on the genesis of volcanic rocks from Vesuvius, Italy, *Journal of Volcanology and Geothermal Research*, *82*(1-4), 53-78.

Bagdassarov, N., H. C. Freiheit, and A. Putnis (2001), Ionic conductivity and pressure dependence of trigonal-to-cubic phase transition in lithium sodium sulphate, *Solid State Ionics*, *143*(3-4), 285-296.

Bagdassarov, N. S., J. Maumus, B. Poe, A. B. Slutskiy, and V. K. Bulatov (2004), Pressure dependence of Tg in silicate glasses from electrical impedance measurements, *Physics and Chemistry of Glasses*, *45*(3), 197-214.

Barczynski, R. J., and L. Murawski (2002), Mixed electronic-ionic conductivity in transition metal oxide glasses containing alkaline ions, *Journal of Non-Crystalline Solids*, *307*, 1055-1059.

Behrens, H., C. Romano, M. Nowak, F. Holtz, and D. B. Dingwell (1996), Near-infrared spectroscopic determination of water species in glasses of system $MAlSi_3O_8$ (M=Li, Na, K): An interlaboratory study, *Chemical Geology*, *128*(1-4), 41-63.

Behrens, H., R. Kappes, and P. Heitjans (2002), Proton conduction in glass - an impedance and infrared spectroscopic study on hydrous $BaSi_2O_5$ glass, *Journal of Non-Crystalline Solids*, *306*(3), 271-281.

Behrens, H., Y. Zhang, and Z. Xu (2004), H_2O diffusion in dacitic and andesitic melts, *Geochimica et Cosmochimica Acta*, *68*(24), 5139-5150.

Brasse, H., P. Lezaeta, V. Rath, K. Schwalenberg, W. Soyer, and V. Haak (2002), The

Bolivian Altiplano conductivity anomaly, *Journal of Geophysical Research-Solid Earth*, *107*(B5), 17.

Caillot, E., M. J. Duclot, J. L. Souquet, M. Levy, F. G. K. Baucke, and R. D. Werner (1994), A unified model for ionic transport in alkali disilicates below and above the glass transition, *Physics and Chemistry of Glasses*, *35*(1), 22-27.

Cioni, R., L. Civetta, P. Marianelli, N. Metrich, R. Santacroce, and A. Sbrana (1995), Compositional layering and syn-eruptive mixing of a periodically refilled shallow magma chamber : the AD 79 Plinian eruption of Vesuvius, *Journal of Petrology*, *36*(3), 739-776.

Cooper, R. F., J. B. Fanselow, and D. B. Poker (1996), The mechanism of oxidation of a basaltic glass : chemical diffusion of network-modifying cations, *Geochimica et Cosmochimica Acta*, *60*(17), 3253-3265.

Crank, J. (1975), The mathematics of diffusion, Second Ed., *Oxford Scientific Publications*, ISBN 2-86883-447-7, 440p.

Déportes, C., M. Duclot, P. Fabry, J. Fouletier, A. Hammou, M. Kleitz, E. Siebert, and J.L. Souquet (1994), *Electrochimie des solides*, Collection Grenoble Sciences, Pug, Grenoble, 437p.

Di Carlo, I., M. Pichavant, S. G. Rotolo, and B. Scaillet (2006), Experimental crystallization of a high-K arc basalt: The golden pumice, Stromboli volcano (Italy), *Journal of Petrology*, *47*(7), 1317-1343.

Di Maio, R., P. Mauriello, D. Patella, Z. Petrillo, S. Piscitelli, and A. Siniscalchi (1998), Electric and electromagnetic outline of the Mount Somma-Vesuvius structural setting, *Journal of Volcanology and Geothermal Research*, *82*(1-4), 219-238.

Dingwell, D. B. (1995), Relaxation in silicate melts: Some applications, in *Structure, Dynamics and Properties of Silicate Melts*, pp. 21-66, Mineralogical Soc America, Washington.

Fulignati, P., P. Marianelli, R. Santacroce, and A. Sbrana (2004), Probing the Vesuvius magma chamber – host rock interface through xenoliths, *Geology Magazine*, 141 (4), 417-428.

Fulignati, P., C. Panichi, A. Sbrana, S. Caliro, A. Gioncada, and A. Del Moro (2005), Skarn formation at the walls of the 79AD magma chamber of Vesuvius (Italy): Mineralogical and isotopic constraints, *Neues Jahrbuch fur Mineralogie, Abhandlungen*, 181 (1), 1-10.

Gaillard, F., B. Scaillet, M. Pichavant, and J. M. Beny (2001), The effect of water and fO_2 on the ferric-ferrous ratio of silicic melts, *Chemical Geology*, *174*(1-3), 255-273.

Gaillard, F., B. Schmidt, S. Mackwell, and C. McCammon (2003), Rate of hydrogen-iron

redox exchange in silicate melts and glasses, *Geochimica et Cosmochimica Acta*, *67* (13), 2427-2441.

Gaillard, F. (2004b), Laboratory measurements of electrical conductivity of hydrous and dry silicic melts under pressure, *Earth and Planetary Science Letters*, *218*(1-2), 215-228.

Gaillard, F., and G. I. Marziano (2005), Electrical conductivity of magma in the course of crystallization controlled by their residual liquid composition, *Journal of Geophysical Research-Solid Earth*, *110*(B6), 12.

Glover, P. W. J., M. J. Hole, and J. Pous (2000), A modified Archie's law for two conducting phases, *Earth and Planetary Science Letters*, *180*(3-4), 369-383.

Heinemann, I., and G. H. Frischat (1993), The sodium transport mechanism in $Na_2O.2SiO_2$ glass determined by the Chemla experiment, *Physics and Chemistry of Glasses*, 34 (6), 255-260.

Henderson, P., J. Nolan, G. C. Cunningham, and R. K. Lowry (1985), Structural control and mechanisms of diffusion in natural silicate melts, *Contributions to Mineralogy and Petrology*, *89*(2-3), 263-272.

Hess, K. U., and D. B. Dingwell (1996), Viscosities of hydrous leucogranitic melts: A non-Arrhenian model, *American Mineralogist*, *81*(9-10), 1297-1300.

Hoffmann-Rothe, A., O. Ritter, V. Haak (2001), Magnetotelluric and geomagnetic modelling reveals zones of very high electrical conductivity in the upper crust of Central Java, *Physics of the Earth and Planetary Interiors*, *124*(3-4), 131-151.

Huebner, J. S., and R. G. Dillenburg (1995), Impedance spectra of hot, dry silicate minerals and rock: qualitative interpretation of spectra, *American Mineralogist*, *80*(1-2), 46-64.

Jambon, A. (1982), Tracer diffusion in granitic melts: experimental results for Na, K, Rb, Cs, Ca, Sr, Ba, Ce, Eu, to 1300°C and a model of calculation, *Journal of Geophysical Research-Solid Earth*, *87*(B13), 10797-10810.

Jones, A. G. (1999), Imaging the continental upper mantle using electromagnetic methods, *Lithos*, *48*(1-4), 57-80.

Kress, V. C., and M. S. Ghiorso (1993), Multicomponent diffusion in basaltic melts, *Geochimica et Cosmochimica Acta*, *57*(18), 4453-4466.

Malki, M., and P. Echegut (2003), Electrical conductivity of the $CaO-SiO_2$ system in the solid and the molten states, *Journal of Non-Crystalline Solids*, *323*, 131-136.

Manzella, A., G. Volpi, A. Zaja, and M. Meju (2004), Combined TEM-MT investigation of

shallow-depth resistivity structure of Mt Somma-Vesuvius, *Journal of Volcanology and Geothermal Research*, *131*(1-2), 19-32.

Maumus, J., N. Bagdassarov, and H. Schmeling (2005), Electrical conductivity and partial melting of mafic rocks under pressure, *Geochimica et Cosmochimica Acta*, *69*(19), 4703-4718.

Mungall, J. E. (2002), Empirical models relating viscosity and tracer diffusion in magmatic silicate melts, *Geochimica et Cosmochimica Acta*, *66* (1), 125-143.

Mysen, M. O., and P. Richet (2005), *Silicate glasses and melts, Properties and structure*, Elsevier, Amsterdam, 544p.

Nascimento M.L.F., and S. Watanabe (2007), Test of the Anderson-Stuart model and correlation between free volume and the 'universal' conductivity in potassium glasses, *Materials Chemistry and Physics*, 105, 308-314.

Nell, J., B. J. Wood, and T. O. Mason (1989), High-temperature cation distributions in Fe_3O_4-$MgAl_2O_4$-$MgFe_2O_4$-$FeAl_2O_4$ spinels from thermopower and conductivity measurements, *American Mineralogist*, *74*(3-4), 339-351.

Nunziata, C., M. Natale, G. Luongo, and G.F. Panza (2006), Magma reservoir at Mt. Vesuvius: Size of the hot, partially molten, crust material detected deeper than 8 km, *Earth and Planetary Science Letters*, *242*(1-2), 51-57.

Park, S. K., and M. N. Ducea (2003), Can in situ measurements of mantle electrical conductivity be used to infer properties of partial melts?, *Journal of Geophysical Research-Solid Earth*, *108*(B5), 2270.

Partzsch, G. M., F. R. Schilling, and J. Arndt (2000), The influence of partial melting on the electrical behavior of crustal rocks: laboratory examinations, model calculations and geological interpretations, *Tectonophysics*, *317*(3-4), 189-203.

Pfeiffer, T. (1998), Viscosities and electrical conductivities of oxidic glass-forming melts, *Solid State Ionics*, *105*, 277-287.

Presnall, D. C., C. L. Simmons, and H. Porath (1972), Change in electrical conductivity of a synthetic basalt during melting, *Journal of Geophysical Research-Solid Earth*, *77*(29), 5665-5672.

Reid, J. E., B. T. Poe, D. C. Rubie, N. Zotov, and M. Wiedenbeck (2001), The self-diffusion of silicon and oxygen in diopside ($CaMgSi_2O_6$) liquid up to 15GPa, *Chemical Geology*, 174, 77-86.

Roberts, J. J., and J. A. Tyburczy (1994), Frequency dependent electrical properties of minerals and partial-melts, *Surveys in Geophysics*, *15*(2), 239-262.

Roberts, J. J., and J. A. Tyburczy (1999), Partial-melt electrical conductivity: Influence of melt composition, *Journal of Geophysical Research-Solid Earth*, *104*(B4), 7055-7065.

Roling, B. (1999), What do electrical conductivity and electrical modulus spectra tell us about the mechanisms of ion transport processes in melts, glasses, and crystals?, *Journal of Non-Crystalline Solids*, *244*(1), 34-43.

Rosi, M., and R. Santacroce (1983), The AD 472 "Pollena"eruption: volcanological and petrological data for this poorly-known, Plinian-type event at Vesuvius, *Journal of Volcanology and Geothermal Research*, *17*(1-4), 249-271.

Rosi, M., C. Principe, and R. Vecci (1993), The 1631 Vesuvius eruption. A reconstruction based on historical and stratigraphical data, *Journal of Volcanology and Geothermal Research*, *58*, 151-182.

Santacroce, R. (Ed) (1987), Somma-Vesuvius, *CNR Quaderni della Ricerca Scientifica*, 114 (8), 230p.

Santacroce, R., R. Cioni, P. Marianelli, and A. Sbrana (2005), Understanding Vesuvius and preparing for its next eruption, in *Cultural responses to the volcanic landscape, The Mediterranean and Beyond*, eds Balmuth et al., pp 27-55, Archeological Institute of America.

Satherley, J., and S. I. Smedley (1985), The electrical conductivity of some hydrous and anhydrous molten silicates as a function of temperature and pressure, *Geochimica et Cosmochimica Acta*, *49*, 769-777.

Scaillet, B., M. Pichavant, and R. Cioni, *Evidence for the shallowing of the Vesuvius reservoir in the upper crust over the last 20 kyr* , submitted to Nature.

Scarlato, P., B. T. Poe, C. Freda, and M. Gaeta (2004), High-pressure/high-temperature measurements of electrical conductivity in basaltic rocks from Mount Etna, Sicily, Italy (vol 109, art no B02210, 2004), *Journal of Geophysical Research-Solid Earth*, *109*(B4), 1.

Tyburczy, J. A., and D. K. Fisler (1995), Electrical properties of minerals and melts, *Mineral Physics and Crystallography, A Handbook of Physical Constants*, pp.185-208, AGU, Whashington, D.C.

Tyburczy, J. A., and H. S. Waff (1983), Electrical conductivity of molten basalt and andesite to 25kilobars pressure: geophysical significance and implications for charge transport and melt

structure, *Journal of Geophysical Research*, *88*(NB3), 2413-2430.

Tyburczy, J. A., and H. S. Waff (1985), High pressure electrical conductivity in naturally occurring silicate liquids, in *Point Defects in Minerals, Geophysical Monogr. Ser.*, vol.31, edited by R.N.Shock, pp.78-87, AGU, Whashington, D.C.

Watson, E. B. (1994), Diffusion in volatile-bearing magmas, in *Volatiles in Magmas*, edited, pp. 371-411, Mineralogical Soc America, Washington.

Wendlandt, R. F. (1991), Oxygen diffusion in basalt and andesite melts – experimental results and discussion of chemical versus tracer diffusion, *Contributions to Mineralogy and Petrology*, *108*(4), 463-471.

Westrich, H. R. (1987), Determination of water in volcanic glasses by Karl-Fischer titration, *Chemical Geology*, *63*(3-4), 335-340.

Wu, X., and Y.-F. Zheng (2003), Compensation effect for electrical conductivity and its applications to estimate oxygen diffusivity in minerals, *Journal of Geophysical Research-Solid Earth*, *108*(B3), 2139.

Zhang, Y., and E. M. Stolper (1991), Water diffusion in a basaltic melt, *Nature*, *351*, 306-309.

Zollo, A., P. Gasparini, J. Virieux, H. Le Meur, G. deNatale, G. Biella, E. Boschi, P. Capuano, R. De Franco, P. dell Aversana, R. de Matteis, I. Guerra, G. Iannaccone, L. Mirabile, and G. Vilardo (1996), Seismic evidence for a low-velocity zone in the upper crust beneath Mount Vesuvius, *Science*, *274*(5287), 592-594.

Zollo, A., P. Gasparini, J. Virieux, G. Biella, E. Boschi, P. Capuano, R. de Franco, R., P. Dell'Aversana, R. de Matteis, G. De Natale, G. Iannaccone, I. Guerra, H. Le Meur, and L. Mirabile (1998), An image of Mt. Vesuvius obtained by 2D seismic tomography, *Journal of Volcanology and Geothermal Research*, *82*(1-4), 161-173.

Appendices (Appendixes)

Appendice 1 : Effet des cristaux et des bulles sur la conductivité électrique

Les mesures expérimentales présentées ci-dessus ont été effectuées dans des verres et liquides magmatiques et l'effet des cristaux a été incorporé en utilisant un formalisme mathématique (loi d'Archie modifiée). Cependant, un magma est composé de trois phases (liquide, cristaux et gaz), chacune ayant une influence plus ou moins significative sur sa réponse électrique.

A.1.1. Intégration de l'effet des cristaux par des formalismes mathématiques

Comme il a été expliqué au Chapitre 2, les mesures électriques dans l'intervalle de cristallisation ont été évitées, les cristaux se développant principalement sur les parois de la cellule de conductivité, engendrant une « pollution » au niveau des électrodes et une perturbation de la mesure. Par conséquent, l'incorporation de l'effet des cristaux sur la conductivité a fait appel à différents formalismes mathématiques, chacun tenant compte de la conductivité et de la teneur en cristaux ainsi que de la conductivité du liquide.

Les mesures de conductivité électrique des cristaux sont nombreuses dans la littérature et l'évolution de leur réponse électrique en fonction de la température est bien connue, comme le souligne la revue de Tyburczy and Fisler (1995). En particulier, les échantillons du Vésuve étudiés présentent des clinopyroxènes et de la leucite, dont les comportements arrhéniens respectifs sont (Hinze et al., 1981 ; Maury, 1968) :

$$\sigma_{cpx} = 124.\exp\left[\frac{-123290}{R.T}\right],$$

$$\sigma_{lc} = 20.9.\exp\left[\frac{-46234}{R.T}\right] \qquad (13)$$

avec σ la conductivité électrique $(ohm.m)^{-1}$, T la température (K) et R la constante des gaz parfaits. On notera le caractère beaucoup plus conducteur de la leucite par rapport au clinopyroxène.

Prendre en considération l'effet des cristaux sur la conductivité globale (*bulk*) revient à considérer un mélange à deux phases, une étant liquide, l'autre solide. Différents formalismes ont été développés (Glover et al., 2000 et références inclues), ce qui les différencie étant basé

essentiellement sur des considérations géométriques (Figure A1). Notons que ces modèles s'appliquent à des phases aussi bien liquides, solides que gazeuses.

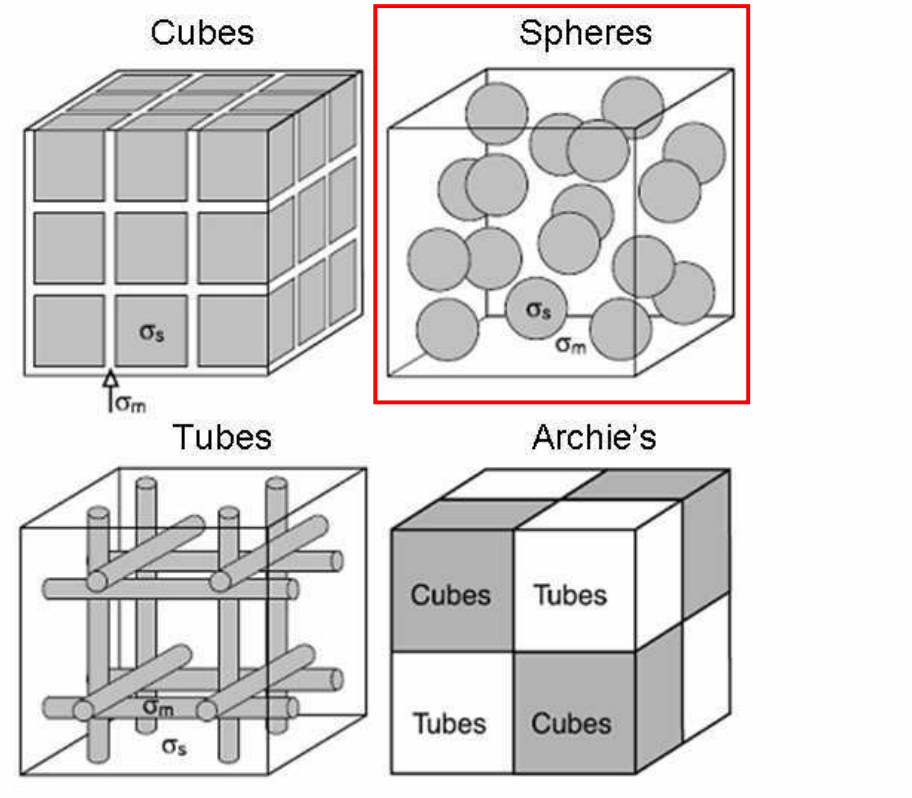


Figure A1 : Examples of melt distribution according to different geometric models (after ten Grotenhuis et al., 2005). σm: electrical conductivity of the melt, σs: electrical conductivity of the the solid phase. We will note that models also work with another nature of grey phase (e.g. gaseous). In the study of Pommier et al. (2008), we adopted the Spheres geometry in order to investigate the electrical response of a partially crystallized magma, using the modified Archie's law.

D'un point de vue géométrique, la présence de cristaux dans un liquide magmatique s'apparente à un modèle de type « Sphères ». Les formalismes d'Hashin-Shtrikman (Hashin and Shtrikman, 1962), de Waff (Waff, 1974), la loi d'Archie modifiée (Glover et al., 2000) et d'autres formalismes basés sur la théorie des milieux effectifs (*Effective Medium Theory*, par ex., Gueguen et al., 1997) font partie de ce type de modèles (Tableau A1). Nous avons adopté dans l'étude précédente la loi d'Archie modifiée (Glover et al., 2000), qui, contrairement à la loi

d'Archie (Archie, 1942 ; Watanabe and Kurita, 1993), assimile les cristaux à des inclusions sphériques peu conductrices et isolées, baignant dans une matrice liquide très conductrice.

Tableau A1 : Summary of some commoner two-phase mixing models for electrical conductivity.

Model	Equation	References
Cube	$\sigma_{eff} = \left[1-(1-X_1)^{\frac{2}{3}}\right]\sigma_1$	Ten Grotenhuis et al., 2005
Tube	$\sigma_{eff} = \frac{1}{3}X_1\sigma_1 + (1-X_1)\sigma_2$	Ten Grotenhuis et al., 2005 and references therein
Archie (Cubes+tubes)	$\sigma_{eff} = CX_1^n\sigma_1$ C: Archie constant, n: cementation exponent	Archie, 1942 ; Watanabe and Kurita, 1993
Modified Archie's (Sphere)	$\sigma_{eff} = \sigma_1(1-X_2)^{(\log(1-X_2^n)/\log(1-X_2))} + \sigma_2 X_2^n$	Glover et al., 2000
Hashin-Shtrikman (Sphere)	HS^+ (upper bound): $\sigma_{eff} = \sigma_1 + \frac{1-X_1}{1/(\sigma_2-\sigma_1) + X_1/3\sigma_1}$ HS^- (lower bound): $\sigma_{eff} = \sigma_2 + \frac{X_1}{1/(\sigma_1-\sigma_2) + (1-X_1)/3\sigma_2}$	Hashin and Shtrikman, 1962
Waff (Sphere, equivalent to HS^+)	$\sigma_{eff} = \frac{\sigma_1 + (\sigma_2-\sigma_1)(1-(2X_1/3))}{1+(X_1/3)(\sigma_2/\sigma_1-1)}$	Waff, 1974

Notes: σ_{eff} is the effective conductivity of the rock, consisting of 2 phases (1 and 2) with individual conductivities σ_1 and σ_2, X_2 being the volume fraction of phase 2 (X_1=1-X_2).

Cette loi a été comparée à d'autres modèles de type « Sphère » et les résultats montrent de faibles différences de conductivité entre les différents formalismes appliqués (Figure A2). Par exemple, dans le cas d'une phonolite hydratée à 815°C et 200MPa, quelle que soit la fraction de liquide, les plus grandes différences n'excèdent pas 0.2(ohm.m)$^{-1}$ (0.1(ohm.m)$^{-1}$ pour des fractions de liquide >0.7).

L'utilisation d'un formalisme mathématique reste une première approximation. La prise en compte des propriétés de transport par les formalismes basés sur la théorie des milieux effectifs peut être approfondie et de récents efforts ont contribué à améliorer le lien entre propriétés physiques et structures polyphasées (Hautot and Tarits, 2002).

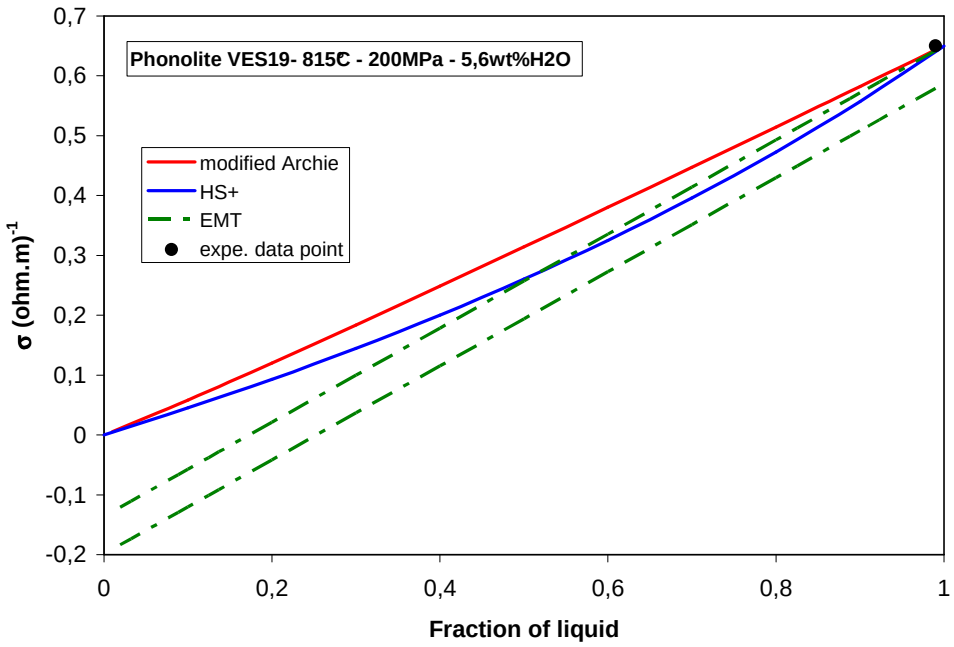


Figure A2 : Modelisation of the electrical conductivity of a phonolitic melt from the Pompei eruption as a function of its crystal content (clinopyroxenes) using different formalisms: the modified Archie's law, the Hashin and Strikman upper bound (HS^+) and the effective medium theory exposed in Gueguen et al. 1997 (EMT). The modified Archie's law and the EMT present conductivity values close to the interval defined by the HS formalism. The experimental data point comes from the study of Pommier et al. (2008).

A.1.2. Importance de l'effet des bulles sur la conductivité électrique

Nous avons considéré que la part de la conductivité de bulles de gaz dans la conductivité globale d'un magma peut être négligée en première approximation, en faisant l'hypothèse que le rôle des bulles de gaz sur la conductivité mesurée est probablement moins important que celui des porteurs de charge dans le liquide ou que celui des cristaux. Afin de tester cette hypothèse, nous avons réalisé une expérience de décompression sur une obsidienne (Gaillard, 2004) hydratée à 3%m H_2O. Une investigation précise de l'effet des bulles nécessiterait notamment de réaliser des expériences avec d'autres types de gaz (CO_2, Cl_2, SO_2…), mais le but est ici d'estimer, qualitativement plus que quantitativement, l'effet d'une phase gazeuse sur la conductivité d'un magma. La synthèse s'est effectuée en autoclave à chauffage interne, à 200MPa, 900°C, dans une

capsule en or, pendant environ 15jours. L'échantillon de départ est un verre issu de cette synthèse, de forme cylindrique. La cellule de mesure, comparable à celle de la Figure 2b, ce chapitre (OD=5, ID=1, L=6mm), a été placée dans un four à pression atmosphérique, à 640°C (i.e. au-dessus de la transition vitreuse). Dans ces conditions de pression et de température, l'eau dissoute dans l'échantillon s'extrait en formant des bulles (de vapeur d'eau) dont la croissance augmentera au cours du temps. L'évolution de l'échantillon a été comparée à l'évolution de sa réponse électrique enregistrée au cours du temps (Figure A3) :

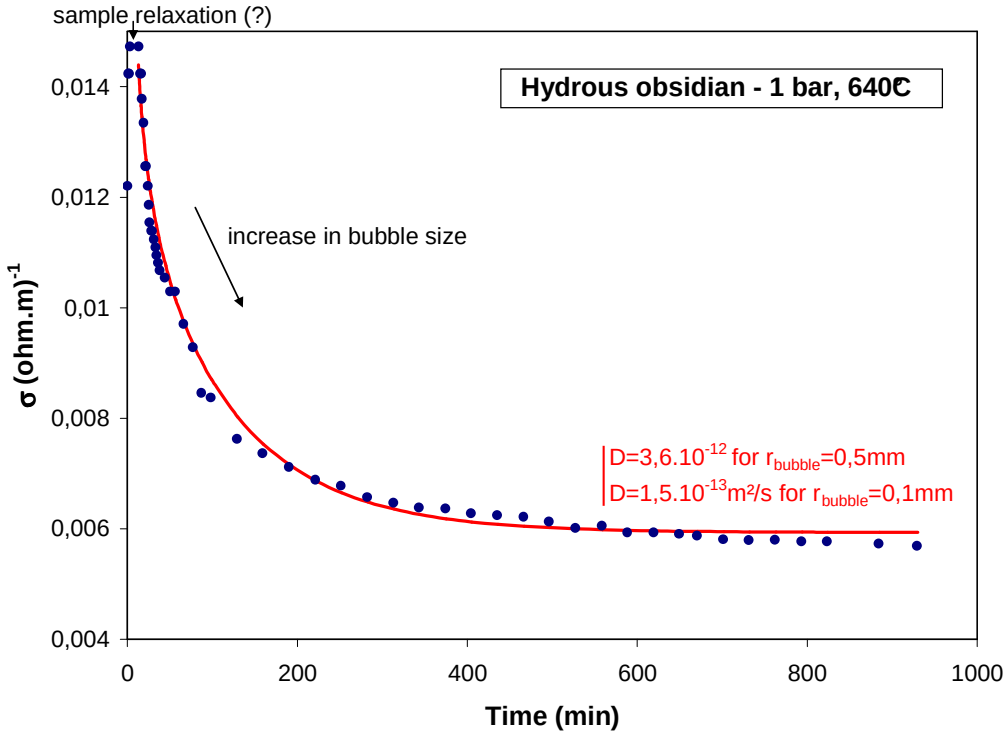


Figure A3: Time-evolution of the electrical conductivity of the hydrous obsidian (synthetized at 200MPa) at atmospheric pressure, 640°C. The decrease in conductivity can be correlated to the growth of bubbles in the melt. The time-evolution of the conductivity decrease is successfully reproduced by a diffusion formalism (Crank, 1975, red line). Calculated D values are in agreement with water diffusivities in rhyolitic melts at 640°C (Zhang and Behrens, 2000; Watson, 1994). The first minutes present an increase in conductivity that can be explained by a relaxation process of the sample due to the change of pressure.

La réponse électrique de l'échantillon au cours du temps se décompose en deux parties. La première, montrant une légère augmentation de la conductivité lors des premières minutes,

peut être interprétée comme la phase de relaxation de l'échantillon dû au changement de pression, ΔP~200MPa (synthèse à 200MPa, mesures à 0.1MPa). La seconde partie, présentant une diminution progressive de la conductivité au cours du temps, peut être reliée à la croissance des bulles de vapeur d'eau dans l'échantillon. Cette interprétation est renforcée par trois constats effectués après l'expérience : 1) la présence de bulles à l'intérieur de l'échantillon 2) l'augmentation de volume de l'échantillon dans la cellule (Figure A4) et 3) l'identification d'un coefficient de diffusion dont la valeur, comme nous allons le voir, est en accord avec la diffusivité de l'eau dans les mêmes conditions.

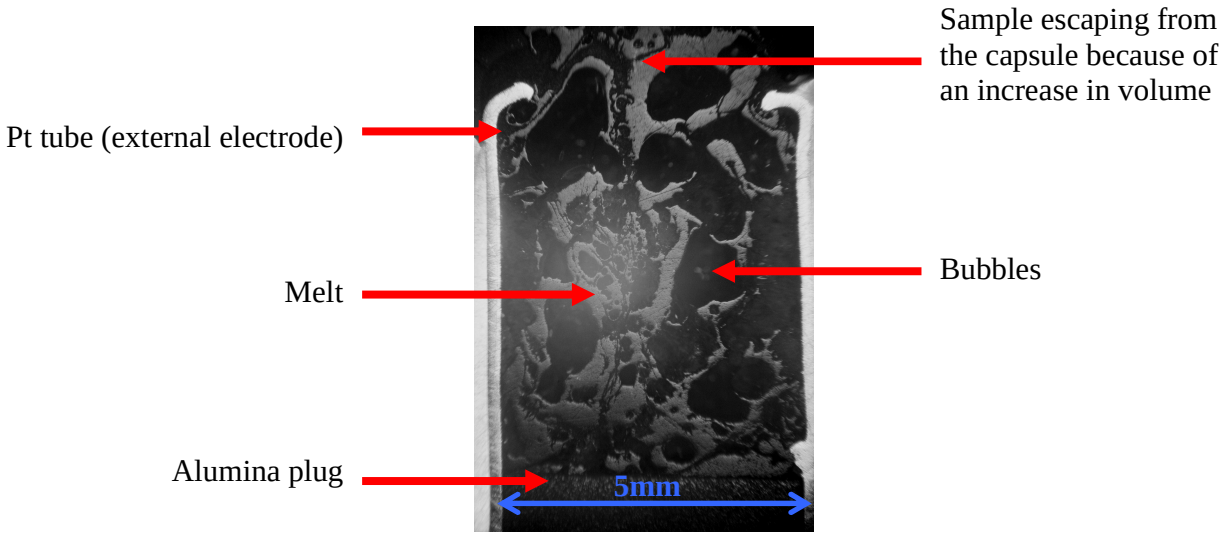


Figure A4: Microphotograph (optical microscope) of the hydrous obsidian after the "decompression" experiment at 640°C and atmospheric pressure. The nucleation and growth of bubbles implied an increase in the sample volume that led the melt to escape from the conductivity cell.

En effet, la croissance des bulles, qui affecte la réponse électrique au cours du temps, peut être reliée au phénomène de diffusion de l'eau dissoute dans le liquide. Nos données de conductivité sont reproduites par le formalisme de Crank (1975) (Figure A3) :

$$\frac{\sigma(t)-\sigma_0}{\sigma_f-\sigma_0} = 1-\frac{6}{\pi}\sum_{i=1}^{\infty}\frac{1}{i^2}\exp(-Di^2\pi^2 t/r) \qquad (14)$$

Avec σ (t) la conductivité $(ohm.m)^{-1}$ à un temps t (s), σ_0 la conductivité à t=0 (correspondant ici à t_{exp}=13min), σ_f la conductivité finale (plateau), r le rayon de la bulle (m), D le coefficient de

diffusion de l'espèce mobile (H_2O, en l'occurrence). Considérant, d'après les observations au microscope, une taille moyenne des bulles de 0.2 à 1mm de diamètre, Eq. 14 fournit des valeurs de D allant de $1.5.10^{-13}m^2/s$ à $3.6.10^{-12}m^2/s$. Ces valeurs sont en accord avec celles obtenues par Watson (1994) et Zhang and Behrens (2000) sur des liquides rhyolitiques à la même température (640°C), fournissant respectivement $D=5.9.10^{-13}m^2/s$ et $6.8.10^{-12}m^2/s$.

Cette expérience montre que la présence de bulles temps à diminuer la conductivité électrique d'un magma (en augmentant sa résistance électrique). Le passage d'un liquide rhyolitique sans bulle (t=0min) à un liquide extrêmement riche en gaz (t>~200min) a provoqué une diminution de la conductivité de 60% (de 0.015 à $0.006(ohm.m)^{-1}$). Une explication possible concernant l'augmentation du caractère résistif d'un magma riche en bulles est que la présence et la croissance de ces bulles « entravent » progressivement la circulation des porteurs de charges dans le liquide, le contournement des bulles représentant une plus grande distance à parcourir.

L'effet des gaz est donc un facteur non négligeable dans la conductivité des magmas riches en bulles. Toutefois, les bulles se formant essentiellement lors de la décompression, la phase gazeuse des magmas est limitée dans les conditions de notre étude. En effet, les magmas du Vésuve ont été considérés dans des conditions de stockage pré-éruptives (par ex., Scaillet et al., 2008), i.e. avant leur remontée en surface. Par conséquent, dans ces conditions, l'effet des bulles sur la conductivité du magma est limité. Cela implique que le modèle à deux phases (liquide et cristaux) de la conductivité des magmas du Vésuve présenté ci-dessus peut être directement utilisé pour interpréter les anomalies de conductivité révélées sur le terrain par la magnétotellurie.

Appendice 2 : Temps de relaxation électrique

A.2.1. Définition et calcul du temps de relaxation électrique

Suite à une perturbation mécanique, thermique ou électrique, un melt silicaté présente un temps d'équilibration de sa structure (Webb and Dingwell, 1995). Ce changement dans la structure du melt (configuration) s'exprime par le temps de relaxation de l'échantillon (Wilding et al., 1996). Raisonner en échelle de temps de relaxation a permis de définir des critères de distinction entre un comportement des melts silicatés à l'équilibre et hors équilibre, permettant

par conséquent de mieux comprendre leur structure et leurs propriétés (Dingwell, 1995). En particulier, le temps de relaxation électrique se définit par:

$$\tau_e = \frac{e_0.\varepsilon}{\sigma} = \frac{D/E}{\sigma} \qquad (15)$$

avec τ_e (ou simplement τ), le temps de relaxation électrique (s), e_0 la permittivité du vide (A.s/V.m), ε la constante diélectrique (adimensionnelle), σ la conductivité électrique $(ohm.m)^{-1}$, D la densité de charge (C/m^2) et E le champ électrique (V/m).

Les scans en fréquence effectués lors des mesures de conductivité électrique permettent de déterminer le temps de relaxation électrique d'un échantillon dans les conditions de température et de pression fixées (Moynihan, 1998 ; Gaillard, 2004). Au sommet de l'arc d'impédance (Chapitre 2, Figure 2.7A):

$$\omega.\tau = 2.\pi.f.\tau = 1 \qquad (16)$$

avec ω la pulsation (s^{-1}), τ le temps de relaxation électrique (s) et f la fréquence (Hz). Cela signifie que la fréquence de la tension sinusoïdale appliquée est égale à la fréquence de la relaxation électrique de l'échantillon.

En pratique, les temps de relaxation ont été déterminés en utilisant l'Eq. 16, plutôt que l'Eq. 15. Deux raisons à ce choix : 1) Eq. 16 permet d'obtenir une valeur de τ de manière très simple, directement à partir du spectre d'impédance, 2) la valeur de ε pour les compositions étudiées est mal connue et la technique de spectroscopie d'impédance n'est pas adaptée pour la déterminer (les techniques de mesure du module complexe (par ex., Grant et al., 1977) seraient en revanche adaptées pour déterminer ε). Toutefois, n'ayant pas accès aux spectres d'impédance dans le domaine liquide (cf Chapitre 2, paragraphe 2.7.2), la détermination du temps de relaxation se limitera au domaine vitreux.

A.2.2. Effet des différents paramètres sur le temps de relaxation électrique

Les effets de la température, de la pression, de la teneur en eau et de la composition des verres sur le temps de relaxation électrique (τ) sont présentés Figure A5. L'augmentation de la température diminue significativement le temps de relaxation. Entre 450 et 830°C, à 400MPa, le temps de relaxation de l'échantillon tephriphonolitique (VS88-65B) passe de 5.10^{-5} à $1.6.10^{-7}$s.

La dépendance de τ à la température peut être exprimée par un formalisme de type arrhénien (Moynihan, 1995):

$$\tau = \tau_0 . \exp\left(\frac{Ea_\tau}{RT}\right) \qquad (16)$$

avec τ_0 le terme pré-exponentiel (s), Ea_τ l'énergie d'activation liée au processus de relaxation (kJ/mol), T la température (K) et R la constante de gaz parfaits. Pour l'ensemble des compositions étudiées, Ea_τ varie de 79.0 à 104kJ/mol à et τ_0 de -28.6 à -24.6s.

L'effet de la pression est moins significatif. Une augmentation de pression contribue à augmenter légèrement le temps de relaxation : à 600°C, pour un verre phonolitique (VES19), τ varie de $2.5.10^{-7}$ à $6.3.10^{-7}$s entre 50 et 400MPa (Figure 5A.A).

Le temps de relaxation électrique augmente avec la teneur en eau (Figure 5A.B). Par exemple, à 500°C et 200-300MPa, le temps de relaxation d'un verre phonolitique croît de $1.6.10^{-6}$ à $2.5.10^{-5}$s lorsque la teneur en eau varie de ~0 à 5.6%m d'eau.

L'effet de la composition sur τ est présenté Figure 5A.C. Le comportement général entre teneur en en alcalins (plus particulièrement la teneur en sodium, principal porteur de charge) et temps de relaxation est linéaire : plus l'échantillon est riche en sodium, plus il se relaxe vite. Cette linéarité s'observe aussi entre composition et conductivité (Figure 5, ce chapitre).

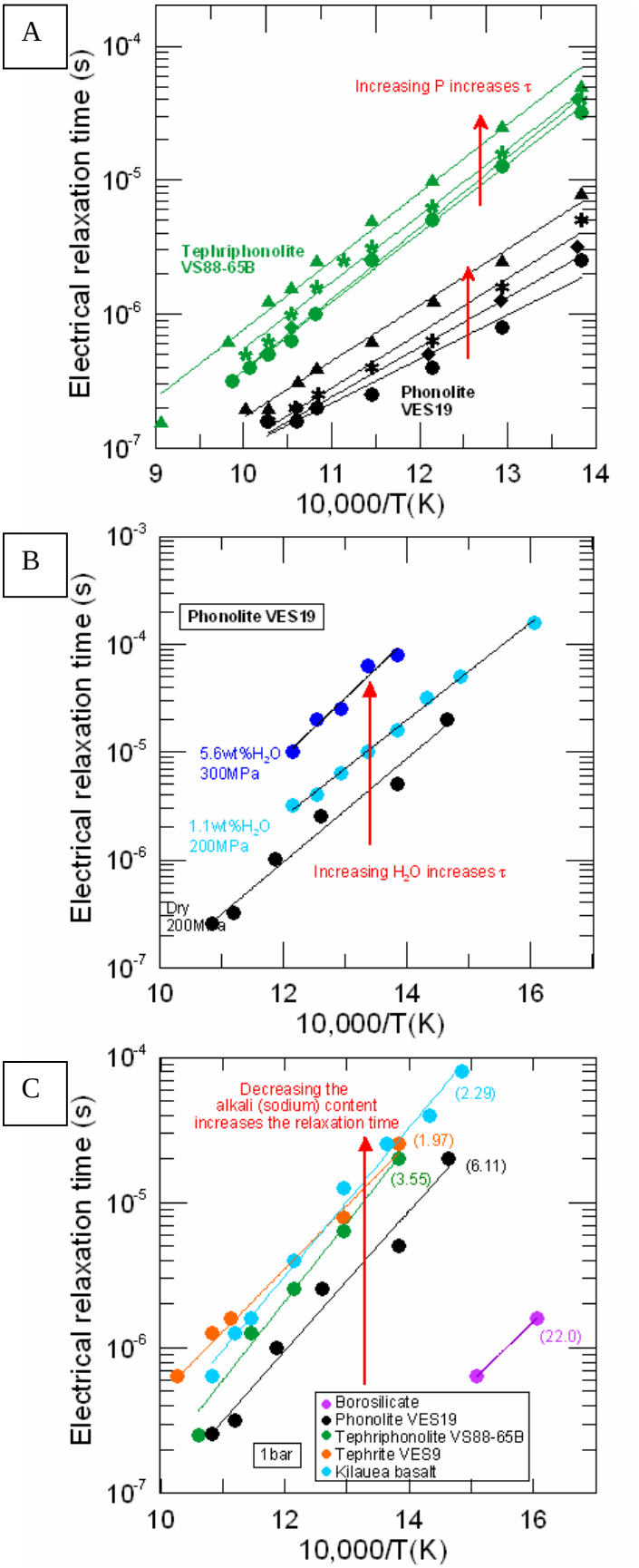


Figure A5 : Electrical relaxation times in the glassy domain. A) Effect of temperature (from 450 to 830°C) and pressure (50 to 400MPa). Examples of the tephriphonolite (VS88-65B) and the phonolite (VES19) from Mt. Vesuvius. Circles: 50MPA, diamonds: 100MPa, stars: 200MPa and triangles: 400MPa. Increasing T decreases τ and increasing P increases τ; B) Effect of the water content for the phonolite VES19, between 0 (dry) and 5.6wt%H_2O. Increasing the water content increases τ; C) Chemical composition effect. Relaxation times of Mt. Vesuvius glasses (tephritic to phonolitic), Kilauea basalt and a borosilicate. The alkali tend to decrease τ. Figures into brackets corresponds to Na_2O content in wt%. In each case, lines correspond to Arrhenian formalisms.

A.2.3. Comparaison avec le temps de relaxation obtenu par des mesures de viscosité

Les temps de relaxation obtenus à l'aide de mesures de viscosité et de mesures électriques est présenté Figure A6 pour trois échantillons de composition Na_2O-$3SiO_2$ (Dingwell, 1995), CaO-Al_2O_3-SiO_2 (Gruener et al., 2001) et phonolitique (cette étude ; Wilding et al., 1996). Comparer des valeurs de temps de relaxation implique pour les échantillons d'avoir subi des traitements thermiques comparables. En effet, la relaxation de la structure d'un verre est fonction de la vitesse à laquelle l'échantillon a été chauffé ou refroidi au cours de son histoire. Considérons, par exemple, un liquide silicaté trempé très rapidement, et qui, par conséquent, n'a pas eu le temps de se relaxer. Lorsque le verre obtenu est réchauffé, deux cas de figure sont envisageables:

- la vitesse à laquelle l'échantillon est réchauffé est suffisamment lente pour permettre à l'échantillon de se relaxer dès le début de la montée en température. Les valeurs de τ (et de la transition vitreuse, Tg) ne seront pas affectées de manière significative par la trempe rapide initiale du liquide. C'est le cas des mesures dans le verre présentées dans ce manuscrit.

- la vitesse à laquelle l'échantillon est réchauffé est trop rapide pour permettre à l'échantillon de se relaxer. Les mesures de τ dans le verre ainsi que la détermination de Tg seront affectées car le liquide n'aura pas pu adapter sa configuration suite au refroidissement.

A une même température, un même verre initialement non relaxé (car refroidi trop rapidement) peut donc présenter des temps de relaxation différents lorsqu'il est réchauffé. Ces τ différents seront fonction de la vitesse à laquelle le verre est réchauffé. Dans la Figure A6, nos valeurs de τ (électrique) mesurées pour la phonolite VES19 peuvent être comparées à celles de τ (viscosité) mesurées pour une phonolite de Teide (TF36.1 et TF36.2, Wilding et al., 1996) car dans les deux cas, le protocole adopté a laissé le temps aux échantillons phonolitiques de se relaxer. La vitesse de chauffage des verres est en effet lente dans les deux études (quelques °C/min).

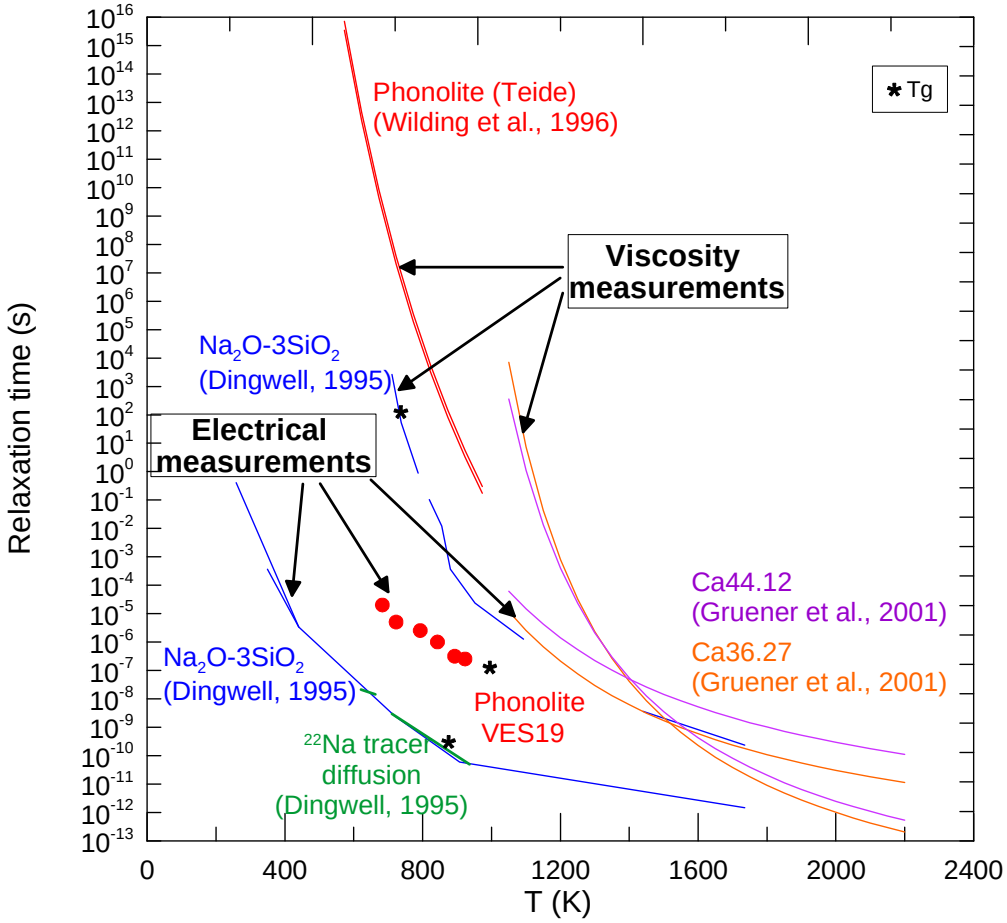


Figure A6: Relaxation map for a natural silicate melt (phonolite), synthetic silicate melts: Na_2O-$3SiO_2$ and CaO-Al_2O_3-SiO_2. Data come from viscometric (Dingwell, 1995, Wilding et al., 1996, Gruener et al., 2001) and electric (this study, Dingwell, 1995, Gruener et al., 2001) property determinations. The diagram shows that electrical relaxation times in silicate glasses are much smaller than those from viscosity measurements, underlining different relaxation modes in the silicate melts structure.

Il apparaît clairement Figure A6 que, pour une même composition, le temps de relaxation τ est beaucoup plus long par les mesures de viscosité que par les mesures électriques. Puisque le temps de relaxation exprime un changement dans la structure de l'échantillon (par ex., Wilding et al., 1996), on en déduit que les modes de relaxation étudiés par les deux méthodes sont différents. La viscosité d'un melt silicaté concernant en particulier les liaisons Si-O (Webb and Dingwell, 1990), elle est essentiellement contrôlée par les tétraèdres de silice qui forment la « charpente » (*silica framework*) du melt. Le phénomène de relaxation étudié par les mesures de viscosité est

donc directement lié à l'adaptation de la charpente aux nouvelles conditions. La conductivité électrique étant mesurée suite à l'application d'un courant électrique à l'échantillon (Roberts and Tyburczy, 1999), le temps de relaxation électrique est lié à la mobilité des ions porteurs de charge (le sodium, dans notre cas) et dépendra peu de la « charpente ». Les faibles valeurs de $\tau_{électrique}$ par rapport à celles de $\tau_{viscosité}$ peuvent donc s'expliquer par la plus grande rapidité (et capacité) des ions à migrer dans l'échantillon comparé à celle liée à un réagencement des tétraèdres de silice.

A haute température, les données de la littérature semblent indiquer une convergence des temps de relaxation $\tau_{viscosité}$ et $\tau_{électrique}$. Cela indiquerait que la mobilité des porteurs de charge serait, à haute température, aussi couplée au flux visqueux (Gruener et al., 2001).

Références

Archie, G.E. (1942), The electrical resistivity log as an aid in determining some reservoir characteristics, *Transactions of the American Institute of Mining and Metallurgical Engineers*, 146, 54-61.

Crank, J. (1975), The mathematics of diffusion, Second Ed., *Oxford Scientific Publications*, ISBN 2-86883-447-7, 440p.

Dingwell, D. B. (1995), Relaxation in silicate melts: Some applications, in *Structure, Dynamics and Properties of Silicate Melts*, pp. 21-66, Mineralogical Soc America, Washington.

Gaillard, F. (2004), Laboratory measurements of electrical conductivity of hydrous and dry silicic melts under pressure, *Earth and Planetary Science Letters*, *218*(1-2), 215-228.

Glover, P. W. J., M. J. Hole, and J. Pous (2000), A modified Archie's law for two conducting phases, *Earth and Planetary Science Letters*, *180*(3-4), 369-383.

Grant, R.J., M.D. Ingram, and A.R. West, (1977), An investigation of B-alumina electrolytes by electric modulus spectroscopy, *Electrochimica Acta*, 22, 729-734.

Gruener, G., P. Odier, D. De Sousa Meneses, P. Florian, and P. Richet (2001), Bulk and local dynamics in glass-forming liquids : A viscosity, electrical conductivity, and NMR study of aluminosilicate melts, *Physical Review B*, vol. 64, 024206.

Gueguen Y., T. Chelidze and M. LeRavalec, (1997), Microstructures, percolation thresholds, and rock physical properties, Tectonophysics, 279 (1-4), 23-35.

Hashin, Z., and S. Shtrikman (1962), On some variational principles in anisotropic and nonhomogeneous elasticity, *Journal of the Mechanics and Physics of Solids*, 10, 335-342.

Hautot, S., and P. Tarits (2002), Effective electrical conductivity of 3-D heterogeneous porous media, *Geophysical Research Letters*, 29(14), doi:10.1029/2002GL014907.

Hinze, E., G. Will, and L. Cemic (1981), Electrical conductivity measurements on synthetic olivines and on olivine, enstatite, and diopside from Dreiser Weiher, Eifel (Germany) under defined thermodynamic activities as a function of temperature and pressure, *Physics of the Earth and Planetary Interiors*, 25, 245-254.

Maury, R. (1968), Conductibilité électrique des tectosilicates. II. Discussion des résultats, *Bulletin de la Société Française de Minéralogie et Cristallographie*, 91, 355-366.

Moynihan, C.T. (1995), Structural relaxation and the glass transition, in *Structure, Dynamics and Properties of Silicate Melts*, pp. 21-66, Mineralogical Soc America, Washington.

Moynihan, C.T. (1998), Description and analysis of electrical relaxation data for ionically conducting glasses and melts, *Solid State Ionics*, 105, 175-183.

Pommier, A., F. Gaillard, M. Pichavant, and B. Scaillet (2008), Laboratory measurements of electrical conductivities of hydrous and dry Mount Vesuvius melts under pressure, *J. Geophys. Res.*, 113, B05205, doi:10.1029/2007JB005269.

Roberts, J. J., and J. A. Tyburczy (1999), Partial-melt electrical conductivity: Influence of melt composition, *Journal of Geophysical Research-Solid Earth*, *104*(B4), 7055-7065.

Scaillet, B., M. Pichavant, and R. Cioni, (2008) Upward migration of Vesuvius magma chamber over the past 20,000 years, *Nature*, 455, doi:10.1038/nature07232.

ten Grotenhuis, S.M., M.R. Drury, C.J. Spiers, and C.J. Peach (2005), Melt distribution in olivine rocks based on electrical conductivity measurements, *Journal of Geophysical Research,* 110(B12201), doi:10.1029/2004JB003462.

Tyburczy, J. A., and D. K. Fisler (1995), Electrical properties of minerals and melts, *Mineral Physics and Crystallography, A Handbook of Physical Constants*, pp.185-208, AGU, Whashington, D.C.

Waff, H.S. (1974), Theoretical considerations of electrical conductivity in a partially molten mantle and implications for geothermometry, *Journal of Geophysical Research,* 79 (26), 4003-4010.

Watanabe, T., and K. Kurita (1993), The relationship between electrical conductivity and melt fraction in a partially molten simple system: Archie's law behaviour, *Physics of the Earth and Planetary Interiors,* 78, 9-17.

Watson, E. B. (1994), Diffusion in volatile-bearing magmas, in *Volatiles in Magmas*, edited, pp. 371-411, Mineralogical Soc America, Washington.

Webb, S.L., and D.B. Dingwell (1990), Non-Newtonian Rheology of Igneous Melts at High Stresses and Strain Rates: Experimental Results for Rhyolite, Andesite, Basalt, and Nephelinite, *Journal of Geophysical Research-Solid Earth*, 95, B10, 15695-15701.

Webb, S.L., and D.B. Dingwell (1995), Viscoelasticity, in *Structure, Dynamics and Properties of Silicate Melts*, pp. 21-66, Mineralogical Soc America, Washington.

Wilding, M., S. Webb, D. Dingwell, G. Ablay, and J. Marti (1996), Cooling rate variation in natural volcanic glasses from Tenerife, Canary Islands, *Contributions to Mineralogy and Petrology*, 125, 151-160.

Zhang, Y., and H. Behrens (2000), H2O diffusion in rhyolitic melts and glasses, *Chemical Geology*, 169, 243-262.

Chapitre 4

Modèle direct de la conductivité électrique du Vésuve

(*Forward modelling of the electrical conductivity of Mount Vesuvius*)

Objectifs de ce chapitre

Un modèle direct de la conductivité (ou résistivité) électrique du Vésuve a été élaboré pour étudier la structure actuelle de cet édifice volcanique. Le modèle est basé sur l'analyse conjointe des mesures électriques en laboratoire, des informations géophysiques et des contraintes pétrologiques et géochimiques. Des simulations 1-D et 3-D ont exploré l'effet de la profondeur, du volume et de la résistivité d'un ou deux réservoirs situés dans la structure. Pour chaque configuration testée, les fonctions de transfert modélisées ont été comparées aux fonctions de transfert du terrain issues des études magnétotelluriques antérieures. Les données du terrain sont reproduites par la seule présence d'une couche très conductrice superficielle (~0.5km de profondeur, 1.2km d'épaisseur, 5ohm.m en résistivité) qui correspond probablement à la saumure observée sous le volcan. Nos résultats sont également consistants avec le refroidissement de petits volumes de magma à faible profondeur (<3-4km). La présence d'un corps conducteur plus profond, à ~8km, est en accord avec les fonctions de transfert du terrain si il possède une résistivité >~100ohm.m et avec des dimensions qui n'excèdent probablement pas celles du cône. D'après le modèle de la conductivité électrique de Pommier et al. [JGR, 2008], une telle valeur de résistivité est compatible avec une chambre magmatique de basse température et riche en cristaux ou avec une plus petite quantité de magma plus chaud interconnecté dans l'encaissant carbonaté plus résistif. La comparaison avec les valeurs des ondes sismiques en utilisant des modèles sismiques tend à favoriser la seconde hypothèse. Nos résultats sont en accord avec une anomalie profonde (8-10km de profondeur) correspondant à un magma tephriphonolitique à 1000°C, contenant 3.5%mH_2O, 30vol.% cristaux, et interconnecté dans les carbonates selon les proportions ~45% de magma - 55% carbonates.

A new petrological and geophysical investigation of the present-day plumbing system of Mount Vesuvius

Article prochainement soumis à G-Cubed.

Pommier A.[1,2], Tarits P.[3], Hautot S.[3], Pichavant M. [1,2], Gaillard F. [1,2], Scaillet, B. [1,2]

[1] *Université d'Orléans, Institut des Sciences de la Terre d'Orléans, UMR 6113, 45067, Orléans, France*

[2] *CNRS/INSU, Institut des Sciences de la Terre d'Orléans, UMR6113, 45071 Orléans, France*

[3] *CNRS/UBO, Institut Universitaire Européen de la Mer, Domaines Océaniques, UMR 6538, Brest, France*

Abstract

A model of the electrical resistivity of Mount Vesuvius has been elaborated to investigate the present structure of the volcanic edifice. The model is based on electrical conductivity measurements in the laboratory, on geophysical information, in particular, magnetotelluric (MT) data, and on petrological and geochemical constraints. Both 1-D and 3-D simulations explored the effect of depth, volume and resistivity of either one or two reservoirs in the structure. For each configuration tested, modelled MT transfer functions were compared to field transfer functions from field magnetotelluric studies. The field electrical data are reproduced with a shallow and very conductive layer (~0.5km depth, 1.2km thick, 5ohm.m resistive) that most likely corresponds to the saline brine present beneath the volcano. Our results are also compatible with the presence of cooling magma batches at shallow depths (<3-4km depth). The presence of a deeper body at ~8km depth, as suggested by seismic studies, is consistent with the observed field transfer functions if such a body has a resistivity >~100ohm.m. According to a petro-physical conductivity model, such a resistivity value is in agreement either with a low-temperature, crystal-rich magma chamber or with a small quantity of hotter magma interconnected in the resistive surrounding carbonates. Comparison with seismic velocity values tends to support the second hypothesis. Our findings are consistent with a deep structure (8-10km depth) made of a tephriphonolitic magma at 1000°C, containing 3.5wt%H_2O, 30vol.% crystals, and interconnected in carbonates in proportions ~45% melt - 55% carbonates.

1. Introduction

Mount Somma-Vesuvius is characterized by a high volcanic risk because of its dangerous past activity in a densely populated area. Its eruptive history has been marked by an alternation of effusive and explosive activity over the last 20kyrs. Since 1944, however, Mt. Vesuvius volcano has entered a dormant period, being nowadays characterized only by a widespread but cold fumarolic activity in the inner slopes and bottom of the crater [Chiodini et al., 2001] and a moderate micro-earthquake activity [DeNatale et al., 2006]. Yet, Mt. Vesuvius is still considered as a very dangerous volcano, its volcanic history suggesting that the longer the quiescent period, the more violent the renewal of activity [Santacroce et al., 1994].

The determination of plausible eruptive scenarios in case of volcanic re-awakening has an obvious direct impact on hazard assessment plans in the Neapolitan area. However, large uncertainties remain with respect to the existence of a present magma reservoir and its storage conditions, in particular size and depth. Past eruptions have been widely investigated and their pre-eruptive conditions are well constrained [e.g. Santacroce, 1983; Rosi and Santacroce, 1983; Rolandi et al., 1993; Cioni et al., 1995; Scaillet et al., 2008]. Proposed future scenarios range from a sub-plinian eruption, similar to 472 or 1631 AD eruptions [Scandone et al., 1993; Santacroce et al., 2005] up to devastating AD79 Pompei-type events associated to a larger magma storage zone that would extend well beyond the size of Mt Vesuvius cone [e.g. Auger et al., 2001; Nunziata et al., 2006].

Numerous geophysical studies aimed at investigating the present inner structure beneath Mt. Vesuvius have detected various seismic, magnetotelluric (MT) and gravimetric anomalies. In particular, a conversion of P to S seismic waves has been evidenced at ~8-10km depth and interpreted as the top of a large magma sill [Zollo et al., 1996, 1998; Auger et al., 2001; Nunziata et al., 2006]. Such an anomaly has also been detected by the MT study of DiMaio et al. [1998]. However, based on combined time-domain electromagnetic and magnetotelluric soundings (TDEM-MT investigation), Manzella et al. [2004] argue that the conductive anomaly detected below Mt. Vesuvius corresponds to a superficial brine layer rather than to the presence of a deep conductive magma body. This is consistent with the gravimetric observations from Berrino and Camacho [2008] that could not detect the deep anomalous layer interpreted by seismic tomography as an extended sill but attributed the different deep anomalies to solidified magma bodies.

In the present paper, we propose a new approach for an improved characterization of the present day plumbing system of Mt Vesuvius. We elaborated a model (both 1-D and 3-D) of the electrical resistivity of the upper crust underneath Mount Vesuvius. This model is based on laboratory measurements of electrical resistivity performed on natural Vesuvius samples [Pommier et al., 2008], on petrological information, in particular, the phase equilibrium relationships of Mt. Vesuvius magmas, and on previous geophysical and geochemical studies. The aim of this paper is three-fold: 1) to define the structure of the volcanic complex that best reproduce the field MT data and that matches petrological constraints, 2) to establish the most reliable hypotheses regarding the storage conditions of a potential magma reservoir, and 3) to underline the need for the acquisition of new MT measurements across Mt Vesuvius cone, particularly for deeper investigations with long period data (>100s).

2. Volcanological background and petrological constraints

Mt. Somma-Vesuvius volcanic complex probably originated from the regional tensile Quaternary tectonics that dissected the Apennine units and deepened the carbonate basement in the Campanian Plain [Bruno et al., 1998; Bianco et al., 1998]. Mt. Vesuvius area is intersected by two regional sets of faults trending NW-SE and NE-SW [Santacroce, 1987] and its present seismic activity has been attributed to both regional and local stress fields [Marzocchi et al., 1993; Bianco et al., 1998 and references therein; DeNatale et al., 2000].

The volcanic activity of Mt. Somma-Vesuvius started between 18 and 37 ka B.P. [Principe et al., 1999], although the earliest magmatic events in the Vesuvian area go back to ca 400 ka [Brocchini et al., 2001; Di Renzo et al., 2007]. It alternated frequent open-conduit activity (effusive eruptions and Strombolian events) with closed conduit conditions, the latter giving rise to Plinian or sub-Plinian eruptions following periods of dormancy lasting several centuries or millenia [Arnò et al., 1987; Santacroce et al., 2008]. The volcano underwent several caldera collapses, produced by at least four Plinian eruptions [Cioni et al., 1999], and the present cone (Mt Vesuvius) was formed since the famous Pompei eruption in 79 AD. Small batches of primitive magmas were discharged during Strombolian events ($<0.001 km^3$) while larger reservoirs of more evolved magmas were involved in Plinian eruptions (from 0.1 to a few km^3) [Rosi et al., 1987].

Table 1. Conditions and electrical resistivity of the rocks forming the present Mt Somma-Vesuvius volcanic complex and of magma of some past eruptions.

Material	Conditions	Resistivity (ohm.m)	References
Volcanic deposits	0-3km depth	~200	Berrino et al., 1998 Manzella et al., 2004 Cella et al., 2007
Brine	1-~3km depth, 450°C NaCl aqueous solution, CO_2-rich vapour phase Salinity: 2-3m	<10	Chiodini et al., 2001 Manzella et al., 2004 Caliro et al., 2005
Magma	-Residual shallow batches: 1-4km depth -Potential deep reservoir: 1-2km thick, 8km depth		Zollo et al., 1998a,b Chiodini et al., 2001 Auger et al., 2001
	Magma pre-eruptive conditions:		
-phonotephrite (1944)	1.5-3km depth, 1100°C ~1wt% H_2O, 20vol%crystals	~2	Rosi and Santacroce, 1983 Cioni et al., 1995
-phonolite (Pompei)	6km depth, 815°C, 6wt%H_2O, 20vol%crystals	~4	Marianelli et al., 1999 Fulignati et al., 2004a,b
-tephriphon. (Pollena)	3km depth, 800 to 1050°C, 3.5 to 6wt%H_2O, 20vol%crystals	2-18	Pommier et al., 2008 Scaillet et al., 2008 Scandonce et al., 2008
Carbonates	~3-13 km depth	2000	Berrino et al., 1998 DiMaio et al.,1998 Manzella et al., 2004
Basement	>13km depth	2000-5000	Berrino et al., 1998 DiMaio et al.,1998
Deep magma source	~60km depth (?)	-	Joron et al., 1987

The variety of rocks forming the volcanic complex is presented in Table 1. Geophysical investigations, constrained by one deep drilling (Trecase well), allowed to define the shallow structure of the volcanic edifice. The subsurface of the volcano is made of volcanic deposits (thickness<3km), consisting of highly fracturated interbedded lava, pyroclastic materials and volcanoclastic, marine and fluvial sedimentary rocks of Pleistocene ages [Santacroce et al., 1983; Zollo et al., 1998, 2002; DeMatteis et al., 2000]. The presence of a shallow brine, included within the volcanic-sedimentary deposits and extending vertically down to the top of the underlying carbonates, has been inferred from various geochemical and geophysical lines of evidence [Chiodini et al., 2001; Caliro et al., 2005; Manzella et al., 2004]. The nature of the present-day fluids circulating in this hydrothermal system is a saline liquid phase coexisting with a CO_2-rich vapour phase [Chiodini et al., 2001; Caliro et al., 2005], Vesuvian magmas being characterized by both high chlorine and CO_2 contents [Cioni et al., 1998; Marianelli et al., 2005; Balcone-Boissard et al., 2008], associated to elevated CO_2 diffuse emissions [Chiodini et al., 2001; Iacono-Marziano et al., 2009 and references therein]. Seismic and gravimetric surveys indicate that the underlying Mesozoic carbonates have a thickness of ~8km, the top being at 2-3km depth in Mt. Vesuvius area, deepening westward from the adjacent Apenninic belt [Bruno et al. 1998; DeNatale et al., 2004; Cella et al., 2007]. This carbonate thick layer is dissected by normal faults at a regional scale, causing a horst and graben-like structure. The metamorphic Campanian basement is encountered at a depth greater than 11km, being characterized by a high density (2,800kg/m^3) [Berrino et al., 1998]. The presence of a deep (mantellic) magma source is poorly constrained but is inferred to lie at 60km depth below Mt. Vesuvius [Joron et al., 1987]. It would be located in the mantle wedge consistent with the presence of a subducted lithospheric slab [Panza et al., 2007]. The Moho discontinuity beneath Mt. Vesuvius is located at ~30km depth [e.g. Ferrucci et al., 1989].

Mt. Vesuvius magmas are generally highly potassic, ranging from slightly silica undersaturated (K-basalt to trachyte) to highly silica undersaturated (K-tephrite to K-phonolite) [Joron et al., 1987; Ayuso et al., 1998; Iacono-Marziano et al., 2009]. Several petrological and geochemical studies contributed to define the pre-eruptive conditions for the past eruptions [e.g. Rosi and Santacroce, 1983; Civetta and Santacroce, 1992; Villemant et al., 1993; Cioni et al., 1995; Marianelli et al., 1995; Fulignati et al., 2004a; Scaillet et al., 2008]. Pressure, temperature and crystal content of the magmas that were involved in the main volcanic events of Mt. Vesuvius, like the Pompei Plinian eruption (79AD), the Pollena subplinian eruption (472 AD) and the last eruptive event from 1944, are presented in Table 1. Petrological and geochemical (isotopic) studies suggest the presence of a “shallow” magmatic

system (<~4km) periodically recharged with the arrival of K-rich magma batches from a "deep" reservoir (>10km depth) [Marianelli et al., 1995; Cioni et al., 1999; Civetta et al., 2004]. Major differences regard both the depth and the size of the magma chamber [e.g. Santacroce, 1983; Marianelli et al., 1999]. The phase equilibria obtained on various Mt Vesuvius magmas led Scaillet et al. [2008] to conclude that the reservoirs that fed the past eruptions migrated from 7-8km to 2-3km depth between AD79 and 1944 events [Cioni et al., 1995; Marianelli et al., 1999; Scandone et al., 2008]. Given that such a shift goes along with an eruptive style, from Plinian to Strombolian [Scaillet et al., 2008], a correct location of the current reservoir depth is central for a proper definition of future eruptive scenarios. The reservoir depth is an important parameter in the forward modelling. The occurrence of high P wave velocities above 3km depth and of local volcano-tectonic earthquakes shallower than 6km depth [Bianco et al., 1998; Lomax et al., 2001] suggest that superficial magma reservoirs of significant size are unlikely.

3. Laboratory and field electrical studies applied to Mount Vesuvius

The electrical properties of rocks and melts can be investigated both in laboratory, using impedance measurements obtained during experiments under pressure and temperature [Pommier et al., 2008 and references therein], and in the field from magnetotelluric (MT) investigation. Several studies [e.g. Wannamaker et al., 2008] have shown that laboratory measurements allow to interpret the MT responses, particularly in terms of storage conditions of a partially molten material.

The electrical resistivity of the main parts of the volcanic edifice is shown in Table 2. The electrical response of various representative Mt. Vesuvius melts (from tephritic to phonolitic compositions) has been studied at high pressure and temperature by Pommier et al. [2008], from which a model to calculate the electrical conductivity of Mt Vesuvius magmas as a function of temperature, pressure, chemical composition, including water content and crystal load has been established (Figure 1). This model allows us to estimate the resistivity of the magma stored in the volcanic complex under the different configurations considered in the forward modelling. The aim of the forward modelling is to define the possible range of the different parameters (resistivity, volume, and depth of the reservoir).

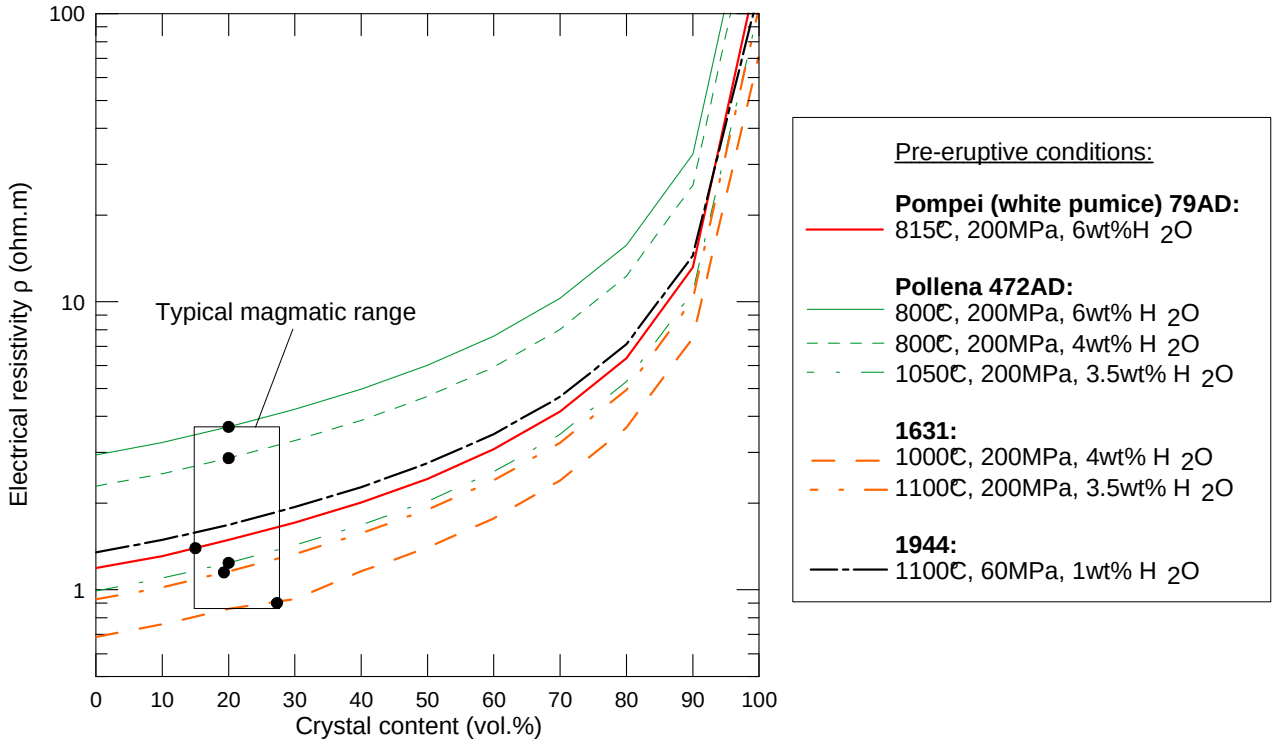


Figure 1: Electrical resistivity of Mount Vesuvius magmas in pre-eruptive conditions for several past volcanic events, using the model of Pommier et al. [2008] and phase relation works from [Scaillet et al., 2008]. Magmatic compositions correspond to the Pompei, the zoned Pollena and 1631 eruptions and the last 1944 volcanic event. Calculations were performed assuming crystals as clinopyroxenes. Dots represent the phenocryst contents of the eruptive products.

A few magnetotelluric studies have been conducted on Mt. Vesuvius [DiMaio et al., 1998; Müller et al., 1999; Manzella et al., 2004; Troiano et al., 2008]. These investigations have provided MT transfer functions at a series of sites on the volcano (Figure 2) presented in form of apparent resistivity and MT impedance phase as a function of the frequency, or the period. These data express the electromagnetic induced response of the Earth to the fluctuations of the natural electromagnetic field, which is a function of the distribution of electrical resistivity in the substratum [Simpson and Bahr, 2005]. Apparent resistivities are shown in the studies from DiMaio et al. [1998] and Manzella et al. [2004]. Only Manzella et al. [2004] show phase data. The position of the stations is presented Figure 2. The apparent resistivities from Manzella et al and DiMaio et al. show comparable patterns as a function of frequency at all sites on the volcano (see Figure 8 in DiMaio et al. [1998] and Figure 2 in Manzella et al. [2004]). This observation suggests that 1) the horizontal structure at the scale of the volcanic edifice may be considered homogeneous to a first approximation, and 2)

small-scale heterogeneities at depth affect only midly the MT transfer functions. The values of the apparent resistivity between the two MT studies are however shifted one with respect to the other (Figure 3). Apparent resistivity values from DiMaio et al. [1998] are ~2 log unit higher than the values from Manzella et al. [2004]. As stressed out by Manzella et al. [2004], the data from DiMaio et al. [1998] are probably distorted by static shift effects, which, in contrast, have been taken into account by Manzella et al. [2004]. According to Troiano et al. [2008], the phases obtained by Di Maio et al. (unfortunately not published) show no significant differences with the phases of Manzella et al. [2004]. This observation is in agreement with a static shift in the data from Di Maio et al., since static shift corresponds by definition to a frequency-independent offset of the magnitudes of MT transfer functions that leaves impedance phases unchanged [Simpson and Bahr, 2005]. The interpretation of the transfer functions by Di Maio et al [1998] and Manzella et al. [2004] are also very different. Di Maio et al. interpret the change in apparent resistivity by the presence of a magma reservoir located at ~8km depth, in agreement with some seismic studies (Zollo et al., 1998; Auger et al., 2001), while Manzella et al. attribute the observed apparent resistivity changes to a shallow conductive brine layer. In the latter study, data inversion focused on depths less than 4km and with no deep reservoir.

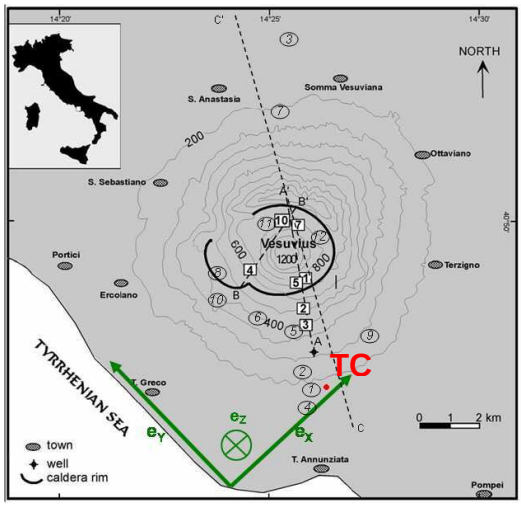


Figure 2: Location map of the Somma-Mount Vesuvius volcanic area (after Manzella et al. [2004]) and location of MT soundings. Boxes with site numbers and profiles AA' and BB' from Manzella et al. [2004]. Ellipses with site numbers and profile CC' from DiMaio et al. [1998]. Sites 8 and 9 from Manzella et al. are not presented since no transfer functions are available for these stations and site 6 was discarded because transfer functions were only partially recorded for this station. e_X, e_Y and e_Z indicate the x, y and z directions, respectively, used for the 3-D forward model presented in the present study. TC: Trecase well.

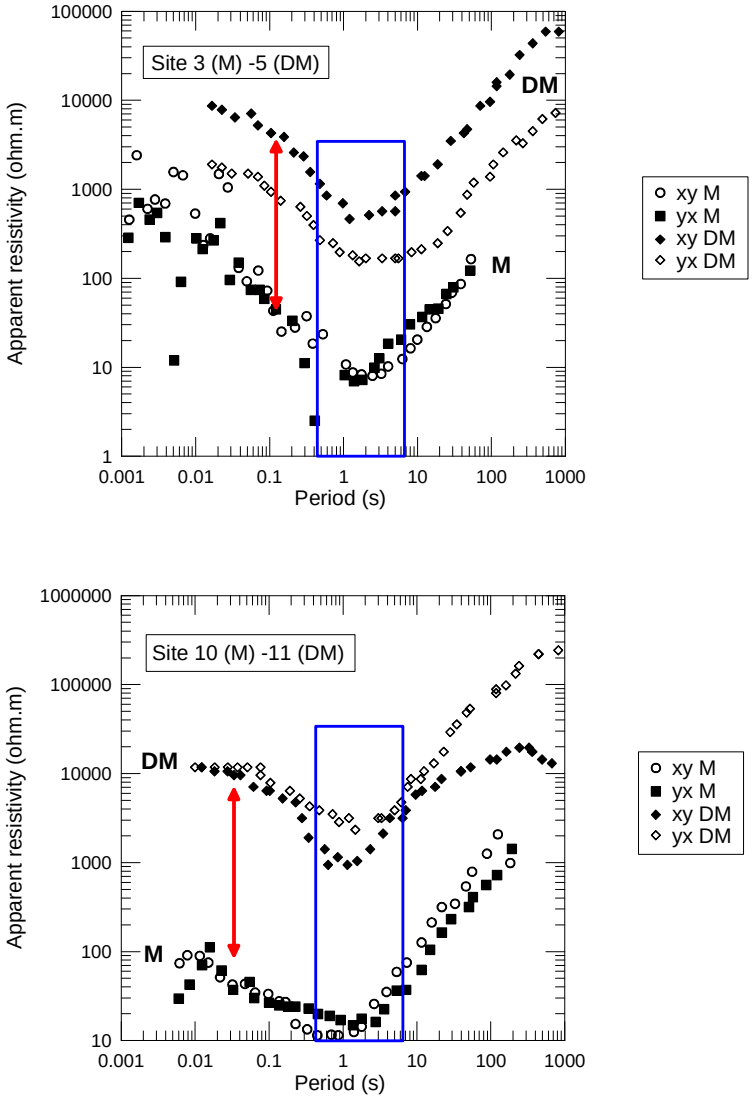


Figure 3: Comparison between apparent resistivity curves from DiMaio et al. [1998] (DM) and Manzella et al. [2004] (M) for two close observation sites (see Figure 4.2) on Mt Vesuvius. A systematic shift of about 2log-units is observed between the curves from the two studies (underlined by the double narrow), whatever the position of the volcano. The data from DiMaio et al. are probably affected by static shift (see text for details). The rectangle serves to locate the position of the systematic minimum in the curves (between 0.4 and 7s).

4. Petro-physical resistivity model

The data set by Manzella et al. 2004 are suitable to investigate whether a possible deep reservoir suggested by several authors is resolved by MT. Both apparent resistivity and phase are available. They are corrected for static shift and the MT penetration depth (e.g. Simpson and Bahr, 2005) is probably large enough to allow us to infer possible structures at depths greater than 4 km. One the other hand, the number of sites is too small for a thorough 3-D

inversion. A different approach is used here. We defined a resistivity model of the volcano edifice based on our knowledge of the lithology, of the resistivity of the main parts of the volcano, and of a petro-physical model of the electrical resistivity of Vesuvius magmas. With this model, we simulated the MT response functions and compared them to the data from Manzella et al. (2004). The aim of these simulations is to define the possible range of the different parameters of shallow and deep reservoirs (resistivity, volume, and depth).

The electrical resistivity of the main parts of the volcanic edifice is shown in Table 2. The characteristics (depth, thickness and volume) of the volcanic deposits, the brine layer, the underlying carbonates and basement as well as the magma reservoir came from geophysical and petrological previous studies (see references in Table 1). The resistivity values of the volcanic deposits, the carbonates and the basement were obtained after the studies of Di Maio et al. [1998] and Manzella et al. [2004], while the resistivity values of the brine and the magma were determined using electrical measurements in laboratory (respectively Quist and Marshall [1968] and Pommier et al. [2008]). The electrical properties of various representative Mt. Vesuvius melts (from tephritic to phonolitic compositions) has been studied at high pressure and temperature by Pommier et al. [2008] from which a model to calculate the electrical resistivity of Vesuvius magmas as a function of temperature, pressure, chemical composition, including water content, and crystal load has been established (Figure 1). This petro-physical model allows us to estimate the resistivity of the magma stored in the volcanic complex under the different configurations considered in the MT simulation.

Our modelling strategy consisted in calculating 1-D resistivity models at each station of Manzella et al. [2004], using the MTInv program of the University of Oulu [Pirttijärvi, 2004]. The initial three-layer model represented the volcanic deposits, the carbonates-basement and the deep magma source (the half-space). Thicknesses and resistivity values come from the literature (see references in Table 1) and the characteristics of these layers are presented in Table 2. We merged the carbonates and the basement into one single layer, because of their similar resistivity values (Table 1). We added a conductive layer, figuring either the brine layer suggested by Manzella et al. 2004 or a large magma reservoir (DiMaio et al. 1998, Zollo et al. 1998), We also considered cases with tthe two conductive bodies .

In order to obtain a resistivity value for the brine, we considered a two-phase material, composed by volcanic deposits and a NaCl aqueous solution under the conditions of Chiodini et al., [2001] (Table 1). We assumed that the effect of the CO_2 vapour phase on brine resistivity is negligible compared to the effect of the dissolved NaCl. The resistivity of the NaCl solution was determined using data from the literature [Quist and Marshall, 1968]. The

resistivity of magmatic liquids was determined using the model of Pommier et al. [2008], as explained above. Two hypotheses were considered for the calculation of the bulk resistivity of the corresponding magma reservoir, either the reservoir was a mixture of magma and a solid matrix (carbonates or volcanic deposits) or it was a homogeneous "chamber" filled with partially crystallized magma.

The Hashin-Shtrikman upper bound, denoted HS^+, was used to calculate the bulk resistivity of the two-phase mixture (either brine or magma reservoir) [Hashin and Shtrikman, 1962]. This model considers a high-conductivity liquid phase (in our case, NaCl solution or magma) surrounding a less conductive material (carbonates or volcanic deposits) [ten Grotenhuis et al., 2005]. The effective conductivity (or resistivity) is given by:

$$\sigma_{eff} = \frac{1}{\rho_{eff}} = \sigma_1 + \frac{1 - X_1}{1/(\sigma_2 - \sigma_1) + X_1/3\sigma_1} \qquad (1)$$

where σ_{eff} and ρ_{eff} are respectively the effective conductivity and resistivity of the two-phase material, σ_1 is the conductivity of phase 1, σ_2 is the conductivity of phase 2, X_1 and X_2 are the proportions (volume fraction) of the two phases (X_1=1-X_2). Resistivity values calculated using the Hashin-Shtrikman formalism were found to match the resistivity range provided by the modified Archie's law [Glover et al. 2000; Pommier et al., 2008], suggesting that both models can be used to estimate the resistivity of the two-phase mixtures considered in this study.

The 1-D simulations were extended to 3-D in order to account for the finite size of the magma chamber and to test the impact of major features on the data, such as the coast effect, the topography, the graben-like structure and the carbonates deepening (see section 2). The 3-D forward problem is solved with the finite difference algorithm proposed by Mackie et al. [1993]. An example of 3-D model is presented in Figure 4. The grid used for 3-D modelling covers the entire Vesuvius area and is centered on the volcano. A higher resolution was adopted in the central area. The model is parametrized by 50 blocks in the x direction, 50 blocks in the y direction (see spatial orientation in Figure 2) and 37 layers in the vertical, z direction. We used a set of 17 periods from 0.1-1000s for the modelling. This period range matches those from Di Maio et al.[1998] and Manzella et al.[2004].

Table 2. Values of the parameters for the forward modelling.

Material	Depth (km)	Thickness (km)	Volume (km^3)	T (°C)	Composition	Resistivity (ohm.m)
Volcanic deposits	0-3	3	-	-	-	100-300
Brine	1-8	0-2	-	400-500	Salinity:2-3m NaCl NaCl solution/solid matrix=0.05-0.25•	0.06-20*
Magma	2-15	0-2	2-"infinite"	700-1100	Tephritic to phonolitic 0 to 6wt% H_2O -Crystal content range: 0-100% : -Magma/carbonates= 0-1 :	 2->8000◊ 2-2000*
Carbonates + Basement	~3-13	>60	-	-	-	2000
Deep magma source	>60	« infinite » (half-space)	-	1300	Basalt + olivine	20*

◊ The model of Pommier et al. [2008] enables ρ_{magma} to be calculated as a function of T, P, H_2O, composition and crystals content.
* Resistivity values obtained using the Hashin-Shtrikman formalism [Hashin and Shtrikman, 1964] and the modified Archie's law [Glover et al., 2000].
• The solid matrix being either the volcanic deposits or the carbonates, depending on the depth of the brine.

Before using the 3-D model to investigate the effect of a magma chamber, notably its volume, we tested the influence of the main known resistivity constrasts. The 3-D structures were embedded into a mean 1-D model derived from the values in Table 1-2 (Figure 4). At first, we included in the model the limits of the shoreline. The value of the electrical resistivity of the sea water was taken to 0.3ohm.m. We found this effect negligible at the sites on the volcano in the period range of interest (less than 200 s). Some structural characteristics like the graben-like structure and the carbonates deepening were also included in the first 3-D simulations. Their influence on the MT transfer functions was also found negligible, owing to 1) a too low contrast in resistivity between the volcanic deposits and the carbonates and 2) the small dimensions of both the graben and the westward deepening.

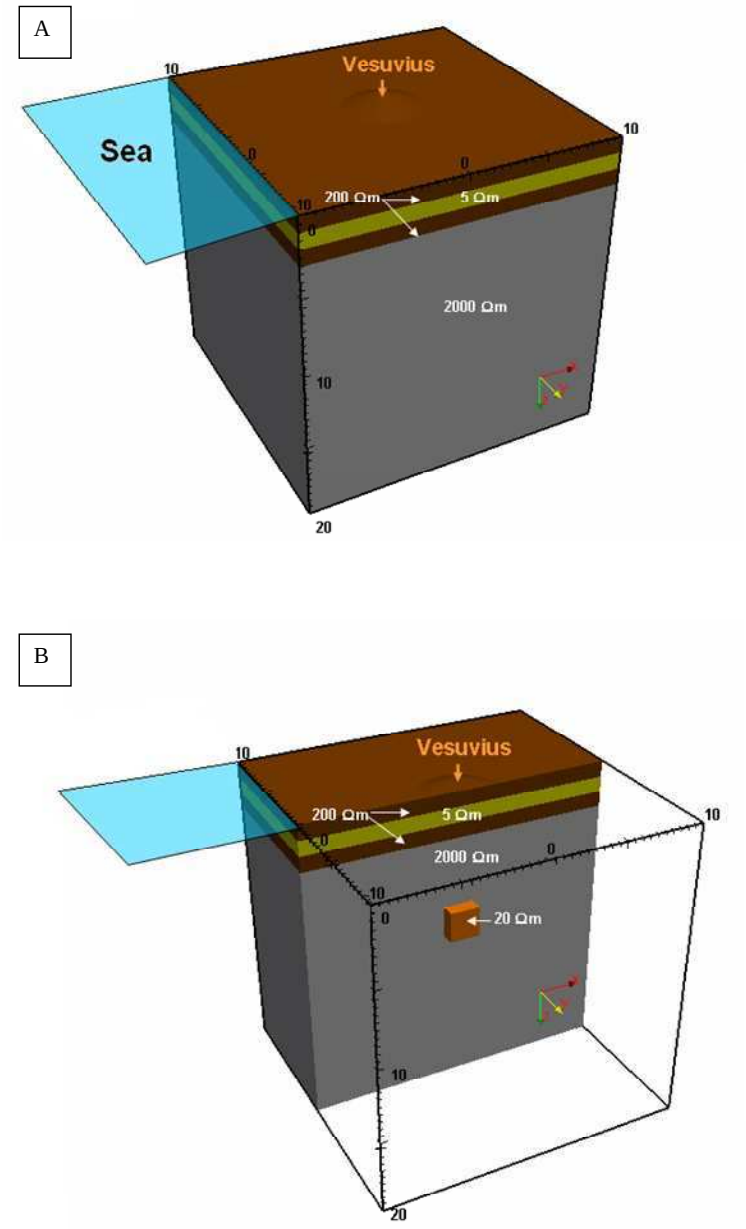


Figure 4: Example of 3-D model of the electrical resistivity distribution under Mount Vesuvius volcano. The figures on the cube edges are in km. A) External view of the model. Layers characteristics presented in Table 2. B) Cut in the middle of the structure, showing the presence of a magma chamber (8km^3, at 7.5km depth, with a resistivity of 20ohm.m). The sea was taken into account in the boundary conditions. Note that a homogeneous half space (20ohm.m) is placed at a depth >60km.

The inclusion of topography turned out to be numerically challenging. Edge points represented the main problem for modelling the topography when topographic steps were beside a site. We observed that the topography effect was essentially responsible for static shifts at the observation sites. We concluded that the corrections carried out by Manzella et al. (2004) were taking care of this problem. While this is probably a severe approximation, we did not find in the modelling any self induction of the static shift that could have biased the corrected response function of Manzella et al. (2004). These corrections have probably taken care of other superficial local static shift effects. We trust that the resulting corrected data are representative of the main induction processes in the volcano that may be modelled with a flat model. This hypothesis has to be tested further with a more complete set of data.

5. Results

The petro-physical 1-D model described in the previous section comprised volcanic deposits, the association carbonate-basement and the deep magma source (as half-space), their thickness and resistivity being listed in Tables 1 and 2. The electrical response of this initial model is presented in Figures 5a and 5b. This model clearly did not reproduce the observation. The data require a conductive layer, as suggested by Manzella et al. [2004]. With the addition of such a layer, the parameters (depth, thickness and resistivity) of the model were varied in order to fit the observed MT transfer functions. We introduced a shallow conductive layer and subsequently a 1-D and a 3-D conductive structure at a greater depth. The main parameters considered in the 3-D modelling were the depth, the volume and the resistivity value (i.e. the composition) of the deep conductive 3-D body.

5.1. Effect of a superficial conductor

The shallow conductive layer introduced in the 1-D model was set at depths ranging from a few hundreds m to a few km. The presence of a conductive layer resulted in a minimum in the apparent resistivity curve as well as a decrease in the impedance phase. The effect of the resistivity of this layer is presented in Figure 5a. This trend is observed in the data of both DiMaio [1998] et al and Manzella et al. [2004] at periods ~1-5s. For each site, the field data from Manzella et al. [2004] were successfully fitted when the top of the conductive layer is at 0.2 to 0.6km depth, with a resistivity of ~4-5ohm.m and a thickness ranging between 1 and 1.7km, depending on the site position (Figure 5b). These parameters did not change much from one site to the other. Hence, based on the layer models obtained for each

site, a general 1-D model of the electrical resistivity below Mt. Vesuvius was defined and is shown on Figure 5c. The superficial conductive layer represents the main conductive body below the volcano, since the field data are reproduced by its only presence. Note that the resistivity here is the effective resistivity described in the previous section.

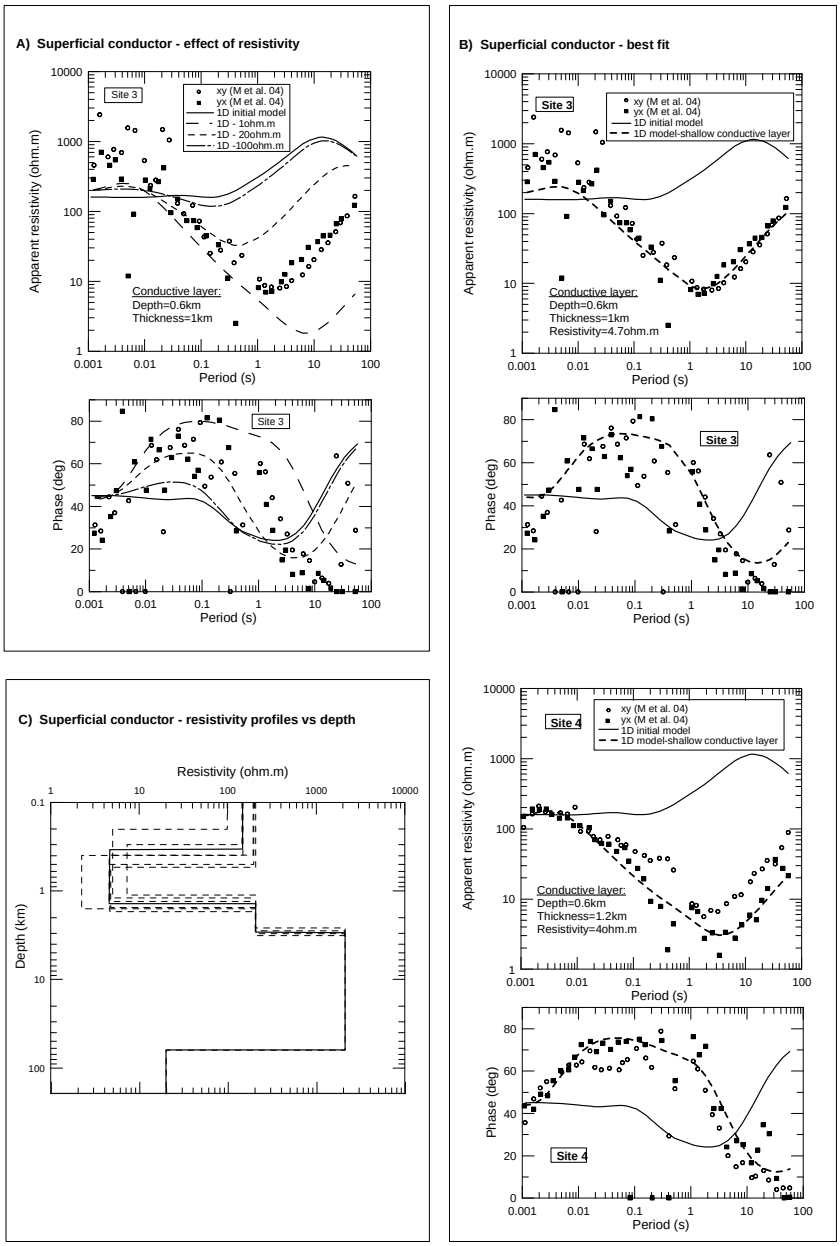


Figure 5: Effect of a superficial conductor on the transfert functions (1-D model) and comparison with the data from Manzella et al. [2004] (M et al. 04). A) Effect of the resistivity of a 1km-thick layer placed at a depth of 0.6km at site 3 in M et al. 04 (see Figure 2). Full line corresponds to the absence of a conductive layer in the model (initial model). B) Best fit to field data in Site 3 and Site 4, obtained with a about 1.1km-thick layer, at 0.6km depth and with a resistivity of 4.7 and 4ohm.m, respectively. C) Resistivity vs depths profiles (dashed lines) for each site in M et al. (04). The general 1-D model is represented by the full line.

5.2. Effect of a deep conductive body

Several 1-D simulations were performed to investigate the effect of a deep additional layer on the MT transfer functions. The shallow conductive layer was not included. The parameters were varied as follow: depth from 3 to 15km, thickness from 0.1 to 2km, resistivity from 0.3 to 2000ohm.m. These wide ranges of values allow to test numerous configurations of the deep structure below the volcano. The main results of these simulations are presented in Figure 6. In particular, several simulations were performed with a 20ohm.m-resistive layer placed at 8km depth, since these values are in agreement with the anomaly detected by DiMaio et al. [1998] as well with the value proposed for magma storage by seismic studies [Zollo et al., 1996; Auger et al., 2001].

As shown in Figure 6, the effect of the resistivity value of the layer is visible at periods >0.1s. The shape of the transfer functions is affected only for a $\rho_{\text{conductive layer}}$<~100ohm.m. For high resistivity values, the curves are similar to the one obtained with the initial model (i.e. with no additional layer, Figure 6a and b).

Increasing the depth of the conductive layer (20ohm.m) increases the apparent resistivity and the phase (Figure 6b). The curves obtained when placing a conductive body at great depths do not fit well the data, whatever the resistivity and thickness.

Increasing the thickness of the layer jointly decreases the apparent resistivity and increases the phase (Figure 6c). Increasing the thickness from 1 to 2km decreases the apparent resistivity from around 200ohm.m at T>2s and increases the phase of ~10° until 20s. Figure 6 underlines that a good fit to the field data is not achieved when a deep conductive layer alone is imposed in the initial model. Whatever the values of the parameters of the conductive layer, the presence of this single deep conductor does not allow to reproduce the MT data.

5.3. Joint effect of shallow and deep conductive bodies

Simulations with two conductive bodies placed respectively at shallow and large depths were performed using 1-D and 3-D simulations. The conditions on the shallow layer have been fixed according to the 1-D model presented in Figure 5c. The 3-D simulations serve principally to investigate the effect of the volume of the conductive deep reservoir on the transfer functions.

As shown on Figure 7, the effect of a deep conductive layer on the transfer functions, when a shallow conductive body is present in the model, is visible for periods > 1s. For example, a 1km-thick conductive layer placed at 5km depth with a very low resistivity (4ohm.m) has an effect at long periods on the apparent resistivity values < 60ohm.m and on

the phase values < 30°. A highly conductive deep body is therefore detectable in this period range on both the apparent resistivity and phase values.

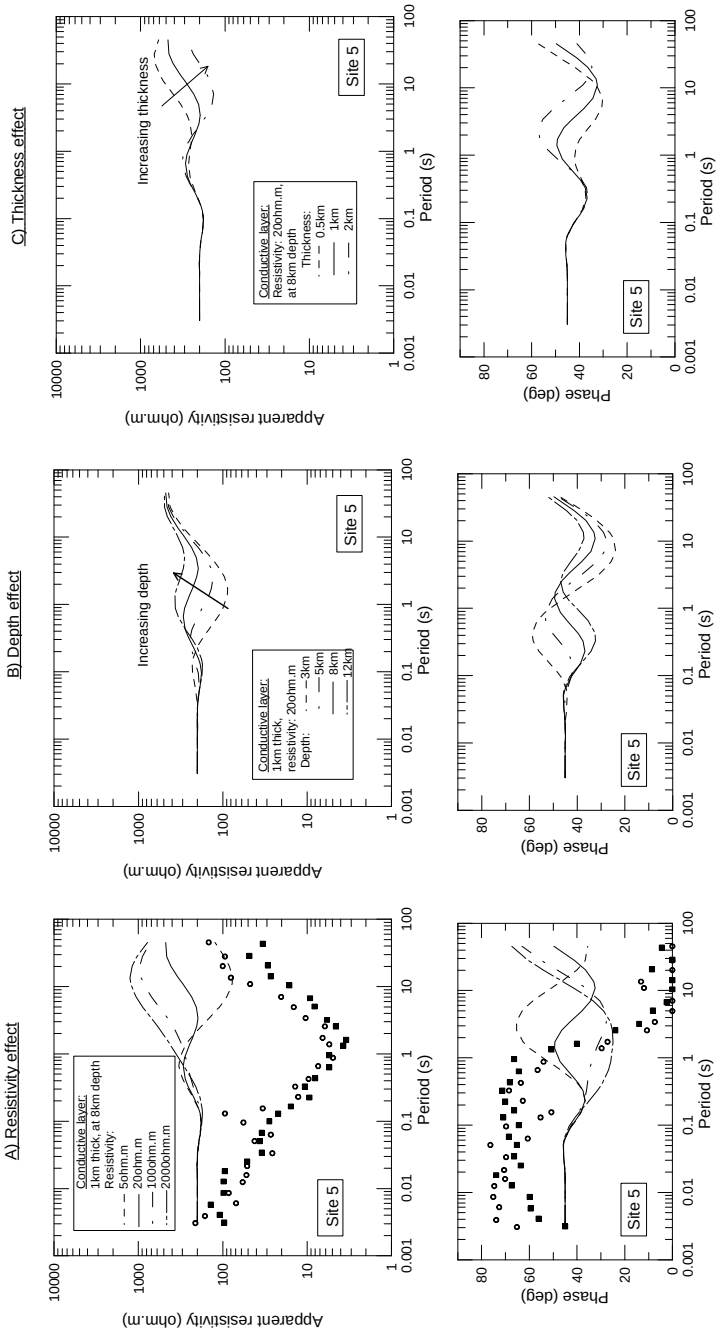


Figure 6: Effect of a deep conductor on the transfert functions (1-D model) (Site 5, M et al. 04). A) Resistivity effect of a deep 1km-thick conductor placed at 8km depth. Comparison with field response (xy (open circles) and yx curves (filled squares)) from Manzella et al. [2004] shows that the only presence of a deep conductor does not allow to reproduce the field response. B) Depth effect of a 1km-thick conductor with a resistivity of 20ohm.m, from 3 to 12km. C) Effect of the thickness of a 20ohm.m conductive body placed at 8km depth. In the three cases, the effect on the transfert functions is visible for periods >0.1s.

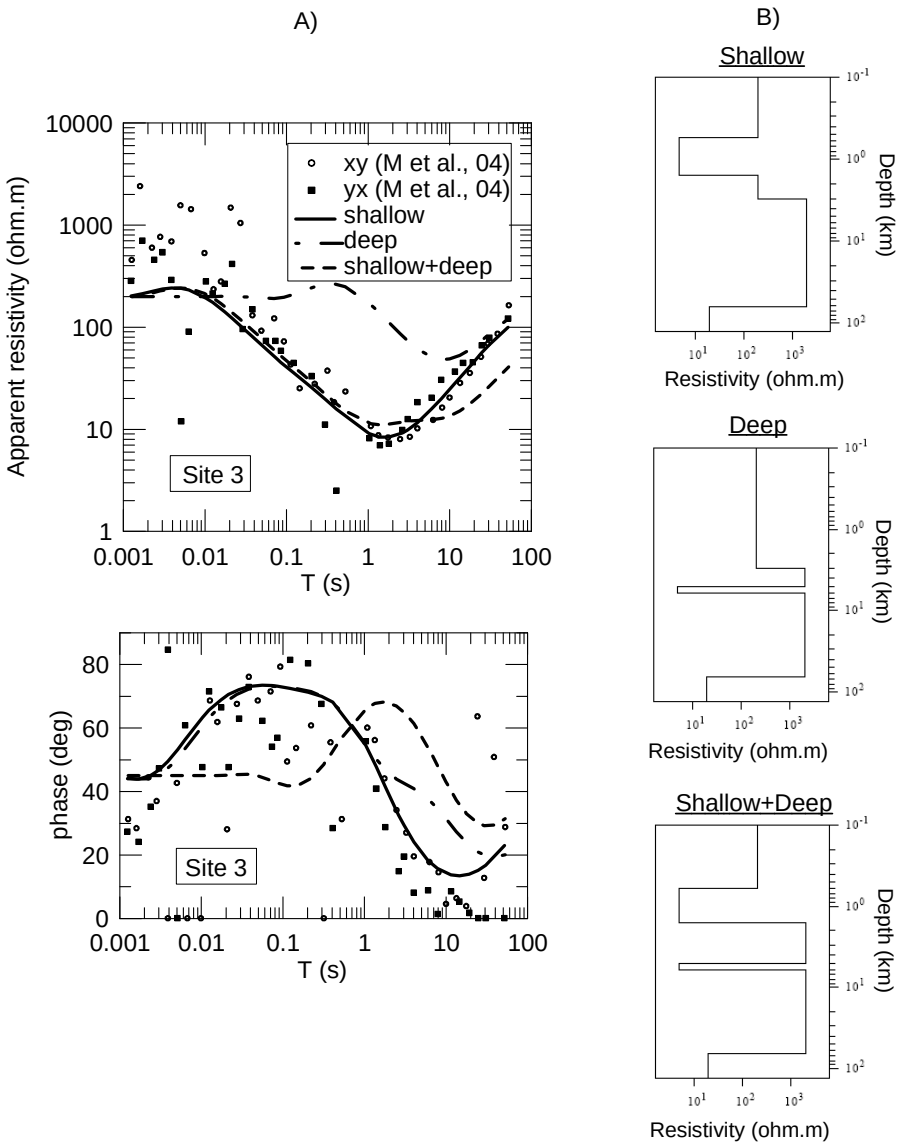


Figure 7: Joint effect of a shallow and a deep conductor on the transfert functions (1-D simulations). Both conductors have a 4ohm.m resistivity. A) Effect on the transfert functions and comparison with the field data from Manzella et al. [2004] (M et al., 04, Site 3). The field data are reproduced by the only presence of a shallow conductor. The addition of a deep conductive body has a small effect on the apparent resistivity and phase curves. B) Resistivity profiles vs depth for the three configurations tested in A) (shallow conductor, deep conductor and shallow and deep conductors), pointing out the resistivity, thickness and depth of the conductors.

The effect of the depth of this deep conductor (here 5ohm.m) is presented in Figure 8 for periods larger than 1s. A significant effect on the MT transfer functions is observed when changing the depth from 4 to 15km. In summary, the presence of an extended thin conductive layer simulating an infinite magma chamber impacts the MT transfer functions significantly at

the longest periods available and increases the misfit between the model response and the data in this period range.

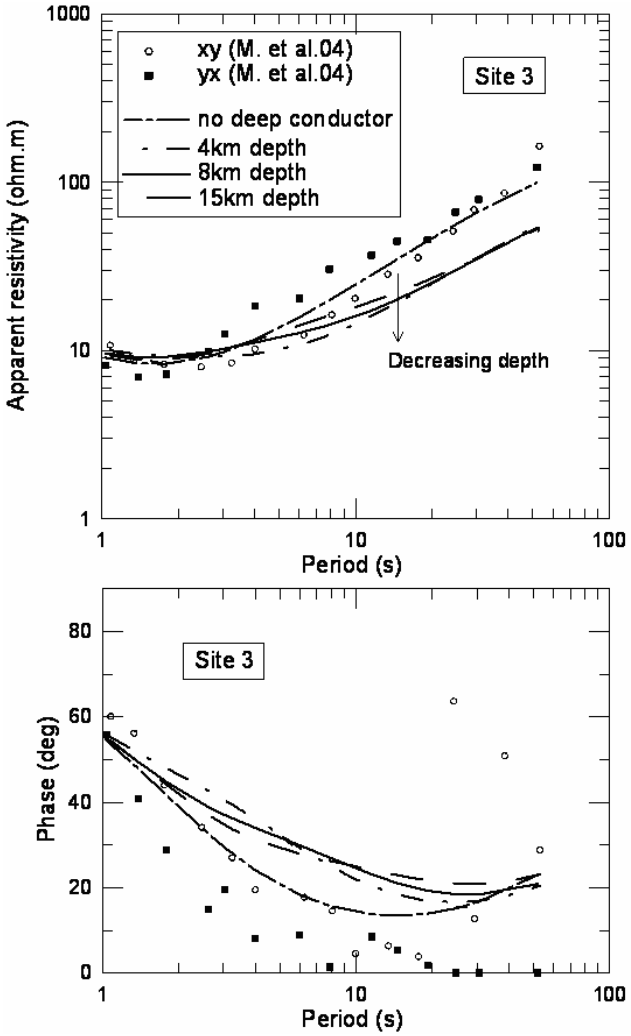


Figure 8: Effect of the depth of a deeper conductor in presence of a shallow conductive body (Site 3, Manzella et al. [2004]). Conditions of the shallow conductor correspond to the best fit in Figure 5 for Site 3 (resistivity of ~5ohm.m, 1km thick, 0.6km depth). Decreasing the depth decreases the apparent resistivity (narrow). Increasing the depth fits better the field data. For comparison, results with only a shallow conductor (no deep conductor) are presented.

Using a 3-D simulation, we tested the effect of the volume of a 20ohm.m conductor (in agreement with the resistivity value proposed by Di Maio et al. [1998]) of finite size located at 8km depth (as suggested by Auger et al. [2001]) on the MT transfer functions (Figure 9a). The highest differences in apparent resistivity and phase between a model with no deep reservoir and a model with a very extended 20ohm.m-resistive body (equivalent to a 1-D layer) reach a few tens of ohm.m and a few degrees, respectively, as noticed in Figure 8. When the body is of smaller size, a clear evidence between the two perpendicular response functions (xy and yx) is observed. The overall change in the apparent resistivity and phase is smaller than for the infinite case, nevertheless substantial. Figure 9b proposes another way to visualize and to explore the volume effect on the apparent resistivity. We present the apparent reistivity as a function of the deep reservoir volume for different periods. For all period, the

misfit is the smallest for small volume, excepted at 1s period at which no effect of the conductive body is visible (Figure 9a). Hence, the trend obtained suggests that a large magma chamber does not reproduce the field data well.

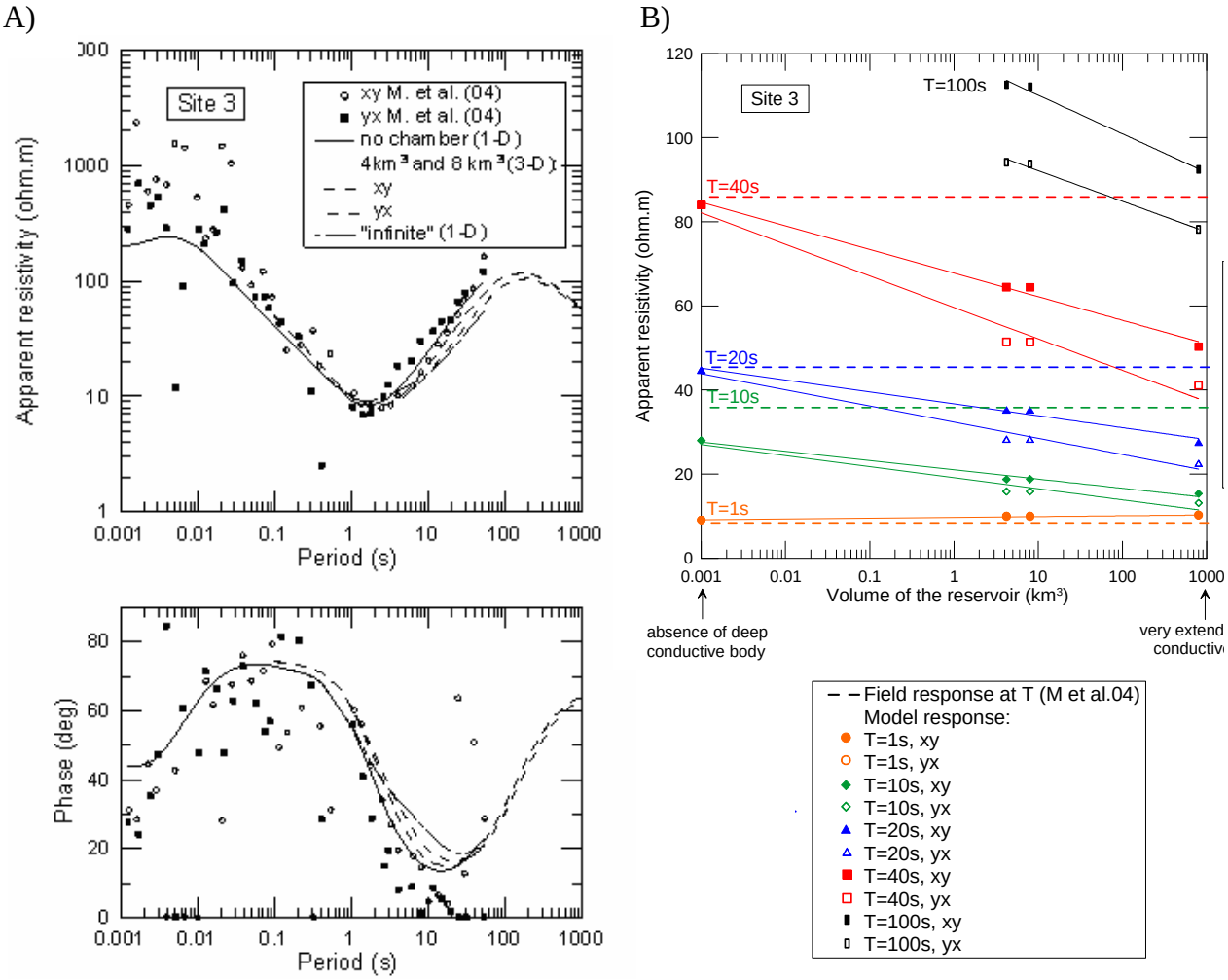


Figure 9: Effect of the volume of a deeper conductor in presence of a shallow conductive body (1-D and 3-D simulations). Same conditions on the shallow body as in Figure 8. A) Field and modelled transfert functions for Site 3 in Manzella et al. [2004]. The deep conductive body has a bulk resistivity of 20ohm.m, is placed at 8km depth and is 1km thick. Volumes were varied by changing in the x and y dimensions (see Figure 2 for spatial orientation). The curves are slightly affected by significant changes in volume reservoir (no visible differences between simulations with 4 and 8km^3). B) Apparent resistivity values from A) as a function of the volume of the reservoir for different periods. This kind of representation clearly suggests that a voluminous chamber do not provide the best fit to field data. Regression lines are just a guide for the eye.

Figure 10 presents the effect on the MT transfer functions of the electrical resistivity of an infinite (1-D) 2km thick deep conductor, placed at 8km depth (in agreement with Auger et al. [2001]). The misfit between the data and the model response increases significantly at long periods when the deep layer has a bulk resistivity smaller than ~100ohm.m). In Figure 9a, this was the 1-D infinite magma chamber that maximized the misfit. Here, for this end member case, the misfit is minimzed – or equivalently the best fit to the field data is obtained - with a resistive deep reservoir, with a bulk resistivity >~100ohm.m.

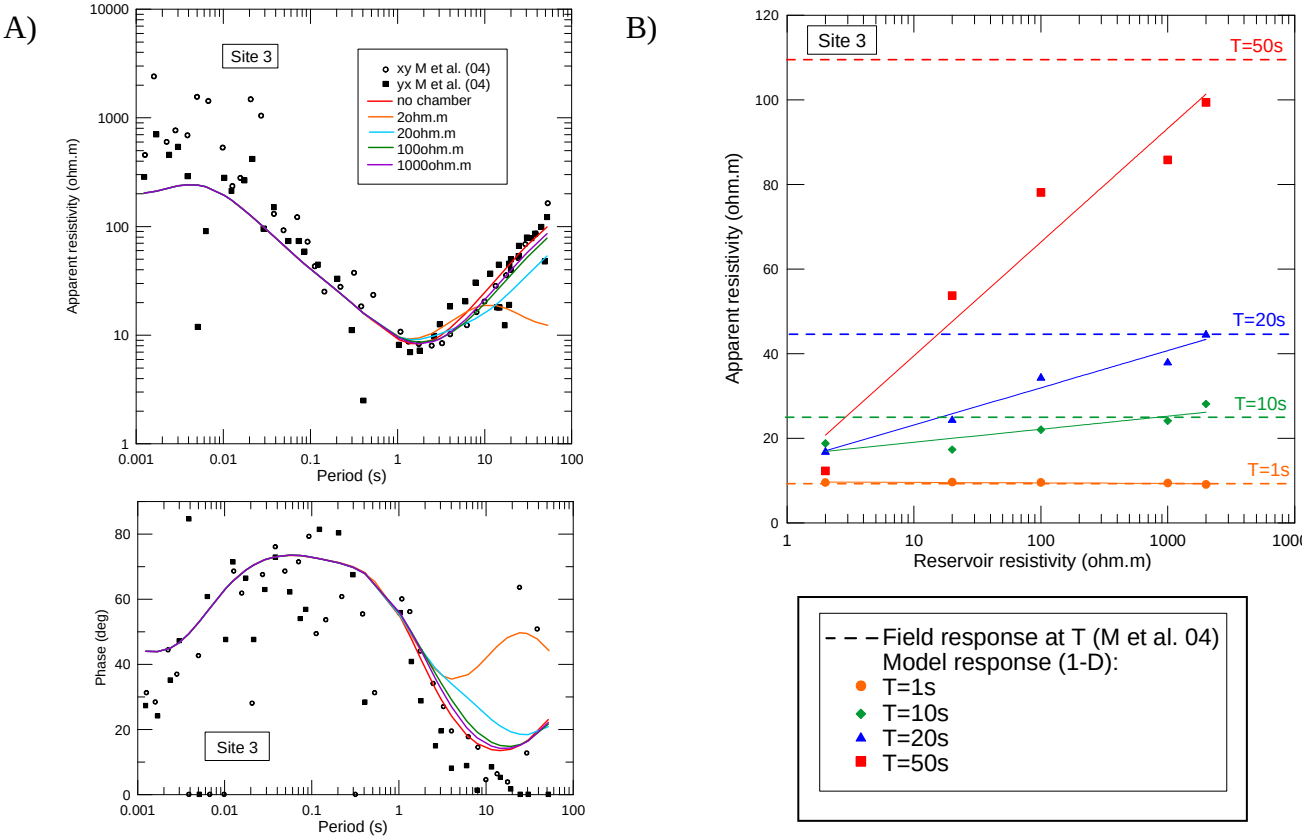


Figure 10: Effect of the resistivity of a deeper conductor in presence of a shallow conductive body (1-D simulations). Same conditions on the shallow body as in Figure 8. A) Field and modelled transfert functions for Site 3 in Manzella et al. [2004]. Deep conductive body placed at 8km depth and is 2km thick. No chamber simulation corresponds to a reservoir as resistive as the surrounding carbonates (ρ=2000ohm.m). A significant effect is observed on the field response for very conductive deep body. B) Apparent resistivity values from A) as a function of the bulk resistivity of the reservoir for four different periods. For periods >10s, the trend obtained suggest that high conductive deep body greatly affects apparent resistivities and thus does not reproduce the field response. Regression lines are just a guide for the eye.

6. Discussion

MT response functions provided by the 1-D and 3-D simulations reproduced successfully the field data. The presence of a shallow conductive structure at a depth <~2km proposed by Manzella et al. [2004] was confirmed. This conductor was observed beneath all sites and could indicate a highly conductive brine [Manzella et al., 2004]. While such a conductor should filter out appreciably the effect of the deep structures, our modelling based on geological and petro-physical constraints suggested that a large magma chamber at depths proposed by other geophysical investigations [e.g. Nunziata et al., 2006] should have produced a detectable signature at the longest periods available in the data set (1-200s). While data are limited in number and somewhat noisy, particularly for the MT phase, the effect of a large magma chamber is significantly above the noise level, especially on the apparent resistivity. At the proposed depth of ~8km [Zollo et al., 1998; Auger et al., 2001], the modelling provided a lower bound for the bulk (or effective) resistivity value of the magma chamber (~100ohm.m).

6.1. Shallow brine

The presence of gas-steam escaping at the summit of Mt Vesuvius suggests that a large amount of hot saline water is present at depth [Chiodini et al., 2001]. The gas-steam is probably of meteoric origin, as observed on other volcanic systems [e.g. Zimmer and Erzinger, 1998]. As suggested by Manzella et al. [2004], hot saline water would be responsible for the observed low resistivity detected by MT data. Our results are consistent with this result, since the MT field data are reproduced by the only presence of a shallow conductor with a resistivity of about ~4-5ohm.m (Figure 5) located at a depth <2km. The conductor depth is in agreement with the observations made by Chiodini et al., [2001] and Manzella et al. [2004]. Using a modified Archie's law [Glover et al., 2000], ~4-5ohm.m corresponds to a mixture of 98% volcanic deposits and 2% NaCl solution (2-3m in concentration, 450°C, Table 1 and 2). The salinity of this hot shallow aquifer provides a sufficient amount of conducting material to explain the modelled bulk conductivity. Hydrothermal brine is likely to cause the high conductivity detected in the transfer functions, thus representing the main present-day conductive body below Mt. Vesuvius.

The large thickness of the brine determined in the forward layer model (~1.2km thick, Figure 5c) is consistent with what has been detected on other volcanic edifices. For instance, 1km-thick brines with resistivities <10ohm.m have been also inferred at Mount Unzen

[Kagiyama et al., 1999], Merapi [Müller and Haak, 2004], and Mount Fuji [Aizawa et al., 2005] volcanoes. The presence of such a thick brine may be explained by the fact that meteoric and hydrothermal fluids probably circulate during several tens of thousand years in the shallow depths of the volcanic structure.

6.2. A magma chamber at shallow depth (<3-4km) ?

6.2.1. The case for a shallow magma chamber

The hypothesis of a shallow magma reservoir originates from the documented decrease of the magma chamber depth with time [Scaillet et al., 2008] and by the fact that small shallow reservoirs located at ~2-4km depth were involved in the last eruptive events (1906 and 1944 eruptions), [Santacroce et al., 1993; Marianelli et al., 1999; Scandone et al., 2008]. It has been underlined that the shallower the reservoir, the hotter the erupted magma [Scaillet et al., 2008]: pre-eruptive magma temperature for the eruptions of 1906 and 1944 (reservoir depth at about 2km) is estimated at 1100°C [e.g. Fulignati et al., 2004b], while for the Pompei eruption (reservoir depth at about 6-8km), it is at 815°C (Cioni et al., 1995; Scaillet et al., 2008]. The resistivity of a shallow magma can be very low and would thus fit well into the ~4-5ohm.m-resistive structure present at shallow depths (Figure 5c). Pommier et al. [2008] have shown that Mount Vesuvius magmas can be as conductive as a brine. For example, the resistivity of tephritic to phonolitic magmas under specific conditions ranges between ~1 and 5ohm.m at 1000°C, for typical magmatic crystal contents at Mt Vesuvius (Figure 1).

The volumes of the shallow magma chambers at Mt. Vesuvius have been estimated to be a few tenths of km^3 [e.g. Santacroce, 1987], corresponding to a cube smaller than $\sim 3.10^7 m^3$. Seismic studies also have suggested that potential shallow reservoirs of significant size are unlikely [Bianco et al., 1998; Lomax et al., 2001]. Such a small conductive body could explain the minimum in apparent resistivity and the decrease in phase curves for observation sites close to the center of the volcano. However, it would be unable to reproduce the similar transfer functions obtained at sites far from the crater, like Sites 3 and 4 in DiMaio et al. [1998] (see Figure 2). Therefore, we suggest that a brine of large lateral extension is the main conductive shallow body below Mt. Vesuvius. This does not rule out the possibility that a cold magma body is present at shallow depths below the volcano. However, any such body should be sufficiently resistive so as not to affect significantly the transfer functions obtained at sites close to the crater.

6.2.2. Unerupted magmas from the 1631-1944 period

Several studies have suggested that no input of fresh magma at shallow depths occurred after the end of the last eruptive event [Chiodini et al., 2001; DeNatale et al., 2004]. The 1631-1944 period probably left unerupted magmas shallow in the volcanic edifice, which are probably the thermal source of the hydrothermal brines. As suggested by Chiodini et al. [2001], the observed decrease in the temperature of the crater fumaroles (from ~700 to 95°C between 1944 and the present time) is best explained by the progressive cooling of shallow magma bodies. These residual batches could correspond to the shallow bodies evidenced in the gravity study of Berrino et al. [1998] since they have a lower density than the density of the surrounding volcanic deposits (2100 and 2400kg/m^3, respectively). With progressive cooling, the resistivity of the magma increases, as modelled by Pommier et al. [2008] and as observed on other volcanoes [e.g. Matsushima et al., 2001]. The bulk resistivity of cooling magma batches at Mt. Vesuvius would thus be higher than ~4-5ohm.m. For example, a hydrous tephriphonolitic magma (3.5wt%H_2O) containing 80vol.% crystals (leucite and clinopyroxene) at 700°C has a resistivity of ~200ohm.m, which is within the range of resistivity of the volcanic deposits (~100-300ohm.m). These cooling magma batches would be hardly detectable by the MT soundings (irrespective from their size).

6.3. Possible deep (>3-4km) magma chamber beneath Mount Vesuvius

As underlined in Figure 7, the presence at shallow depths of the high conductive brine is probably responsible for a screen effect that makes detection of deeper conductive bodies difficult. Deep anomalies below a superficial conductive layer are detectable by the MT method in volcanic contexts [e.g. Whaler and Hautot, 2006; Umeda et al., 2006]. However, their detectability requires a large volume (several tens of km^3) of very conductive magma (ρ<10ohm.m). A crystal-rich magma body would be difficult to detect at Mt. Vesuvius because of a low resistivity contrast with the surrounding carbonates. As suggested by Figure 9a, it would also be difficult to detect a small magma chamber below the conductive superficial brine even if the magma resistivity is low. The volume of the magma chambers located at depths ≥3-4km that fed the Pollena and Pompei eruptions was estimated to be a few km^3 [Rosi et al., 1987]. More generally, the maximum volume of magma chambers for the past eruptions during the last 20kyrs is a few km^3 [e.g. Santacroce, 1983]. Considering a mean alimentation rate at Mt Vesuvius of 1.6.10^{-3}km^3/yr, in agreement with the estimation made by Rosi et al. [1987], a volume of fresh magma could be stored since 1944 eruption of 0.104km^3.

Since a conductive body below the brine is hardly detectable (Figure 7), these small volumes of magma will only slightly affect the transfer functions. Therefore, even considering the hypothesis of an input of fresh magma, the MT response functions would not significantly change because the volume of hot magma would be very small.

From the forward model simulations, we inferred that a very large and hot magma chamber, of an extension much larger than the size of Mt Vesuvius cone, is not likely. As shown in Figure 9b, such a reservoir does not provide the best fit to the data. This conclusion contrasts with the interpretation of several seismic experiments [Zollo et al., 1996, 1998; Auger et al., 2001; Nunziata et al., 2006] that suggest the presence of an extended (>400km^2 and 1-2km thick, according to Auger et al. [2001]) low-velocity layer at 8-10km depth. However, both lateral and vertical extensions of the deep anomaly are difficult to constrain from seismic data, as stressed by Zollo et al. [1998]. Our simulation results are consistent with the gravimetric observations from Berrino et al. [1998] and Berrino and Camacho [2008] that did not detect a potentially extended magma reservoir below Mt Vesuvius. It is likely that a large deep anomaly would affect gravimetric profiles, since the density of molten magma (<2,480kg/m^3, Cassano and LaTorre, 1987) is significantly lower than that of the surrounding carbonates (2,600-2,800kg/m^3, Berrino et al., 1998). The deep anomalies detected by gravimetric studies were interpreted as solidified magma bodies [De Natale et al., 2004; Berrino and Camacho, 2008]. More generally, we note that the unlikely presence of an extended hot magma reservoir also represents a case against a potential interconnection of Mt Vesuvius and Phlegrean Fields feeding systems.

Our forward model has shown that field data are reproduced by the sole presence of the superficial brine and that the presence of a deep conductor does not significantly improve the fit to the field data (Figure 7). However, the model is also compatible with the presence of a deep level of magma storage. The field response is indeed still reproduced when a resistive reservoir is placed at depth, as long as the bulk electrical resistivity of the magma storage zone is >100ohm.m (Figure 10). Using the modified Archie's law (Eq. 1) and the Hashin-Shtrikman formalism [Glover et al., 2000; Hashin and Shtrikman, 1962], a resistive anomaly >100ohm.m allows two hypotheses to be envisaged (Figure 11). A first hypothesis considers the presence of a waning chamber. According to the model of Pommier et al., [2008], a magma resistivity >100ohm.m would correspond to phonolitic or tephriphonolitic melts at 800°C, with 6 or 4wt%H_2O respectively, and with a crystal content (clinopyroxene) >80%vol. It would thus be consistent with a low-temperature, crystal-rich magma chamber. This deep reservoir could be in the final stage of solidification, i.e. hardly or not eruptable. A second

hypothesis considers the presence of a deep growing magma chamber. In this case, the magmatic system would be composed of a magma with a crystal content that matches pre-eruptive conditions (i.e. 20-30% crystals, Figure 1), interconnected in the more resistive carbonates. The quantity of magma requested to match a bulk resistivity value of 100ohm.m corresponds for example to ~30% of a tephriphonolitic magma (800°C, 4wt%H_2O, 25vol.%crystals) interconnected in 70% carbonates or to ~2% of the same magma at 1000°C (fully liquid) interconnected in 98% carbonates [Glover et al., 2000; Pommier et al., 2008].

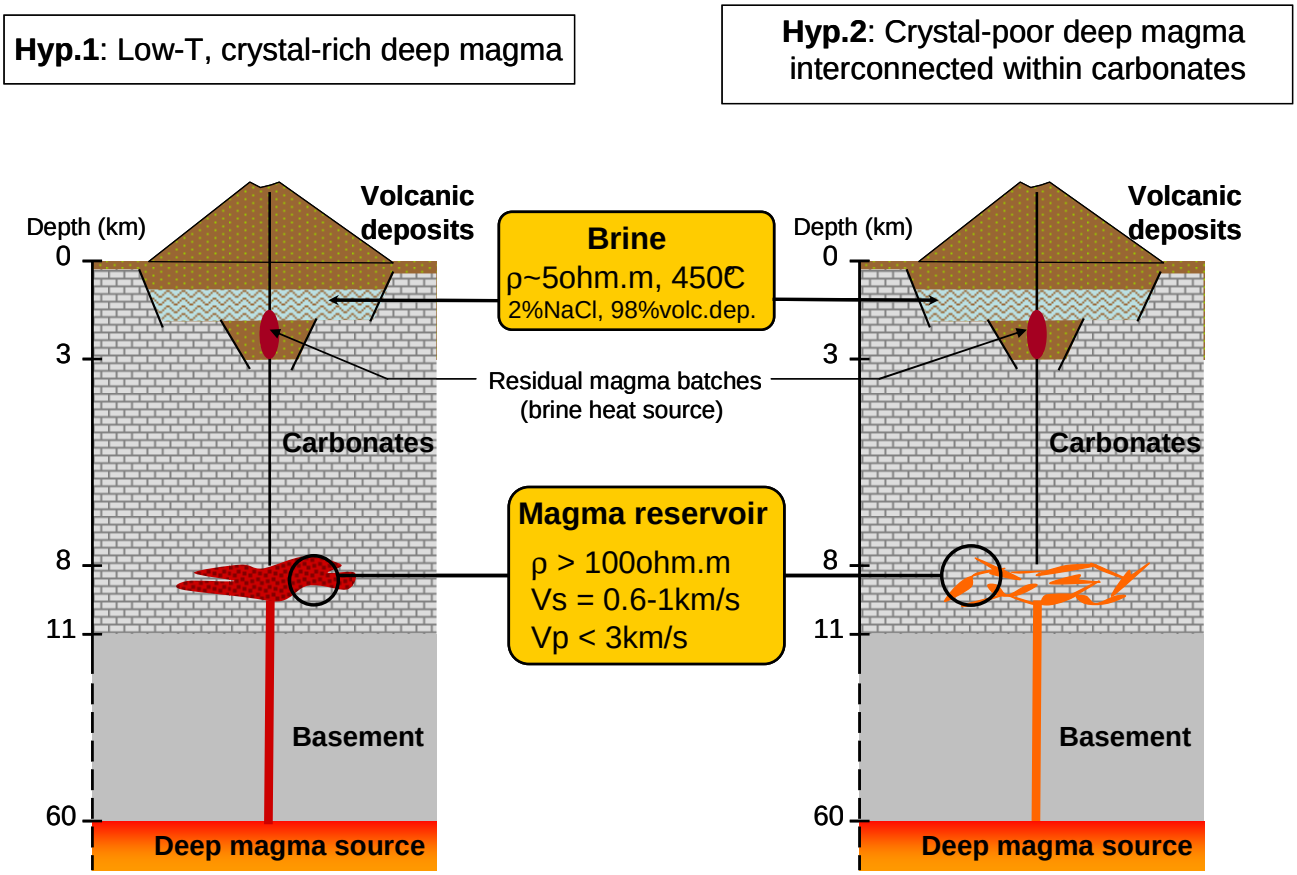


Figure 11: Possible scenarios concerning the presence of a deep magma chamber below Mt. Vesuvius based on the results from the forward modelling of the resistivity and petrological and geophysical constraints. A first hypothesis (Hyp.1) considers a low-temperature and crystal-rich magma. The second hypothesis (Hyp. 2) explains the deep geophysical anomaly by the presence of a hot (crystal-poor) magma interconnected within the surrounding carbonates. Models relating the seismic wave velocities to magma structure and properties [Mainprice, 1997] support Hyp.2. See text for details.

6.4. Comparison with seismic studies

As mentioned above, the results from our simulations are compatible with a low-conductive reservoir whose depth is in agreement with the depth of the anomaly detected by seismic studies (8-10km) [Zollo et al., 1996, 1998; Auger et al., 2001]. However, our study would tend to suggest that the reservoir size is probably smaller than the size proposed by seismic interpretations. Still, P and S waves values depend on the material properties and can thus be compared to the two hypotheses regarding magma storage conditions formulated on the basis of our model (Figure 11). The low-velocity zone, interpreted as a partially molten layer [Zollo et al., 1996, 1998; Auger et al., 2001, Nunziata et al., 2006], is characterized by Vs values of about 0.6-1km/s and Vp values <3km/s. Since the seismic properties depend on the composition and microstructure of melt and crystals, models have been proposed to relate seismic waves to properties of partially molten rocks, principally based on the effective media theory [Mainprice, 1997; Taylor and Singh, 2002]. We have considered the two hypotheses presented in Figure 11. According to the models from Mainprice [1997] and Taylor and Singh [2002], a reservoir filled with a liquid matrix and solid inclusions (crystals) (hypothesis #1, Figure 11) would have Vp values well above 3km/s, which is not in agreement with the Vp values measured in seismic studies.

We considered the model of Mainprice [1997] to test hypothesis #2. Based on Vs and Vp values, this model provides an estimation of the fraction of a low-polymerized melt at 1200°C connected in a denser rock matrix at 6-8km depth. However, petrological studies have shown that Mt Vesuvius magmas stored at these depths probably have lower temperatures, (800°C-1100°C) (Table 1). Laboratory seismic studies have underlined that decreasing the melt temperature increases Vs and Vp values [e.g. Caricchi et al., 2008]. Seismic models also suggest that S and P-waves values will be unchanged if the fraction of a colder melt decreases. According to the study of Caricchi et al. [2008] and the model of Mainprice [1997], the Vs and Vp values recorded below Mt Vesuvius appear to be in agreement with >50% of melt stored at 1200°C interconnected in <50% of carbonates (rock matrix). Since such an anomaly has a minimum bulk electrical resistivity of 100ohm.m, a minimum resistivity of the melt of about 50ohm.m is calculated using the modified Archie's law. This resistivity range is in agreement with a primitive K-basaltic magma near liquidus containing 3wt%H_2O [Pommier et al., 2008]. For melt temperatures lower than ~1100°C, the field value of Vs is in agreement with a greater melt fraction (and, thus, a smaller carbonate proportions), while the field value of Vp is too low to be reproduced by the seismic model of Mainprice

[1997]. For instance, the Vs value (0.6-1km/s) is in agreement with >60% of melt stored 800°C and <40% carbonates but the Vp value (<3km/s) corresponding to these conditions is estimated to be >4km/s. Hence, when considered together, the results from both magnetotelluric and seismic studies suggested that the deep geophysical anomaly is due to a hot magma interconnected in the surrounding carbonates.

7. Conclusions

A model of the electrical resistivity of Mt. Vesuvius has been elaborated using the available electrical measurements in laboratory, geophysical data and petrological constraints. This model reproduces successfully the field data from magnetotellurics studies. The shallow brine is identified as the main conductive body beneath the volcano since its only presence allows to reproduce the field transfer functions. Regarding the occurrence of a shallow magma reservoir, the presence of cooling magma is found to be possible, whereas the hypothesis of a hot magma appears unlikely, although it can not be totally excluded. Both 1-D and 3-D simulations show that the resistivity of a conductive reservoir located at 8-10km depth should be >100ohm.m. The model would also tend to suggest that the volume of the reservoir is unlikely to extend spatially well beyond the cone dimensions. Our findings suggest that the deep anomaly detected by geophysical studies corresponds to either a low-temperature and crystal-rich magma or a hotter magma interconnected within the surrounding carbonates. A comparison with seismic wave velocity values, using seismic models to interpret wave velocities in terms of magma structure, tends to favour the second hypothesis. The quantity and the quality of MT data at Mt Vesuvius are nevertheless the main limit to the forward modelling, underlining the need for the acquisition of new MT measurements on Mt Vesuvius, particularly at periods >100s and with a higher resolution. The acquisition of data at these periods would allow to place constraints on the deep magma feeding system.

Acknowledgements

This study is part of the PhD of A. Pommier. The ISTO group thanks A. Siniscalchi and Z. Petrillo for having answered to solicitations at the beginning of this study. This study has been supported by the French national agency for research, ANR JC05-42707 (Electrovolc) attributed to F. Gaillard. MTInv is a free geophysical software by M. Pirttijärvi's (http://www.cc.oulu.fi/~mpi/Softat/).

References

Aizawa, K., R. Yoshimura, N. Oshiman, K. Yamazaki, T. Uto, Y. Ogawa, S.B. Tank, W. Kanda, S. Sakanaka, Y. Furukawa, T. Hashimoto, M. Uyeshima, T. Ogawa, I. Shiozaki, A.W. Hurst (2005), Hydrothermal system beneath Mt. Fuji volcano inferred from magnetotellurics and electric self-potential, *Earth Planet. Sci. Lett.*, 235(1-2), 343-355.

Arnò V., C. Principe, M. Rosi, R. Santacroce, A. Sbrana, and M.F. Sheridan (1987), Eruptive history. In: Santacroce, R. (Ed.), Somma–Vesuvius. *Quad. Ric. Sci*., vol. 114, pp. 53–103.

Auger, E., P. Gasparini, J. Virieux, and A. Zollo (2001), Seismic evidence of an extended magmatic sill under Mt. Vesuvius, *Science*, *294*(5546), 1510–1512, doi:10.1126/science.1064893.

Ayuso, R. A., B. De Vivo, G. Rolandi, R. R. Seal, and A. Paone (1998), Geochemical and isotopic (Nd-Pb-Sr-O) variations bearing on the genesis of volcanic rocks from Vesuvius, Italy, *J. Volcanol. Geotherm. Res.*, *82*(1–4), 53–78, doi:10.1016/S0377-0273(97)00057-7.

Balcone-Boissard, H., B. Villemant, G. Boudon, and A. Michel (2008), Non-volatile vs volatile behaviours of halogens during the AD79 plinian eruption of Mt. Vesuvius, Italy, *Earth Planet. Sci. Lett*., 269(1-2), 66-79.

Berrino, G., G. Corrado, and U. Riccardi (1998), Sea gravity data in the Gulf of Naples: a contribution to delineating the structural pattern of the Vesuvian area, *J. Volcanol. Geotherm. Res.*, 82, 139-150.

Berrino, G., and A.G. Camacho (2008), 3D Gravity Inversion by Growing Bodies and Shaping Layers at Mt. Vesuvius (Southern Italy), *Pure Appl. Geophys*., 165, 1095–1115.

Bianco, F., M. Castellano, G. Milano, G. Ventura, and G. Vilard (1998), The Somma–Vesuvius stress field induced by regional tectonics: evidences from seismological and mesostructural data, *J. Volcanol. Geotherm. Res.*, 82(1-4), 199-218.

Brocchini, D., C. Principe, D. Castradori, M.A. Laurenzi and L. Gorla (2001), Quaternary evolution of the southern sector of the Campanian Plain abd early Somma-Vesuvius activity: insights from the Trecase 1 well, *Mineral. and Petrol*., 73(1-3), 67-91.

Bruno, P.P.G., G. Cippitelli, and A. Rapolla (1998), Seismic study of the Mesozoic carbonate basement around Mt. Somma–Vesuvius, Italy, *J. Volcanol. Geotherm. Res.*, 84, 311-322.

Caliro, S., G. Chiodini, R. Avino, C. Cardellini, F. Frondini (2005), Volcanic degassing at Somma–Vesuvio (Italy) inferred by chemical and isotopic signatures of groundwater, *Applied Geochem.*, 20(6), 1060-1076.

Caricchi, L., L. Burlini, and P. Ulmer (2008), Propagation of P and S-waves in magmas with different crystal contents: Insights into the crystallinity of magmatic reservoirs, *J. Volcanol. Geotherm. Res.*, 178 (4), 740-750.

Cassano, E. and P. La Torre (1987) Geophysics. In: Santacroce, R. (Ed.), Somma–Vesuvius. *Quad. Ric. Sci.*, vol. 114, 103-131.

Cella, F., M. Fedi, G. Florio, M. Grimaldi, and A. Rapolla (2007), Shallow structure of the Somma–Vesuvius volcano from 3D inversion of gravity data, *J. Volcanol. Geotherm. Res.*, 161, 303-317.

Chiodini, G., L. Marini, and M. Russo, Geochemical evidence for the existence of high-temperature hydrothermal brines at Vesuvio volcano, Italy, *Geochim. Cosmochim. Acta*, *65(13), 2129-2147.*

Cioni, R., L. Civetta, P. Marianelli, N. Metrich, R. Santacroce, and A. Sbrana (1995), Compositional layering and syn-eruptive mixing of a periodically refilled shallow magma chamber: The AD 79 Plinian eruption of Vesuvius, *J. Petrol.*, *36*(3), 739–776.

Cioni, R., P. Marianelli and R. Santacroce (1998) Thermal and compositional evolution of the shallow magma chambers of Vesuvius: Evidence from pyroxene phenocrysts and melt inclusions, *J. Geophys. Res.*, 103, B8, 18277-18294.

Cioni R., R. Santacroce, and A. Sbrana (1999), Pyroclastic deposits as a guide for reconstructing the multi-stage evolution of the Somma-Vesuvius caldera, *Bull. Volcanol.*, 60, 207–222.

Civetta, L., and R. Santacroce [1992], Steady state magma supply in the last 3400 years of Vesuvius activity, *Acta Vulcanol*., 2, 147-159.

Civetta, L., M. D'Antonio, S. de Lorenzo, V. di Renzo, and P. Gasparini (2004), Thermal and geochemical constraints on the 'deep' magmatic structure of Mt. Vesuvius, *J. Volcanol. Geotherm. Res.*, 133, 1-12.

DeMatteis, R., D. Latorre, A. Zollo, and J. Virieux (2000), 1D P-velocity models of Mt. Vesuvius volcano from the inversion of TomoVes96 first arrival time data. *Pure Appl. Geophys*., 157, 1643-1661.

De Natale, G., S. Petrazzuoli, C. Troise, F. Pingue, and P. Capuano, (2000), Internal stress field at Mount Vesuvius : a model for background seismicity at a central volcano. *J. Geophys. Res.*, 105 (B7), 16207-16214.

DeNatale, G., C. Troise, R. Trigila, D. Dolfi, and C. Chiarabba (2004), Seismicity and 3-D substructure at Somma–Vesuvius volcano: evidence for magma quenching, *Earth Planet. Sci. Lett.*, 221(1-4), 181-196.

DeNatale, G., C. Troise, F. Pingue, G. Mastrolorenzo, and L. Pappalardo (2006), The Somma–Vesuvius volcano (Southern Italy): Structure, dynamics and hazard evaluation, *Earth-Science Reviews*, 74(1-2), 73-111.

Di Maio, R., P. Mauriello, D. Patella, Z. Petrillo, S. Piscitelli, and A. Siniscalchi (1998), Electric and electromagnetic outline of the Mount Somma-Vesuvius structural setting, *J. Volcanol. Geotherm. Res.*, *82*(1–4), 219–238, doi:10.1016/S0377-0273(97)00066-8.

Di Renzo, V., M.A. Di Vito, I. Arienzo, A. Caradente, L. Civetta, M. D'Antonio, F. Giordano, G. Orsi and S. Tonarini (2007) Magmatic history of Somma-Vesvius on the basis of new geochemical and isotopic data from a deep borehole (Camaldoli della Torre), *J. Petrol.*, 48(4), 753-784.

Ferrucci, F., G. Gaudiosi, N.A. Pino, G. Luongo, A. Hirn, and L. Mirabile (1989), Seismic detection of a major Moho upheaval beneath the Campania volcanic area (Naples, Southern Italy), *Geophys. Res. Lett*., 16, 1317-1320.

Fulignati, P., P. Marianelli, R. Santacroce, and A. Sbrana (2004a), Probing the Vesuvius magma chamber–host rock interface through xenoliths, *Geol. Mag.*, *141*(4), 417–428, doi:10.1017/S0016756804009392.

Fulignati, P., P. Marianelli, N. Métrich, R. Santacroce, and A. Sbrana (2004b), Towards a reconstruction of the magmatic feeding system of the 1944 eruption of Mt Vesuvius, *J. Volcanol. Geotherm. Res.*, *133*, *13-22.*

Glover, P. W. J., M. J. Hole, and J. Pous (2000), A modified Archie's law for two conducting phases, *Earth Planet. Sci. Lett.*, *180*(3–4), 369–383, doi:10.1016/S0012-821X(00)00168-0.

Hashin, Z., and S. Shtrikman (1962), On some variational principles in anisotropic and nonhomogeneous elasticity, *J. Mech. Phys. Solids*, 10, 335-342.

Hautot, S., R. T. Single, J. Watson, N. Harrop, D. A. Jerram, P. Tarits, K. Whaler, and G. Dawes (2007), 3-D magnetotelluric inversion and model validation with gravity data for the investigation of flood basalts and associated volcanic rifted margins, *Geophys. J. Int*.,170, 1418–1430.

Iacono-Marziano, G., F. Gaillard, and M. Pichavant (2008), Limestone assimilation by basaltic magmas: an experimental re-assessment and application to Italian volcanoes, *Contrib. Mineral. Petrol.*, 155, 719-738.

Iacono-Marziano, G., F. Gaillard, B. Scaillet, M. Pichavant, and G. Chiodini (2009), Role of non-mantle CO2 in the dynamics of volcano degassing: The Mount Vesuvius example, *Geology*, G25446.

Joron, J.L., N. Métrich, M. Rosi, R. Santacroce, and A. Sbrana (1987), Chemistry and petrography, In: Santacroce, R. (Ed.), Somma–Vesuvius. Quad. Ric. Sci, vol. 114, 197-234.

Kagiyama, T., H. Utada, T. Yamamoto (1999), Magma ascent beneath Unzen Volcano, SW Japan, deduced from the electrical resistivity structure, *J. Volcanol. Geotherm. Res., 89(1-4*), *35-42.*

Lomax, A., A. Zollo, and P. Capuano (2001), Precise, absolute, earthquake location under Somma Vesuvius using a new 3D velocity model, *Geophys. J. Int.* 146, 316-331.

Mackie, R.L., T.R. Madden, and P.E. Wannamaker (1993), Three-dimensional magnetotelluric modeling using difference equation – Theory and comparisons to integral equation solutions, *Geophysics*, 58, 215-226.

Mainprice, D. (1997), Modelling the anisotropic seismic properties of partially molten rocks found at mid-ocean ridges, *Tectonophysics, 279(1-4), 161-179.*

Manzella, A., G. Volpi, A. Zaja, and M. Meju (2004), Combined TEM-MT investigation of shallow-depth resistivity structure of Mt. Somma-Vesuvius, *J. Volcanol. Geotherm. Res.*, *131*(1–2), 19–32, doi:10.1016/S0377-0273(03)00313-5.

Marianelli, P., N. Metrich, A. Sbrana (1999), Shallow and deep reservoirs involved in magma supply of the 1944 eruption of Vesuvius, *Bull. Volcanol*., 61, 48-63.

Marzocchi, W., R. Scandone, and F. Mulargia (1993), The tectonic setting of Mount Vesuvius and the correlation between its eruptions and the earthquakes of the Southern Apennines, *J. Volcanol. Geotherm. Res.*, 58, 27-41.

Matsushima, N., H. Oshima, Y. Ogawa, S. Takakura, H. Satoh, M. Utsugi, Y. Nishida, Magma prospecting in Usu volcano, Hokkaido, Japan, using magnetotelluric soundings, *J. Volcanol. Geotherm. Res.*, 109, 263-277.

Müller, M., A. Hordt, and F.M. Neubauer (1999), Electromagnetic technique's success at Vesuvius points to use in forecasting eruptions, *EOS Trans*., 80, 393-401.

Müller, A., and V. Haak (2004), 3-D modeling of the deep electrical conductivity of Merapi volcano (Central Java): integrating magnetotellurics, induction vectors and the effects of steep topography, *J. Volcanol. Geotherm. Res., 138(3-4), 205-222.*

Nunziata, C., M. Natale, G. Luongo, and G. F. Panza (2006), Magma reservoir at Mt. Vesuvius: Size of the hot, partially molten, crust material detected deeper than 8 km, *Earth Planet. Sci. Lett.*, *242*(1–2), 51–57, doi:10.1016/j.epsl.2005.12.002.

Panza, G.F., A. Peccerillo, A. Aoudia, B. Farina (2007), Geophysical and petrological modelling of the structure and composition of the crust and upper mantle in complex

geodynamic settings: The Tyrrhenian Sea and surroundings, *Earth-Science Reviews, 80(1-2), 1-46.*

Pirttijärvi, M. (2004), MTInv, 1-D interpretation of magnetotelluric EM soudings, version 1.3 manual. University of Oulu, 8pp.

Pommier, A., F. Gaillard, M. Pichavant, and B. Scaillet (2008), Laboratory measurements of electrical conductivities of hydrous and dry Mount Vesuvius melts under pressure, *J. Geophys. Res., 113*, B05205, doi:10.1029/2007JB005269.

Principe, C., D. Brocchini, and M. Perillo (1999), The "Cognoli di Trocchia" volcano and Monte Somma growth. *Plinius*, 22, 316 –317.

Quist, A. S., and W. L. Marshall (1968), Electrical conductances of aqueous sodium chloride solutions from 0 to 800°C and at pressures to 4000 bars. *J. Phys. Chem. 72,684-703.*

Rolandi, G., G. Mastrolenzo, A.M. Barrella, and A. Borrelli (1993), The Avellino plinian eruption of Somma-Vesuvius (3,760 y. B.P.): the progressive evolution from magmatic to hydromagmatic style, *J. Volcanol. Geotherm. Res.*, 58, 67–88.

Rosi, M., and R. Santacroce (1983), The AD 472 "Pollena" eruption: Volcanological and petrological data for this poorly-known, Plinian-type event at Vesuvius, *J. Volcanol. Geotherm. Res., 17*(1–4), 249–271, doi:10.1016/0377-0273(83)90071-9.

Rosi, M., R. Santacroce, and M.F. Sheridan, (1987), Volcanic hazard. In: Santacroce, R. (Ed.), Somma–Vesuvius. *Quad. Ric. Sci.*, vol. 114, 197-234.

Santacroce, R., 1983. A general model for the behavior of the Somma-Vesuvius volcanic complex. *J. Volcanol. Geotherm. Res.*, 17, 237-248.

Santacroce, R. (Ed.) (1987), Somma-Vesuvius, CNR Quad. Ric. Sci., 114(8), 230 pp.

Santacroce, R., A. Bertagnini, L., Civetta, P., Landi, A., Sbrana (1993), Eruptive dynamics and petrogenetic processes in a very shallow magma reservoir : The 1906 eruption of Vesuvius, *J. Petrol*., 34, 383-425.

Santacroce, R., R. Cioni, L. Civetta, P. Marianelli, and N. Métrich (1994), How Vesuvius works, *Atti Conv. Lincei* 112, 185-196.

Santacroce, R., R. Cioni, P. Marianelli, and A. Sbrana (2005), Understanding Vesuvius and preparing for its next eruption, in *Cultural Responses to the Volcanic Landscape: The Mediterranean and Beyond*, edited by M. S. Balmuth et al., pp. 27–55, Archeol. Inst. of Am., Boston, Mass.

Scaillet, B., M. Pichavant, and R. Cioni (2008), Upward migration of Vesuvius magma chamber over the past 20,000 years, *Nature,* 455, 216-219, doi:10.1038/nature07232.

Scandone, R., L. Giacomelli, and F. Fattori Speranza (2008), Persistent activity and violent strombolian eruptions at Vesuvius between 1631 and 1944, *J. Volcanol. Geotherm. Res*., 170, 167-180.

Scandone, R., L. Giacomelli, and P. Gasparini (1993), Mount Vesuvius: 2000 years of volcanological observations. *J. Volcanol. Geotherm. Res*., 58, 5–25.

Simpson, F., and K. Bahr (2005), Practical Magnetotellurics, Cambridge University Press, 270 pp.

Taylor, M.A.J., and S.C. Singh (2002), Composition and microstructure of magma bodies from effective medium theory, *Geophys. J. Int.*, 149(1), 15-21.

Ten Grotenhuis, S.M., M.R. Drury, C.J. Spiers, and C.J. Peach (2005), Melt distribution in olivine rocks based on electrical conductivity measurements, *J. Geophys. Res.*, *110*, B12201, doi: 10.1029/2004JB003462.

Troiano, A., Z. Petrillo, M. G. Di Giuseppe, M. Balasco, I. Diaferia, B. Di Fiore, A. Siniscalchi, and D. Patella (2008), About the shallow resistivity structure of Vesuvius volcano, *Annals Geophys*., 51(1), 181-189.

Umeda K., K. Asamori, T. Negi, Y. Ogawa (2006), Magnetotelluric imaging of crustal magma storage beneath the Mesozoic crystalline mountains in a nonvolcanic region, northeast Japan, *Geochem. Geophys. Geosyst.*, 7, Q08005, doi:10.1029/2006GC001247.

Villemant, B., R. Trigila, and B. DeVivo, Geochemistry of Vesuvius volcanics during 1631-1944 period, *J. Volcanol. Geotherm. Res*., 58 (1-4), 291-313.

Wannamaker, P.E., D.P. Hasterok, , J.M. Johnston, J.A. Stodt, D.B. Hall, T.L. Sodergren, L. Pellerin, V. Maris, W.M. Doerner, K.A. Groenewold, and M.J. Unsworth, (2008), Lithospheric dismemberment and magmatic processes of the Great Basin-Colorado Plateau transition, Utah, implied from magnetotellurics, *G cubed*, 9(5), doi:10.1029/2007GC001886.

Whaler, K.A., and S. Hautot (2006), The electrical resistivity structure of the crust beneath the northern Main Ethiopian Rift, *from:* Yirgu, G., Ebinger, C.J. Maguire, P.K.H. (eds) 2006. *The Afar Volcanic Province within the East African Rift System.* Geological Society, London, Special Publications, 259, 293-305.

Zimmer, M., and J. Erzinger (1998), Geochemical monitoring on Merapi volcano, Indonesia, *Mitt. Dtsch. Geophysik. Ges. e.V.*, DGG Spec. Vol. 3 (ISSN 0947-1944), pp. 89-92.

Zollo, A., P. Gasparini, J. Virieux, H. le Meur, G. de Natale, G. Biella, E. Boschi, P. Capuano, R. de Franco, P. dell'Aversana, R. de Matteis, I. Guerra, G. Iannaccone, L. Mirabile,

G. Vilardo (1996), Seismic evidence for a low-velocity zone in the upper crust beneath Mount Vesuvius, *Science*, *274*(5287), 592–594, doi:10.1126/science.274.5287.592.

Zollo, A., P. Gasparini, J. Virieux, G. Biella, E. Boschi, P. Capuano, R. de Franco, P. Dell'Aversana, R. de Matteis, G. De Natale, G. Iannaccone, I. Guerra, H. Le Meur and L. Mirabile (1998), An image of Mt. Vesuvius obtained by 2D seismic tomography, *J. Volcanol. Geotherm. Res.*, *82*(1–4), 161–173, doi:10.1016/S0377-0273(97)00063-2.

Zollo, A., W. Marzocchi, P. Capuano, A. Lomax, and G. Iannacone (2002), Space and time behaviour of seismic activity at Mt. Vesuvius volcano, Southern Italy, *Bull. Seismol. Soc. Am.*, 92, 625-640.

Chapitre 5

Etude cinétique de l'état redox des melts basaltiques en utilisant les mesures électriques

(Study of the kinetics of the redox state of basaltic melts using electrical measurements)

Objectifs de ce chapitre

La fugacité en oxygène (fO_2) est un paramètre clé dans le contrôle des interactions physico-chimiques entre réservoirs au sein du manteau ou entre le manteau et la croûte, avec, par exemple, le contrôle de la spéciation des fluides et des melts. L'état redox du manteau a donc une importance non négligeable sur la genèse des magmas et leur dégazage. La conductivité électrique a été mesurée sur des liquides basaltiques en temps réel, suite à des changements de fO_2, dans le but d'étudier les cinétiques redox. Les expériences ont été menées à 1atm dans un four vertical, entre 1200°C et 1400°C, en utilisant de l'air, du CO_2 pur ou un mélange CO/CO_2, la fugacité en oxygène variant de 10^{-8} à 0.2 bars. Les ratios fer ferrique/fer ferreux ont été déterminés par des dosages colorimétriques. Un petit effet, mais détectable, de la fO_2 sur la conductivité électrique est observé. Plus le melt est réduit, plus la conductivité est grande. Une loi d'Arrhénius modifiée prend en compte à la fois les effets de la température et de la fO_2 sur la conductivité électrique. Nous montrons que les changements en fonction du temps de la conductivité, suite à des changements de fO_2, contrôlent la vitesse des changements de Fe^{2+}/Fe^{3+}. Le changement de conductivité en fonction du temps correspond à un processus limité par la diffusion dans le cas des réductions sous $CO\text{-}CO_2$ et des oxydations à l'air. Cependant, une réaction à l'interface gaz-melt limite probablement l'oxydation du melt sous CO_2 pur. Les vitesses de réduction et d'oxydation sont similaires et augmentent avec la température. Ces vitesses varient de 10^{-9} à $10^{-8} m^2/s$ sur l'intervalle de température 1200-1400°C et présentent une énergie d'activation >200kJ/mol. Le mécanisme redox expliquant le mieux nos résultats implique un mouvement coopératif des cations et de l'oxygène, permettant de reproduire les vitesses élevées d'oxydation-réduction.

Time-dependent changes of the electrical conductivity of basaltic melts with redox state

Article accepté à Geochimica et Cosmochimica Acta le 4 décembre 2009.

Pommier A.[1], Gaillard F. [1], Pichavant M. [1].

[1] *CNRS/INSU, Université d'Orléans, Université François Rabelais-Tours, Institut des Sciences de la Terre d'Orléans, UMR 6113, 45067, Orléans, France*

Abstract

The electrical conductivity of basaltic melts has been measured in real-time after fO_2 step-changes in order to investigate redox kinetics. Experimental investigations were performed at 1 atm in a vertical furnace between 1200°C and 1400°C using air, pure CO_2 or CO/CO_2 gas mixtures to buffer oxygen fugacity in the range 10^{-8} to 0.2 bars. Ferric/ferrous ratios were determined by wet chemical titrations. A small but detectable effect of fO_2 on the electrical conductivity is observed. The more reduced the melt, the higher the conductivity. A modified Arrhenian equation accounts for both T and fO_2 effects on the electrical conductivity. We show that time-dependent changes in electrical conductivity following fO_2 step-changes monitor the rate of Fe^{2+}/Fe^{3+} changes. The conductivity change with time corresponds to a diffusion-limited process in the case of reduction in $CO\text{-}CO_2$ gas mixtures and oxidation in air. However, a reaction at the gas-melt interface probably rate limits oxidation of the melt under pure CO_2. Reduction and oxidation rates are similar and both increase with temperature. Those rates range from 10^{-9} to $10^{-8} m^2/s$ for the temperature interval 1200-1400°C and show activation energy of about 200kJ/mol. The redox mechanism that best explains our results involves a cooperative motion of cations and oxygen, allowing such fast oxidation-reduction rates.

1. INTRODUCTION

Several studies have revealed the important controls of redox potential, usually quantified as oxygen fugacity (fO_2), on metal/silicate melt, crystal/melt and gas/melt equilibria (Carmichael and Ghiorso, 1990; Righter and Drake, 1996; Moretti and Papale, 2004; Gaillard and Scaillet, 2009). This makes redox condition of basaltic melts one of the most critical parameter influencing many planetary processes, involving core formation, mantle melting and

metasomatism, crystallization of magmas and magma degassing (Righter and Drake, 1996; Herd, 2008; Frost and McCammon, 2008). Several multivalent elements determine the fO_2 of basaltic melts (Fe, C, H, O, S), but the ferric/ferrous ratio of the melt is commonly used to monitor redox changes in magmatic processes (Kress and Carmichael, 1991; Behrens and Gaillard, 2006). The oxygen fugacity of a basalt is generally defined relatively to the one of a solid buffer, such as, from the more reducing to the more oxidizing, Iron-Wustite (IW), Quartz-Fayalite-Magnetite (QFM), Nickel-Nickel Oxide (NNO) (Herd, 2008).

Present-day basaltic lavas on Earth display a range in oxygen fugacity from 3 log-units below NNO to 4 log-units above NNO, corresponding to ferric/total iron ratios ranging from less than 10 to ~70% (Botcharnikov et al., 2005; Carmichael, 1991). Martian basalts record more reduced oxygen fugacities, ranging from 0.5 log-units to 3.5 log-units below NNO (Herd et al., 2002). Such variations in planetary basalts oxygen fugacity might reflect fundamental heterogeneities in the redox state of their source region but fO_2 can be also modified during melting, crystallization and degassing processes. Since such modifications can be kinetically controlled, a correct interpretation of fO_2 variabilities requires the understanding of the mechanisms and rate of changes in the redox potential in basalts. In this paper, we use electrical conductivity measurements to further document mechanisms and kinetics of redox changes in basaltic melts.

2. PREVIOUS WORKS

Mechanisms of oxidation/reduction of silicate melts have been actively investigated (e.g. Schreiber et al., 1986 and references therein). In H-bearing and H-free basaltic systems, reduction/oxidation reactions are commonly associated with the development of redox reaction fronts and are diffusion-limited (Wendlandt, 1991; Cooper et al., 1996a, b; Everman and Cooper, 2003; Gaillard et al., 2003a). For H-bearing systems, Gaillard et al. (2003b) calculated that H_2 mobility should rate-limit redox changes in basalts. In H-free systems, different rate-limiting species have been proposed. Oxidation-reduction reactions have been initially associated to the diffusion of oxygen (self-diffusion of oxygen; Wendlandt, 1991). However, self-diffusion experiments do not involve gain or loss of oxygen (^{16}O-^{18}O substitutions are involved) whereas redox experiments implicitly require a change in the oxygen/cations ratio. Variable-valence ions have been found to enhance oxygen fluxes (Beerkens and de Waal, 1990). Redox experiments are usually related to oxygen (O_2) chemical diffusion experiments (Schreiber et al., 1986). For glasses or melts of similar composition, oxygen tracer diffusivity (D*) is commonly several orders of magnitude slower than oxygen chemical diffusivity (D, Schreiber et al., 1986; Cook et

al., 1990; Wendlandt, 1991) (Appendix 1). Such discrepancies between O diffusion coefficients have been interpreted in terms of different transport mechanisms, oxygen self- or tracer diffusion involving mobility of discrete cation-oxygen species within the melt while oxygen chemical diffusion is dominated by the migration of cationic species. Cooper et al. (1996b) have demonstrated that the diffusion of an oxygen species is not required during redox reactions in melts and that the change in the oxygen/cations ratio is best accommodated by cations rather than oxygen diffusivity due to their greater mobility.

Oxygen self and chemical diffusion studies performed on synthetic (Sasabe and Goto, 1974; Dunn, 1982; Schreiber et al., 1986; Cook et al., 1990; Cook and Cooper, 2000; Reid et al., 2001) and natural silicate melts (Dunn, 1983; Canil and Muehlenbachs, 1990; Wendlandt, 1991; Cooper et al., 1996a) have demonstrated the dependence of both kind of diffusion mechanisms on the melt structure. This was also confirmed by other studies of iron redox reactions (e.g. Magnien et al., 2008). All that tends to underline that the Network Formers (Si, Al) lower the oxygen diffusivity (D) whereas the Network Modifiers (divalent cations and alkali) have the opposite effect. In basaltic melts, oxygen self-diffusion data were found to be comparable to divalent cations diffusivities. For example, in a basaltic melt at 1300°C, Muehlenbachs and Kushiro (1974) and Lesher et al. (1996) measured oxygen diffusivities (D*) of ~4.10^{-12} m²/s and 6.10^{-12} m²/s, respectively. This result questions the assumption of Cooper et al. (1996a, b) that $c_{O2-}D_{O2-}$ (and $c_{O2}D_{O2}$) < $c_{\text{modifier cations}}D_{\text{modifier cations}}$, c_x being the concentration of x.

The electrical conductivity, σ, reveals the mobility of the charge carriers in presence of a gradient in electrical potential and is an efficient probe of mass transfer processes within silicate melts and magmas. Previous studies have shown that it is extremely sensitive to many parameters, including temperature (T), pressure (P), melt composition (Tyburczy and Waff, 1983, 1985; Gaillard, 2004; Gaillard and Iacono Marziano, 2005; Pommier et al., 2008). However, the dependence of electrical conductivity of silicate melts to redox conditions has remained poorly documented. The only study on the subject (Waff and Weill, 1975) found no significant variation in σ with fO_2 and suggested to neglect the influence of fO_2 on the electrical properties of silicate melts.

We have undertaken a systematic investigation of the influence of fO_2 on the electrical response of two different basaltic melts at 0.1MPa and different temperatures. The study was motivated by (1) the need to reexamine the conclusions of Waff and Weill (1975) in the light of recent methodological advances in the field of electrical measurements and (2) the need to understand redox kinetics and mechanisms in natural silicate melts, the electrical conductivity being here used as a probe for investigating mass transfer properties. Modern techniques of

measurements of electrical conductivity such as impedance spectroscopy (Huebner and Dillenburg, 1995) allows the electrical response to be separated in terms of an imaginary and a real part, the latter corresponding unambiguously to the electrical resistance of the sample. In the case of oxidation/reduction reactions, the real time electrical response of the melts was not monitored in previous studies (Waff and Weill, 1975) and is therefore unknown. In our study, the electrical conductivity was continuously measured from step changes in fO_2 until the attainment of redox equilibrium. In turn, this allows conductivity changes to be interpreted in terms of kinetics and mechanisms of redox changes in the melt. Equilibrium conductivities were extracted from the evolution of σ-time plots and used to establish the dependence of the electrical conductivity with fO_2 for the two basaltic melts and different temperatures investigated. The conductivity measurements were complemented by major element and FeO analyses of experimental glasses in order to relate the electrical and redox state of the studied melts. For most experiments, the kinetics of the electrical response can be satisfactorily fitted by a diffusion formalism, suggesting that both oxidation and reduction reactions are kinetically limited by diffusion. The high values of the calculated diffusion coefficients ($\sim 10^{-9} m^2/s$ for our investigated T range) can be explained by redox mechanisms involving both oxygen and cations fluxes.

3. EXPERIMENTS

3.1. Starting products

The starting materials are two different basalts: one collected from the active vent of Pu'u' 'O'o volcano (Kilauea, Hawaii) in 2007 and a tephrite (VES9) coming from a 8th century eruption of Mt. Vesuvius (Italy). Chemical analyses of the starting glasses are given in Table 1. Each rock was finely crushed in an agate mortar. The powder was dried and then melted in air at 1400°C during ~1h. Therefore, all starting glass samples were prepared under strongly oxidizing conditions (log fO_2=-0.69). Quenching resulted in bubble-free glasses that were drilled to cylinders (6 mm OD, 6.5-10 mm length), and directly loaded in the electrical conductivity cell. NBO/T ratios (number of non-bridging oxygens divided by number of tetrahedral cations) of the two glasses, calculated considering Fe as both FeO and Fe_2O_3 and neglecting the presence of Ti (Mysen and Richet, 2005), are 0.56 for the Kilauea basalt and 0.55 for the Mt. Vesuvius tephrite. This underlines a similar polymerization of the tephrite and the basalt.

Table 1: Composition of the starting glasses (in wt %). Figures into brackets correspond to the concentrations of major oxides in mol %.

Sample	VES9		Kilauea	
SiO_2	49.2	(54.6)	50.0	(55.2)
TiO_2	0.96	(0.80)	2.41	(2.00)
Al_2O_3	15.1	(9.90)	13.2	(8.62)
FeO	1.73	(1.61)	3.16	(2.92)
Fe_2O_3	6.08	(2.54)	8.58	(3.57)
MnO	0.20	(0.19)	0.13	(0.12)
MgO	6.26	(10.3)	7.50	(12.3)
CaO	11.5	(13.6)	10.6	(12.5)
Na_2O	1.97	(2.12)	2.29	(2.45)
K_2O	5.98	(4.23)	0.38	(0.27)
F	0.14		-	
Cl	0.12		-	
S	0.05		-	
Total	99.7	(100)	97.89	(100)
NBO/T	0.73		0.80	

3.2. Experimental setup

All experiments were performed in a one atmosphere vertical furnace. Experimental temperatures ranged from 1200 to 1400°C. Temperature, monitored with a *Eurotherm* controller, was measured by a type-S thermocouple, placed adjacent to the conductivity cell, and is known to within +/- 2°C. The sample and the thermocouple were both located in the 3 cm hot spot of the furnace. Experimental redox conditions were controlled by the gaseous atmosphere present in the furnace. Three types of gaseous atmospheres were employed: air, pure CO_2 and CO-CO_2 mixtures. Note that experiments using only CO_2 are never performed under pure CO_2, since a small quantity of CO is always present in the gas bottle. This small amount of CO (in general < a few tens of ppm) allows the gas atmosphere to act as a buffer.

For air, the tube furnace was left open to the ambient atmosphere. In contrast, for both CO_2 and CO-CO_2 mixtures, gases were flown through the furnace (typical flow rates were 200cc/min). For CO-CO_2 mixtures, three different gas proportions (39.7% CO_2/1.6% CO; 38.8% CO_2/5.9% CO; 36.5% CO_2/17.5% CO) were imposed using electronic flowmeters. Redox conditions (fO_2) were calculated from Deines et al. (1974) and directly measured using a zirconia electrolyte cell. These are referenced against the Ni-NiO equilibrium at 0.1MPa (Pownceby and O'Neill, 1994). For pure CO_2 gas, ΔNNO values range from 3.45 to 4.00 (Table 2 and 3); for

$CO\text{-}CO_2$ gas mixtures, ΔNNO values divide into three groups (0.75-1.40; -0.35-0.45; -1, Table 2 and 3), depending on the specific gas mixture imposed.

Conductivity measurements were performed using a two-electrode configuration on cylindrical samples (Gaillard, 2004; Pommier et al., 2008, Figure 1a). Glass samples of 6mm OD and 8-9mm length were typically used. The inner electrode of the conductivity cell is a 1mm Pt wire inserted in the center of the glass sample and the external electrode is a Pt tube surrounding the sample. The drilled alumina ceramic part located at the bottom of the conductivity cell prevents the two electrodes from being in contact (Figure 1a). This configuration ensures the stability of the cell during the experiment. We assume that no convection occurs in the samples since the Rayleigh number is very small (<200, Jaupart and Tait, 1995), due to the small dimensions of the samples. Thermodiffusion (Soret effect) requires the presence of a thermal gradient, which is not the case in our experiments (thermal gradient <1-2°C). At the end of the experiment, the conductivity cell and the sample were removed from the furnace and allowed to cool down under room conditions. Quenched glasses from selected conductivity charges were collected and prepared for FeO titration and electron microprobe analyses.

3.3. Experimental strategy

For each experiment at a given temperature, two fO_2 steps were performed. Electrical measurements were recorded continuously until the attainment of the different equilibrium redox states. Reduction experiments consisted in an initial relatively oxidizing step followed by a final step under more reducing conditions. Oxidation experiments were the reverse of reduction experiments: an initial relatively reducing step was followed by a more oxidizing step. In practice, fO_2 changes were obtained by switching either from air or pure CO_2 to $CO\text{-}CO_2$ mixtures (reductions), or from $CO\text{-}CO_2$ mixtures to air or pure CO_2 (oxidations). On the basis of voltage measurements using the zirconia probe, changing fO_2 from $CO\text{-}CO_2$ to pure CO_2 or air and reciprocally takes approximately a few minutes. Electrical measurements during this transition period were discarded. For oxidations in air, the conductivity cell was taken out of the furnace during the evacuation of the $CO\text{-}CO_2$ gas mixture and then replaced in the furnace at T. Durations for each fO_2 steps ranged between 90 and 1900min (Table 2).

In parallel to electrical conductivity experiments, experiments were performed in order to determine Fe^{2+}/Fe^{3+} and other chemical changes associated with the real-time evolution of the oxygen fugacity. These experiments (designated below as analytical experiments, Table 3) used the same sample configuration and dimensions as the conductivity experiments (Figure 1b).

Similarly, only one end of the glass cylinder was in contact with the furnace atmosphere. T and fO_2 conditions were selected to match those in conductivity experiments. Samples have been rapidly quenched before redox equilibrium, as monitored from the electrical measurements, was attained. Experimental glasses were analyzed for FeO titration and electron microprobe analyses.

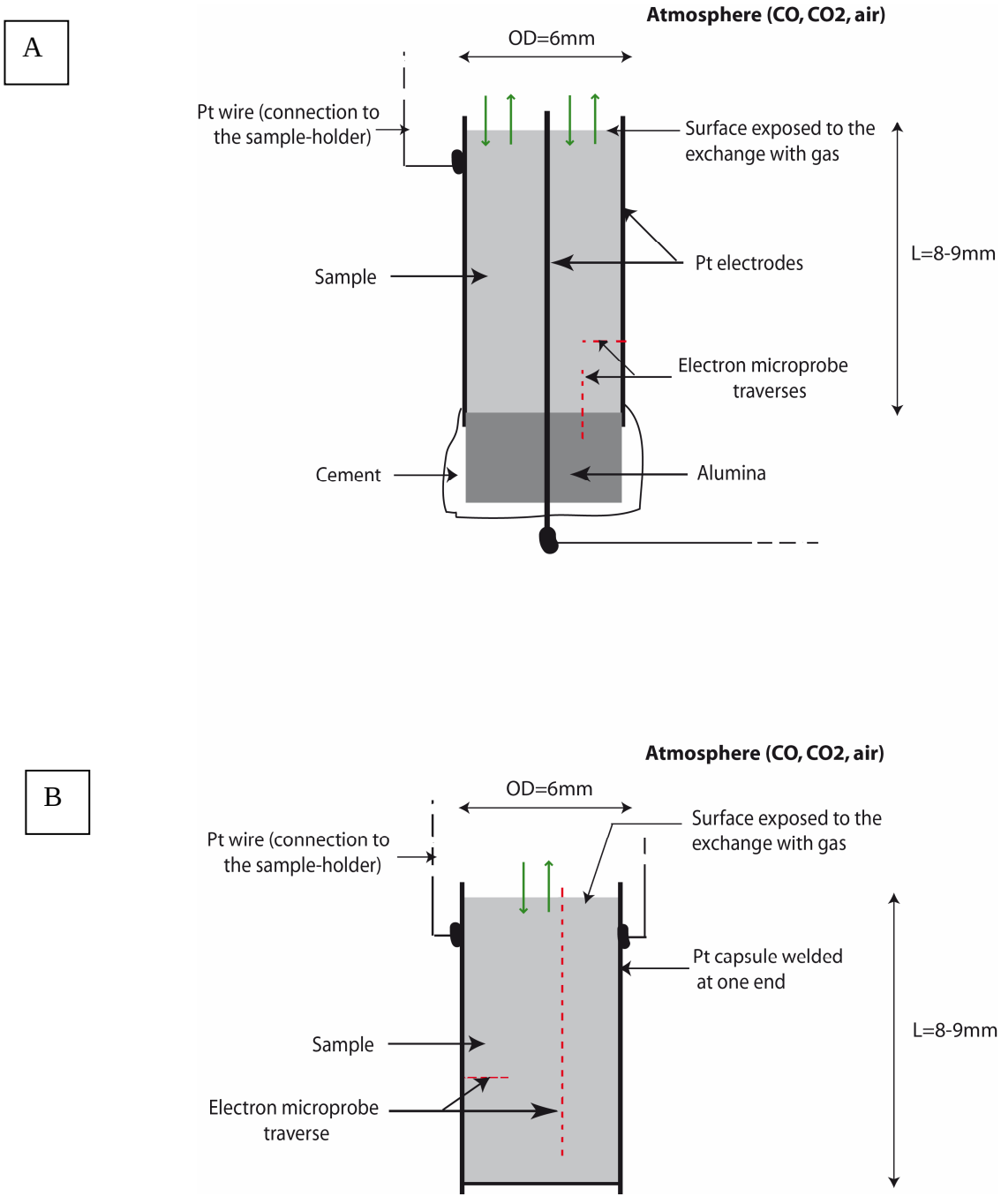


Figure 1: Description of (A) the conductivity cell and (B) the sample configuration for analytical experiments. The arrows represent the exchange with the gaseous atmosphere at the unique interface sample/gas. The straight lines represent the three types of microprobe traverses performed after the redox experiments (see text).

Table 2: Conditions and results of the conductivity experiments.

Run	Sample	Initial conditions (Step 1)					Final conditions (Step 2)						
		T(°C)	Gas	log fO_2 ◊	ΔNNO	Duration (min)	T(°C)	Gas	log fO_2 ◊	ΔNNO	Duration (min)	σ eq (ohm.m)$^{-1}$	t eq (min)[a]	at. Fe^{2+}/Fe
Reduction														
#1	Ves	1200	CO_2	-3.74	4.00	1050	1200	$CO-CO_2$	-6.30	1.40	1650	0.63	1042	1.24
#2	Ves	1250	CO_2	-3.50	3.70	1320	1250	$CO-CO_2$	-5.80	1.40	630	0.82	491	2.00
#4	Kil	1200	CO_2	-3.74	4.00	1370	1200	$CO-CO_2$	-6.30	1.40	1410	1.00	778	2.24
#5	Kil	1200	CO_2	-3.74	4.00	1290	1200	$CO-CO_2$	-7.25	0.45	1860	1.04	874	-
#6	Kil	1300	CO_2	-3.24	3.45	280	1300	$CO-CO_2$	-5.31	1.35	430	1.50	203	-
#7	Kil	1300	CO_2	-3.24	3.45	1010	1300	$CO-CO_2$	-6.70	0.00	290	1.65	124	2.55
#8	Kil	1300	Air	-0.69	6.00	200	1300	$CO-CO_2$	-7.67	-1.00	230	1.83	118	2.41
#9	Kil	1400	Air	-0.69	5.10	200	1400	$CO-CO_2$	-4.98	0.75	180	2.99	86.5	1.64
#10	Kil	1400	Air	-0.69	5.10	190	1400	$CO-CO_2$	-6.12	-0.35	80	3.10	72.5	-
Oxidation														
#1rev	Ves[1]	1200	$CO-CO_2$	-6.30	1.40	1650	1200	CO_2	-3.74	4.00	2500	0.60	2500	1.00
#5rev	Kil[2]	1200	$CO-CO_2$	-7.25	0.45	1860	1200	CO_2	-3.74	4.00	1030	0.81	1000	1.58
#6rev	Kil[3]	1300	$CO-CO_2$	-5.31	1.40	430	1300	CO_2	-3.24	3.45	1530	1.27	1200	1.46
#7rev	Kil[4]	1300	$CO-CO_2$	-6.70	0.00	290	1300	CO_2	-3.24	3.45	910	1.42	720	1.47
#12	Kil*	1400	$CO-CO_2$	-4.98	0.75	100	1230	Air	-0.69	6.73	1380	0.98	560	0.37
#13	Kil*	1400	$CO-CO_2$	-6.12	-0.35	100	1230	Air	-0.69	6.84	1350	0.95	735	0.32
#14	Kil*	1400	$CO-CO_2$	-4.98	0.75	100	1300	Air	-0.69	6.00	1300	1.26	472	0.52
#15	Kil	1300	$CO-CO_2$	-6.70	0.00	260	1300	Air	-0.69	6.00	380	1.11	250	-
#10rev	Kil[5]	1400	$CO-CO_2$	-6.12	-0.35	80	1400	Air	-0.69	5.10	200	2.18	111	0.69

[1-5] Reduction reverse (Starting glass is final glass from a reduction experiment; Both have the same run number).

* Initial fO2 step performed at T=1400°C>T of conductivity experiment (Final conditions) in order to increase the kinetics of the reduction phase.

◊ fO_2 in bar.

[a] Time necessary for σ(t)=σ eq (plateau value), calculated as $t=L^2/D$, with L=length of the glass sample.

Table 3: Conditions and results of the analytical experiments.

Run	Sample	Initial conditions (Step 1)						Final conditions (Step 2)			
		T(°C)	Gas	log fO_2 ◊	ΔNNO	Duration (min)	at. Fe^{2+}/Fe^{3+}	T(°C)	Gas	log fO_2 ◊	ΔNNO	Duration (mi
Reduction												
#4-QR	Kil	1200	CO_2	-3.74	4.00	1000	0.95	1200	CO-CO_2	-6.30	1.40	300
#5-QR	Kil	1200	CO_2	-3.74	4.00	1000	0.95	1200	CO-CO_2	-7.25	0.45	45
#6-QR	Kil	1300	CO_2	-3.74	4.00	1000	0.80	1300	CO-CO_2	-5.31	1.35	45
Oxidation												
#12-QO	Kil	1230	CO-CO_2	-6.30	1.40	900	-	1220	Air	-0.69	6.00	330
#14-QO	Kil[1]	1400	CO-CO_2	-4.98	0.75	100	-	1300	Air	-0.69	6.00	200

* Duration of Step 2 corresponds to t_{quench}.

[1] This experiment is to be compared with experiment #14 in Table 2, although the difference in T regarding the initial conditions.

◊ fO_2 in bar.

3.4. Acquisition and reduction of the electrical data

In this study, electrical conductivities were derived from complex impedance spectroscopy (Roberts and Tyburczy, 1994). Electrical impedances of samples were determined at variable frequencies using a Solartron 1260 Impedance Gain Phase Analyzer, (Schlumberger Co.), equipped with Zview software package (Huebner and Dillenburg, 1995; Gaillard, 2004; Maumus et al., 2005). Each measurement consisted in a scan in frequency from 1 Hz to 10^6 Hz, lasting typically about 1min. For each frequency, the complex impedance was recorded. The experimental procedure, including details on the calibration process, is detailed in Pommier et al. (2009, in press). The reproducibility of the data has been demonstrated in Pommier et al. (2008).

The complex impedance, Z, can be written as the sum Z'+jZ", with Z' the real part and Z" the imaginary part of Z (and j^2=-1). The electrical response of the sample to a scan in frequency is directly observed in the Nyquist plane (Z', Z") (Figure 2), from which the value of the electrical resistance R is deduced (e.g. Huebner and Dillenburg, 1995). The non semi-circle shape of the impedance spectra is due to the fact that the samples are very conductive on the investigated T range, implying their electrical resistance to be smaller than the inductive effects (Z"<0). The corresponding electrical conductivity value σ is then deduced using the geometric factor G (Gaillard, 2004; Pommier et al., 2008):

$$\sigma = (G.R)^{-1} \qquad (1)$$

The geometric factor varies from 0.022 to 0.037 m. The uncertainty on σ due to error propagation of typical uncertainties on R (R is known to +/- 0.5 ohm in the investigated T range), L, d_{ext} and d_{int} (uncertainties on the length and the two diameters are 0.1mm) is in the range of 4.7-9% for both our Kilauea and Mt.Vesuvius samples.

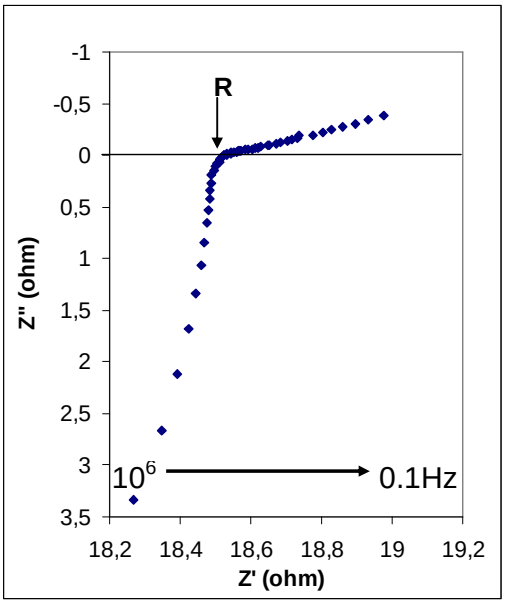


Figure 2: Electrical response observed in the Nyquist plan (Z', Z'') for the Kilauea basalt at 1300°C, during oxidation in air. The first part of the response (Z'<R) represents the electrical response of the sample while the second part (Z'>R), represents the effect of the interface between the sample and the electrode. R (resistance of the sample (ohm)) is obtained for Z" = 0 and represents the real part of the complex impedance (here, R~18.5ohm).

For fixed T and fO_2 conditions and for each starting glass composition, time series measurements were conducted. They consisted in the successive acquisition of electrical measurements (each comprising a scan in frequency from 1 Hz to 10^6 Hz) until a stable value of R (and, thus, of σ) was reached (plateau values). The time interval between two electrical measurements ranged from 30 s to 1 hr depending on the evolution of the electrical response with time: at the beginning of the experiment, small time intervals were required since the electrical response changed rapidly; on the contrary, at the end of the experiment, the small changes in the electrical response (plateau values) allowed the use of longer time spans.

3.5. Analytical techniques

Experimental glasses were observed optically under a microscope, in order to check for the presence of crystals and bubbles. Crystals were found to be present in some oxidation experiments performed at 1200°C in air for the Kilauea basalt. Results from these experiments were discarded and are not presented.

A Camebax SX-50 electron microprobe (BRGM-CNRS-Université d'Orléans) was used to analyze both the starting and the experimental glasses. Analyses were conducted at 15kV, 6nA, 10s on peak and 5s on background. Both spot analyses and traverses were performed. Traverses served to evaluate the degree of iron loss from the melt to the Pt electrodes and the extent of Al^{3+} incorporation and diffusion from the ceramic part of the conductivity cell into the melt (Figure 1b). In the analytical charges, EMPA traverses at the gas/melt interface were used to determine the type and importance of major elements fluxes to redox changes (see Figure 1).

The FeO concentration of the starting and experimental glasses was determined by colorimetric redox titration (Gaillard et al., 2003b). With this method, the sample is dissolved in $HF+H_2SO_4$ solution and the titration is then performed using a potassium dichromate solution. The equivalence volume provides the value of the concentration of FeO. At least 25mg of sample powder were used for the titration in order to ensure accuracy and reproducibility. The Fe_2O_3 concentration is then calculated from:

$$Fe_2O_3=1.1113.(FeO_{tot}-FeO), \qquad (2)$$

where Fe_2O_3 is the concentration in ferric iron (wt%), FeO_{tot} is the total iron concentration (wt%) measured by electron microprobe and FeO is the concentration of ferrous iron (wt%) determined as above. FeO and Fe_2O_3 concentrations are then used to calculate the at. Fe^{2+}/Fe^{3+} ratio.

4. RESULTS

4.1. Melt-conductivity cell interactions

Spot electron microprobe analyses performed in the center of the glass cylinders in most cases showed no significant changes in major element oxides in comparison with starting glass compositions. Exceptions were experiments performed at the lowest temperatures (1200°C) for the Kilauea glass and at log fO_2 = -3.74 and -0.69 (fO_2 in bar) (see Table 2). For those samples, the variations in major elements concentration can be explained by the crystallization of Fe-Ti-Mg oxides observed in the experimental glasses. These observations indicate that no noticeable alkali volatilization occurred during these redox experiments.

The glass-Pt interface shows no significant variations in oxide concentrations, except for FeO, as already observed by Pommier et al. (2008). On average, iron depletions range between 2 and 7% relative. A maximum depletion of 15% FeO relative affecting the melt on a distance <500microns was found only for the longest experiments, for which the experimental duration exceeded the average run duration by several hours. For instance, in experiment #5 (one of the longest experiments (Table 2), thus particularly exposed to Fe losses), the iron content close to the electrode is ~4.3% mol oxide against 4.6% mol oxide in the starting glass, corresponding to a decrease of 6.5% compared to the FeO content. Iron depletions affect a distance in the Pt electrode <100microns (Figure 3a), thus insignificantly modifying the iron content in the glass (Figure 3b). As a result, the bulk data (electrical conductivity and wet chemistry) will not be significantly affected by Fe losses to Pt electrodes.

The glass-alumina interface presents on most samples a nearly continuous 10-30 μm thick layer comprising Al-Mg-Fe spinel and some scattered plagioclase crystals. The contribution of these crystals to the measured electrical conductivity was evaluated according to the method exposed in Pommier et al. (2008). Calculations show that the contribution of the crystals is less than 1% of the measured conductivity.

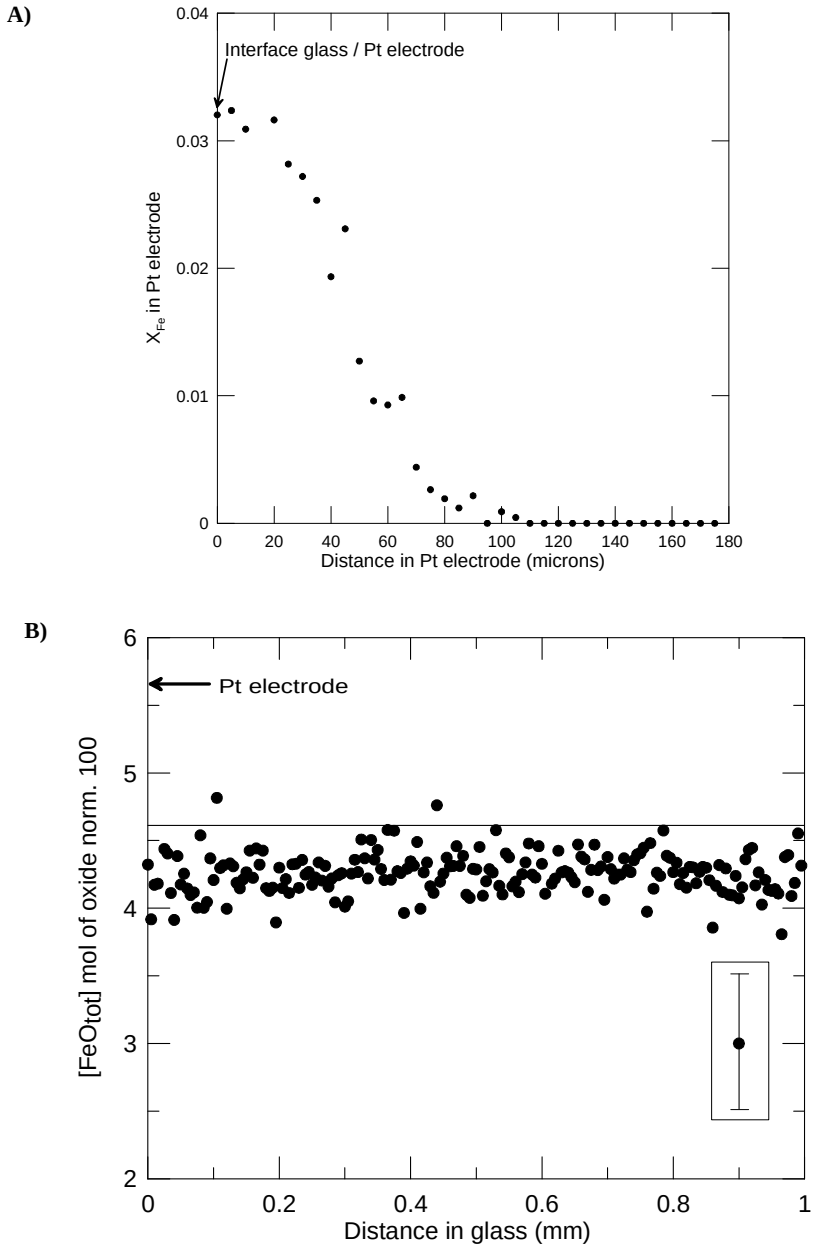


Figure 3 : Iron losses, example of the redox experiment at 1200°C (run #5). A: Molar fraction of metallic iron in the Pt electrode after. The EMPA profile shows that iron contamination affects the electrode on a distance <100microns. B: Concentration of total iron in mol of oxide normalized to 100. No noticeable iron depletion is detected in the sample, even at the interface glass/Pt electrode. Error estimation is presented in the box.

4.2. Effect of oxygen fugacity and temperature on the electrical conductivity

Electrical conductivities of the Kilauea sample measured at temperatures ranging from 1200 to 1400°C and covering a range of oxygen fugacities of $10^{-7.7}$ to 0.2 bar are shown in Figure

4. These are steady-state values of electrical conductivity associated with chemical equilibrium at the set fO_2. A small but clearly detectable effect of oxygen fugacity on the electrical conductivity is demonstrated for each isotherm. The more reduced the melt, the higher the electrical conductivity. For comparison, no effect of fO_2 on the electrical conductivity was observed in the study of Waff and Weill (1975). For both Kilauea and Vesuvius samples, the change in electrical resistance following a change in redox conditions is about a few ohms, largely exceeding the sensitivity of our measurements (better than 0.1%) at given T and fO_2. A small effect of composition is observed, the VES9 sample being less conductive than the Kilauea sample at 1200 and 1300°C (σ_{eq} values in Table 2).

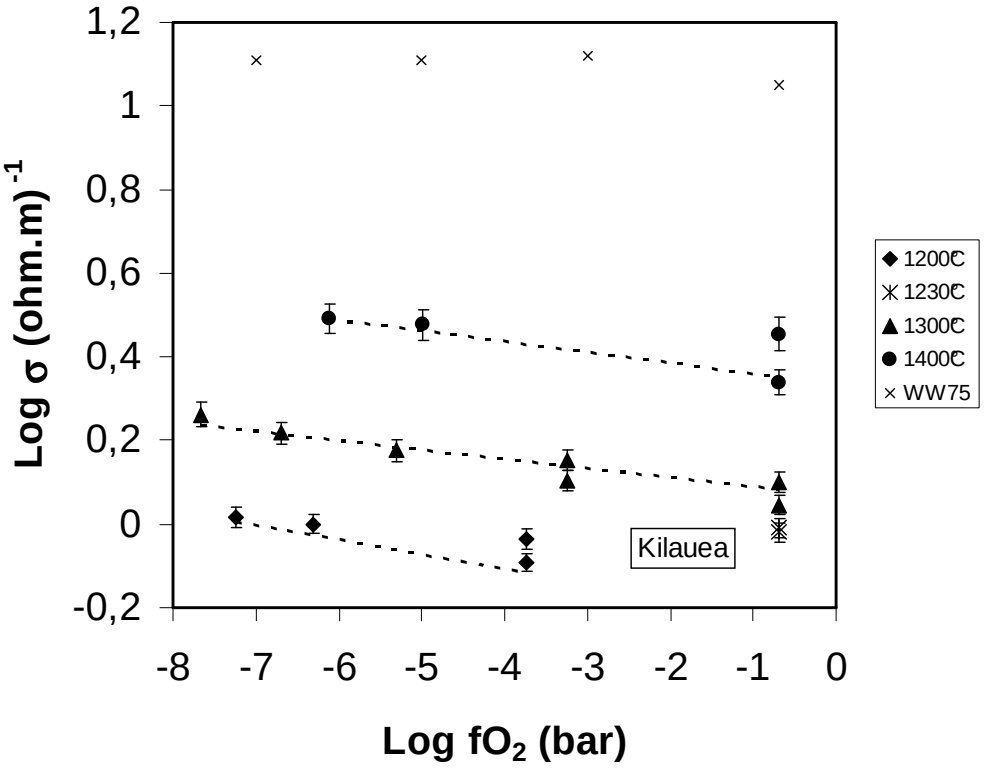


Figure 4: Electrical conductivity at the chemical equilibrium of the Kilauea sample as a function of oxygen fugacity, for T ranging from 1200°C to 1400°C. The conductivity slightly increases with decreasing the fO_2. The electrical conductivity is more strongly dependent on T than fO_2. Experimental conditions are indicated in Table 2. Dashed lines correspond to Eq.4. The electrical conductivity of the PG-16 basaltic melt at 1400°C from Waff and Weill (1975) (WW75) is shown for comparison.

At 1300°C, for the Kilauea sample, a change in fO_2 of 8 log-units modifies the electrical conductivity of ~0.2 log-unit (Figure 4). A similar effect is observed at the other investigated temperatures. For a given fO_2, the electrical conductivity increases with temperature (Figure 4).

The influence of temperature (increase of ~1.2 log units from 1200 to 1400°C) appears to be similar at low and high fO_2. This temperature dependency of the conductivity can be fitted by an Arrhenius equation:

$$\sigma = \sigma_0 . \exp\left[\frac{-Ea_\sigma}{RT}\right] \qquad (3)$$

with σ the electrical conductivity $(ohm.m)^{-1}$, σ_0 the pre-exponential factor $(ohm.m)^{-1}$, Ea_σ the activation energy (J/mol), R the universal gas constant $(J.K^{-1}.mol^{-1})$ and T the temperature (K). Depending on the gas atmosphere, linear least-squares regression analysis of electrical data yields different activation energies that are presented in Table 4. Since a small effect of fO_2 on σ was detected in our experiments, we have introduced in the Arrhenian formalism the fO_2 parameter. Depending on both T and the redox conditions, the electrical conductivity of both Kilauea and Mt. Vesuvius melts can be expressed as

$$\sigma = (9.4.10^3) . \exp\left[\frac{-117074}{RT}\right] . (f_{O2})^{-0.03} \qquad (4)$$

Eq.4 reproduces measured conductivity values for all the experiments with a correlation coefficient of 0.93 and an average error of 11.6% relative.

Table 4: Arrhenius parameters for the investigated samples.

Gas	Log fO_2 ◊	ΔNNO	Fe^{2+}/Fe^{3+}(%at)	$Ln\sigma_0$ $(ohm.m)^{-1}$	Ea_σ (kJ/mol)
Mt. Vesuvius sample (T range [1200-1250°C])					
$CO-CO_2$ mixture 1	[-6.30; -5.80]	~1.40	[1.24;2.00]	7.57	98
Kilauea sample (T range [1200-1400°C])					
Air	0.68	~7	[0.32;0.92]	7.21	90
CO_2	[-3.74; -3.24]	[3.45; 4.00]	[1.22;1.58]	9.16	114
$CO-CO_2$ mixture 1	[-6.30; -4.98]	[0.75; 1.40]	[1.64;2.24]	9.20	113
$CO-CO_2$ mixture 2	[-7.25; -6.12]	[-0.35; 0.45]	2.55*	9.16	112

◊ fO_2 in bar.
*one wet chemical analysis (run #7 in Table 2).

4.3. Time-dependent changes in electrical conductivity during redox reaction

At a given temperature, the time necessary to reach a stable value of the conductivity (t_{eq}) following a change in redox state is approximately the same for a reduction under CO-CO_2 and an oxidation in air, while longer time spans are needed for oxidations under CO_2 (Table 2). At 1200°C, for both reduction and oxidation experiments, a stable (plateau) value of the conductivity is reached in more than 15hours, while less than 2hours are needed at 1400°C.

Results of typical reduction and oxidation (in air) experiments are presented in Figure 5a and 5b (experiments #6 and #15, respectively, Table 2). For both types of experiments, the exponential shape of the electrical response with time underlines similar reaction mechanisms and kinetics. For the experiment with pure CO_2 (Figure 5c), the electrical response is more linear with time, which contrasts with the curves obtained either for oxidation in air or for reductions in CO-CO_2. Changing the CO_2 flow rate in the furnace does not significantly change the shape of the electrical response with time (Figure 5c). The negligible effect of the gas flow rate on the kinetics of oxidation is in agreement with the observations made by Schreiber et al. (1986) using different air flow rates.

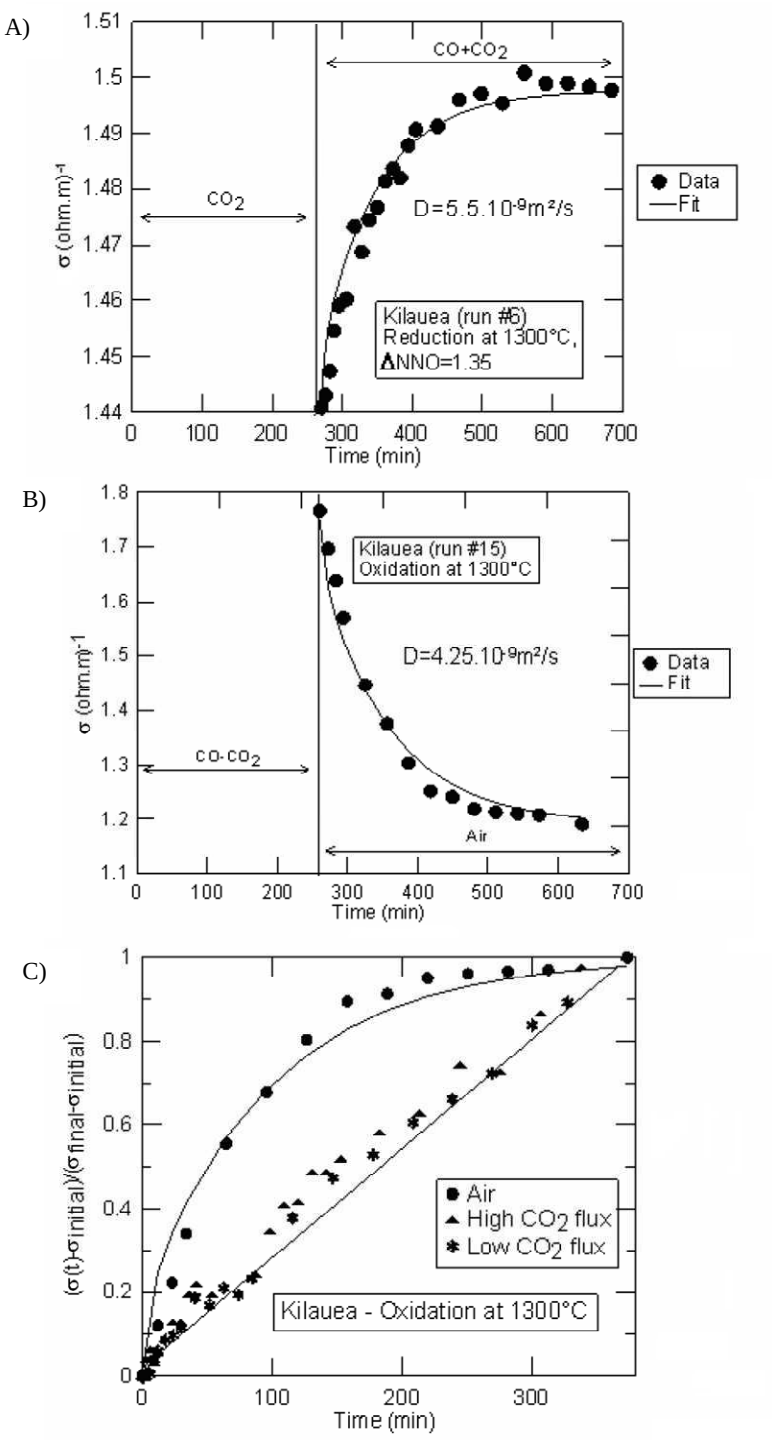


Figure 5: Experimental measurements showing changes in electrical conductivity in function of elapsed time. A: Reduction example (run #6); B: Oxidation example (run #15). The solid lines correspond to the calculated conductivity with the diffusion equation of Crank (see text). C: Advancement of oxidation reaction in air and CO_2 as a function of time. The diffusion profile obtained in air contrasts with the more linear trend obtained under CO_2. Triangles and diamonds underline that the non diffusion kinetics under CO_2 is not function of the gas flow in the furnace. Straight line is just a guide for the eyes.

4.4. Variations in major element chemical concentrations

Electron microprobe traverses were performed in quenched samples from the analytical experiments to detect possible variations in major elements concentrations (Si, Al, Fe, Mg, Ca, Na, K) associated with redox changes. Traverses were performed in the longitudinal section of the samples, from the interface with gas to at least 4mm inside the glass sample (Figure 1b). The spatial resolution of the probe analyses is +/-5 microns.

Examples of microprobe traverses are presented in Figure 6 (traverses A and B: reductions; traverse C: oxidation). For clarity, we state here the presence of three parts in our samples (these parts will be interpreted Part 5 in terms of redox fronts): (1) The interface zone between gas and glass (<1mm depth), from the gas/sample interface to ξ', is characterized by important variations in the concentration of network forming and network modifying cations in the quenched glass samples. ξ' is defined graphically and corresponds to the point at which the concentration of major elements presents an inflexion. For example, in experiment #6-QR (traverse A), this zone presents a relative increase of 5-8% in SiO_2 and Na_2O and 30% in K_2O and a decrease of 5-8% in MgO and CaO to 22% in FeO. (2) An inner zone begins at a depth >1mm (ξ') and extends as far as > 5 mm depending on experimental duration. It presents slight fluctuations in alkali and Mg and Ca concentrations. In experiment #14-QO (traverse C), this zone presents an increase of 4% relative in CaO and MgO and a decrease of 8.8% relative in Na_2O. (3) A third zone, located near the bottom of the capsule, can be detected on some profiles (traverse B). This part of the sample is identified as the unreacted melt, the compositions in this zone corresponding to the starting glass compositions. Traverses performed on samples from conductivity experiments with duration exceeding t_{eq} have flat profiles for all major elements (traverse D).

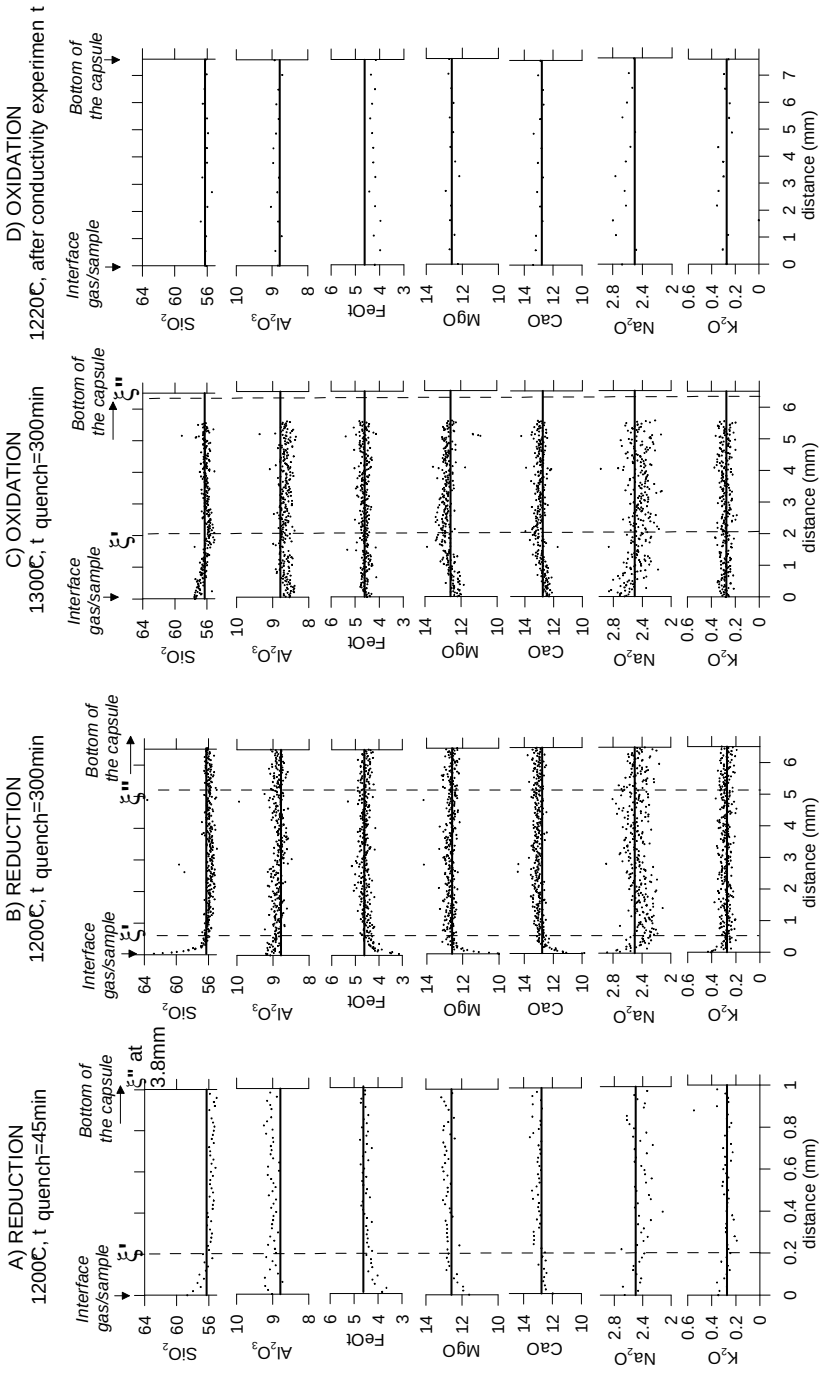


Figure 6: Microprobe traverses from the gas/sample interface in Kilauea samples quenched during redox experiments and after conductivity experiment. A) 1300°C, log fO_2=-5.31, t quench=45min (run #6-QR); B) 1200°C, log fO_2=-6.30, t quench=300min (run #4-QR); C) 1300°C, log fO_2=-0.68, t quench=300min (run #14-QO); D) 1230°C, log fO_2=-0.69 (run#12). Traverse D stresses that chemical compositions of starting glass and glass after the conductivity experiment are similar. Oxides concentrations are given in mol normalized to 100. Variations in oxides concentrations allow to distinguish an interface zone, from the interface with gas to ξ' (dashed line, approximative localisation). The second internal front, ξ'', delimiting the unreacted melt, is calculated using D values from Eq.7.

4.5. FeO concentrations and evolution of glass Fe^{2+}/Fe^{3+}

Wet chemistry was used to determine the bulk value of Fe^{2+}/Fe^{3+} in glasses before and after most experiments (Tables 2 and 3). Analyses showed that the range of oxygen fugacities we investigated results in a range of at.Fe^{2+}/Fe^{3+} of approximately 0.32 to 2.55 (Figure 7a).

The rate of change of Fe^{2+}/Fe^{3+} with time was documented in both reduction and oxidation experiments. Fe^{2+}/Fe^{3+} were measured at different time intervals following either a reduction (experiment #4, values at t=0, 300 and 1410min; #5, values at t=0, 45 and 1860min; #6, values at t=0, 45 and 430min) or an oxidation (experiment #12, values at t=0, 330 and 1380min; #14, values at t=0, 200 and 1300min) (Tables 2 and 3). For both reduction and oxidation, the rate of change of Fe^{2+}/Fe^{3+} is clearly nonlinear with time (Figure 7b). For example, oxidation in air of the Kilauea sample (experiment #14) shows a decrease in at. Fe^{2+}/Fe^{3+} from 1.64 (t=0) to 0.52 at equilibrium (t_{eq}=1300min, Figure 7b). The intermediate value at t=200min (0.83, Table 3) represents a change of ~80% toward the equilibrium value.

5. DISCUSSION

5.1. Ferrous / ferric ratio and electrical conductivity

5.1.1. Why does the ferrous/ferric ratio change the electrical conductivity ?

Sodium has been identified in several studies of electrical conductivity of natural melts as the main charge carrier (Tyburczy and Waff, 1983, 1985; Gaillard, 2004; Pommier et al., 2008). The contribution of the different ionic species (Na^+, K^+, Ca^{2+}, Mg^{2+}, Si^{4+}, Al^{3+}, O^{2-}) can be discriminated using the Nernst-Einstein equation (cf Gaillard, 2004, Pommier et al., 2008):

$$\sigma_i = \frac{D_i.q_i^2.N_i}{k_B.T.Hr} \qquad \sigma_{measured} = \sum_i \sigma_i$$

where D_i is the coefficient of diffusion of an ion i (m^2/s), q_i its charge (C), N_i the concentration of i (m^{-3}), k_B is the Boltzmann constant, T is the absolute temperature (K) and Hr the Haven ratio. D_i values are taken from Chakraborty (1995), calculated at 1300°C. For the Kilauea basalt, at 1300°C, this equation underlines that the contribution of sodium to the bulk conductivity is ~80%, and the contribution of potassium is only 11%. This is coherent with the fact that the potassium cation is larger than Na and, thus, is supposed to diffuse in the melt with a slower rate than sodium. (usually, D_{Na}~10.D_K, Chakraborty, 1995). The contributions of calcium and oxygen are 3% and 4% respectively. The contributions of Mg, Si and Al are <1%. These calculations

underline, in particular, that the contribution of divalent cations to the measured conductivity is negligible in an alkali-rich melt. The identification of sodium as the main charge carrier in our melts implies that the changes observed in the electrical response of the samples during a redox reaction (i.e. an increase in σ during a reduction, a decrease in σ during an oxidation) can be related to the modifications affecting the mobility of sodium.

Other mobile species that do not control the measured electrical conductivity of the melt (such as electrons or electron holes) are not supposed to significantly affect the shape of the impedance spectra. Thus, their possible contribution to the redox mechanisms can not be observed directly using the interpretation of spectra.

Structural studies have well established that alkali charge-compensate tetrahedrally coordinated cations such as ferric iron (e.g. Thornber et al., 1980; Dickenson and Hess, 1981; Mysen, 1983; Kress and Carmichael, 1988; 1991; Lange and Carmichael, 1989; Tangeman et al., 2001; Mysen and Richet, 2005). The charge-compensation reaction can be written in a structural way (Mysen and Richet, 2005) as follows:

$$SiO_2 + NaFe^{III}O_2 \leftrightarrow \frac{1}{2}Na_2O + Fe^{II}O + SiO_{2.5} \qquad (5)$$

where ferric iron is charge-compensated by sodium on the left hand-side of the equation. This equilibrium enlightens the double role of sodium, being either a charge compensator (left hand-side of the equation) or a network modifier (NM) (right hand-side). During an oxidation, the observed decrease in electrical conductivity most likely reflects a restricted mobility of sodium, since it is structurally associated to tetrahedrally coordinated units with ferric iron. On the contrary, under more reduced conditions, less of such units are present within the melt. Thus, sodium mobility is enhanced, consistent with the observed increase in electrical conductivity. It is important to note that Eq. 5 considers only part of ferric iron as NF and part of ferrous iron as NM in the melt. Previous studies have shown that the presence of sodium in silicate melts promotes the formation of ferric iron (e.g. Kress and Carmichael, 1988).

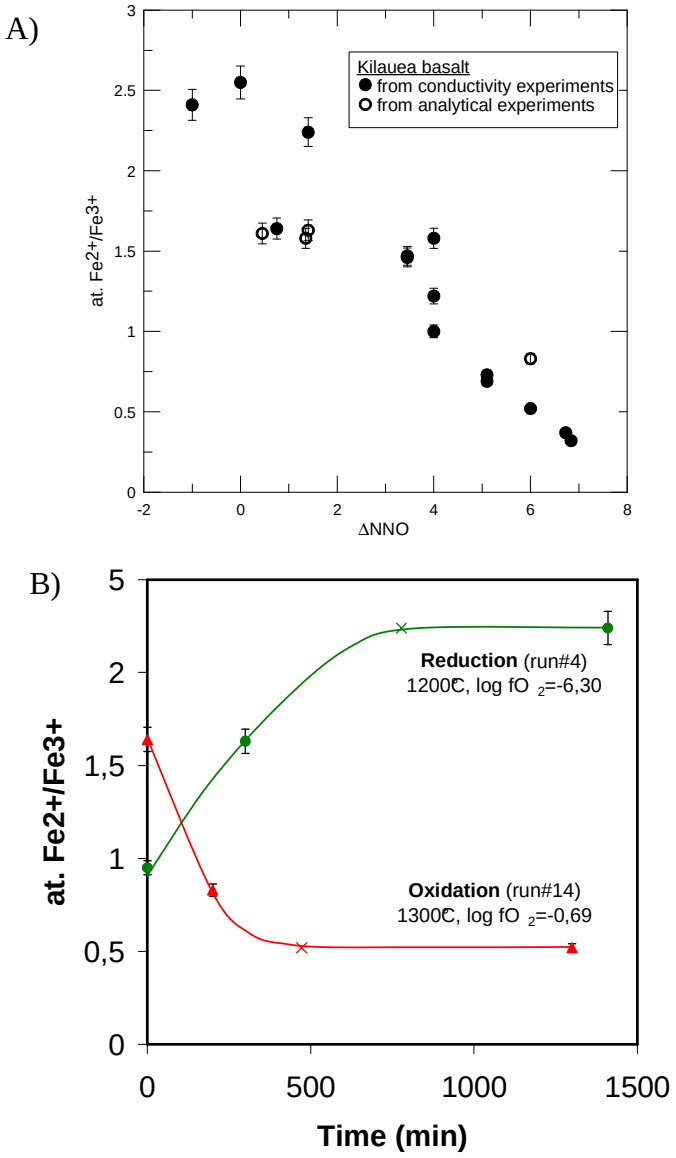


Figure 7: A) Ferrous-ferric ratio with ΔNNO for conductivity and analytical experiments performed on the Kilauea sample. See Tables 2 and 3 for experimental conditions. B) Equilibration time as a function of the ferrous-ferric ratio for the Kilauea sample. Examples of a reduction at 1200°C, log fO_2=-6.30 and of an oxidation at 1300°C, in air. The small error bars underline the high reproducibility of the wet chemical analyses. Crosses represent the attainment of chemical equilibrium (plateau value), determined using electrical measurements (see text for details). The curves are just a guide for the eye.

5.1.2. Time evolution of the electrical conductivity and ferrous/ferric ratio

In our experiments, the temporal changes of both the electrical conductivity and the ferrous/ferric ratio have been monitored. To analyze these temporal evolutions, it is convenient to use the progress variable ε defined as (Crank, 1975; Wendlandt, 1991):

$$\varepsilon(X) = (X(t)-X_0)/(X_{eq}-X_0) \qquad (6)$$

with X being either σ or Fe^{2+}/Fe^{3+}, X(t) the value of X at t, X_0 its initial value and X_{eq} its equilibrium value (plateau value). Both ε(σ) and ε(Fe^{2+}/Fe^{3+}) are compared in Figure 8 for experiments #4 (values at t=0, 300 and 1410min), #5 (t=0, 45 and 1860min), #6 (t=0, 45 and 430min) and #14 (t=0, 200 and 1300min) (Tables 2 and 3). The data fall on the straight line 1:1. This single trend underlines that, during a redox reaction, the electrical conductivity and the ferric/ferrous ratio increase or decrease with the same rate. Thus, the evolution of the electrical conductivity with time is identical to that of the redox ratio of the melt. It follows that the time-

dependence of the electrical response of the sample can be directly related to redox changes within the melt.

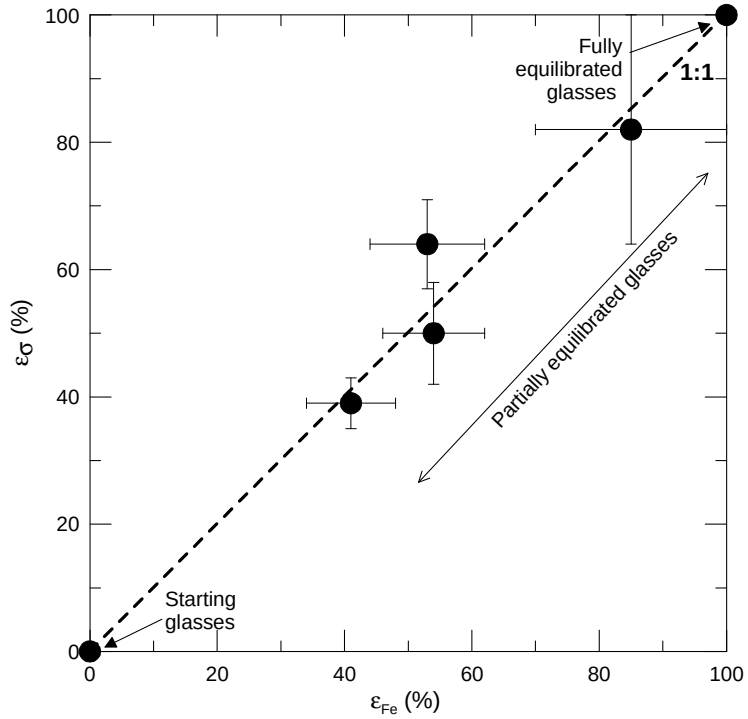


Figure 8: Comparison between the evolution of the electrical response of the sample and the evolution of the ferrous-ferric ratio (in %). Data points fall on the straight line 1:1, indicating similar kinetics of the evolution of the conductivity and of the redox ratio in the melt.

5.2. Determination of a bulk diffusion coefficient and transport properties

The experimental arrangement used in this study (Figure 1) is compatible with the mathematical model of the diffusion process applied to a plane sheet (Schreiber et al., 1986). In this model, diffusion occurs in a medium bounded by two parallel planes, with a constant flux on the upper boundary. Uniform initial distribution is considered. If diffusion-limited, the evolution of the electrical conductivity in response to a change in oxygen fugacity can be described by the following solution to the equation of one-dimensional diffusion:

$$\frac{\sigma(t)-\sigma_{initial}}{\sigma_{equilibrium}-\sigma_{initial}} = 1-\sum_{n=0}^{\infty}\frac{8}{(2n+1)^2\pi^2}.\exp\left[\frac{-D(2n+1)^2\pi^2 t}{4L^2}\right] \qquad (7)$$

with $\sigma(t)$ the electrical conductivity $(ohm.m)^{-1}$ at time t (s), $\sigma_{initial}$ the electrical conductivity $(ohm.m)^{-1}$ at t=0, $\sigma_{equilibrium}$ the electrical conductivity $(ohm.m)^{-1}$ at $t=t_{eq}$, D the bulk diffusion coefficient (m^2/s), and L the length of the sample (m) (Crank, 1975, p.48). Eq.7 assumes a

constant D as a function of time at a given temperature. The corresponding bulk redox front delimits the unreacted melt and is represented by ξ" on Figure 6.

Experimental data on the changes of conductivity with time (Figures 5a; b) were fitted using Eq. 7 and bulk diffusivity values (D) were determined. This approach proved successful for the reduction experiments performed with CO-CO_2 and the oxidation experiments in air (Figure 5a; b), suggesting that both redox reactions are diffusion-limited processes. Calculated values of D are similar within uncertainties when determined at the same temperature, underlining that reduction and oxidation kinetics operate at the same rates (Figure 9a). In contrast, oxidation performed under CO_2 is not compatible with Eq.7 and, therefore, in this case the redox evolution is not rate-limited by diffusion (Figure 5c). In general, redox studies have been performed assuming that the processes studied are diffusion-limited. Our approach, consisting in following redox processes in real-time and with high accuracy, suggests that the nature of the gaseous oxygen carrier influences the redox kinetics and that, the redox processes under CO_2 are probably not diffusion-limited. A linear evolution of the electrical conductivity with time is clearly observed, independently of the gas flux. A few previous studies have reported non-diffusion-limited processes during redox experiments under pure CO_2 (Goldman, 1983; Goldman and Gupta, 1983; Schreiber et al., 1986; Roskosz et al., 2008). Most likely, the linear changes shown in Figure 5c reveal a specific rate-limiting process at the gas/melt interface (e.g. surface diffusion, chemical reaction).

The temperature dependence of the calculated D values follows an Arrhenian dependence (Figure 9a):

$$D = D_0 . \exp\left[\frac{-Ea_D}{RT}\right] \qquad (8)$$

with Ea_D the activation energy (kJ/mol) and D_0 the pre-exponential factor (m^2/s). Our diffusivity values range from 10^{-9} to $10^{-8} m^2/s$ for the T range 1200-1400°C. These diffusion rates are comparable to typical alkali self-diffusion coefficients in basaltic melts from literature (Henderson, 1985; Chakraborty, 1995). Comparable diffusivity values are also calculated using the Nernst-Einstein equation (Eq. 5) and assuming that sodium is the unique charge carrier in the melt (i.e. $\sigma_{equilibrium}=\sigma_{Na+}$). These two points underline the importance of the role of sodium in the investigated redox processes. However, the high values of activation energy ($Ea_D \geq 200$kJ/mol, Figure 9a, b) calculated from Eq.8 are similar to activation energy for alkali-Earth elements (LaTourrette et al., 1996; Chakraborty, 1995) and oxygen self-diffusion (Lesher et al., 1996; Tinker et al., 2003) in silicate melts and is higher than the one expected for alkali self-diffusion (~100kJ/mol, Chakraborty, 1995) (see also Appendix 2).

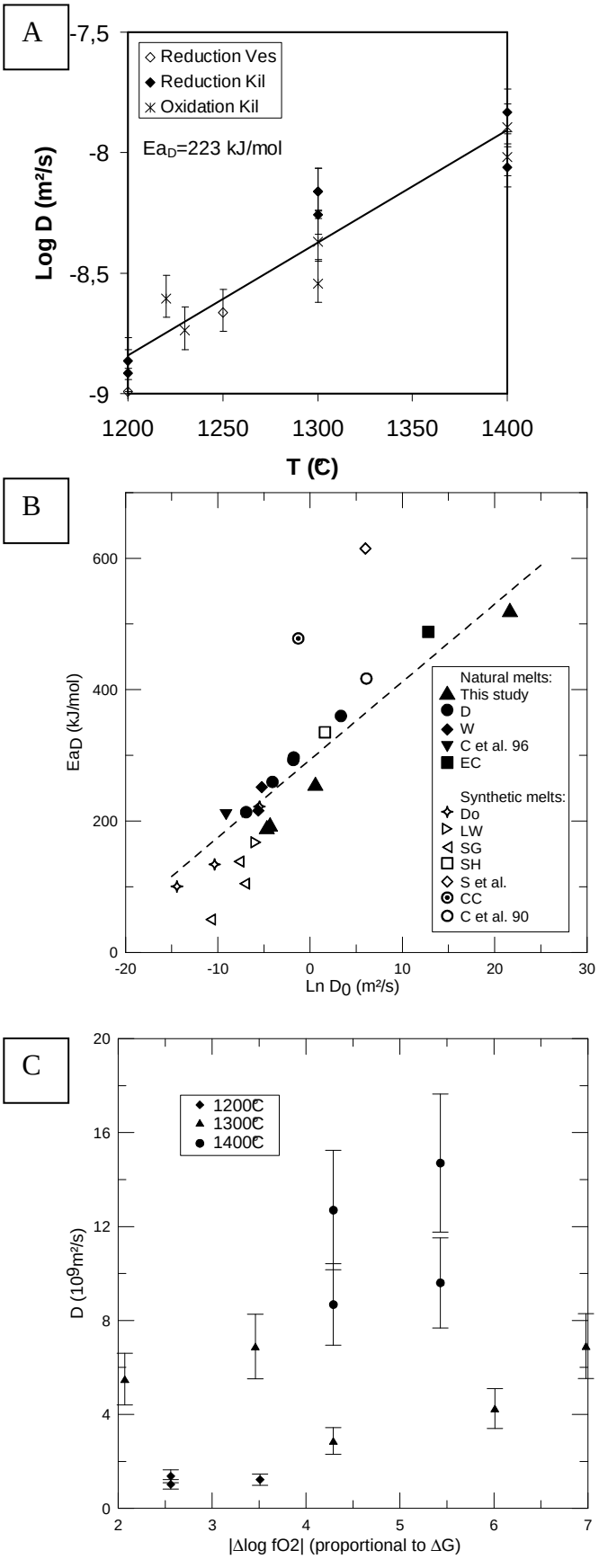


Figure 9: Calculated bulk diffusivity values. A) Diffusion coefficients calculated using the equation of diffusion (Eq. 7, cf Crank, 1975, p.48) vs temperature. Data are presented for both reduction (open diamonds: VES sample; filled diamonds: Kil sample) and oxidation (stars, Kil sample). Experimental conditions are detailed in Table 2. The general regression (straight line) yields a correlation factor of 0.81, underlining similar kinetics for both reduction and oxidation. The similar D values for the two basaltic samples can be explained by the small differences in the chemical compositions (Table 1). B) Compensation plot for the diffusion coefficients from this study (triangles, calculated using Eq. 7) and from other studies, attributed to either the diffusion of oxygen or of divalent cations (D: Dunn, 1983; W: Wendlandt, 1991; C et al. 96: Cooper et al., 1996; EC: Everman and Cooper, 2003; Do: Doremus, 1960; LW: Lawless and Wedding, 1970; SG: Sasabe and Goto, 1974; SH: Semkow and Haskin, 1985; S et al.: Schreiber et al., 1986; CC: Cook and Cooper, 2000; C et al. 90: Cook et al., 1990). Data for natural and synthetic silicate melts. The dashed line represents the compensation law for natural melts (Eq.9). C) Calculated diffusing rates as a function of oxygen fugacity variations (proportional to the driving potential). Data at 1200°C (Kilauea and Mt Vesuvius samples), 1300°C and 1400°C (Kilauea sample).

Activation energy and pre-exponential term for redox kinetics in melts obtained in this study and previous ones (Lawless and Wedding, 1970; Sasabe and Goto, 1974; Doremus, 1960; Dunn, 1983; Semkow and Haskin, 1985; Schreiber et al., 1986; Cook et al., 1990; Wendlandt, 1991; Cooper et al., 1996; Cook and Cooper, 2000; Everman and Cooper, 2003) are plotted in a compensation plot (Figure 9b). The compensation law for natural melts ($r^2>0.91$) is:

$$Ea_D = 11.84.LnD_0+293.5 \quad (9)$$

The single trend stresses that the kinetics of redox changes in our study is essentially similar to that found in other studies.

Figure 9c presents the calculated oxidation-reduction rates as a function of oxygen fugacity variations. Variations of fO_2 (initial fO_2 – final fO_2) are directly correlated to variations of the driving potential (or driving force, $\Delta\mu$) of the redox reaction occurring in the melt:

$$\Delta\mu = \Delta (R.T.Ln\ fO_2) \quad (10)$$

No clear evidence of such a dependence of D values is observed for our experiments, even for the experiments at 1300°C that involve the largest $|\Delta \log fO_2|$ (from 2 to 7). Figure 9c suggests that a possible dependence of D to variations of fO_2 is too weak to be discriminated and that the high D values calculated in our redox experiments can not be explained by variations of the driving potential.

5.3. Redox dynamics

Redox mechanisms are proposed on the basis of conductivity measurements, chemical titrations, mass balance calculations, EMPA profiles and previous redox studies. EMPA profiles (Figure 6) show complex pattern of chemical zonation, which are however difficult to interpret in terms of cation fluxes, since a change in cation content can be caused by the dilution effect of other mobile species. Microprobe traverses were nevertheless used to detect an internal reaction front, ξ', whose location is presented in Figure 6. ξ' corresponds to an inflexion point in the chemical profiles.

ξ' is different from the bulk reaction front ξ'' provided by bulk diffusion coefficients (Eq.7). The identification of these two fronts stresses out two different steps of one reaction or two different reactions that are all part of the redox mechanisms. Position of ξ' at t corresponds to diffusivities in the melt of $\sim 10^{-11} m^2/s$ for both reductions and oxidations, using the following equation:

$$D=L^2/t \quad (11)$$

D the diffusion coefficient (m²/s), L defining the distance between ξ' and the gas/melt interface (m), t the time of quenching (s). These values are much lower than bulk diffusivities deduced from conductivity measurements using Eq.7 (10^{-9}-10^{-8} m^2/s). The progression rate of ξ' compares well with self-diffusivities of O and Si in basaltic liquid (Canil and Muehlenbachs, 1990; Lesher et al., 1996) and with the rate laws derived by Cooper and coworkers using similar methodologies (identification of a migration front of cations). Another argument for O and Si mobility in the interface zone is that our Ea_D values are comparable with Ea values from viscosity measurements (Giordano et al., 2008), which are based on the Si-O bounds (and oxygen mobility). The mobility of Si as Si-O has been previously suggested by Terai and Oishi, 1977. This suggests that Si-O mobility defines the progression of ξ', which is not considered in the model of Cooper et al. (1996b). Si-O species are less mobile than sodium and they are not charged species. Thus, they do not directly influence the observed changes in conductivity. However, their migration could influence the charge carrier mobility. The effect of Si-O on σ would thus be indirect and part of the cations mobility can be interpreted as a consequence of Si-O migrations.

The progression rate of ξ', graphically deduced from EMPA profiles, is slower than the progression rate of ξ'', determined using electrical measurements and corresponding to the rate of the evolution of the redox ratio. This implies that apparent divalent cation migration and Fe^{2+}/Fe^{3+} changes are kinetically decoupled. This was not observed in previous studies that proposed redox mechanisms controlled by divalent cations mobility, since the time-evolution of the Fe^{2+}/Fe^{3+} ratio was not monitored in these studies (e.g., Cooper et al., 1996b). The rate laws of the evolution of ξ'' observed in our study are comparable to the kinetics of iron redox reactions in silicate melts (e.g. Magnien et al., 2008).

A schematic drawing of reduction and oxidation dynamics at the scale of the sample are proposed in Figure 10. The model considers the main fluxes of mobile species and, in particular, the rate-limiting ionic fluxes that probably hide other minor processes occurring at the same time. This implies that metastable structures that are probably formed during the initial stages of the redox reaction are not represented. We assume that the influence of these structures on the calculations of diffusion coefficients of mobile species during the redox reaction can be neglected. The model used to represent the evolution of a redox reaction is based on a Fickian formalism. This simple approach can be used as a first approximation which allows us to explain the D values in terms of major cation fluxes. The fluxes of cations (j_i) between the free surface

(ξ_0) and the bulk reaction front ξ" have been analyzed using the Fick-Einstein equation applied to ionic materials (Cooper et al., 1996a):

$$j_i = \frac{x_i.D_i}{\lambda_i.Vm.\Delta\xi}.\ln\left(\frac{f_{O2}^{\xi=0}}{f_{O2}^{\xi"}}\right) \qquad (11)$$

with x_i the molar fraction of the cation i (Na^+, K^+, Ca^{2+}, Mg^{2+}, Fe^{2+}), D_i its diffusion coefficient (m^2/s), λ_i the stoechiometric coefficient, Vm the molar volume of the reduced or oxidized melt (m^3/mol), Δξ the distance between the free surface and the bulk reaction front (m), and f_{O2} the oxygen fugacity (Pa) (with the superscript indicating location). The f_{O2} ratio expresses the difference in oxygen chemical potential between reacted and unreacted melt (i.e. between ξ_0 and ξ"). D values for cations come from the literature (Henderson et al., 1985; Chakraborty, 1995; Lesher et al., 1996) and are assumed to be constant during the redox reaction. λ_i values correspond to the number of mol of cation in the oxidized form (molecular form) that is produced when one mole of O_2 reacts with cation i. Details on the calculations of λ_i are presented in Appendix 3. Δξ is calculated using Eq. 10 with $D=D_{bulk}$ (from Eq.7) and $t=t_{quench}$ (Table3).

In the case of redox mechanisms driven by a single kind of ionic species (e.g. divalents cations, Cooper et al., 1996), the motion of the redox front into the melt with time can be written as follows:

$$\frac{d\Delta\xi}{dt} = \lambda_{M^{2+}}.j_{M^{2+}}.Vm = \frac{x_{M^{2+}}.D_{M^{2+}}}{\Delta\xi}.\ln\left(\frac{f_{O2}^{\xi_0}}{f_{O2}^{\xi"}}\right) \qquad (13)$$

M^{2+} being a divalent cation. These mechanisms were observed for experimental timescales of a few seconds or minutes (Cooper et al., 1996b; Everman and Cooper, 2003) or in the glass region (Cooper et al., 1996a; Cook and Cooper, 2000). As discussed before, at the timescale of our experiments (i.e. several hours), redox dynamics in the basaltic melts probably not come down to the only divalent cation fluxes. Our study suggests that oxygen, and alkalis also probably contribute significantly to the advancement of the bulk redox front ξ". The time-evolution of the redox front becomes:

$$\frac{d\Delta\xi}{dt} = \left(\sum_{M^{2+}}\lambda_{M^{2+}}.j_{M^{2+}} + \sum_{A^+}\lambda_{A^+}.j_{A^+} + \lambda_{O^{2-}}.j_{O^{2-}} + \lambda_{h^\cdot}.j_{h^\cdot}\right).Vm \qquad (14)$$

with M^{2+}= Ca^{2+}, Mg^{2+}, Fe^{2+}, A^+= Na^+, K^+ and $h^\cdot$ the electron holes. $\lambda_{M2+}=\lambda_{A+}=2$, $\lambda_{O2-}=2$, $\lambda_{h.}=4$ (Appendix 3).

Si^{4+} and Al^{3+} ions are not considered in the present redox model. No evidence of free Si^{4+} ions has been found in previous studies (Bockris et al., 1952; Semkow and Haskin, 1985). The very high bond energy of Si-O (~373kJ/mol, Bockris et al., 1952) strengthens the low probability

for Si^{4+} ions to exist in a free state capable of migration within the melt. A significant role of aluminium in redox mechanisms has never been observed, to our knowledge.

The fluxes of considered cations are calculated using Eq.12 and the flux of oxygen can be expressed by:

$$j_{O^{2-}} = \frac{x_{O^{2-}}.D_{O^{2-}}}{2.Vm.\Delta\xi}.\ln\left(\frac{f_{O2}^{\xi=0}}{f_{O2}^{\xi''}}\right) \qquad (15)$$

where $x_{O^{2-}} = \frac{n_{oxygen}}{n_{total}}$. n_{oxygen} corresponds to the total oxygen content of the melt. n_{total} corresponds to the amount of oxygen and cations. Both n_{oxygen} and n_{total} are determined by mass balance calculations. As in Cooper et al. (1996a), the flux of electron holes ($j_{h.}$) was calculated using the charge neutrality condition:

$$\sum_i z_i.j_i = \left(\sum_{cations} z_{cations}.j_{cations}\right) - 2j_{O^{2-}} + j_{h^{\cdot}} = 0 \qquad (16)$$

where $z_{cations}$ corresponds to the valence of the cations. Calculation of $d\xi/dt$ using Eq. 14 for the quenched experiments yields similar values for oxidation and reduction at the same temperature. For instance, $d\xi/dt = 2.2.10^{-7}$m/s and 8.10^{-8}m/s for experiments #12-QO and #4-QR, respectively (Table 3).

As shown in Figure 10, the incorporation (oxidation) or release (reduction) of oxygen leads to competitive mechanisms between the different ionic species. At the internal front ξ', variations of Na^+ mobility are related to the reduction or oxidation of ferric or ferrous iron, respectively. In oxidation and reduction experiments, the reacted melt (delimited by front ξ") is characterized by opposite fluxes of oxygen and cations. The smaller amounts of network-modifier cations compared to oxygen anions imply electron holes to charge-balance O^{2-} fluxes.

According to Eq. 12 and 14, the evolution of the redox front as a function of time can be written as follows:

$$\Delta\xi.d\Delta\xi = \sum_i Ai.dt \qquad \text{with} \qquad Ai = x_i.D_i.\ln\left(\frac{f_{O2}^{\xi_0}}{f_{O2}^{\xi''}}\right) = \lambda_i.j_i.Vm \qquad (17)$$

Integration of Eq. 17 leads to the following parabolic kinetic law:

$$\int_{\xi_0=0}^{\xi''} \Delta\xi . d\Delta\xi = \sum_i Ai . \int_{t_0=0}^{t} dt \quad \Rightarrow \quad \frac{\xi''^2}{t} = 2.\sum_i Ai \qquad (18)$$

The term $\frac{\xi''^2}{t}$ (in m²/s) corresponds to a bulk diffusion coefficient associated to the redox reaction and, thus, should be compared to the values of the redox front diffusion coefficient D_{bulk} calculated using Eq. 7. Numerical calculations yield values of $\frac{\xi''^2}{t}$ similar to the measured D_{bulk} (Eq.7 and Figure 9a): between ~$1.8.10^{-9}$m²/s at 1200°C and ~$4.5.10^{-9}$m²/s at 1300°C. This implies that the evolution of the redox front with time can be explained by a mechanism involving co-operative fluxes of cations, oxygen and electron holes. The contribution of cations and oxygen to the redox mechanisms are in agreement with the high activation energy values calculated using Eq.8 (>200kJ/mol). The calculated fluxes of cation (Eq. 12) needed to match the global redox kinetics are however small (10^{-11}-10^{-13} mol.m^{-2}.s^{-1}). This is consistent with the absence of noticeable cations variations in the inner part of the quenched samples using EMPA profiles (distance>ξ', see Figure 6). Highest values of fluxes correspond to oxygen and sodium (~10^{-11} mol.m^{-2}.s^{-1}, whereas fluxes of potassium and divalent cations are ~10^{-12}-10^{-13} mol.m^{-2}.s^{-1}), implying that these two species are the main contributors to the redox dynamics.

The mechanism that occurs to finally provide a uniform chemistry (e.g. from profile C to D in Figure 6) probably consists in a reequilibration of electrochemical potential. This reequilibration would correspond, in the case of our samples, to a coupled exchange of moving back alkali and divalent cations.

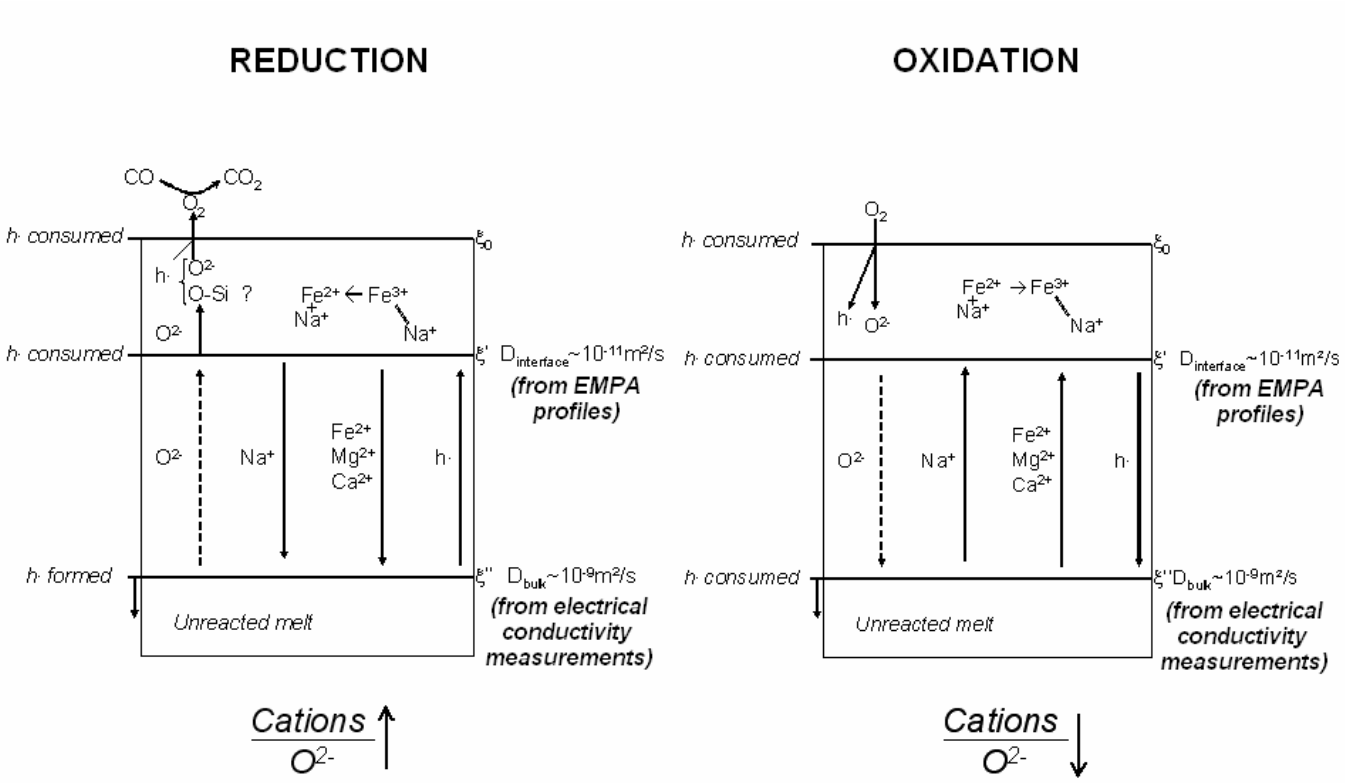


Figure 10: Redox dynamics in the Kilauea basalt in the T range 1200-1400°C. Both reduction and oxidation involve chemical reactions at the free surface of the sample (ξ_0) and at two internal fronts (ξ' and ξ"). At ξ_0, oxygen is released or incorporated in the melt, with $h^{\cdot}$ being consumed or absorbed, respectively. At the internal front (ξ'), Fe^{3+} is reduced to Fe^{2+} (reduction) or Fe^{2+} is oxidized to Fe^{3+} (oxidation), implying variations on Na^{+} mobility, and thus on the electrical response of the melt (see text for details). The measured bulk diffusion coefficient corresponds to the second internal front (ξ"). Competitive mechanisms occur between oxygen and cations diffusion. The smaller amounts of network-modifier cations compared to oxygen anions imply electron holes to charge-balance O^{2-} fluxes. The high diffusivities of $h^{\cdot}$ probably enhance oxygen and cations diffusion, since the D values are deduced from electrical measurements and are thus related to charged mobile species. Oxygen probably moves in the melt as both ionic (O^{2-}) species, as underlined by several studies (e.g. Goldman and Gupta, 1983; Dunn, 1983; Schreiber et al., 1986; Wendlandt, 1991) and as oxide species, since spectroscopic studies showed that most bridging oxygens have cations in their first coordination shell, forming Q species (e.g. Stebbins, 1995).

6. CONCLUSION AND REDOX EXCHANGES IN NATURE

Electrical measurements have been used to investigate in real-time redox kinetics in basaltic liquids after fO_2-step changes. Data were recorded between 1200 and 1400°C, on the fO_2 range 10^{-8}-0.2 bars. Electrical conductivity was found to increase slightly with decreasing fO_2. A modified Arrhenius law expressing the dependence of the electrical conductivity to both fO_2 and T has been proposed. The evolution of electrical conductivity, based on sodium mobility, reproduces the evolution of the ferric/ferrous ratio of the melt. Reduction under CO-CO_2 and oxidation in air are diffusion-limited processes, whereas a gas-melt interface reaction probably rate-limit oxidation under pure CO_2. The high diffusion rates (10^{-9}-10^{-8}m²/s) and activation energies (>200 kJ/mol) calculated on the investigated T range in basaltic melts can be explained by redox mechanisms involving co-operative alkali, divalent cations and oxygen fluxes.

According to Gaillard et al. (2003a), attainment of redox equilibrium in hydrogen-bearing melts was found to be rate-controlled by H_2 fluxes in the melt at a reaction front corresponding to:

$$H_2 + 2\ FeO_{1.5} = 2\ FeO + H_2O \qquad (18)$$

This statement was particularly supported by the fact that H_2 migration in the melt is much faster than divalent cations migration calculated after Cooper and coworkers. For example, at 1300°C, at f_{H2}=1 and 100bar, Gaillard et al. (2003a) calculated reaction rates of iron redox changes in hydrous magmas of ~$2.5.10^{-12}$ and 10^{-9} m²/s, respectively, while extrapolation of D values of Cooper et al. (1996a) at the same T in basaltic melts provides a reaction rate of ~4.10^{-13} m²/s. Our results, however, indicate reaction rates of 10^{-9}-10^{-8}m²/s at 1300°C, which exceed well the rates extrapolated from Cooper et al (1996a). The hydrogen-dominated mechanisms exposed in Gaillard et al. (2003a) will therefore not necessarily operate in basaltic systems because cooperative motions of oxygen and cations revealed in our study can be faster than exchanges rate-limited by H_2 fluxes. Only for fH_2 values exceeding 50 bars, reaction rates are nearly equivalent, implying that the mechanisms of Gaillard et al. might affect basalts under specific conditions such as in moderately oxidized mantle wedge (water-rich at NNO). However, in most conditions experienced by basaltic liquids (i.e. moderately hydrated), the mechanism we revealed in our study should dominate the kinetics of redox potential re-equilibration.

Acknowledgements

This paper is part of the PhD of A. Pommier. The authors are grateful to T. Orr for providing Kilauea sample and R. Cioni for Mt Vesuvius sample. R.F. Cooper, M. Roskosz and an anonymous reviewer are warmly thanked for helpful comments and fruitful discussions. P. Ulmer is acknowledged for his careful editorial work. This study has been supported by the French national agency for research, ANR JC05-42707 (Electrovolc) attributed to F. Gaillard.

References

Beerkens, R.G.C., and H. de Waal (1990), Mechanism of oxygen diffusion in glassmelts containing variable-valence ions, *J. Am. Cearm. Soc.*, 73 (7), 1857-1861.

Behrens, H., and F. Gaillard (2006), Geochemical aspects of melts: volatiles and redox behavior, *Elements*, 2 (5), 275-280.

Bockris, J. O'M., J.A. Kitchener, S. Ignatowitcz, and J. W. Tomlinson (1952), Electric conductance in liquid silicates, *Trans. Farad. Soc.*, 48 (6), 536-548.

Botcharnikov, R. E., J. Koepke, F. Holtz, C. McCammon, and M. Wilke (2005), The effect of water activity on the oxidation and structural state of Fe in a ferro-basaltic melt, *Geochim. Cosmochim. Acta*, 69 (21), 5071-5085.

Canil, D. and K. Muehlenbachs (1990), Oxygen diffusion in an Fe-rich basalt melt, *Geochim. Cosmochim. Acta*, 54, 2947-2951.

Carmichael, I. S. E. (1991), The redox states of basic and silicic magmas-a reflection of their source region, *Contrib. Mineral. Petrol.*, 106 (2), 129-141.

Carmichael, I. S. E. and M. S. Ghiorso (1990), The effect of oxygen fugacity on the redox state of natural liquids and their crystallizing phases, *Modern source of igneous petrology: understanding magmatic processes*, vol. 24, 191-212.

Chakraborty, S., (1995), Diffusion in silicate melts, in Structure, dynamics and properties of silicate melts, *Reviews in Mineralogy*, vol. 32, 411-503.

Cook, G. B., R. F. Cooper and T. Wu (1990), Chemical diffusion and crystalline nucleation during oxidation of ferrous iron-bearing magnesium aluminosilicate glass, *J. Non-Cryst. Solids*, 120, 207-222.

Cook, G. B., and R. F. Cooper (2000), Iron concentration and the physical processes of dynamic oxidation in an alkaline earth aluminosilicate glass, *Am. Mineralogist*, 85, 397-406.

Cooper, R. F., J. B. Fanselow, and D. B. Poker (1996a), The mechanism of oxidation of a basaltic glass: chemical diffusion of network-modifying cations, *Geochim. Cosmochim. Acta*, 60(17), 3253-3265.

Cooper, R. F., J. B. Fanselow, J. K. R. Weber, D. R. Merkley, and D. B. Poker (1996b), Dynamics of oxidation of a Fe2+-bearing aluminosilicate (basaltic) melt, *Science*, 274, 1173-1176.

Crank, J. (1975), The Mathematics of Diffusion, 2nd ed., 440 pp., Claredon, Oxford, U.K.

Deines, P., R. H. Nafziger, G. C. Ulmer, and E. Woermann (1974), Temperature-oxygen fugacity tables for selected gas mixtures in the system C-H-O at one atmosphere total pressure, *Bull. Earth and Mineral Sciences*, Experiment Station, 88, 130pp., University Park, Pennsylvania, USA.

Dickenson, M.P., and P.C. Hess (1981), Redox equilibria and the structural role of iron in alumino-silicate melts, *Contrib. Mineral. Petrol.*, 78, 352-357.

Doremus, R. H. (1960), Diffusion of oxygen from contracting bubbles in molten glass, *J. Amer. Ceram. Soc*., 43(12), 655-661.

Dunn, T. (1982), Oxygen diffusion in three silicate melts along the join diopside-anorthite, *Geochim. Cosmochim. Acta*, 46, 2293-2299.

Dunn, T. (1983), Oxygen chemical diffusion in three basaltic liquids at elevated temperatures and pressures, *Geochim. Cosmochim. Acta*, 47, 1923-1930.

Dunn, T. and C. M. Scarfe (1986), Variation of the chemical diffusivity of oxygen and viscosity of an andesite melt with pressure at constant temperature, *Chem. Geology*, 54, 203-215.

Everman, R. L. A. and R. F. Cooper (2003), Internal reduction of an iron-doped magnesium aluminosilicate melt, *J. Amer. Ceram. Soc*., 86(3), 487-494.

Frost, D. J., and C. A. McCammon (2008), The redox state of the Earth's mantle, *Annual Rev. Earth and Planet. Sciences*, 36, 389-420.

Gaillard, F., B. Scaillet and M. Pichavant (2002), Kinetics of iron oxidation-reduction in hydrous silicic melts, *Am. Mineralogist*, 87(7), 829-837.

Gaillard, F., B. Schmidt, S. Mackwell and C. McCammon (2003a), Rate of hydrogen-iron redox exchange in silicate melts and glasses, *Geochim. Cosmochim. Acta*, 67 (13), 2427-2441.

Gaillard, F., M. Pichavant, and B. Scaillet (2003b), Experimental determination of activities of FeO and Fe2O3 components in hydrous silicic melts under oxidizing conditions, *Geochim. Cosmochim. Acta*, 67 (22), 4389-4409.

Gaillard, F. (2004), Laboratory measurements of electrical conductivity of hydrous and dry silicic melts under pressure, *Earth Planet. Sci. Lett.*, 218(1–2), 215–228, doi:10.1016/S0012-821X(03)00639-3.

Gaillard, F., and G. Iacono-Marziano (2005), Electrical conductivity of magma in the course of crystallization controlled by their residual liquid composition, *J. Geophys. Res*., 110, B06204, doi:10.1029/ 2004JB003282.

Gaillard, F., and B. Scaillet (2009), The sulfur content of volcanic gases on Mars, *Earth Planet. Sci. Lett.*, 279, 34-43.

Giordano, D., J. K. Russell, and D. B. Dingwell (2008), Viscosity of magmatic liquids: A model, *Earth Planet. Sci. Lett.*, 271(1-4), 123-134.

Goldman, D. S. (1983), Oxidation equilibrium of iron in borosilicate glass, *J. Amer. Ceram. Soc*., 66(3), 205-209.

Goldman, D. S. and P. K. Gupta (1983), Diffusion-controlled redox kinetics in a glassmelt, *J. Amer. Ceram. Soc*., 66(3), 188-190.

Henderson, P., J. Nolan, G. C. Cunningham, and R. K. Lowry (1985), Structural control and mechanisms of diffusion in natural silicate melts, *Contrib. Mineral. Petrol*., 89(2 – 3), 263 – 272, doi:10.1007/BF00379459.

Herd, C. D. K., L. E. Borg, J. H. Jones, and J. J. Papike (2002), Oxygen fugacity and geochemical variations in the martian basalts: implications for martian basalt petrogenesis and the oxidation state of the upper mantle of Mars, *Geochim. Cosmochim. Acta*, 66(11), 2025-2036.

Herd, C. D. K. (2008), Basalts as probes of planetary interior redox state, *Reviews in Mineralogy and Geochemistry*, 68, 527-553.

Huebner, J. S., and R. G. Dillenburg (1995), Impedance spectra of hot, dry silicate minerals and rock: Qualitative interpretation of spectra, *Am. Mineral*., 80(1– 2), 46–64.

Jaupart, C., and Tait, S. (1995), Dynamics of differentiation in magma reservoirs, , *J. Geophys. Res.*, 100, B9: 17615-17656.

Kress, V. C., and I. S. E. Carmichael (1988), Stoichiometry of the iron oxidation, *Am. Mineral.*, 73(11-12), 1267-1274.

Kress, V. C., and I. S. E. Carmichael (1991), The compressibility of silicate liquids containing Fe2O3 and the effect of composition, temperature, oxygen fugacity and pressure on their redox states, *Contrib. Mineral. Petrol*., 108(1-2), 82-92.

Lange, R. A. and I. S. E. Carmichael (1989), Ferric-ferrous equilibria in Na2O-FeO-Fe2O3-SiO2 melts – effects of analytical techniques on derived partial molar volumes, *Geochim. Cosmochim. Acta*, 53(9), 2195-2204.

La Tourrette, T., G.J. Wasserburg and A.J. Fahey (1996), Self diffusion of Mg, Ca, Ba, Nd, Yb, Ti, Zr, and U in haplobasaltic melt, *Geochim. Cosmochim. Acta*, 60(8), 1329-1340.

Lawless, W. N., and B. Wedding (1970), Photometric study of the oxygen diffusivity in aluminosilicate glass, *J. Appl. Phys.*, 41, 1926-1929.

Lesher, C.E., R.L. Hervig and D. Tinker (1996), Self diffusion of network formers (silicon and oxygen) in naturraly occurring basaltic liquid, *Geochim. Cosmochim. Acta*, 60(3), 405-413.

Magnien, V., D. R. Neuville, L. Cormier, J. Roux, J.-L. Hazemann, D. de Ligny, S. Pascarelli, I. Vickridge, O. Pinet, and P. Richet (2008), Kinetics and mechanisms of iron redox reactions in silicate melts: the effects of temperature and alkali cations, *Geochim. Cosmochim. Acta*, 72(8), 2157-2168 .

Maumus, J., N. Bagdassarov, and H. Schmeling (2005), Electrical conductivity and partial melting of mafic rocks under pressure, *Geochim. Cosmochim. Acta*, 69(19), 4703–4718, doi:10.1016/j.gca.2005.05.010.

Moretti, R., and P. Papale (2004), On the oxidation state and volatile behavior in multicomponent gas-melt equilibria, *Chem. Geology*, 213, 265-280.

Moynihan, C.T., Description and analysis of electrical relaxation data for ionically conducting glasses and melts, *Solid State Ionics* 105 (1998), 175-183.

Muelhenbachs, K. and I. Kushiro (1974), Oxygen isotope exchange and equilibrium of silicates with CO_2 or O_2, Carnegie Instn Geophys. Laboratory, 73, 232-236.

Mysen, B. O. (1983), The structure of silicate melts, *Ann. Rev. Earth Planet. Sci.*, 11, 75-97.

Mysen, M. O., and P. Richet (2005), Silicate Glasses and Melts, Properties and Structure, 544 pp., Elsevier, Amsterdam, Netherlands.

Pettersen, C., and R. F. Cooper (2008), Float-reaction between liquid bronze and magnesium aluminosilicate and ZnO-doped magnesium aluminosilicate glass-ceramic-forming glassmelts, *J. Non-Cryst. Solids*, 354, 3194-3206.

Pommier, A., F. Gaillard, M. Pichavant, and B. Scaillet (2008), Laboratory measurements of electrical conductivities of hydrous and dry Mount Vesuvius melts under pressure, *J. Geophys. Res.*, 113, B05205, doi:10.1029/2007JB005269.

Pommier, A., M. Malki, F. Gaillard, and M. Pichavant (2009), Methodological re-evaluation of the electrical conductivity of silicate melts, *Am. Mineralogist*, accepted.

Pownceby and O'Neill (1994), Thermodynamic data from redox reactions at high temperatures. IV. Calibration of the Re-ReO2 oxygen buffer from EMF and NiO+Ni-Pd redox sensor measurements, *Contrib. Mineral. Petrol*., 118, 130 – 137.

Reid, J. E., B. T. Poe, D. C. Rubie, N. Zotov, and M. Wiedenbeck (2001), The self-diffusion of silicon and oxygen in diopside ($CaMgSi_2O_6$) liquid up to 15 GPa, *Chem. Geology*, 174, 77-86.

Righter, K., and M. J. Drake (1996), Core formation in the Earth's Moon, Mars and Vesta, *Icarus*, 124, 513-529.

Roberts, J. J., and J.A. Tyburczy (1994), Frequency-dependent electrical properties of minerals and partial melts, *Surveys in Geophysics*, 15(2), 239-262.

Roselieb, K., and A. Jambon (2002), Tracer diffusion of Mg, Ca, Sr and Ba in aluminosilicate melts, *Geochim. Cosmochim. Acta*, 66, 109–123.

Roskosz, M., M. J. Toplis, D. R. Neuville, and B. O. Mysen (2008), Quantification of the kinetics of iron oxidation in silicate melts using Raman spectroscopy and assessment of the role of oxygen diffusion, *American Mineralogist*, 93(11-12), 1749-1759.

Sasabe, M., and K. S. Goto (1974), Permeability, diffusivity, and solubility of oxygen gas in liquid slag, *Metall. Transactions*, 5, 2225-2233.

Semkow, K. W. and L. A. Haskin (1985) Concentrations and behavior of oxygen and oxide ion in melts of composition CaO-MgO-$XSiO_2$, *Geochim. Cosmochim. Acta*, 49(9), 1897-1908.

Schmalzried, H. (1984), Oxide solid-solutions and its internal reduction reactions, *H. Ber. Bunsen-Ges. Phys. Chem.*, 88, 12, 1186-1191.

Schreiber, H. D., and S. J. Kozac, A. L. Fritchman, D.S. Goldman, and H. A. Schaeffer (1986), Redox kinetics and oxygen diffusion in a borosilicate melt, *Physics Chem. Glasses*, 27(4), 152-177.

Tangeman, J. A., R. Lange, and L. Forman (2001), Ferric-ferrous equilibria in K_2O-FeO-Fe_2O_3-SiO_2 melts, *Geochim. Cosmochim. Acta*, 65(11), 1809-1819.

Thornber, C. R., P. L. Roeder, and J. R. Foster (1980), The effect of composition on the ferric-ferrous ratio in basaltic liquids at atmospheric pressure, *Geochim. Cosmochim. Acta*, 44, 525-532.

Tinker, D., C. E. Lesher, and I. Hutcheon (2003), Self-diffusion of Si and O in diopside-anorthite melt at high pressures, *Geochim. Cosmochim. Acta*, 67(1), 133-142.

Tyburczy, J. A., and H. S. Waff (1983), Electrical conductivity of molten basalt and andesite to 25 kilobars pressure: Geophysical significance and implications for charge transport and melt structure, *J. Geophys. Res.*, 88(B3), 2413–2430, doi:10.1029/JB088iB03p02413.

Tyburczy, J. A., and H. S. Waff (1985), High pressure electrical conductivity in naturally occurring silicate liquids, in Point Defects in Minerals, Geophys. Monogr. Ser., vol. 31, edited by R. N. Shock, pp. 78– 87, AGU, Washington, D.C.

Waff, H. S., and D. F. Weill (1975), Electrical conductivity of magmatic liquids: effects of temperature, oxygen fugacity and composition, *Earth Planet. Sci. Lett.*, 28, 254–260.

Wendlandt, R. F. (1991), Oxygen diffusion in basalt and andesite melts: experimental results and discussion of chemical versus tracer diffusion, *Contrib. Mineral. Petrol*., 108, 463-471.

Appendix 1: On the difference between oxygen self-diffusion (D*) and chemical diffusion (D) coefficients

As underlined by Cooper et al. (1996a), two kinds of experiments are commonly used to study diffusion-limited oxidation/reduction kinetics: oxygen self-diffusion and chemical diffusion (redox) experiments. By "chemical diffusion experiments", we consider experiments that let the sample equilibrate with a change in the gaseous atmosphere. The diffusing species, depending on the authors, are oxygen or cations or both (this study). By "oxygen self-diffusion experiments", we consider experiments (mainly isotopic) that study the tracer (or network) diffusion of oxygen. As shown in the following Figure A, several orders of magnitude separate values of chemical diffusion coefficients and oxygen self-diffusion coefficients for similar silicate melts compositions (D>D*). For example, in a basaltic melt at 1300°C, in air, the self-diffusion coefficient of oxygen is estimated at $\sim 6.5.10^{-12} m^2/s$ (Canil and Muehlenbachs, 1990) while we calculated from our study a bulk chemical diffusion coefficient of $\sim 3.5.10^{-9} m^2/s$.
Differences have been interpreted in terms of diffusion mechanisms, chemical diffusion involving the diffusion of molecular oxygen, vacancies or cations and tracer diffusion involving the migration of ionic species (Schreiber et al., 1986; Wendlandt, 1991; Cooper et al., 1996a).

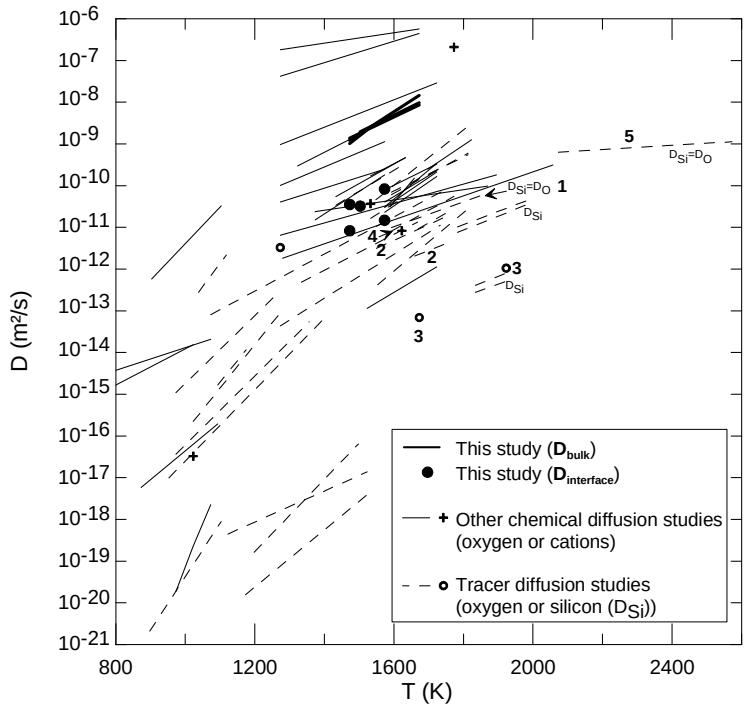


Figure A: Comparison between chemical diffusion experiments and oxygen self-diffusion experiments. Diffusion coefficients as a function of temperature. Data from this study (bold full lines and filled circles) and other chemical diffusion studies (full lines and crosses) and tracer diffusion studies (dashed lines and empty circles). Data are taken from this study and from May et al. (1974) and references therein; Schreiber et al. (1986) and references therein; Canil and Muehlenbachs (1990); Cook et al. (1990); Wendlandt (1991); Cooper et al. (1996); Cook and Cooper (2000); Smith and Cooper (2000); Reid et al. (2001); Everman and Cooper (2003); Magnien et al. (2008). 1: Tinker et al. (2003) and Lesher et al. (1996); 2: Dunn (1982); 3: Shimizu and Kushiro (1984); 4: Canil and Muehlenbachs (1990); 5: Reid et al. (2001).

Appendix 2: Estimation of a normalized driving force

Another way to interpret the temperature-dependence of diffusivity values is to consider a normalized driving force $\Delta G/RT$. Over the investigated T range, this normalized driving force ranges from 21 at 1473K to 16 at 1673K (223/10.6 and 223/13.9, respectively). Using the following equation (Schmalzried, 1984),

$$k' = \lambda . D' . (\Delta G/RT) \qquad (A0)$$

an average diffusion coefficient D' can be deduced; k' is the reaction-rate constant (i.e. the one resulting from our electrical meaurements) and λ is a stoechiometric factor. In Evermann and

Cooper, 2003, λ is taken as 5. If we consider that λ is related to the motion of oxygen, $\lambda = 2$ (cf Appendix 3).

For instance, at 1473K, $k' \sim 10^{-9} m^2/s$. Depending on the value of λ, $D' = 2.3.10^{-11}$ or $1.10^{-11} m^2/s$. These D' values are consistent with self-diffusivity values for divalent cations but also for oxygen in basaltic melts (cf Fig. 10.18 in Mysen and Richet, 2005). These calculations underline that fluxes of divalent cations and oxygen probably also contribute to the redox dynamics, cooperating with alkali fluxes.

Appendix 3: Relation of the mobile species fluxes to the evolution of the inner redox front

Redox processes in magmas can be expressed by changes of the ferric/ferrous ratio (Kress and Carmichael, 1988; Dunn and Scarfe, 1986). The corresponding equilibrium can be written as follows:

$Fe^{2+} + ¼\ O_2 = Fe^{3+} + ½\ O^{2-}$ (A1)

The quantity of oxygen consumed or produced in (A1) has direct implications on the structure of the melt and other cations configuration. These cations are considered to be present in the melt under molecular and ionic forms, what can be written by the following equilibria:

$MO = M^{2+} + ½\ O_2 + 2\ e^-$, with M=Ca, Mg (A2)

$A_2O = 2A^+ + ½\ O_2 + 2\ e^-$, with A=Na, K (A3)

Or, rescaling to the stoechiometric coefficient of oxygen in (A1):

$½\ MO = ½\ M^{2+} + ¼\ O_2 + e^-$, with M=Ca, Mg (A'2)

$½\ A_2O = A^+ + ¼\ O_2 + e^-$, with A=Na, K (A'3)

We can define the amount of cation in the oxidized form (molecular form) that is produced when one mole of O_2 reacts with cation i (ionic form) by the following stoechiometric coefficients λ:

$\lambda_{M2+} = \lambda_{A+} = 2$

Regarding oxygen anion, the reaction to consider is:

$½\ O^{2-} = ¼\ O_2 + e^-$ (A4),

what leads to $\lambda_{O2-} = 2$.

Finally, the stoechiometric coefficient corresponding to the electron holes contribution in the redox process can be evaluated using the following equilibria:

$h^{\cdot} + ½\ O^{2-} = ¼\ O_2 + e^-$ (A5)

(A5) implies $\lambda_{h^{\cdot}}=4$.

The evolution of the inner redox front with time can thus be written as:

$$\frac{d\xi}{dt} = \left(\sum_{M^{2+}} \lambda_{M^{2+}} . j_{M^{2+}} + \sum_{A^+} \lambda_{A^+} . j_{A^+} - j_{O^{2-}} + j_{h^{\cdot}} \right) . Vm$$

$$= \left(\sum_{M^{2+}} 2 . j_{M^{2+}} + \sum_{A^+} 2 . j_{A^+} + 2\, j_{O^{2-}} + 4\, j_{h^{\cdot}} \right) . Vm$$

Chapitre 6

Bilan et conclusions

(*Summary and conclusions*)

Les principaux résultats de cette thèse mettent en lumière l'importance des mesures de conductivité électrique dans l'étude de problématiques géologiques. Une étude méthodologique comparant les mesures à deux et quatre électrodes a contribué à mettre en évidence et à corriger les erreurs affectant les mesures électriques à deux électrodes. Cela a permis d'améliorer la qualité des mesures électriques appliquées aux matériaux géologiques, les mesures à deux électrodes étant principalement utilisées par la communauté géologique.

Les propriétés de transport de verres et liquides silicatés naturels ont été étudiées et leur dépendance à la température, à la pression, à la teneur en eau, à la composition et à la fugacité en oxygène a été quantifiée. La conductivité électrique augmente avec la température, la teneur en eau et la teneur en alcalins et diminue lorsque la pression augmente. Elle est essentiellement contrôlée par la diffusivité du sodium, identifié comme le porteur de charge principal. L'application de la loi d'Arrhénius a permis d'estimer l'énergie d'activation (Ea) et le volume d'activation (ΔV) pour chaque échantillon, dans le domaine vitreux et liquide : 60-<150kJ/mol et ~20cm^3/mol, respectivement, pour les compositions du Vésuve, ~100kJ/mol pour le basalte du Kilauea. Des lois de compensation, reliant énergie d'activation et terme pré-exponentiel (σ_0) issus de la loi d'Arrhénius, ont été établies et s'appliquent à une large gamme de compositions magmatiques. A partir de nos données expérimentales, une méthode semi-empirique a été développée pour déterminer Ea, σ_0, ΔV. Cette méthode s'est avérée être efficace pour prédire la conductivité électrique des magmas du Vésuve ainsi que pour d'autres compositions.

Une application géophysique de nos mesures électriques en laboratoire a été consacrée à l'édifice volcanique du Vésuve. Pour la première fois, des mesures en laboratoire, des mesures géophysiques, des données pétrologiques et géochimiques ont été mises en commun pour résoudre un problème volcanologique. Le modèle direct (1-D et 3-D) de la conductivité du Vésuve a d'abord permis de montrer que la saumure superficielle est responsable des variations observées dans les fonctions de transfert, ce qui en fait par conséquent le principal corps conducteur sous le volcan. Les conditions sur cette saumure ont été précisées (~0.5km de profondeur, 1.2km d'épaisseur, 5ohm.m en résistivité). En ce qui concerne un potentiel réservoir de magma superficiel, nos résultats se sont avérés être compatibles avec du magma en cours de refroidissement, remonté mais non émis au cours d'éruptions passées. La

présence d'un magma plus chaud à des profondeurs <4km n'est pas exclue, mais n'est pas l'hypothèse la plus probable. En ce qui concerne l'anomalie détectée sur le terrain à 8-10km de profondeur, nos simulations ont montré qu'elle est compatible avec un réservoir dont les dimensions n'excèdent probablement pas les dimensions du cône et ayant une résistivité >100ohm.m, ce qui correspond à un magma de basse température et très cristallisé ou à un magma plus chaud et en plus petite quantité, interconnecté dans l'encaissant (carbonates). Une comparaison avec les données sismiques acquises sur le volcan, en utilisant des modèles sismiques reliant vitesse des ondes P et S à la structure du magma, favorise la seconde hypothèse. Par ailleurs, notre modèle a permis de souligner le manque de données électriques robustes à longues périodes sur le terrain, et par conséquent la nécessité de mener d'autres études magnétotelluriques sur le Vésuve.

Une application géochimique des mesures électriques en laboratoire s'est concentrée sur l'étude des réactions redox dans les melts basaltiques. Les mesures électriques ont ici été utilisées pour étudier en temps réel les cinétiques redox à haute température (1200-1400°C) suite à des changements de fugacité en oxygène (fO_2 de 10^{-8} à 0.2bars). Nous avons montré que la conductivité augmente légèrement lorsque la fO_2 diminue, et avons exprimé la dépendance de la conductivité à la fO_2 et à la température au moyen d'une loi d'Arrhénius modifiée. L'évolution de la conductivité électrique au cours du temps, fonction de la mobilité du sodium dans le melt, a été corrélée à l'évolution du ratio fer ferrique/fer ferreux. Les réductions sous CO-CO_2 et les oxydations à l'air sont des processus limités par la diffusion alors que les réactions sous CO_2 sont probablement limitées par la vitesse de la réaction. Des valeurs élevées des coefficients de diffusion (10^{-9}-10^{-8}m²/s) et des énergies d'activation correspondantes (Ea_D>200kJ/mol) ont été calculées et expliquées par des mécanismes redox impliquant une coopération entre flux d'alcalins, de cations divalents, et d'oxygène.

La combinaison des mesures électriques -menées afin de quantifier à la fois propriétés de transport et processus de diffusion au sein des magmas- et la modélisation de ces données a permis d'améliorer la précision des études des propriétés physico-chimiques des magmas et, par conséquent, d'améliorer la compréhension des phénomènes magmatiques dans la croûte terrestre.

The main results of this thesis enlightened the importance of electrical conductivity measurements as part of the study of geological problems. A methodological study comparing two- and four-electrode measurements contributed to underline and to correct the errors affecting the two-electrode measurements. This allowed to improve the quality of electrical

measurements applied to geological materials, since two-electrode measurements are principally used by geologists.

Transport properties of natural silicate glasses and liquids have been investigated and their dependence to temperature, pressure, water content, composition and oxygen fugacity has been quantified. The electrical conductivity increases with temperature, water content and alkali content and decreases with increasing pressure. It is essentially controlled by sodium diffusivity, identified as the main charge carrier. The application of the Arrhenius law allowed to estimate the activation energy (Ea) and activation volume (ΔV) for each sample, in the glassy and liquid domain: 60-<150kJ/mol and ~20cm^3/mol, respectively, for Mount Vesuvius compositions, ~100kJ/mol for the Kilauea basalt. Compensation laws, linking activation energy and pre-exponential term (σ_0) from the Arrhenius law, have been established and can be applied to a large magmatic composition range. From our experimental data, a semi-empirical method has been developed in order to determine Ea, σ_0 and ΔV. This method turned out to be efficient to predict the electrical conductivity of magmas from Mount Vesuvius as well as for other compositions.

A geophysical application of our electrical measurements in laboratory has been dedicated to Mount Vesuvius volcanic edifice. For the first time, laboratory measurements, geophysical measurements, petrological and geochemical data have been confronted to solve a volcanological problem. The forward model (1-D and 3-D) of the conductivity of Mount Vesuvius first allowed to show that the superficial brine is responsible of the observed variations in the transfer functions. As a result, this brine is the main conductive body below the volcano. The brine storage conditions have been precised (~0.5km depth, thickness of 1.2km, resistivity of 5ohm.m). As regards a potential shallow magma reservoir, our results are compatible with cooling residual magma not expulsed during the past eruptions. The presence of a hotter magma at depths >4km is not excluded but is not the most probable hypothesis. Concerning the field anomaly detected at 8-10km depth, our simulations showed that it is compatible with a reservoir whose dimensions do not probably exceed the cone dimensions and whose resistivity is >100ohm.m, corresponding to a low-temperature and crystal-rich magma or to a hotter magma interconnected in the surrounding carbonates. A comparison with seismic data recorded on the volcano, using seismic models relating P and S waves velocity to magma structure, supports the second hypothesis. Our model contributed to underline the lack of robust field electrical data at high periods and, thus, the necessity to conduct other magnetotelluric studies at Mount Vesuvius.

A geochemical application of electrical laboratory measurements focused on the study of redox reactions in basaltic melts. Electrical measurements are here used to study in real time the redox kinetics at high temperatures (1200-1400°C) following oxygen fugacity changes (fO_2 from 10^{-8} to 0.2bars). We showed that the conductivity increases slightly when decreasing the fO_2 and expressed the dependence of the conductivity to fO_2 and temperature using a modified Arrhenius law. The evolution of the electrical conductivity with time, function of sodium mobility in the melt, has been correlated to the evolution of the ferric/ferrous ratio. Reductions under CO-CO_2 and oxidations in air are diffusion-limited processes whereas oxidations under CO_2 are probably reaction rate-limited processes. High values of diffusion coefficients (10^{-9}-10^{-8} m^2/s) and of activation energies (Ea_D>200kJ/mol) have been calculated and explained by redox mechanisms involving cooperative fluxes of alkali, divalent cations and oxygen.

The association of electrical measurements -conducted to quantify both transport properties and diffusion processes in magmas- and the modelling of these data allowed to improve the precision of the studies of the physical and chemical properties of magmas, and, as a result, to improve the understanding of magmatic phenomena in the Earth's crust.

Suggestions pour de prochaines études (*Suggestions for future research*)

Les magmas étant des suspensions à trois phases (liquide, cristaux et bulles), leurs propriétés physiques et chimiques sont contrôlées par la présence et les interactions entre ces composants. Les propriétés des magmas ne peuvent se limiter à être simplement recalculées en utilisant des modèles et formalismes élaborés pour reproduire le comportement de magmas contenant des cristaux et des bulles, en particulier car les effets liés aux interactions entre les phases sont approximés. Des mesures expérimentales sur des échantillons à trois phases sont nécessaires et un effort doit être fourni dans ce sens.

L'étude redox réalisée au cours de cette thèse (Chapitre 5) est totalement innovante. Elle offre de larges perspectives en ce qui concerne les études électriques en laboratoire, principalement pour deux raisons : 1) cette étude démontre que les mesures électriques peuvent suivre en temps réel l'évolution d'une réaction chimique, 2) elle souligne aussi que les phénomènes de diffusion, qui, certes, n'engendrent que de petits changements sur la réponse électrique d'un melt silicaté, peuvent être étudiés *in situ* à l'aide de la technique de spectroscopie d'impédance. Par exemple, des mesures électriques conduites sur un assemblage basalte-olivine (analogue croûte-manteau) au cours du temps permettraient

d'étudier les cinétiques et les mécanismes de diffusion de contamination de la croûte terrestre. Une autre application, d'ordre volcanologique, consisterait en l'étude des cinétiques de décompression de magmas riches en volatils (s'inscrivant, en quelque sorte, dans la continuité de l'expérience réalisée sur une obsidienne hydratée à 1bar, présentée au Chapitre 3).

Le lien entre viscosité et conductivité mériterait d'être exploré en détail, de manière à comprendre précisément à l'échelle atomique ce que mesure réellement chacune des deux grandeurs physiques. Les mécanismes de conduction tout comme la nature des porteurs de charge permettent ou empêchent de relier viscosité et conductivité électrique. Une telle étude impliquerait non seulement de coupler les mesures électriques et de viscosité mais aussi d'utiliser des techniques de spectroscopie et de modélisation.

Les mesures électriques ont un avantage significatif sur les mesures sismiques : elles sont techniquement plus simples à mettre en œuvre et les résultats obtenus en laboratoire peuvent être directement appliqués au terrain. Des problèmes d'échelle semblent davantage affecter les mesures sismiques en laboratoire, ce qui ne permet pas d'interpréter aussi facilement les anomalies géophysiques. Notre étude au Vésuve a montré que faire le lien entre laboratoire et terrain contribue de manière efficace à résoudre un problème volcanologique. L'approche proposée par le modèle direct (Chapitre 4) peut non seulement s'appliquer à la volcanologie mais aussi à des problématiques mantelliques et, en cela, elle doit être considérée dans les futurs travaux géophysiques.

Magmas being three-phase suspensions (liquid, crystals and bubbles), their physical and chemical properties are controlled by the presence and the interactions between these components. Magma properties can not come down to be only calculated using models and formalisms elaborated to reproduce the behavior of magmas containing crystals and bubbles, particularly because the effects due to the interactions between the different phases are approximated. Experimental measurements on three-phase samples are necessary and an effort should be done in this direction.

The redox study achieved during this thesis (Chapter 5) is completely innovative. It offers large perspectives as regards electrical studies in laboratory for two main reasons: 1) this study demonstrates that electrical measurements can follow in real time the evolution of a chemical reaction, 2) it also underlines that diffusion phenomena, which, of course, only involve small changes in the electrical response of a silicate melt, can be studied in an in situ way using the technique of impedance spectroscopy. For instance, electrical measurements conducted on a basalt-olivine mixture (crust-mantle analog) with time would allow to

investigate the diffusion kinetics and mechanisms of the contamination of the Earth crust. Another application, of volcanological order, would consist in the study of the kinetics of decompression of volatile-rich magmas (this would be in line with the experiment performed on a hydrous obsidian at 1bar, presented in Chapter 3).

The link between viscosity and conductivity would deserve further consideration, in order to understand precisely at an atomic scale what really measures each of both physical quantities. Conduction mechanisms as well as the nature of the charge carriers allow to relate viscosity to conductivity or prevent from doing it. Such a project would not only imply to couple electrical and viscosity measurements but to use techniques of spectroscopy and modelling, too.

Electrical measurements have a significative advantage compared to seismic measurements : they are technically easier to implement and the results obtained in laboratory can directly be applied to the field. Scaling problems seem to affect more seismic measurements in laboratory, what does not allow to interpret so easily the geophysical anomalies. Our study of Mount Vesuvius showed that linking laboratory and field measurements contributes efficiently to solve a volcanological problem. The approach proposed by the forward model (Chapter 4) can not only be applied to volcanoes but also to problems regarding the mantle and should thus be considered in the geophysical works to come.

Anne POMMIER

Propriétés électriques des magmas

Résumé :

Les expériences ont été menées pour déterminer les propriétés électriques des verres et liquides silicatés du Vésuve et du Kilauea par spectroscopie d'impédance. Une étude méthodologique des mesures à deux et quatre électrodes a amélioré la qualité des mesures électriques. Les mesures ont été faites entre 400 et 1400°C, 0.1 et 400MPa et pour des fugacités en oxygène de 10^{-8} à 0.2 bar. La conductivité électrique croît avec la température, les teneurs en eau et sodium et lorsque pression et fO_2 diminuent. Des lois d'Arrhénius ont été déterminées dans les verres et liquides pour étudier les propriétés de transport. Des énergies d'activation de 60 à 150kJ/mol et un volume d'activation de 20cm^3/mol ont été calculés. Une méthode semi-empirique a été déduite pour estimer la conductivité d'une large gamme de melts. Une application géophysique de nos résultats a consisté en un modèle direct de la conductivité du Vésuve. Les fonctions de transfert s'expliquent par la seule présence d'une saumure. Sa forte conductivité rend la détection d'un corps magmatique profond difficile. Cependant, nos simulations ont démontré que les données géophysiques actuelles sont en accord avec un réservoir de magma cristallisé ou du magma plus chaud interconnecté dans l'encaissant carbonaté. Une application géochimique a consisté au suivi en temps réel des cinétiques redox dans des basaltes, en utilisant la dépendance au temps de la conductivité suite à un changement de fO_2. L'évolution de la conductivité au cours du temps, liée à la mobilité du sodium, est identique à celle du ratio fer ferrique/fer ferreux du melt. La réduction sous CO-CO_2 et l'oxydation à l'air sont limitées par la diffusion, mais pas l'oxydation sous CO_2, probablement à cause de réactions à l'interface gaz/melt. Les valeurs calculées élevées de diffusivité et d'énergie d'activation ont été expliquées par des mécanismes redox impliquant une coopération entre flux d'alcalins, de cations divalents et d'oxygène.

Mots clés : conductivité électrique, melts silicatés, propriétés de transport, Vésuve, modèle direct, dynamiques redox.

Electrical properties of magmas

Summary :

Experiments were conducted to determine the electrical properties of silicate glasses and liquids from Mt Vesuvius and Kilauea volcanoes using impedance spectroscopy. A methodological study of the two and four electrode measurements improved the quality of the electrical measurements. Measurements were performed between 400 and 1400°C, from 0.1 to 400MPa and for oxygen fugacities ranging from 10^{-8} to 0.2 bar. The electrical conductivity increases with increasing temperature, water content, sodium content and with decreasing pressure and fO_2. Arrhenius laws were determined for glasses and liquids to investigate the transport properties. Activation energies from 60 to 150kJ/mol and an activation volume of 20cm^3/mol were calculated. A semi-empirical method was deduced to estimate the conductivity of a wide range of melts. A geophysical application of our results consisted in the forward modelling of the conductivity of Mt Vesuvius. Transfer functions are explained by the only presence of a brine. Its high conductivity makes difficult the detection of a deeper magmatic body. Still, our simulations demonstrated that present geophysical data are compatible with a crystallized magma reservoir or a hotter magma interconnected in the surrounding carbonates. A geochemical application consisted in the monitoring in real-time of redox kinetics in basaltic liquids, using the time-dependence of electrical conductivity following fO_2 step changes. The evolution of the conductivity with time, related to sodium mobility, is identical to that of the ferric/ferrous ratio of the melt. Reduction under CO-CO_2 and oxidation in air are diffusion-limited, while oxidations under CO_2 are not, probably due to gas/melt interface reactions. High calculated diffusivities and activation energies have been explained by redox mechanisms involving cooperative alkali, divalent cation and oxygen fluxes.

Keywords : electrical conductivity, silicate melts, transport properties, Mt. Vesuvius, forward modelling, redox dynamics.

Institut des Sciences de la Terre d'Orléans
(ISTO-UMR6113-CNRS/Université d'Orléans)
1A rue de la Férollerie
45071 Orléans Cedex 2, FRANCE